

Fast Plane Wave Imaging

Jensen, Jonas; Jensen, Jørgen Arendt; Stuart, Matthias Bo

Publication date:
2017

Document Version
Publisher's PDF, also known as Version of record

[Link back to DTU Orbit](#)

Citation (APA):
Jensen, J., Jensen, J. A., & Stuart, M. B. (2017). Fast Plane Wave Imaging. Technical University of Denmark, Department of Electrical Engineering.

DTU Library

Technical Information Center of Denmark

General rights

Copyright and moral rights for the publications made accessible in the public portal are retained by the authors and/or other copyright owners and it is a condition of accessing publications that users recognise and abide by the legal requirements associated with these rights.

- Users may download and print one copy of any publication from the public portal for the purpose of private study or research.
- You may not further distribute the material or use it for any profit-making activity or commercial gain
- You may freely distribute the URL identifying the publication in the public portal

If you believe that this document breaches copyright please contact us providing details, and we will remove access to the work immediately and investigate your claim.

PhD Thesis



Fast Plane Wave Imaging

Jonas Jensen

Supervised by: Professor Jørgen Arendt Jensen, PhD, Dr. Techn.

Co-supervised by: Associate Professor Matthias Bo Stuart, PhD

Technical University of Denmark
Kgs. Lyngby, Denmark 2017

Contents

Preface	vii
Summary	ix
Resumé	xi
Acknowledgements	xiii
Abbreviations	xv
1 Introduction	1
1.1 Motivation	1
1.2 Objective and contributions	4
1.3 Publications in the thesis	4
1.4 Publications not included in the thesis	5
1.5 Structure of the thesis	6
2 Blood flow imaging in parallel systems	9
2.1 Parallel imaging and acquisition systems	9
2.2 Focusing in parallel imaging	11
2.3 Estimation of blood flow velocities	13
2.4 Estimation of blood flow velocity vectors	16
2.5 Fast and slow velocity flow	20
3 Plane wave image quality optimization	23
3.1 Background and purpose	23
3.2 Emitted field for a plane wave	24
3.3 Imaging performance measures	26
3.4 Method for optimization of image quality	26
3.5 Simulations	28
3.6 Measurements	31

3.7	Discussion and summary	34
4	Plane wave vector flow imaging	39
4.1	Background and purpose	39
4.2	Methods for transverse oscillation and directional beamforming	40
4.3	Method for simulations and experiments	44
4.4	Straight vessel phantoms	46
4.5	CFD simulation of carotid bifurcation	49
4.6	<i>In vivo</i> carotid bulb	52
4.7	Slow velocity flow	54
4.8	Discussion and summary	55
5	<i>In vivo</i> study of plane wave vector flow imaging	57
5.1	Background and purpose	57
5.2	Methods for experiments	58
5.3	Methods for evaluation	59
5.4	Comparison between phantom VFI and CFD simulation	60
5.5	Precision of VFI <i>in vivo</i>	63
5.6	<i>In vivo</i> complex flow patterns	66
5.7	Discussion and summary	67
6	Plane wave slow flow imaging in the human placenta	71
6.1	Background and purpose	71
6.2	Data acquisition	73
6.3	Data processing	73
6.4	Results	75
6.5	Discussion and summary	81
7	Vector velocity volume flow estimation	83
7.1	Introduction	83
7.2	Volume flow estimation	84
7.3	Sources of error	85
7.4	Theoretical analysis	86
7.5	Clinical scans	88
8	Project Conclusion and Perspectives	91
	Bibliography	93
	References from Chapter 1	93
	References from Chapter 2	93
	References from Chapter 3	101
	References from Chapter 4	102

References from Chapter 5	105
References from Chapter 6	105
References from Chapter 7	107
Paper I	109
Paper II	125
Paper III	131
Paper IV	145
Paper V	151
Paper VI	157
Paper VII	175
Paper VIII	189

Preface

This PhD thesis has been submitted to the Department of Electrical Engineering at the Technical University of Denmark in partial fulfillment of the requirements for acquiring a PhD degree. The research providing the foundation for the thesis has been conducted over a period of three years from May 1, 2014, to April 30, 2017 at the Center for Fast Ultrasound Imaging (CFU), Department of Electrical Engineering. The project has been supervised by Prof. Jørgen Arendt Jensen, PhD, Dr. Techn, and co-supervised by Assoc. Prof. Matthias Bo Stuart, PhD. The project was financially supported by grant 82-2012-4 from the Danish National Advanced Technology Foundation and BK Ultrasound Aps, Denmark.

From June to October 2016 I had the privilege of spending an external research stay in Paris as a visiting PhD student in Prof. Mickael Tanter's group at the Institut Langevin, ESPCI Paris. In addition to this, I had the opportunity to attend conferences in Chicago (USA), Taipei (Taiwan), Tours (France), and Helsingborg (Sweden). Travelling to these places to present and discuss my research has been a huge experience and broadened my horizon of both the technical and clinical side of medical ultrasound.

Jonas Jensen
Kgs. Lyngby, Denmark
April 2017

Summary

This PhD project investigates and further develops methods for ultrasound plane wave imaging and blood flow estimation with the objective of overcoming some of the major limitations in conventional ultrasound systems, which are related to low frame rates and only estimation of velocities along the ultrasound beam.

The first part of the contribution investigates the compromise between frame rate and plane wave image quality including the influence of grating lobes from a λ -pitch transducer. A method for optimizing the image quality is suggested, and it is shown that the frame rate can be increased by a factor of three without loss of image quality for a particular $\lambda/2$ -pitch transducer, when compared to a λ -pitch transducer.

The second part presents a method for high frame rate 2-D vector flow imaging. The method was validated in simulations and measurements, and it is shown that angles can be estimated with a bias and standard deviation less than 2° , and the velocity magnitude can be estimated with a bias and standard deviation less than 4 % over a large range of beam-to-flow angles. The vector flow method was also investigated under laminar and complex flow conditions in the carotid arteries in ten healthy volunteers. Complex flow patterns were measured in an anthropomorphic flow phantom and showed good agreement with the velocity field simulated using computational fluid dynamics.

The last part of the contribution investigates two clinical applications. Plane wave imaging was used for slow velocity flow estimation in the human placenta, which made it possible to map the vessel resistance in several fetal arteries. Finally, vector flow imaging was used for volume flow estimation in patients undergoing dialysis. The sources of error related to the volume flow estimation were investigated, making it possible to compensate for the errors.

The developed techniques for plane wave imaging using high frame rates and/or estimation of 2-D vector flow may give the clinicians new tools for assessing the health of blood vessels and aid while examining patients with cardiovascular and organ diseases.

x

Resumé

(Summary in Danish)

I dette Ph.D. projekt er metoder inden for ultralydsbilleddannelse og estimering af blodets strømninger blevet undersøgt og videreudviklet ved brug af plane ultralydsbølger. Formålet har været at overkomme nogle af de største udfordringer i konventionelle ultralydssystemer, som er begrænset af lav temporal opløsning og kun estimering af blodet strømning langs ultralydsbølgens udbredelsesretning.

Den første del af afhandlingen omhandler kompromiset mellem temporal opløsning og billedkvalitet samt indflydelsen af gittersløjfer fra en λ -pitch transducer. En metode til optimering af billedkvalitet blev foreslået, og det blev vist, at den temporale opløsning, *frame rate*, kan blive øget tre gange uden at miste billedkvaliteten, når man anvender en specifik $\lambda/2$ -pitch transducer i stedet for en λ -pitch transducer.

En metode til estimering af blodets 2-D vektorhastigheder med en høj temporal opløsning er præsenteret i den anden del af afhandlingen. Metoden blev valideret i simuleringer og fantommålinger, og det blev demonstreret, at vinkler kan estimeres med et bias og en standard afvigelse under 2° , og at størrelsen af hastighedsvektoren kan estimeres med et bias og en standard afvigelse under 4 %. Metoden til estimering af vektorhastigheder blev også undersøgt for laminare og komplekse strømningsforhold i halspulsåren på ti raske frivillige. Komplekse strømningsmønstre blev målt i et antropomorft flow fantom og viste god overensstemmelse med et simuleret hastighedsfelt, som var baseret på simuleringermodeller.

To kliniske anvendelser er undersøgt i den sidste del af afhandlingen. Plane bølger blev brugt til at estimere blodets langsomme strømningshastigheder i moderkagen på gravide kvinder. Metoden gjorde det muligt at kortlægge de føtale arteriers strømningsmodstand. Afslutningsvis blev vektorhastigheder brugt til at estimere volumen flow i patienter i dialysebehandling. Fejlkilder relateret til volumen flow estimering blev undersøgt, hvilket gjorde det muligt at kompensere for fejlene.

De udviklede teknikker med plane ultralydsbølger ved høj *frame rate* og/eller 2-D vektorhastigheder kan give klinikerne nye redskaber til at undersøge blodkar samt være en hjælp ved undersøgelser af patienter med kardiovaskulære sygdomme og organsygdomme.

Acknowledgements

First of all, I would like to thank my supervisor, Prof. Jørgen Arendt Jensen, who has contributed with exceptional guidance, has been a tremendous source of knowledge, and supported the project with great motivation. Thank you for letting me participate in this exciting research project. It has been a privilege to work in your highly skilled research group with some of the best facilities in the world. I would also like to thank my co-supervisor, Assoc. Prof. Matthias Bo Stuart, who has always taken the time to help me and provided me with vast knowledge, constructive advice, and invaluable discussions, which have been essential for this project.

I want to thank all of my colleagues at CFU, in the CMUT group at DTU Nanotech, and the MDs at Rigshospitalet. You have all contributed to an excellent working environment, which I have enjoyed both academically and socially. I want to thank my office mate Carlos Armando Villagómez-Hoyos for the good discussions we have had and for teaching me so much about velocity estimators and echo-canceling.

A special thanks goes to Prof. Mickael Tanter from Institut Langevin, ESPCI Paris for letting me join his research group for almost five months in the summer and fall of 2016. His group gave me the best possible experience and contributed to making the stay a joy while at work and after work in the wonderful city of Paris. In particular, I thank Marion Imbault and Bruno-Felix Osmanski for contributing to the project, and Edouard Lecarpentier from the Maternité Port-Royal Hospital for helping me with scanning volunteers during several late afternoons. I would also like to thank the Idella foundation for supporting my external research stay financially.

Finally, a huge thanks goes to my family. Also to you, Alfonso Ma-Tay, for always supporting me and for your kind help in correcting my texts.

Abbreviations

AVF	Arteriovenous fistula
CCA	Common carotid artery
CFD	Computational fluid dynamics
CFM	Color flow mapping
DB	Directional beamforming
DTU	Danmarks Tekniske Universitet (Technical University of Denmark)
ECA	External carotid artery
$F\#$	F-number, equal to the focal length divided by the aperture diameter
FDA	Food and Drug Administration
FWHM	Full-width at half-maximum
HRI	High resolution image
ICA	Internal carotid artery
IEC	International Electrotechnical Commission
IUGR	Intrauterine growth restriction
LRI	Low resolution image
PRF	Pulse Repetition Frequency
PSF	Point-spread-function
RF	Radio frequency
RI	Resistivity index
ROI	Region of interest
SA	Synthetic aperture
SARUS	Synthetic aperture real-time ultrasound system
SD	Standard deviation
SNR	Signal to Noise Ratio
SVD	Singular value decomposition
TO	Transverse oscillation
UDT	Ultrasound dilution technique
US	Ultrasound
VFI	Vector flow image

CHAPTER 1

Introduction

1.1 Motivation

The cardiovascular system is essential for the human body to function. It allows blood to flow from the heart to all tissues of the body and back. Blood carries nutrients, oxygen, and carbon dioxide, and exchanges waste products with all types of tissues. Hormones, components of the immune system, and enzymes are also transported in the blood to the entire body. The cardiovascular system has an important role in providing correct functioning of the immune system, regulating blood pressure, and maintaining homeostasis. The structure of the cardiovascular system into arteries, capillaries, and veins is extensive. Blood is pumped from the heart into large, elastic arteries, which branch into progressively smaller arteries. Blood flows from arteries into capillaries, where the exchange between blood and tissue occurs. Blood returns to the heart through the venous system.

Given the importance of the cardiovascular system, the function and health of the heart and blood vessels is crucial. Diseases affecting the cardiovascular system are called cardiovascular diseases and are the leading cause of death worldwide (WHO 2015). The diseases include coronary artery diseases, stroke, aortic aneurysms, thrombosis, and artery disease. Furthermore, restrictive liver conditions, chronic kidney disease, and intrauterine growth restriction during pregnancy are organ diseases, which may affect the dynamics of blood flow. Atherosclerosis is a precursor to many of the cardiovascular diseases, and involves the build up of a plaque in the walls of arteries. The plaque may grow and rupture to narrow (stenose) or completely occlude the vessel. Blood clots formed in veins and arteries may also travel to another location in the body to occlude smaller vessels. Plaque growth and vessel occlusion result in a disturbed blood flow pattern and may lead to a sudden deficit of oxygenated blood to the tissues. Cell death and organ failure may result in fatal consequences.

Several medical imaging modalities have the ability to image blood vessels and quantify blood flow in the human body. Magnetic Resonance Imaging (MRI), X-ray computed tomography (CT), ultrasound imaging, and plethysmography are imaging techniques, which are used to study the function and health of the cardiovascular system. Advances within medical imaging have provided researchers and medical doctors with a new knowledge and understanding of the human physiology and mechanisms causing cardiovascular diseases. Each of the imaging modalities has its advantages and limitations and are preferred depending on the application. Ultrasound imaging is the preferred

and dominating imaging modality for real-time imaging and quantification of blood flow velocities. Unlike many other imaging modalities, ultrasound provides excellent temporal and spatial resolution, is relatively inexpensive, safe, and can be applied at the patient bedside. Ultrasound has different modes for visualization, so that vessel and tissue anatomy is showed on gray-scale B-mode images, color-encoded indication of blood flow velocities in color flow mapping (CFM), and single-point estimation of velocities as a function of time in spectrograms (spectral Doppler), when quantitative measures are needed.

However, there are important limitations of current commercial ultrasound systems, which include: (1) a relatively low frame rate is attainable and a limited amount of data is available for velocity estimation, and (2) only 1-D velocity estimation of the blood flow is possible. These limitations are further explained below along with possible solutions to the problems.

In relation to the low frame rate, the attainable frame rate in ultrasound systems is related to the emissions of sound waves, where data are acquired sequentially line by line. For flow estimation, sound is emitted in the same direction a number of times and the movement is estimated from the acquired sequential data. This limits the frame rate and region of interest significantly. Relatively few emissions are employed per focusing line to maintain a decent frame rate, but it results in poor precision of the velocity estimates and low sensitivity to slow velocity flow. Furthermore, the sequential data acquisition implies only optimal focusing at one depth, which restricts the attainable image quality.

To overcome these limits it has been suggested to insonify a large region using either spherical or plane waves. Rather than beamforming a single image line per emission, several image lines are beamformed in parallel for the entire image. The image is only focused in receive as there is no transmit focusing. The focusing in transmit can be restored or synthesized by combining beamformed images acquired from other transmit events. The parallel imaging technique is referred to as synthetic aperture (SA) imaging (Jensen, S. Nikolov, et al. 2006), when spherical waves are emitted, and plane wave or ultrafast imaging, when plane waves are emitted (Tanter and Fink 2014). Both techniques rely on the same principles of beamforming entire images and restoring the transmit focus by combining beamformed images, and thus, breaking with the conventional line-by-line data acquisition. Parallel acquisition systems are needed for the techniques, as several lines are beamformed in parallel. The advantages of SA and plane wave imaging are very high acquisition rates for a large region of interest, so that the full dynamics of complex blood flow patterns can be followed at thousands of frames per second. Since continuous data is available everywhere in the image, it is possible to average over a large number of emissions in the velocity estimators, which improves the precision of the estimates. For slow flow imaging, the acceleration of flow is low and this makes it possible to average over an even larger number of emissions to increase sensitivity and detectability. This is also an advantage for tissue echo-canceling (clutter) filters, which has further improved flow sensitivity (Demene et al. 2015).

High frame rate imaging may, however, result in issues related to the image quality,

where important tradeoffs still have to be made with the frame rate. Furthermore, artifacts can be introduced due to the emission of unfocused waves and the intermission motion of tissue. These considerations should be subject for further research.

In relation to the 1-D velocity estimation of blood flow, only the velocity component along the ultrasound beam is measured in conventional ultrasound systems. The measured velocity is thus a 1-D estimate of the true velocity magnitude, which has components in two or three dimensions. The 1-D estimate derived from spectral Doppler is usually corrected by the angle between the flow direction and the ultrasound beam to obtain the full 2-D velocity magnitude in the scan plane. The beam-to-flow angle is determined by the operator based on the vessel orientation on the B-mode image. The correction only works when laminar flow is parallel to the vessel, and the angle should be below 60° to maintain an accurate estimate (Kruskal et al. 2004). However, this is often not the case as most major blood vessels run parallel to the skin surface, and are curved and have branches and stenosed regions. The resulting blood flow pattern is non-laminar and very complex, and the flow angle changes within the cardiac cycle and depending on spatial location. This is especially the case for patients with severe cardiovascular diseases. CFM and spectral Doppler have therefore limited use in complex vessel geometries and stenosed regions, because blood flow patterns remain unrevealed and the velocity estimates are prone to large errors (Stewart 2001).

Methods for finding the velocity components in two or three directions have therefore been suggested since the 1970s. Several methods exist, each with its own advantages and disadvantages, and some of them will be reviewed in the next chapter. The combination of 2-D vector flow methods and parallel imaging has improved performance of velocity estimators and shown great potential for visualizing fast transient flow events (Hansen et al. 2009). Vector flow estimation combined with parallel imaging has attracted a lot of attention in recent years as several research groups also have gained access to parallel acquisition systems. Methods have been developed, combined and refined, leading to better performance and more quantitative estimates (Jensen, S. I. Nikolov, et al. 2016). This improves the precision of derived quantitative measures, e.g. volume flow, resistivity index, stenosis degree, and pressure gradients. Furthermore, the angle independent velocities make the examination less dependent on the operator.

Despite these advances, it is important to appreciate that each velocity estimator has its own advantages and disadvantages regarding performance, computational load, and applications. Especially, the performance for estimation of both laminar and complex blood flow patterns has only been sparsely investigated in the literature, in addition to which clinical applications the techniques are suited for. Further research is needed to assess the possibilities and drawbacks associated with parallel imaging and flow estimation.

1.2 Objective and contributions

This thesis investigates and further develops methods for plane wave imaging and flow estimation with the objective of overcoming some of the major limitations in conventional ultrasound systems, which are related to low frame rates and only estimation of velocities along the ultrasound beam.

The contribution falls within three parts: (1) a plane wave B-mode sequence is designed and optimized with respect to image quality and frame rate, (2) plane wave imaging and vector flow methods are combined to yield the 2-D motion of the blood, and the method is investigated for both complex and laminar flow *in vivo* in a small group of healthy volunteers, and (3) clinical applications of plane wave imaging for slow velocity flow estimation in the human placenta as well as volume flow estimation in patients undergoing dialysis are investigated.

1.3 Publications in the thesis

B-mode imaging

I **J. Jensen**, M. B. Stuart, and J. A. Jensen

"Optimized Plane Wave Imaging for Fast and High-Quality Ultrasound Imaging"
Published in *IEEE Trans. Ultrason., Ferroelec., Freq. Contr.*, Vol. 63, No. 11, p. 1922-1934 (2016).

II **J. Jensen**, M. B. Stuart, and J. A. Jensen

"Increased Frame Rate for Plane Wave Imaging Without Loss of Image Quality"
Published in *Proceedings of IEEE Ultrason. Symp.*, p. 1-4 (2015).

Vector flow imaging

III **J. Jensen**, C. A. Villagómez-Hoyos, M. B. Stuart, C. Ewertsen, M. B. Nielsen, and J. A. Jensen

"Fast Plane Wave 2-D Vector Flow Imaging Using Transverse Oscillation and Directional Beamforming"
Accepted for publication in *IEEE Trans. Ultrason., Ferroelec., Freq. Contr.* (2017).

IV **J. Jensen**, M. B. Stuart, and J. A. Jensen

"High Frame Rate Vector Velocity Estimation using Plane Waves and Transverse Oscillation"
Published in *Proceedings of IEEE Ultrason. Symp.*, p. 1-4 (2015).

V **J. Jensen**, C. A. Villagómez-Hoyos, M. B. Stuart, C. Ewertsen, M. B. Nielsen, and J. A. Jensen

"In Vivo High Frame Rate Vector Flow Imaging Using Plane Waves and Directional

Beamforming"

Published in *Proceedings of IEEE Ultrason. Symp.*, p. 1-4 (2016).

VI **J. Jensen**, C. A. Villagómez-Hoyos, J. B. Olesen, B. Tomov, R. Moshavegh, S. Holbek, M. S. Traberg, M. B. Stuart, C. Ewertsen, K. L. Hansen, C. Thomsen, M. B. Nielsen, and J. A. Jensen

"Accuracy and Precision of Plane Wave Vector Flow Imaging for Laminar and Complex *In Vivo* Flow"

Submitted to *Ultrasound Med. Biol.*, (2017).

Clinical applications

VII **J. Jensen**, J. B. Olesen, M. B. Stuart, P. M. Hansen, M. B. Nielsen, and J. A. Jensen

"Vector velocity volume flow estimation: Sources of error and corrections applied for arteriovenous fistulas"

Published in *Ultrasonics*, Vol. 70, p. 136-146 (2016).

VIII **J. Jensen**, J. B. Olesen, P. M. Hansen, M. B. Nielsen, and J. A. Jensen

"Accuracy and Sources of Error for an Angle Independent Volume Flow Estimator"

Published in *Proceedings of IEEE Ultrason. Symp.*, p. 1-4 (2014).

1.4 Publications not included in the thesis

- M. B. Stuart, **J. Jensen**, A. H. Brandt, S. Nikolov, M. B. Nielsen and J. A. Jensen
"In-Vivo Synthetic Aperture and Plane Wave High Frame Rate Cardiac Imaging"
Published in *Proceedings of IEEE Ultrason. Symp.*, p. 1209-1212 (2014).
- M. B. Stuart, **J. Jensen**, T. di Ianni and J. A. Jensen
"Image Quality Degradation from Transmit Delay Profile Quantization"
Published in *Proceedings of IEEE Ultrason. Symp.*, p. 1-4 (2015).
- A. H. Brandt, **J. Jensen**, K. L. Hansen, P. Hansen, T. Lange, M. Rix, J. A. Jensen, L. Lönn and M. B. Nielsen
"Surveillance for hemodialysis access stenosis: usefulness of ultrasound vector volume flow"
Published in *J. Vasc. Access*, p. 453-552 (2016).
- R. Moshavegh, **J. Jensen**, C. A. Villagómez-Hoyos, M. B. Stuart, M. C. Hemmsen and J. A. Jensen
"Optimization of Synthetic Aperture Image Quality"
Published in *Proceedings of SPIE Med. Imag.*, p. 97900Z-97900Z-9 (2016).

1.5 Structure of the thesis

The thesis starts out with assembling the relevant literature and technical background related to the conducted research. The subsequent chapters concern the scientific contribution and are structured to demonstrate the progress from plane wave B-mode imaging, to 2-D vector flow imaging, and to applications of slow velocity flow imaging and volume flow estimation. Not all details from the described studies have been included in order to improve the flow of the text, and the reader is therefore occasionally referred to the appended papers.

Chapter 2 gives a historic perspective by describing the developments within parallel imaging and acquisition systems. An overview of previous published literature on blood velocity estimation in ultrasound is given, and the extension of the techniques from line-by-line imaging to parallel imaging is presented.

Chapter 3 presents a method for optimizing parameters affecting the image quality in plane wave imaging. The number of emissions and steering angles is optimized to attain the best images with the highest frame rate possible. The impact of grating lobe artifacts is investigated by comparing the image quality for a λ -pitch transducer to a $\lambda/2$ -pitch transducer.

Chapter 4 presents a method for vector flow imaging using plane waves for data acquisition. Following a theoretical description of the velocity estimator, the approach is tested in simulations and measurements of straight vessel phantoms. A computational fluid dynamics (CFD) simulation of complex flow patterns in a carotid bifurcation model is used to study the method under more realistic conditions, and it is succeeded by an *in vivo* scan. Finally, a phantom measurement of slow velocity flow is presented.

Chapter 5 continues the study from Chapter 4 by investigating the accuracy and precision of the plane wave vector flow method *in vivo* under laminar and complex flow conditions. An anthropomorphic flow phantom is scanned and the estimates are compared to a CFD simulation for finding the accuracy of the method. The precision of the velocity estimates is studied in scans of the carotid artery among ten healthy volunteers.

Chapter 6 shows examples from a study where plane wave imaging is applied clinically for estimating slow velocity flow in the small vasculature of the human placenta. 1-D velocity estimation is combined with heart rate detection to map the resistivity of fetal arteries inside the placenta.

Chapter 7 deviates from the previous chapters as it investigates a method for vector velocity volume flow estimation and its sources of error. Line-by-line imaging is used for the data acquisition, but it can be extended to plane wave imaging. The method is applied

clinically for scans of arteriovenous fistulas in hemodialysis patients.

Chapter 8 concludes the thesis by summarizing the major results and learnings achieved in the project. The chapter provides suggestions for further research and puts the project into perspective.

CHAPTER 2

Blood flow imaging in parallel systems

2.1 Parallel imaging and acquisition systems

The core technology in ultrasound scanners is the beamformer, which conventionally utilizes a sequential line-by-line data acquisition and processing. Parallel imaging techniques break with this standard by insonifying a larger field of view and beamforming several lines simultaneously per emission. Examples of parallel imaging techniques are synthetic aperture and plane wave imaging. The developments within these imaging techniques happened at the same time, where one originated from radar and the other from optics. In this section, both are described briefly along with parallel acquisition systems.

Synthetic aperture techniques were originally developed for radar systems and have been investigated in ultrasound imaging since the early 1970s (Flaherty, Erikson, and Lund 1967; Prine 1972). The initial studies used a direct implementation of the SA principle from radar, a monostatic approach where a single element was used for transmission and reception, and the transmitter/receiver then was moved to continue the process (Jensen, S. Nikolov, et al. 2006). The first attempts suffered from very low signal-to-noise ratio (SNR), but this issue was partially solved in the early 1990s by replacing the single-element transmission with multi-element transmissions of the subaperture. O'Donnell and Thomas (O'Donnell and Thomas 1992) used a circular aperture and Karaman et al. (Karaman, Li, and O'Donnell 1995) extended it to plane apertures. Lockwood et al. (Lockwood and F. Foster 1995; Lockwood, Talman, and Brunke 1998) used sparse synthetic aperture systems for 3D imaging and Nikolov et al. (S. I. Nikolov and Jensen 2002) studied virtual sources located behind the array in SA imaging. In all cases, time-delays are applied on the multi-element subaperture to transmit a spherical wave, which emulates the emission from a point (single element) in front of or behind the transducer. The point is termed a virtual source.

Fink et al. (Fink 1992) worked also on parallel imaging techniques and made important contributions in the field of plane wave imaging. His group was inspired by optics and adapted approaches from optical holography, where a single and wide field-of-view ultrasound beam was transmitted into the medium. The image was then reconstructed from backscattered echoes using a time-reversal focusing concept (Fink 1992), which corresponds to parallel receive beamforming. Fink's group was primarily interested in

real-time imaging of the transient propagation of shear mechanical waves in human tissue to assess local viscoelastic properties. Also dubbed transient elastography, the technique required high frame rates with thousands of frames per second to follow the induced displacements on a millimetre scale. The concept was demonstrated using plane wave transmissions and parallel receive beamforming, and the high-frame rate plane wave imaging technique was named ultrafast imaging (Sandrin, Catheline, et al. 1999; Tanter, Bercoff, et al. 2002). The approach was also used for the first *in vivo* clinical study of ultrafast imaging for breast cancer diagnosis (Bercoff, Chaffai, et al. 2003). While the ultrafast imaging approach with a single transmitted plane wave worked well for transient elastography, poor image quality was attained when they applied the technique for B-mode imaging of complex speckle media. Montaldo et al. (Montaldo et al. 2009) proposed therefore in 2009 to transmit several steered plane waves and coherently sum the individually beamformed images to rebuild a dynamic transmit focusing. This imaging principle is similar to SA imaging proposed in the 1990s.

Another method for high-frame rate imaging was proposed by Lu (J. Y. Lu 1997, 1998), who used a pulsed plane wave in transmission and limited-diffracting array beam weighting in reception. By performing a spatial Fourier transformation of the object function, an image was reconstructed. It was later proposed to add multiple limited-diffracting beams and steered plane waves to perform spatial compounding (Cheng and J. Lu 2006).

The techniques for parallel imaging require dedicated parallel imaging systems for data acquisition. The developments of the systems have taken place since the late 1970s along with important contributions within parallel imaging. Delannoy et al. (Delannoy et al. 1979) presented in 1979 one of the first ultrasound systems capable of an analog-based parallel processing. The system was designed to achieve higher frame rates in cardiac imaging than conventional systems. A single unfocused acoustical pulse was transmitted by a transducer, and the system was capable of forming 20 beamformed image lines in parallel. The technology at that time was limited in both the electronics and processing power, but showed the concepts of high-frame-rate imaging using a parallel system.

Another parallel system capable of high-frame-rate imaging was the Explososcan system developed at Duke University in 1984, which was presented by Shattuck et al. (Shattuck et al. 1984). A parallel processing approach for phased-array sector scanning was implemented, and it was based on the transmission of a slightly defocused (broadened) ultrasound beam and the parallel processing of four beamformed image lines. The four parallel lines in receive were beamformed by properly delaying the received signals in an analog circuit. The data acquisition rate was thereby increased by a factor of four compared to conventional systems. Moreover, an implementation of the approach for volumetric imaging was later proposed in 1991 by Smith and von Ramm (Smith, Pavy, and Ramm 1991; von Ramm, Smith, and Pavy 1991).

During the 1990s, the development from analog systems to digital beamformers and systems with a high channel count and sampling rates opened new possibilities for parallel imaging systems. It was possible to store data for all receive channels and for

each emission, which was a requirement for full parallel beamforming and imaging. A key step in this development was the introduction of the first digital research systems for parallel beamforming pioneered by Jensen et al. (Jensen, Holm, et al. 1999) and Sandrin et al. (Sandrin, Catheline, et al. 1999) in 1999. More parallel acquisition systems emerged in the late 2000s, including a system by Lu et al. (J. Lu, Cheng, and Wang 2006) and the ULA-OP system (Tortoli, Bassi, et al. 2009). The systems made it possible to perform parallel imaging and velocity estimation *in vivo* and to demonstrate the improved performance compared to conventional ultrasound imaging. This was shown, e.g. by Gammelmark et al. (Gammelmark and Jensen 2003; Pedersen, Gammelmark, and Jensen 2007) for anatomical imaging, where SA imaging was combined with temporal encoded excitation signals to increase the imaging depth.

Following the developments in parallel imaging including advances in parallel acquisition systems, the technology has started to be implemented into commercially available ultrasound systems. The clinical Aixplorer system (Supersonic Imagine, Aix en Provence, France) and the Verasonics research platform (Verasonics, Redmond, WA) were among the first commercial systems for parallel imaging. Systems such as the Philips EPIQ systems (Philips Healthcare, Eindhoven, Netherlands) and GE Vivid systems (GE Vingmed, Horten, Norway) also use parallel imaging. This has accelerated research in the field of high-frame rate imaging as more research groups have obtained access to the systems, and it has also moved research out of academic labs and into clinics (Tanter and Fink 2014). Several applications of fast parallel imaging in medical ultrasound have emerged along this development, including blood flow imaging (S. I. Nikolov and Jensen 2003), shear wave elastography (Sandrin, Tanter, et al. 2002; Bercoff, Tanter, and Fink 2004), estimating the local pulse wave velocity (Hasegawa and Kanai 2008; Vappou, Luo, and Konofagou 2010), imaging of contrast agents (Couture, Fink, and Tanter 2012), and imaging of brain activity (Mace et al. 2011).

2.2 Focusing in parallel imaging

The focusing principle for plane wave and SA imaging is fundamentally the same and is shown in Fig. 2.1. At each transmit event, an ultrasound wave is transmitted from the whole array aperture for plane wave imaging, or from a single or a group of elements for SA imaging. The delay profile of the emitted sound wave is adjusted to yield either a plane or spherical wave, which is steered and propagates in a given direction. Backscattered echoes are then recorded using all elements on the receive aperture. A full image can be focused in receive and reconstructed to yield a low resolution image (LRI), which has no transmit focusing. A new group of elements can be excited or a plane wave can be steered in another direction to yield a new LRI. The transmit-receive process is repeated for a desired number of transmit events. Combining all the LRIs for all emissions gives a high resolution image (HRI), which has fully dynamic transmit and receive focusing. The combination of LRIs is performed by summing in phase the signals, and the process is

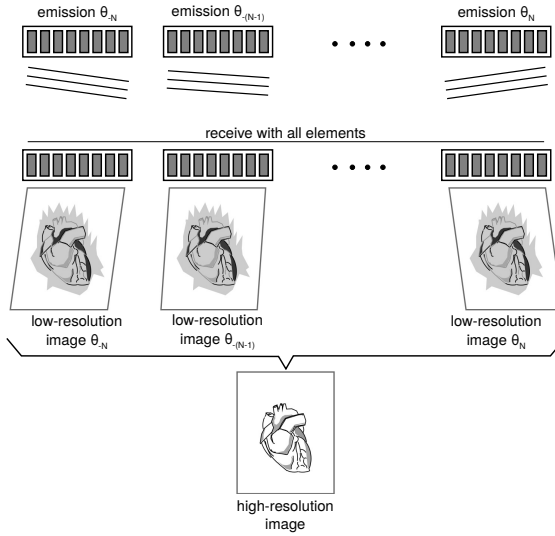


Figure 2.1: Imaging principle in parallel imaging for emission of plane waves. For each emission, the signals are received on all transducer elements to yield LRIs. The combination of these LRIs yields a HRI. Modified from (S. I. Nikolov and Jensen 2001).

often referred to as coherent compounding for plane wave imaging.

The focusing is performed by calculating the delays for the emitted field as shown in Fig. 2.2. Only the focusing of plane waves is here derived, but a similar derivation follows for SA. This section follows the derivation by Jensen et al. (Jensen, S. I. Nikolov, et al. 2016). The reference point for the plane wave in Fig. 2.2 is \vec{r}_r , the field point is given by r_p , and r_d is the unit vector for the plane wave propagation direction. The time t_{dp} for the plane wave to arrive at the field point is

$$t_{dp} = \frac{\vec{r}_d \cdot (\vec{r}_p - \vec{r}_r)}{c}, \quad (2.1)$$

when the plane wave is emitted at \vec{r}_r at time $t = 0$. Here, the speed of sound is c . The time-of-flight for the backscattered wave to propagate from the field point to the receiving element \vec{r}_i is

$$t_r(\vec{r}_i, \vec{r}_p) = \frac{|\vec{r}_i - \vec{r}_p|}{c} \quad (2.2)$$

The total time from transmission to reception is then

$$t_{dp} + t_r(\vec{r}_i, \vec{r}_p) = \frac{\vec{r}_d \cdot (\vec{r}_p - \vec{r}_r)}{c} + \frac{|\vec{r}_i - \vec{r}_p|}{c}, \quad (2.3)$$

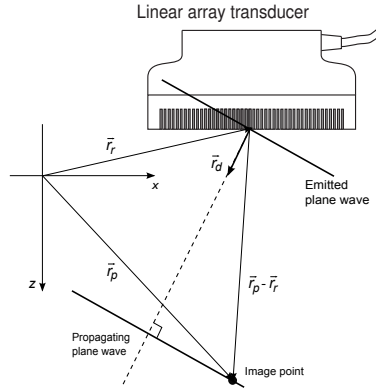


Figure 2.2: Plane wave focusing. A steered plane wave is emitted in a direction given by the vector r_d , and the image point is given by r_p . Obtained from (Jensen, S. I. Nikolov, et al. 2016).

which corresponds to the sample to select in the received signal. The calculation of both transmit and receive times is performed throughout the image to perform focusing for all image points.

2.3 Estimation of blood flow velocities

The principle of 1-D velocity estimation in modern pulse-echo systems is to emit a number of ultrasound pulses in the same direction and compare the received signals to find a spatial shift, which is converted to a velocity. A number of methods have been proposed for estimating the velocity using line-by-line imaging, and the methods can be extended to parallel imaging systems.

2.3.1 Spectral estimator

By sampling data at a fixed depth, a received sampled signal $x(i)$ is acquired over several ultrasound emissions i . The signal will oscillate, if blood flow has a velocity component along the ultrasound beam. The frequency of the oscillation f_p depends on the center frequency f_0 of the emitted pulse and the velocity magnitude v_z of the moving blood scatterers,

$$f_p = \frac{2v_z}{c} f_0, \quad (2.4)$$

where c is the speed of sound (Jensen 1996). The frequency f_p of the sampled signal is often still denoted the Doppler frequency (Evans and McDicken 2000), but the frequency

is actually not related to the classic Doppler effect, where a Doppler shift frequency is observed between a transmitted continuous wave signal and the received signal.

With a collection of scatterers moving at different velocities, a spectral density of the signal is obtained, which is related to the density of velocities. Applying the Fourier transform to $x(i)$, yields the frequency (spectral) distribution of the blood scatterers at time instant t , which is converted to a velocity distribution. A short-time Fourier transform at several time instances yields a spectrogram, often referred to as the Doppler spectrum. Since the resolution in the Fourier domain (number of Fourier components) is related to the number of pulse emissions, a relatively high number of emissions are used (usually 64-128) to yield an acceptable resolution. It makes the spectral estimator useful only at a single image point (or within a range gate) for conventional line-by-line imaging.

The spectral estimator can also be directly applied to parallel imaging. The advantage is that the spectrogram can be calculated at each image point, since continuous data are available everywhere in the image (Bercoff, Montaldo, et al. 2011; Ekroll, Dahl, et al. 2014). Medical doctors usually derive quantitative parameters from the spectrogram, e.g. peak velocities, RI, and volume flow, and these parameters can be derived at arbitrary multiple locations in the image when using parallel imaging. It leads to a larger information content in the image compared to the single image point analysis in line-by-line imaging. However, a number of plane or spherical waves are usually used for the focusing in parallel imaging, which implies a lower effective pulse repetition frequency (PRF). This lowers the maximum detectable velocity.

2.3.2 Phase-shift estimator

The phase-shift estimator is the most used velocity estimator in ultrasound systems. It is computationally efficient, and only a few emissions (usually 8-16) can be used for estimating the velocity. It is therefore applied for line-by-line CFM, where the frame rate needs to be at an acceptable level.

The received sampled signal $x(i)$ at a specific depth is converted to complex IQ data, so that the direction of the velocity can be obtained

$$r(i) = x(i) + jy(i), \quad (2.5)$$

where x is the real part and y is the imaginary part of the complex signal. The emission number is i . The quadrature part of the IQ data are obtained by applying the Hilbert transform ($y = \mathcal{H}\{x\}$) to the sampled in-phase data x or by sampling x at a quarter of a wavelength λ , i.e. a $\pi/2$ phase shift.

The phase-shift estimator finds the mean phase-shift between consecutive received signals from the emitted pulses. The mean phase of the complex signal $r(i)$ is then converted to a mean velocity. Namekawa et al. (Namekawa et al. 1982) developed an autocorrelation estimator for calculating the phase-shift, and it was further developed by

Kasai et al. (Kasai et al. 1985). The autocorrelation estimator is:

$$v_z = -\frac{c}{4\pi f_0 T_{prf}} \cdot \arctan \left(\frac{\sum_{i=1}^{N_i-1} y(i)x(i-1) - x(i)y(i-1)}{\sum_{i=1}^{N_i-1} x(i)x(i-1) - y(i)y(i-1)} \right) \quad (2.6)$$

where N_i is the number of emissions per estimate, f_0 is the center frequency of the emitted pulse, and T_{prf} is the time between consecutive pulses. The consecutive received signals are assumed to be narrowband within the corresponding transmit frequency f_0 . This is usually ensured by transmitting relatively long pulses of several cycles. However, tissue attenuation and scattering effects can increase the bandwidth of the received signal, whereby the narrowband assumption is violated. This can result in errors when estimating the phase of the signal, which actually consists of several frequencies and phases. Another disadvantage of the phase-shift estimator is aliasing, where the uniqueness of the inverse trigonometric function is within $\pm\pi$. It sets a limit on the maximum detectable velocity,

$$v_{max} = \frac{c}{4} \frac{1}{f_0 T_{prf}}. \quad (2.7)$$

Applying the phase-shift estimator to parallel imaging yields similar advantages and disadvantages as for the spectral estimator. Compared to line-by-line imaging, a larger number of emissions can also be used for the velocity estimation without sacrificing frame rate. This improves the precision of the estimates. In addition to averaging velocity estimates over the pulse length as in line-by-line imaging, velocities can also be averaged spatially over image points in a small region to improve precision.

2.3.3 Time-shift estimator

The time-shift, or cross-correlation, estimator finds the time-shift between consecutive received signals. The time between signals directly reveals the velocity of the moving blood scatterers. Dotti et al. (Dotti et al. 1976) proposed the time-shift estimator for blood velocity estimation, and Bonnefous and Pesqué (Bonnefous and Pesqué 1986) further developed the estimator and demonstrated the performance. The cross-correlation of two consecutive received signals r_1 and r_2 is

$$R_{12}(\tau) = \frac{1}{2T} \int_T r_1(t)r_2(t+\tau)dt, \quad (2.8)$$

where T is the observation time and τ is the lag. The lag or time-shift $\tau = t_s$, where the correlation function R_{12} has its peak value, is the time of maximum correlation between the signals. The time-shift can be converted to velocity, when the time between pulse emissions is known. The time-shift estimator does not rely on assumptions of the frequency content in the signal, and the shift is considered for all frequencies. For a narrowband signal, the time-shift estimator is equal to a phase-shift estimation. For broadband signals, the performance of the time-shift estimator increases, since the risk of

detecting false peaks in R_{12} reduces. Short emitted pulses are therefore employed for this estimator. The estimator is not aliased limited, and if there is a high correlation between the received signals, the maximum detectable velocity can be several orders of magnitude higher than for a phase-shift estimator. Disadvantages of the time-shift estimator are its computational expense and the reduced performance for high beam-to-flow angles (S. G. Foster, Embree, and O'Brien 1990).

The time-shift estimator was developed for line-by-line imaging, but can be applied to parallel imaging. Nikolov and Jensen (S. I. Nikolov and Jensen 2001, 2003) used the time-shift estimator for finding the axial velocity component in SA imaging. They also introduced the idea of detecting the movement of blood scatterers between HRIs, because the correlation is higher between HRIs than between individual LRIs. This is the basic principle used for velocity estimation in parallel imaging.

2.4 Estimation of blood flow velocity vectors

Estimation of the velocity component in two or three dimensions has been a research subject for several years with the first methods introduced in the early 1970s. Several methods have subsequently been proposed and in recent years, vector flow methods have attracted a lot of interest. This section introduces the cross-beam method, speckle tracking, transverse oscillation and directional beamforming methods. The extension of the methods from line-by-line imaging to parallel imaging is also explained. Spectral-based methods (Newhouse et al. 1987; Tortoli, Bambi, and Ricci 2006; Osmanski, Montaldo, and Tanter 2015) and color Doppler-derived vector flow mapping (Ohtsuki and Tanaka 2006; Garcia et al. 2010) are also important methods for vector flow imaging, but are not detailed below.

2.4.1 Cross-beam methods

The cross-beam (or multibeam, or Vector Doppler) method was one of the first methods for finding the flow vector (Peronneau et al. 1974; Dunmire et al. 2000). The approach uses multiple beams from different angles to derive the 2-D (or 3-D) velocity vector. A velocity estimate is found along each of the beams using any of the 1-D methods described in Section 2.3, and a triangulation of the velocity components gives the 2-D velocity vector. At least two beams with different insonification angles are needed to estimate the two 1-D velocity estimates along the beams, which give rise to two independent realizations of linear equations. The two equations have two unknowns, v_x and v_z , and the equations are solved for the unknowns. The first versions of the cross-beam methods used two separate transducers as transmitters/receivers and the velocity vector was estimated at the single point of overlap between the crossing beams (Fahrbach 1970). Later, the development of array transducers took advantage of beam steering and of splitting the aperture into sub-apertures, which also enabled deriving the velocity vectors over an entire field of view (Phillips, Kadi, and Ramm 1995; Capineri, Scabia, and Masotti 2002). It also allowed

using a single transmit event and then receiving on two sub-apertures. Errors in velocity estimation along the beams give rise to a significant variance in the triangulated vector estimates. One way to overcome this issue is to extend the principles to a multibeam implementation (Fox 1978). Using several realizations of the velocity measurements, an overdetermined system of equations is solved for the velocity vector by least-squares fitting (Tsang, B. Y. S. Yiu, and A. C. H. Yu 2009; B. Y. Yiu, Lai, and A. C. Yu 2014).

The accuracy of the cross-beam method depends on the angle between the beams. A small angle difference reduces the accuracy and precision of the velocity estimates, and this is a problem for larger depths as the angle difference here is smaller. It is therefore advantageous to use a large aperture. Another challenge with the cross-beam method is the resulting large $F\#$ and poor lateral resolution when using a small sub-aperture for beamforming. It makes it difficult to accurately track blood scatterers in smaller vessels.

The cross-beam method has also been combined with plane waves, where the crossing beams are replaced by overlapping regions of steered plane waves. It increases the frame-rate and the field-of-view compared to single beam acquisitions. Tanter et al. (Tanter, Bercoff, et al. 2002) applied plane waves and the cross-beam method for 2-D tissue motion estimation, and Ekroll et al. (Flynn et al. 2011; Ekroll, Swillens, et al. 2013) for blood flow imaging. Other authors have extended the methods into 3-D (Provost et al. 2014; Correia et al. 2016) and to real-time implementations (Ricci, Bassi, and Tortoli 2014).

2.4.2 Speckle tracking

The speckle tracking method was proposed in 1987 by Trahey et al. (Trahey, Allison, and Ramm 1987), and the technique originated from optical particle image velocimetry (PIV). Light-scattering particles are used in PIV for measuring the velocity components in fluid dynamics, but for ultrasound speckle tracking contrast agents or the blood cells are used as tracers. The size of the blood scatterers ($7 \mu\text{m}$) is much less than the fundamental resolution of the ultrasound system (usually 0.1-0.8 mm) (Jensen 1996), which gives rise to an interference pattern, or *speckle*, in the presence of many blood scatterers. It is assumed that the local speckle pattern is sufficiently preserved from one frame to the next one. The basic principle is therefore to use snapshots of blood speckle patterns acquired at different emissions. A kernel region is tracked within a larger search region, and the best match between two speckle images defines the vector of motion. The best match is found using the 2-D cross-correlation function or block-matching algorithms. There is a tradeoff between the kernel size and spatial velocity resolution. A larger kernel improves velocity accuracy and precision, but degrades spatial resolution. The size of the search region defines the maximum detectable displacements, which means the speckle tracking avoids aliasing limitations. The theoretical maximum detectable displacement is larger than for phase-shift estimators, however, large search regions increase the risk of detecting wrong peaks in the correlation function. A problem for the initial studies was the sequential acquisition of B-mode lines, which resulted in an asymmetric range

of measurable velocities, increased decorrelation of speckle patterns, and limited high velocity estimation. By acquiring multiple receive beams simultaneously and at a higher frame rate, Bohs et al. (Bohs et al. 1998) solved some of the issues and presented the method as ensemble tracking for tissue motion estimation. However, the 2-D cross-correlation makes speckle tracking a computationally expensive method and compromises of the kernel size and spatial velocity resolution have to be made to achieve acceptable processing time.

The most successful implementations of speckle tracking (ensemble tracking) were the use of parallel imaging, which provided high frame rates with small inter-frame movements of blood scatterers. Sandrin et al. (Sandrin, Manneville, and Fink 2001) combined speckle tracking and fast plane wave imaging for 2-D velocity estimation for experimental flow imaging. Udesen et al. (Udesen, Gran, Hansen, et al. 2008) used speckle tracking, unsteered plane waves, and temporal encoding to increase the SNR. Thereby, the first *in vivo* scans for fast blood flow 2-D VFI were demonstrated. Hansen et al. (Hansen et al. 2009) demonstrated several *in vivo* examples of complex flow patterns in major arteries and veins of healthy volunteers. Impressive results were obtained, where vortices, back-flow and fast transient flow phenomena were revealed with a high frame rate. More recently, the technique has been used with steered plane waves (Fadnes, Ekroll, et al. 2015; Saris et al. 2016), applied to flow in fast-beating hearts of neonates (Fadnes, Nyrnes, et al. 2014), and for intra-cardiac volumetric 3-D VFI (Wigen and Løvstakken 2016).

2.4.3 Transverse Oscillation

The oscillating pressure field with a frequency of f_0 along the ultrasound beam makes it possible to detect a frequency or phase shift. In the direction transverse to the ultrasound beam, no oscillation of the field is present. It is not possible to detect a phase-shift and the velocity component of moving blood scatterers. Jensen and Munk (Jensen and Munk 1998) and Anderson (Anderson 1998) introduced the idea of making a transverse oscillation (TO) in the ultrasound field. Thereby, the received signals become sensitive to both an axial and lateral motion in the field, where the transverse velocity is proportional to the transverse frequency. The TO field is usually created in the receive beamforming by changing the apodization function to contain two separate peaks. A two-peak apodization generates a sinusoidal oscillation in the field, as predicted by the Fourier relation between the transducer's apodization and the field at the focus or far field. A transverse oscillation can also be generated in the Fourier domain, known as k -space, as introduced by Liebgott (Liebgott 2010; Varray and Liebgott 2013). It is performed in the Fourier domain by filtering the beamformed image in the lateral dimension and only select k -space components around a desired lateral oscillation frequency.

The conventional implementation of TO uses line-by-line imaging, and two parallel receive beams are formed around each transmit beam. The receive beams are displaced by a quarter of the lateral wavelength, $\lambda_x/4$, to yield a 90° spatial phase shift between

the beams. Thereby a spatial quadrature signal is generated to determine the direction of the transverse velocity component, comparable to performing a Hilbert transform of the signals for axial estimation. For a pulsed field, it can be challenging to perform focusing with a predicted separation of $\lambda_x/4$, and deviations in the formed Hilbert transform pair may result in significant biases of the estimates. Optimization schemes have to be employed to avoid this (Liebgott, Wilhelm, et al. 2007; Jensen, Brandt, and Nielsen 2015). An alternative is to beamform a directional line at each depth transverse to the ultrasound beam and perform a Hilbert transform on this signal. The approach was presented as directional TO (Jensen 2015).

A special fourth-order autocorrelation estimator was developed for estimating the lateral velocity component independent of the axial component (Jensen 2001)

$$v_x = \frac{\lambda_x}{4\pi T_{prf}} \cdot \arctan \left(\frac{\Im\{R_1(1)\}\Re\{R_2(1)\} + \Im\{R_2(1)\}\Re\{R_1(1)\}}{\Re\{R_1(1)\}\Re\{R_2(1)\} - \Im\{R_1(1)\}\Im\{R_2(1)\}} \right) \quad (2.9)$$

where R_1 and R_2 are the complex autocorrelation signals of two generate signals, \Re denotes the real part and \Im the imaginary part. The estimator decouples the transverse oscillation from the axial oscillations, and scatterer movement traversing the field at any angle can be estimated. The autocorrelation estimator is relatively inexpensive in terms of computational load, and has similarities with the traditional autocorrelation estimator for axial movement: it is a phase-shift estimator and is limited by aliasing,

$$v_{x,max} = \frac{1}{4} \frac{\lambda_x}{T_{prf}}. \quad (2.10)$$

The performance of TO has been investigated extensively, including simulations and phantom measurements (Udesen and Jensen 2006) and *in vivo* scans for blood flow imaging (Udesen, Nielsen, et al. 2007). The TO VFI method is also implemented on commercial BK ultrasound scanners, where real-time studies can be conducted. The TO method has also been expanded to 3-D by implementation on an experimental scanner (Pihl and Jensen 2014; Pihl, Stuart, et al. 2014; Holbek et al. 2017). Furthermore, TO is applicable for tissue motion estimation, and Basarab et al. (Basarab et al. 2009) developed a phase-based block-matching approach for TO fields.

TO has been combined with SA (Liebgott, Basarab, et al. 2008) and plane waves (Salles et al. 2015) for tissue motion estimation, and for blood flow estimation (Lenge et al. 2015), where a phase-based block-matching estimator was used.

2.4.4 Directional beamforming

In conventional ultrasound velocity estimation systems, image lines are beamformed along the ultrasound direction and velocities are estimated along the beam. Directional beamforming (DB) uses the idea that lines can also be beamformed in any other desirable direction, when element RF-data are available and a weakly focused transmit field spans the image lines. This can be employed for velocity estimation by beamforming directional

signals along the actual flow direction and then estimate the velocity magnitude along the directional line. The advantage of beamforming lines along the flow direction is that a high signal correlation is maintained between the directional signals. This results in more precise and accurate velocity estimates. The DB approach was introduced by Jensen in 2003 (Jensen 2003; Jensen and Bjerngaard 2003) and the initial implementation used a weakly focused field. It was also shown that the method works especially well in combination with SA imaging and plane waves (Jensen and S. I. Nikolov 2004; Udesen, Gran, and Jensen 2005). High frame rates can be obtained and a large number of emissions can be used for velocity estimation.

The velocity magnitude is calculated by estimating the spatial (time) shift of signals along the directional line. The time-shift estimator (Section 2.3.3) is employed for finding the lag $\tau = l_{max}$ of the maximum cross-correlation R_{12} , which corresponds to

$$|v| = \frac{l_{max}\Delta r}{T_{prf}N_t}, \quad (2.11)$$

where Δr is the spatial sampling interval and N_t is the number of LRIs per HRI. The DB estimator has the same properties as the time-shift estimator, which includes the capability of estimating high velocities.

However, the flow direction needs to be known in advance for DB. This may be determined manually from the B-mode image, or by using automatic angle estimation procedures for obtaining vector flow. The automatic approaches use either the normalized correlation function (NCF) (Jensen and Oddershede 2006; Kortbek and Jensen 2006), or velocities estimated on the LRIs to numerically triangulate the flow angle (Villagomez-Hoyos et al. 2016). Accurate estimation of the flow angle can be obtained, but the approaches are computationally intensive as lines have to be beamformed at every angle in a 360° polar grid and for every estimation point. For the NCF approach, a normalized cross-correlation is estimated as a function of the beamformed angles θ_m

$$R_{12n}(\theta_m) = \left(\frac{\max(R_{12}(l, \theta_m))}{R_{11}(0, \theta_m)} \right), \quad (2.12)$$

where $\max(R_{12}(l, \theta_m))$ is the maximum value of the cross-correlation for the angles θ_m and $R_{11}(0, \theta_m)$ is the power of the signal. The correct flow angle is found where $R_{12n}(\theta_m)$ has its peak value.

2.5 Fast and slow velocity flow

As described in the previous sections, the combination of blood flow estimation and fast parallel imaging solves several of the issues in conventional line-by-line imaging by providing higher frame rates, more precise velocity estimates, and continuous data everywhere in the image. Furthermore, parallel imaging gives large flexibility when

designing the emission sequence, which is an advantage for both fast and slow velocity flow estimation. The flow sequence can be made short to enable very high frame rates fast enough to capture rapid, transient flow events in major vessels and the heart.

An important advantage in parallel imaging systems is the possibility for increasing sensitivity to slow velocity flow. This was indicated by Bercoff et al. (Bercoff, Montaldo, et al. 2011), where a long sequence with 16 plane waves were employed for imaging small blood vessels. The large number of combined plane waves increased SNR and improved the contrast of the HRI, which increased sensitivity to smaller vessels with lower blood flow velocities. Continuous data makes it possible to average over very long times, which improves the echo-canceling and the precision of the velocity estimates (Jensen, S. I. Nikolov, et al. 2016). The high sensitivity for estimating slow velocity flow was excellently demonstrated by Macé et al. (Mace et al. 2011). Flow in a rat brain was imaged using steered plane waves, and it was possible to follow the change in blood flow during an epileptic seizure.

Plane wave image quality optimization

This chapter presents an overview of the findings made in the peer-reviewed Paper I. The paper describes a method for optimizing parameters affecting the image quality in plane wave imaging, and image quality for a λ -pitch linear array transducer is compared with a $\lambda/2$ -pitch transducer. The first part of the chapter gives a background on the subject and describes the emitted field for a plane wave. Then, the method for optimization of the image quality is presented, and results from simulations and measurements are presented in the last part of the chapter. For a further in-depth description of the study the reader is referred to Paper I in the appendix.

3.1 Background and purpose

As described in Section 2.2, the principle of plane wave focusing relies on synthesizing the transmit focus by emitting a number of steered plane waves into the tissue. For each transmit event, a full image is focused in receive to yield a low-resolution image (LRI). Each LRI has low contrast, therefore, to regain contrast, a number of LRIs are combined to yield a high-resolution image (HRI). The frame rate reduces when increasing the number of LRIs, thus, there is a tradeoff between image quality and frame rate. It is important to keep the frame rate high by using as few emissions as possible, but still obtaining high-quality images useful for the imaging of moving structures, for fast flow estimation, and for image segmentation. An optimization of the imaging and transducer parameters is needed to investigate the best tradeoff between frame rate and image quality. The choice of maximum steering angle and number of emissions have a significant impact on the image quality for plane-wave imaging, and Montaldo et al. (Montaldo et al. 2009) showed how to obtain images of comparable quality to line-by-line imaging. More recent studies rely on a more or less empirical selection of plane waves for the B-mode sequences, but there is a need for investigating the compromise between image quality and frame rate from a substantiated and engineering point of view.

The transducer pitch relative to the wavelength λ should also be considered for optimization of the image quality. For a transducer pitch equal to or larger than λ , grating lobes are generated in the emitted field within the image plane, when an unfocused wave is emitted. The grating lobes give rise to artifacts in the beamformed image. In order to

suppress the grating lobe artifacts, the number of emissions at different steering angles can be increased by sacrificing the frame rate. However, grating lobes are not generated using a $\lambda/2$ -pitch transducer, and might, potentially, increase the frame rate without compromising the image quality.

Small parts imaging using SA or plane waves has so far been performed with commercially available λ -pitch transducers, which are actually intended for line-by-line imaging with no steering of the beams (Nikolov and Jensen 2003; Jensen and Nikolov 2004; Hansen et al. 2009; Montaldo et al. 2009; Bercoff et al. 2011; Denarie et al. 2013; Ekroll et al. 2013; Yiu and Yu 2013). For small parts imaging, the pitch size is often a compromise between a high center frequency, a wide aperture to obtain a large field of view, and the limitation of 192-256 channels in commercial scanners. The resulting size of the pitch is often λ . If a $\lambda/2$ -pitch is desired in combination with the same aperture size, the compromise can only be met by using more channels or a lower center frequency.

The purpose of the study was to optimize all these parameters and at the same time balance image quality and frame rate. A method was suggested for optimizing the number of plane wave emissions and maximum steering angles to obtain high-quality images. The method was applied for a λ -pitch and $\lambda/2$ -pitch transducer, but it is a general design approach, which can be applied for any transducer.

3.2 Emitted field for a plane wave

To obtain the best possible image quality, it is essential that the emitted field for the plane wave is as desired without grating lobes and edge waves. The range in which plane waves can be steered is determined by the angular response of the transducer elements and should also be investigated for the applied transducer.

3.2.1 Grating lobes and edge waves

The top image in Fig. 3.1 shows the simulated emitted field for a λ -pitch transducer with no transmit apodization. A plane wave is steered at -10° , but a stream of energy - a grating lobe - is built up behind the wave front and travels in the direction of the red arrow. The large spatial extent of the grating lobe in the near field results in energy transmitted in an undesired direction and ultimately in artifacts. Grating lobes arise due to the spatial (under-)sampling of an aperture into array elements, and the beam pattern in the far field has a grating lobe at

$$\theta_g = \arcsin(\lambda/p + \sin(\theta_s)), \quad (3.1)$$

where λ is the wavelength, p is the transducer pitch, and θ_s is the steering angle of the beam off the center axis. While grating lobes lie within the imaging plane for a pitch of λ , grating lobes are moved outside the imaging plane for a $\lambda/2$ -pitch. This is shown in the center image in Fig. 3.1.

The spherical waves in the image are edge waves generated by the transducer edges. It is possible to suppress the edge waves by using apodization in transmit (weighting of

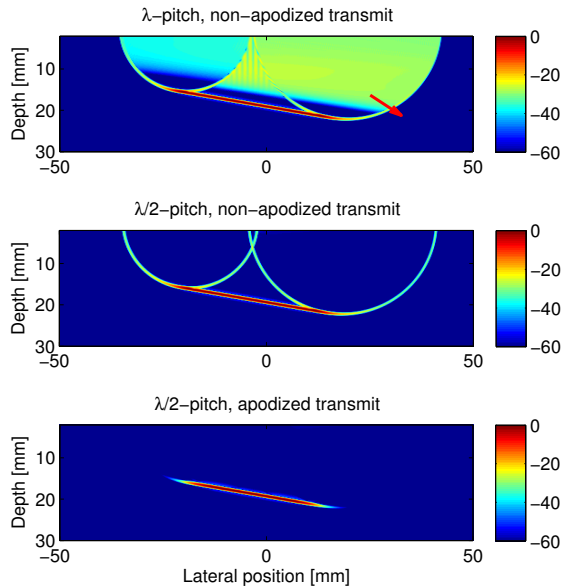


Figure 3.1: Field II simulation of the emitted field for a plane wave steered at -10° . The top image is for a λ -pitch array with no transmit apodization, the middle image is for a $\lambda/2$ -pitch, and the bottom image is for a $\lambda/2$ -pitch array with Tukey window as transmit apodization. From Paper I.

element responses). For the bottom image in Fig. 3.1, a Tukey apodization (weight 0.5) was applied and it efficiently suppressed the edge waves.

3.2.2 Angular response of elements

The angular response of a transducer element, or its directivity pattern, determines the element's acceptance angle. It is related to how much a plane wave can be steered. This is important to know for the optimization purposes and was investigated in simulations and measurements. The acceptance angle of an element was investigated by applying a model from Oddershede and Jensen (Oddershede and Jensen 2007). The model uses the amplitude drop and phase errors for emitted wave signals measured at positions along an arc to determine whether the signals are valuable in an SNR sense. Amplitude drop and phase errors were estimated from the simulated pressure field using the Field II program (Jensen and Svendsen 1992; Jensen 1996). A single element was excited and calculations were performed along an arc at a fixed radial distance from the transducer element. The amplitude drop with respect to the maximum amplitude and the phase error relative to the expected phase were estimated. The resulting acceptance angle was $\pm 38^\circ$ according to

the model. This is the range in which the plane waves can be steered. More details on the angular response are given in Paper I in the appendix.

Correspondence between the simulation and actual measurements was ensured by measuring the emitted pressure field using a hydrophone. The hydrophone scanned along the transducer at a fixed depth, and the same setup and imaging situation was simulated. The energy of the emitted field measured with the hydrophone was in good agreement with simulation results: the average error was 5.1 %.

3.3 Imaging performance measures

Image quality is characterized by the point-spread-function (PSF), which is the response of the ultrasound system to a point source. The PSF fully summarizes the performance of the ultrasound system applied with the choice of transmit and receive combinations. Two performance measures were here used for evaluating the image quality of the plane wave images: the detail resolution and the contrast resolution.

3.3.1 Detail resolution

The detail resolution is calculated as the -6 dB width of the main lobe of the PSF, i.e, the full-width at half-maximum (FWHM). It is determined by the bandwidth of the system and the size of the aperture ($F\#$). FWHM measured in the lateral direction is also dependent on the maximum steering angle of the emitted plane wave.

3.3.2 Contrast resolution

The contrast resolution or the cystic resolution describes the ability to detect an anechoic cyst in a uniform scattering medium. Side lobes and grating lobes increase the clutter energy outside the main lobe of the PSF, which is quantified by the cystic resolution. It has been quantified by Ranganathan and Walker (Ranganathan and Walker 2007) to be the ratio of energy outside a circular region of radius R to the total PSF energy

$$\text{contrast}(R) = \sqrt{\frac{E_{out}(R)}{E_{total}}}, \quad (3.2)$$

where E_{out} is the PSF energy outside a circular region with radius R centered at the peak of the PSF and E_{total} is the total energy. A single number can be obtained by calculating the relative energy for a fixed radius, which in this case was $R = 2.5\lambda$ ($R_{2.5\lambda}$).

3.4 Method for optimization of image quality

The method for optimization of image quality relied on the theory of Pareto optimality (Deb 2005; Coello, Lamont, and Veldhuizen 2007). Pareto optimality is relevant for

multiobjective optimization problems, where the aim is to find good compromises among two or more objectives rather than searching for a single optimum solution. The set of compromise solutions are the Pareto optimal solutions, which represent a tradeoff between the objectives. The method is illustrated in Fig. 3.2 and explained below.

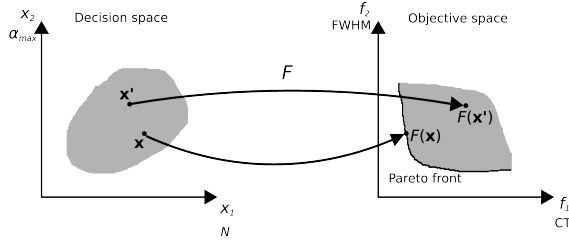


Figure 3.2: Illustration of the decision space containing the independent variables x_1 and x_2 , and the objective space with the dependent variables F_1 and F_2 . Here, the number of emissions N and max steering angle α_{max} were used in the decision space, while contrast and FWHM were the objectives. The Pareto front is shown as a black curve. From Paper I.

A solution $\mathbf{x} = \{x_1, x_2\}$ is Pareto optimal, if there exists no other solution \mathbf{x}' for which $\mathbf{v} = F(\mathbf{x}')$ dominates $\mathbf{u} = F(\mathbf{x})$. Here, F is the objective function, which maps from decision space to objective space. The set of objectives \mathbf{v} is dominating \mathbf{u} , $\mathbf{v} \preceq \mathbf{u}$, if \mathbf{v} is no worse than \mathbf{u} in all objectives, and \mathbf{v} is strictly better than \mathbf{u} in at least one objective. A Pareto optimal solution is defined as

$$\mathcal{P}^* := \{\mathbf{x} \mid \nexists \mathbf{x}' : F(\mathbf{x}') \preceq F(\mathbf{x})\}. \quad (3.3)$$

A set of Pareto optimal solutions are collectively called the Pareto front. The black curve in the objective space in Fig. 3.2 illustrates the Pareto front.

The Pareto front represents solutions where it is impossible to improve one of the variables without deteriorating the other. By using Pareto optimality, the objective space, which contains all possible solutions, may be reduced to solutions, which are Pareto optimal. Tradeoffs may then be made among the Pareto-optimal solutions.

The purpose was here to optimize plane wave images for small parts imaging in a sector directly below the transducer. In ultrasound imaging, PSFs are spatial variant, i.e. their characteristics vary in space. Point targets were therefore simulated individually at several depths (at 9, 20, 34, 44, and 60 mm) and placed in a grid along the center line and 10 mm laterally. The number of plane wave emissions, N , and the maximum steering angle, α_{max} , were the independent variables in the decision space to optimize. The lateral FWHM and contrast were the dependent variables (or objectives), which were found by evaluating the image quality of the PSF for the corresponding combination of N and α_{max} . By using several \mathbf{x} , i.e. all combinations of N and α_{max} for a given image of the point target, the corresponding FWHM and contrast were calculated and a Pareto

Table 3.1: Parameters used for simulation and measurements.

Parameter	λ -pitch transducer	$\lambda/2$ -pitch transducer
Number of elements	96	192
Center frequency f_0	4.1 MHz	4.1 MHz
Wavelength λ	0.376 mm	0.376 mm
Element pitch	0.4 mm (1.06λ)	0.2 mm (0.53λ)
Element height	6 mm	6 mm
Elevation focus	38 mm	38 mm
Cycles m in emitted pulse	1	1
Transmit apodization	Tukey (weight 0.5)	Tukey (weight 0.5)
Receive apodization	Hamming	Hamming
Receive $F\#$	1	1
Max angle α_{max}	$\pm 38^\circ$	$\pm 38^\circ$

front was constructed for each point target. The knee-point solution on the Pareto front represented a good tradeoff between FWHM and contrast, and special attention was given to this solution.

3.5 Simulations

3.5.1 Simulation setup

Simulations were performed in Field II using two transducers with parameters as listed in Table 3.1. The transducer pitches were approximately λ and $\lambda/2$. The $\lambda/2$ -pitch transducer had twice as many elements as the λ -pitch transducer to maintain the same aperture width. Point targets were simulated at five axial distances: at 9 mm, 20 mm, 34 mm, 44 mm, and 60 mm, and placed along the center line of the transducer and 10 mm laterally. Plane wave emissions were uniformly distributed between maximum steering angles of -38° and $+38^\circ$, and the smallest angle step was 0.25° . Simulated and beamformed LRIs were subsequently combined to HRIs by summation of IQ-data and using all combinations of α_{max} and N .

3.5.2 Simulation results

Fig. 3.3 shows simulated PSFs for the λ -pitch and $\lambda/2$ -pitch transducer, where the dynamic range is 60 dB, $\alpha_{max} = 20^\circ$, and $N = 21$. This was the optimal setup for the $\lambda/2$ -pitch transducer according to the Pareto optimization as will be explained below. It can be observed that the transducers attained similar image quality for PSFs below 25 mm, while the image for the λ -pitch transducer contained artifacts off to the sides and below the PSFs to a depth of 25 mm. The artifacts were due to grating lobes in the emitted field.

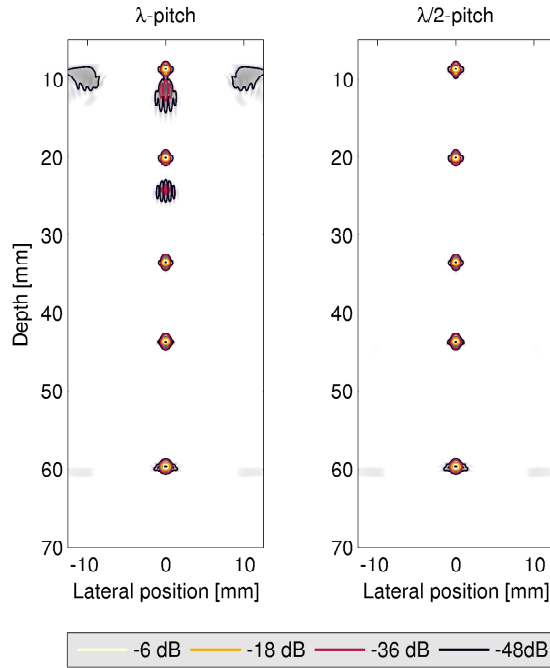


Figure 3.3: Simulated PSFs using a λ -pitch (left) and $\lambda/2$ -pitch transducer (right). Dynamic range is 60 dB, $\alpha_{max} = 20^\circ$, and $N = 21$. From Paper I.

The optimization procedure was applied separately for each of the point targets simulated with the λ -pitch and $\lambda/2$ -pitch transducers. Results are here shown for the point target at 34 mm simulated with the λ -pitch transducer and provides as an example of the procedure.

Image quality in terms of lateral FWHM and contrast with all the combinations of α_{max} and N are shown in Fig. 3.4. As expected, lateral FWHM was mainly determined by α_{max} , while the contrast was mainly dependent on N . To limit the number of considered HRIs for the Pareto optimization, it was required that lateral FWHM improved by 2.5 % when steering 2° or more, and that the contrast improved by 1 % when using four more emissions. The borderlines, where the requirements were no longer fulfilled, are shown in Fig. 3.4 (white curves). The remaining data points for FWHM and contrast were used to construct the scatter plot shown in Fig. 3.5. A Pareto front was also constructed based on the criteria of minimizing FWHM and contrast as explained in Section 3.4. The Pareto front contained eight Pareto solutions, which are labelled 1-8 and may be identified with corresponding N and α_{max} in Fig. 3.4 (green dots).

A Pareto front was generated for each of the point targets so that attention could be

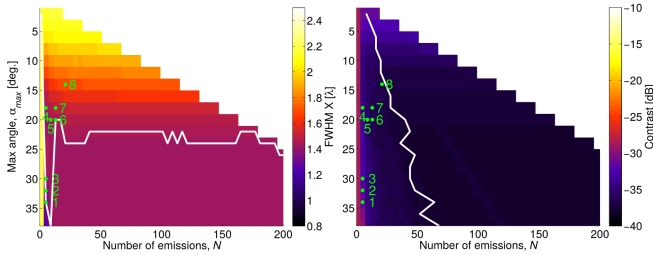


Figure 3.4: Image quality for a point target at 34 mm for all the combinations of α_{max} and N using the λ -pitch transducer. Left: FWHM. Right: contrast. White curves: borderlines. Green dots: Pareto optimal solutions. From Paper I.

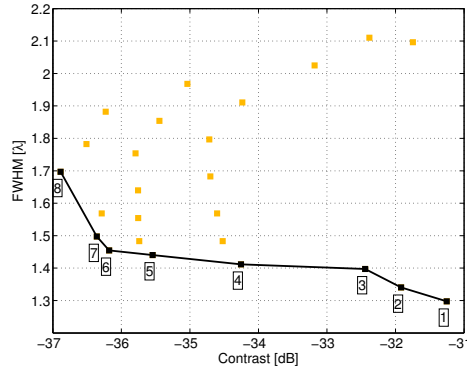


Figure 3.5: Scatter plot of FWHM-contrast pairs from the simulated PSF at 34 mm for the λ -pitch transducer. Black squares: Pareto optimal solutions. Black curve: Pareto front. From Paper I.

drawn to all solutions on the Pareto fronts. The information was merged into Fig. 3.6, where N and α_{max} corresponding to the Pareto optimal solutions are shown for all depths along the center line. Knee-point solutions from the Pareto front are marked with asterisks. It is interesting to note that Pareto optimal solutions for both transducers for point targets at 34, 44, and 60 mm are mainly placed in the bottom-left corner of the figures, i.e., for $10^\circ \leq \alpha_{max} \leq 20^\circ$ and $10 \leq N \leq 20$. A larger α_{max} and the same N were beneficial for the $\lambda/2$ -pitch transducer closer to the transducer, while a higher number of emissions ($N > 60$) was beneficial for the λ -pitch transducer.

Fig. 3.6 reveals the angle span and emission span for the Pareto optimal solutions at the different depths. Tradeoffs may then be made among the solutions by considering FWHM and contrast for the combinations of N and α_{max} . A setup of $\alpha_{max} = 20^\circ$ and

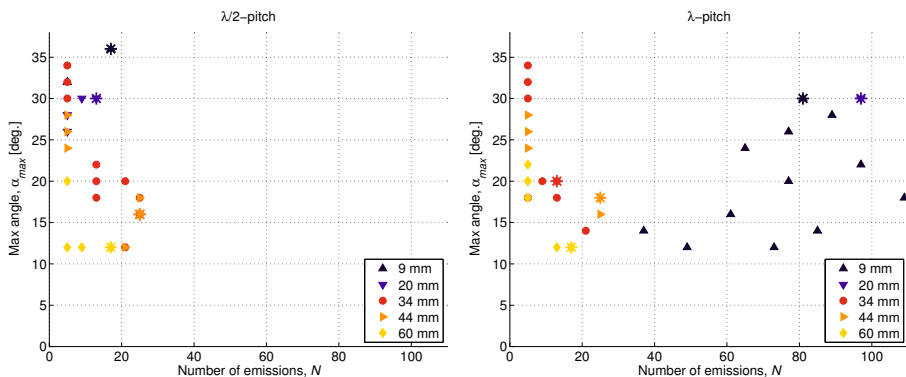


Figure 3.6: Maximum steering angles α_{max} and number of emissions N corresponding to the Pareto optimal solutions on the Pareto fronts for the $\lambda/2$ -pitch (left) and λ -pitch transducer (right). Knee-point solutions are marked with asterisks. From Paper I.

$N = 21$ was here chosen for the $\lambda/2$ -pitch transducer, which gave a contrast of -37 dB at both 9 mm and 34 mm. FWHM was 1.5λ at 9 mm. To balance frame rate and image quality at depths from 0-60 mm for the λ -pitch transducer, a setup of $\alpha_{max} = 20^\circ$ and $N = 61$ was chosen. The resulting contrast was -29 dB at 9 mm and -37 dB at 34 mm. If only 21 emissions were used, the contrast would degrade by 15 dB, which was mainly due to grating lobe artifacts. The optimal setup for a λ -pitch transducer, thus, used three times more emissions than the $\lambda/2$ -pitch transducer for imaging at depths from 0 to 60 mm. For imaging in deeper regions than 25 mm, only 21 emissions were optimal for both the transducers.

As discussed in this section, it is very challenging to obtain acceptable contrast close to the λ -pitch transducer, which had a contrast 10-15 dB worse than the $\lambda/2$ -pitch transducer. Fig 3.7 shows contrast for a point target at 9 mm for all combinations of N and α_{max} , and FWHM is shown for $N = 21$. The contrast could only be kept below -30 dB for the λ -pitch transducer by using small steering angles around 10° . The $\lambda/2$ -pitch transducer attained contrast below -30 dB for larger angles, which also improved resolution. Increasing α_{max} from 20° to its limit at 38° improved FWHM by 0.4λ , while maintaining a high contrast for the $\lambda/2$ -pitch. This combination could be interesting for very shallow imaging.

3.6 Measurements

3.6.1 Measurement setup

The plane wave B-mode sequence was implemented on the experimental scanner SARUS (Jensen, Holten-Lund, et al. 2013). A linear array transducer with the same parameters as

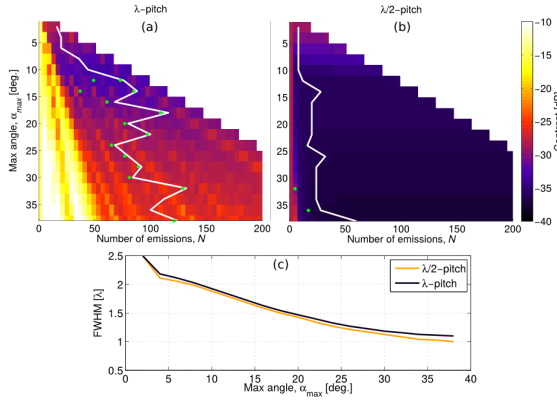


Figure 3.7: Image quality of a point target at 9 mm for all combinations of N and α_{max} . In (a) and (b), contrast is shown for the λ -pitch transducer and $\lambda/2$ -pitch transducer, respectively. FWHM is shown in (c) for $N = 21$. The white curves are at the borderlines, and green dots are Pareto optimal solutions. From Paper I.

the $\lambda/2$ -pitch transducer in Table 3.1 was employed, and the imaging setup was identical to simulations. Emissions for the $\lambda/2$ -pitch and λ -pitch transducer were interleaved in a sequence with a pulse repetition frequency (PRF) of 5 kHz. By exciting the first and second element simultaneously on the $\lambda/2$ -pitch array, then the third and fourth element simultaneously, and so forth, a λ -pitch transducer with 96 elements was emulated in transmit. Stored channel data from pair-wise elements were averaged to emulate the receive part of a λ -pitch transducer. A water tank phantom containing five wires was scanned. The common carotid artery was also scanned *in vivo* with a cross-sectional view.

Before conducting the *in vivo* scan, the derated spatial peak, temporal average intensity $I_{spta.3}$ was measured to be 92.5 mW/cm^2 for the *in vivo* scan sequence with a PRF of 5 kHz, and derated MI was 1.03. This is within FDA limits, which are 720 mW/cm^2 and 1.9 (FDA 2008). The transducer surface temperature rise was 7.5°C for an excitation voltage of 100 V and 30 min. of scan. This is within IEC limits of 10°C temperature rise for 30 min. scan (IEC 2015).

3.6.2 Results from measurements

Fig. 3.8 shows a scan of the wire at 9 mm, where the number of emissions was varied for the λ -pitch (left images) and $\lambda/2$ -pitch transducer (right images). As revealed in the simulations, this depth was of particular interest, because a large difference in contrast was obtained for the transducers. Fig. 3.8 shows that there were no or negligible grating lobe artifacts present for the $\lambda/2$ -pitch transducer - even for a low number of emissions. Off-axis energy lobes and artifacts below the PSF were present for the λ -pitch transducer,

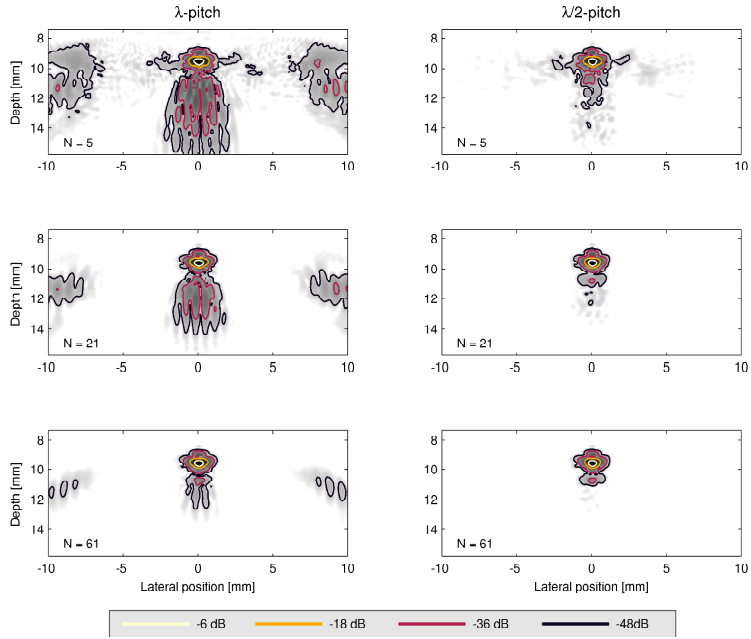


Figure 3.8: Scans of wire at 9 mm depth. Images in the left column are for the λ -pitch transducer and in the right column for the $\lambda/2$ -pitch transducer. The number of emissions N is 5 (top), 21 (center), and 61 (bottom), and $\alpha_{max} = 20^\circ$. From Paper I.

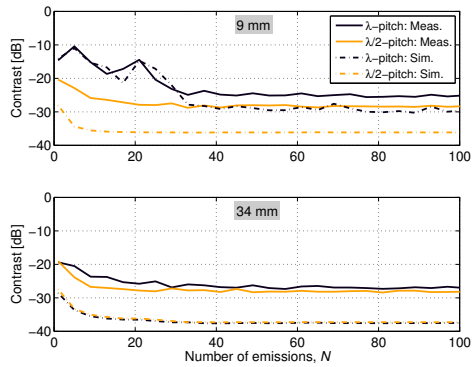


Figure 3.9: Contrast as a function of N for $\alpha_{max} = 20^\circ$. The top figure is for a PSF at 9 mm and the bottom figure for a PSF at 34 mm. From Paper I.

and increasing the number of emissions only partly reduced the artifacts.

The contrast is shown as a function of N for PSFs at 9 and 34 mm in Fig. 3.9. Measurements were consistent with simulations for the λ -pitch transducer at 9 mm, however, there was an 8-10 dB difference in contrast between simulations and measurements for the $\lambda/2$ -pitch transducer. The same difference appeared for both transducers at 34 mm and was due to additional clutter just behind the measured PSF. The clutter might be due to a long impulse response of the transducer and/or related to artifacts arising from quantization of the transmit delay profile. The latter will be addressed in the next section.

The optimized sequences for the transducers were also applied for a cross-sectional scan of the carotid artery. Figs. 3.10 and 3.11 show a frame using 21 and 61 emissions, respectively. The image quality was clearly degraded for the λ -pitch transducer compared to the $\lambda/2$ -pitch transducer, when using only 21 emissions. Clutter from grating lobe artifacts appeared inside the vessel lumen. The image quality was improved when using 61 emissions with the λ -pitch transducer, however, there was still some clutter inside the vessel. The clutter was significantly reduced on the image for the $\lambda/2$ -pitch transducer.

3.7 Discussion and summary

This study demonstrated that good control over the emitted plane wave front should be ensured to avoid grating lobes. The $\lambda/2$ -pitch transducer avoided the grating lobes, which would otherwise give artifacts outside the main response of the PSF. The important selections of plane wave steering angles and number of emissions were made by using a proposed optimization method. The method was applied for a λ -pitch and $\lambda/2$ -pitch array, but may be applied for any transducer and imaging region. The Pareto optimization reduced the number of possible setups, so the user only had to make decisions among Pareto optimal setups.

The best image quality for the $\lambda/2$ -pitch transducer was attained close to the transducer surface, where a large steering angle was advantageous in combination with 21 emissions. Using a pulse repetition frequency of 5 kHz, the sequence produced 238 frames/s. The number of emissions had to be increased by a factor of three for the λ -pitch transducer to obtain acceptable image quality close to the transducer. In regions deeper than 25 mm, 21 emissions within the same angle span was sufficient for both transducers. For high depths, the region of overlap for emitted plane waves was restricted to smaller steering angles, which effectively limited the resolution and contrast. In this case, it may be an advantage to employ spherical waves, which was later investigated in a similar optimization study by Moshavegh et al. (Moshavegh et al. 2016). Hasegawa and de Korte (Hasegawa and Korte 2016) also studied the image quality in SA imaging using a $\lambda/2$ -pitch transducer and obtained slightly improved contrast for the same number of emissions, when using a $\lambda/2$ rather than λ . A disadvantage of using a pitch of $\lambda/2$ is that twice as many channels are needed compared to a λ -transducer, if the aperture width has to be maintained. The transducer kerf may also be a consideration, because the area of inactive material is

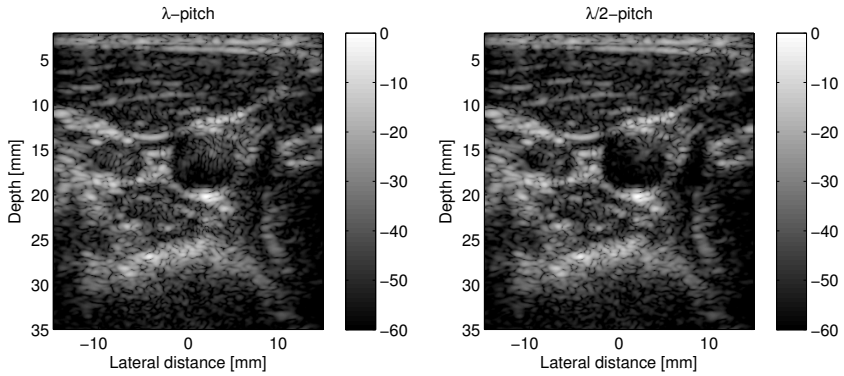


Figure 3.10: *In vivo* cross-sectional images of the carotid artery using 21 emissions and $\alpha_{max} = 20^\circ$. For the λ -pitch (left) and $\lambda/2$ -pitch transducer (right). From Paper I.

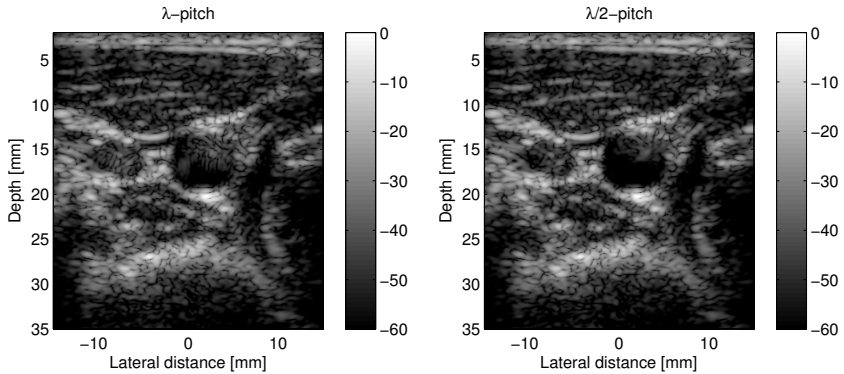


Figure 3.11: *In vivo* cross-sectional images of the carotid artery using 61 emissions and $\alpha_{max} = 20^\circ$. For the λ -pitch (left) and $\lambda/2$ -pitch transducer (right). From Paper I.

doubled. Using even more elements or capacitive micromachined ultrasonic transducers (Haller and Khuri-Yakub 1996) may compensate for this.

Even though the $\lambda/2$ -pitch transducer improved image quality and frame rate compared to the λ -pitch transducer, there were differences between simulations and measurements according to Fig. 3.8 and 3.9. Simulations represent an ideal situation, and the differences between simulations and measurements indicate that there still are factors, which impact the image quality. Measurements may be affected by imperfections such as transducer elements not sitting in a perfect plane and non-uniform characteristics of the lens, and also by temporal quantization effects. These factors impact the emitted field by creating

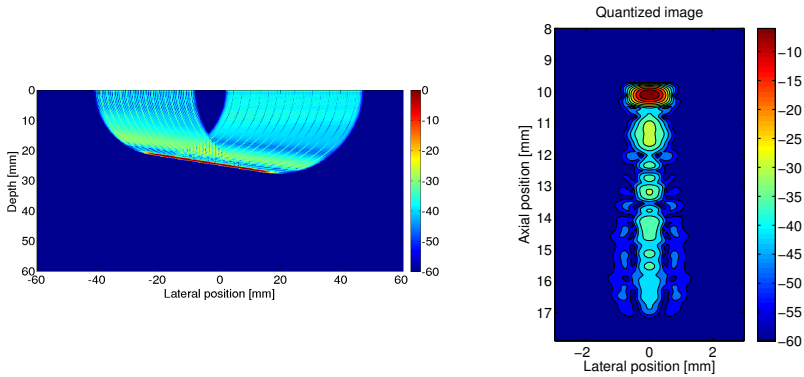


Figure 3.12: The left image shows a simulation of the emitted field for a fixed time for a plane wave steered at -9° . The transmit delay profile was quantized at 70 MHz. The right image shows the PSF for the quantized setup using a sequence of 10 plane waves steered between -9° and 9° . From (Stuart et al. 2015).

undesired lobes. It worsens the focusing and may increase the level of side-lobes and tails in the PSF. A further investigation of the imperfections may reveal which factors dominate and how they can be corrected in order to obtain measured images of improved quality. Specifically, the impact of quantizing the transmit delay profile was investigated by Stuart et al. (Stuart et al. 2015). Temporal quantization effects vary with, e.g. element pitch, pulse frequency, the transmit sampling frequency, and steering angle of the plane wave. As an example, Fig. 3.12 (left) shows the emitted field for a plane wave steered at -9° , where $f_0 = 7$ MHz, the pitch is $\lambda/2$, and the transmit sampling frequency is 70 MHz. Temporal quantization induces phase errors in the delay profile and generates lobes in the emitted field. The resulting image of the PSF is shown in Fig. 3.12 (right), where similar artifacts appear as for the spatial quantization using the λ -pitch transducer (see Fig. 3.8). It was also shown in the paper that it is possible to restore the image quality by providing individually phase-shifted excitation waveforms to each transducer element (Stuart et al. 2015).

With a better understanding of the parameters affecting image quality and frame rate in plane wave imaging, the focus is moved to blood flow imaging in the rest of the thesis. For flow sequences, the number of emissions is usually kept low (one to five emissions) to maintain a high frame rate. The influence from grating lobes should also be acknowledged for flow sequences, which is apparent in the images of the PSF in the top row of Fig. 3.8, where only five emissions were used. The contrast was degraded for the λ -pitch transducer and the peak amplitude of the artifacts was around -22 dB. With a moving vessel wall, it may result in false velocity estimates. Most superficial vessels are placed at depths from 0 to 25 mm, where the λ -pitch transducer gives artifacts,

and it indicates the need for a $\lambda/2$ -pitch transducer in blood flow estimation. In the next chapter, a plane wave sequence with only three steered emissions is used for vector flow estimation. The $\lambda/2$ -pitch transducer is employed to ensure that no grating lobes are generated from the spatial sampling of the aperture. Furthermore, due to the short length of the B-mode sequence (21 emissions), the sequence is interleaved with flow emissions to obtain high-quality B-mode images in parallel to the flow estimates.

CHAPTER 4

Plane wave vector flow imaging

This chapter presents an overview of the findings made in Paper III and Paper V. The papers describe a method for vector flow imaging, where plane waves are combined with transverse oscillation and directional beamforming to yield accurate and precise estimates. In this chapter, a background on the subject is given, and the method for vector flow imaging is explained. Results from simulations and measurements are presented in the last part of the chapter. A measurement of slow velocity flow is also included. For a further in-depth description of the study the reader is referred to Paper III in the appendix.

4.1 Background and purpose

As motivated in Chapter 1, there is a need for combining (vector) flow estimators with fast parallel imaging to obtain frame rates high enough to capture the temporal changes in the blood flow. By breaking with the sequential data acquisition, full flow dynamics of both fast and slow flow can be estimated. This can be achieved by using plane waves, which provide very high frame rates for the data acquisition. Several successful techniques of plane wave vector flow imaging have been proposed, including cross-beam Doppler (Ekroll et al. 2013; Yiu, Lai, and Yu 2014), transverse oscillation (TO) (Lenge et al. 2015), directional beamforming (DB) (Udesen, Gran, and J. A. Jensen 2005), and speckle tracking (Udesen, Gran, Hansen, et al. 2008).

Cross-beam Doppler and TO are the most computationally efficient methods for vector flow imaging, where only two lines are beamformed for each estimation point. However, the precision for cross-beam Doppler and TO decreases for high and low beam-to-flow angles, respectively (Udesen and J. A. Jensen 2006; Fadnes et al. 2015). The DB approach has the highest precision, but it comes with a higher computational cost (J. A. Jensen 2014b). The cost comes mainly from the angle estimator, because signals have to be beamformed in a star-shaped pattern and cross-correlated at every angle and for each estimation point. As an example, if lines are beamformed at every 5° to cover a total of 180° as in (J. A. Jensen and Oddershede 2006), a total of 36 directional lines have to be beamformed for every estimation point in each frame. This should be compared to the two lines required for cross-beam Doppler and TO.

The improved performance of DB compared to TO comes, thus, at the expense of a higher beamforming load. The purpose of this study was to develop and investigate a method for vector flow imaging, where the performance of the obtained velocity estimates

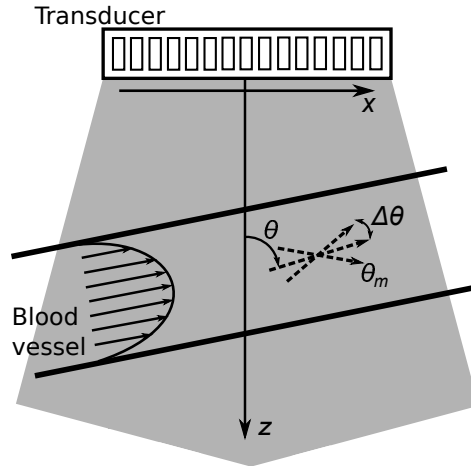


Figure 4.1: Plane wave emissions are used to insonify flow in a vessel. Directional lines are beamformed at angles θ_m around the initial TO angle estimate θ at a single velocity estimation point. From Paper III.

was improved when comparing to TO, while a low beamforming load was maintained.

4.2 Methods for transverse oscillation and directional beamforming

This section describes the approach for vector flow imaging using TO and DB. First, TO is used to find an initial estimate of the flow angle. Then, the angle estimate is refined by a DB step, where three directional lines are beamformed around the TO angle. The velocity magnitude is estimated along a fourth line beamformed in the refined flow direction. The method is presented as TO-DB. The principle of the method, when using plane wave imaging, is shown in Fig. 4.1. The TO and DB steps are described below, and the beamforming load of the methods are calculated in the last part of the section.

4.2.1 Transverse oscillation

A TO field is conventionally created in the receive beamforming stage by using an apodization function with two separate peaks. This may be problematic when combining steered plane waves, because the TO fields on LRIs created from the individual steered plane waves may interfere constructively and destructively when forming the HRI. Fig. 4.2A shows the TO fields on LRIs from plane waves steered at -15° , 0° , and 15° . The resulting TO on the HRI is suppressed, and the lateral frequency content is broadband.

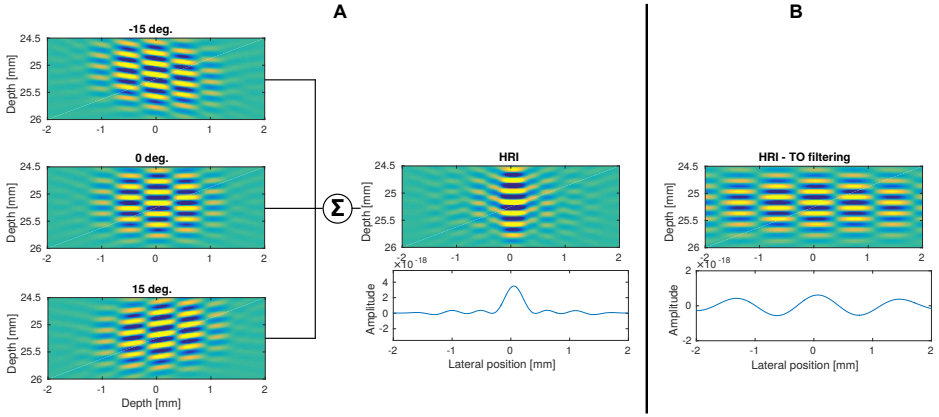


Figure 4.2: TO in plane wave imaging. **A:** Beamformed LRIs for plane waves steered at -15° , 0° , and 15° , and the resulting HRI. The blue curve below the HRI is the amplitude along a lateral line. **B:** The HRI after TO filtering in the Fourier domain.

However, the TO field can also be generated in the Fourier domain, or k -space, to provide better control over the TO field. The method works in the Fourier domain by filtering the conventionally beamformed and focused HRI in the lateral dimension and only select k -space components around a desired lateral oscillation frequency. Any interferences between LRIs are thus avoided. The TO field after TO-filtering is shown in Fig. 4.2B, which has the required narrowband frequency content laterally. The Fourier-domain approach was first introduced for tissue motion estimation (Varray and Liebgott 2013; Salles et al. 2015), and is here applied for blood flow imaging.

The k -space of beamformed data for an HRI before TO-filtering is illustrated in Fig. 4.3 (top). The signal oscillation in the axial direction is identified with Fourier components centered at the pulse center frequency, $f_z = f_0$, while there is no oscillation laterally. Fig. 4.3 (middle) shows a filter $G(f_z, f_x)$ consisting of Gaussian windows centered around a desired TO frequency f_{0x} ,

$$G(f_z, f_x) = \exp\left(-2(\pi\sigma_x(f_x - f_{0x}))^2\right) + \exp\left(-2(\pi\sigma_x(f_x + f_{0x}))^2\right), \quad (4.1)$$

where σ_x is the width of the Gaussian window and f_x is the lateral oscillation frequency. A filter consisting of other window functions may also be used, e.g. a Hanning, Hamming, or Tukey window. The filtering is performed by multiplying the filter with the Fourier transformed image, which gives the TO image in Fig. 4.3 (bottom). The values for f_{0x} and σ_x should be selected so that the k -space components contain energy from blood flow and not only from noise.

Since the data is already Fourier transformed, the direction of the flow is found after keeping only one quadrant of the Fourier spectrum. This avoids applying the Fourier

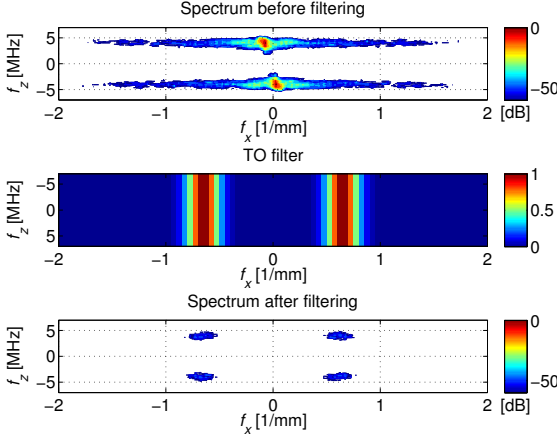


Figure 4.3: The 2-D Fourier spectrum of a beamformed RF image is shown in the top image. The spectrum of the TO filter $G(f_z, f_x)$ is shown in the middle, and the spectrum of beamformed RF image after applying the TO filter is shown in the lower image. From Paper III.

transform on the TO image or having a spatial quadrature between two beamformed signals (J. A. Jensen 2016). The transverse velocity component v_x is then found by employing a standard fourth order autocorrelation estimator (J. A. Jensen 2001), while a cross-correlation estimator is employed for the axial velocity component v_z (Bonnefous and Pesqué 1986). A TO angle estimate, θ , is calculated from the estimated v_x and v_z .

4.2.2 Directional beamforming

The initial TO angle estimate is refined using directional beamforming. A signal $y_d(k)$ is directionally beamformed at an estimation point with the angle θ . The pulse repetition period is T_{prf} and the number of LRIs per HRI is N_t , thus, correlating signals from two HRIs gives

$$R_{12}(l) = \frac{1}{N_k + 1} \sum_{k=-N_k/2}^{N_k/2} y_d^{(n)}(k) y_d^{(n+N_t)}(k+l), \quad (4.2)$$

where $y_d^{(n)}(k)$ is the directional signal focused after emission n , and N_k is the number of samples in $y_d(k)$.

Beamforming signals at three angles $\theta_m \in \{\theta - \Delta\theta, \theta, \theta + \Delta\theta\}$ (see Fig. 4.1) yield correlation functions $R_{12}(l, \theta_m)$. They are used to calculate the normalized cross-

correlation estimate

$$R_{12n}(\theta_m) = \left(\frac{\max(R_{12}(l, \theta_m))}{P_{12}(\theta_m)} \right), \quad (4.3)$$

which gives the maximum normalized cross-correlation as a function of the three angles. $P_{12}(\theta_m)$ is the power of the signals. $R_{12n}(\theta_m)$ has three values, when three angles are used for directional beamforming. The angle estimate, $\hat{\theta}$, is found as the angle yielding the largest correlation

$$\theta_d = \arg \max_{\theta_m} \{R_{12n}(\theta_m)\}. \quad (4.4)$$

The accuracy of the angle estimate is also improved by parabolic interpolation of $R_{12n}(\theta_m)$ (Foster, Embree, and O'Brien 1990). The three angle estimates - one for each line - are sufficient to perform the parabolic interpolation. The selection of $\Delta\theta$ can be a fixed angle span or depend on the estimated TO angle, where the latter is used for this study and further explained in Section 4.3.

A fourth directional line is then beamformed at the refined angle estimate $\hat{\theta}$. The velocity magnitude is found from the lag l_{max} , where $R_{12}(l, \hat{\theta})$ has its maximum, and convert the lag to velocity magnitude

$$|v| = \frac{l_{max}\Delta r}{T_{prf}N_t}, \quad (4.5)$$

where Δr is the spatial sampling interval.

4.2.3 Beamforming load

The beamforming load for the TO, TO-DB, and DB methods are detailed in this section. The calculations are made for a single velocity estimation point.

For the TO method, two beamformed lines are required: an axial line containing N_z samples and a lateral line N_x samples, in total

$$N_{TO} = N_z + N_x. \quad (4.6)$$

For TO-DB, four directional lines, each containing N_x samples, are beamformed in addition to the two lines for TO

$$N_{TO-DB} = N_z + 5 \cdot N_x. \quad (4.7)$$

For conventional DB, the number of directional lines are usually 36 (J. A. Jensen and Oddershede 2006):

$$N_{DB} = 36 \cdot N_x. \quad (4.8)$$

Typical values for the number of samples are $N_z = 30$ and $N_x = 250$ for line lengths of 1.5λ axially and 12.5λ laterally/directionally. Using (4.6) and (4.7), the ratio between the TO-DB and TO method is 4.6. The ratio between the DB and TO-DB method using (4.7) and (4.8) is 7. Thus, the beamforming load for TO-DB is 4.6 times larger than for TO, but seven times smaller than for conventional DB.

Table 4.1: Transducer and acquisition parameters.

Parameter	Value
Number of elements	192
Transducer center frequency f_0	4.1 MHz
Element pitch	0.2 mm
Element height	6 mm
Elevation focus	38 mm
Cycles in emitted pulse	1.5 (flow) and 1 (B-mode)
Transmit apodization	Tukey (weight 0.5)
Pulse repetition frequency (PRF)	10 kHz
Max steering angle	15° (flow) and 20° (B-mode)
Number of plane waves	3 (flow) and 21 (B-mode)

Table 4.2: Processing parameters.

Parameter	TO	TO-DB
Receive apodization	Tukey (weight 0.5)	Tukey (weight 0.5)
Receive $F\#$	0.8	0.8
Sampling interval dr	$\lambda/20$	$\lambda/20$
Desired lateral wavelength	1.53 mm	-
TO window size	1.5 mm	-
Number of HRI/estimate	32	32
Line length	-	12.5λ

4.3 Method for simulations and experiments

A number of experiments were performed to test the accuracy and precision of the TO-DB vector flow estimator. These included simulations and measurements of flow in straight-vessel phantoms, realistic flow derived from computational fluid dynamics (CFD) simulated in a carotid bifurcation model, and an *in vivo* scan. This section describes the imaging setup and methods for simulations and measurements.

The same transducer as for the B-mode study in Chapter 3 was employed, and a duplex sequence was constructed to interleave both B-mode and flow emissions. After the emission of three steered flow emissions, a B-mode emission was transmitted. The resulting effective pulse repetition frequency was $\text{PRF}_{\text{eff}} = \text{PRF}/4$ for flow estimation. The optimized B-mode sequence from Chapter 3 was used to construct a B-mode image. Parameters are listed in Table 4.1 and 4.2.

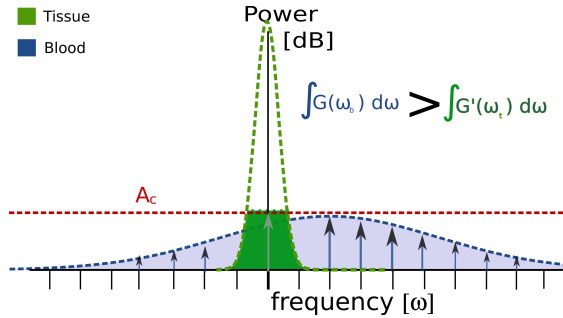


Figure 4.4: Velocity spectra for the tissue signal (green curve) and blood signal (blue curve). The energy-based echo-canceling filter limits the velocity spectrum of tissue to an energy cut-off A_c . The energy of tissue signal (green area) is overpowered by the energy of the blood signal (blue area). From Paper III.

At each velocity estimation point, an axially and laterally beamformed line were used to estimate v_z and v_x using the TO method. The TO angle estimate θ was refined in the TO-DB step by beamforming three directional lines at each estimation point: one at the TO angle θ and at $\pm\Delta\theta$. No TO filtering was applied for the directionally beamformed lines. The selected angle span $\Delta\theta$ depended on the estimated TO angle:

$$\begin{aligned} \Delta\theta &= 2^\circ \text{ for } |\theta| \geq 80^\circ, \\ \Delta\theta &= 5^\circ \text{ for } 50^\circ \leq |\theta| < 80^\circ, \\ \Delta\theta &= 10^\circ \text{ for } |\theta| < 50^\circ. \end{aligned} \quad (4.9)$$

The selection of $\Delta\theta$ was based on the standard deviation (SD) of the TO angle estimate θ from previous experiments (Udesen and J. A. Jensen 2006; J. Jensen, Stuart, and J. A. Jensen 2015). As the SD covers 68 % of the estimates around θ , it is 68 % confident that the flow angle is within $\Delta\theta$, when considering a normal distribution.

Echo-canceling of beamformed data was performed with a Hoeks filter (Hoeks, Hennerici, and Reneman 1991) for simulated and measured flow in a flow rig. For the *in vivo*, an energy-based filter with manual threshold was used (Villagomez-Hoyos 2016; Villagomez-Hoyos, Stuart, Bechsgaard, et al. 2016). This filter was used instead of a conventional frequency cut-off filter to better separate the blood signal from the tissue signal of the moving vessel wall. The velocity spectra of blood and tissue tend to overlap more for transverse flow estimation as shown in Fig. 4.4, and it makes it difficult to use a frequency cut-off. The energy-based filter uses energy characteristics of blood and tissue, and tissue components are attenuated by limiting the energy of the tissue velocity spectrum to a cut-off threshold A_c . Energy of the narrow-band tissue signal, $\int G'(\omega_t) d\omega$, is thereby overpowered by the energy of the more broad-band blood signal $\int G(\omega_b) d\omega$.

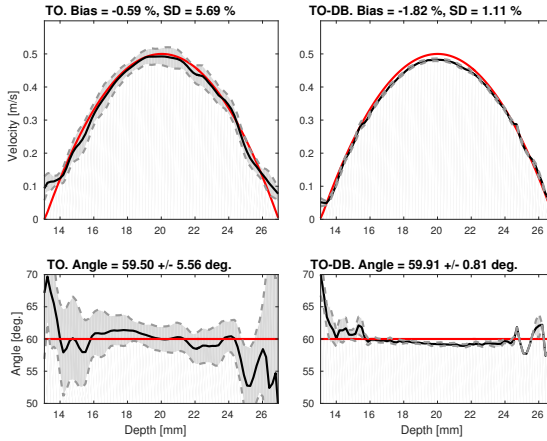


Figure 4.5: Simulated velocity profiles for a straight vessel phantom at a 60° beam-to-flow-angle. Velocity magnitude (top) and angles (bottom) for TO (left) and TO-DB (right). Mean estimates are shown in black with ± 1 SD and true profiles are in red. From Paper III.

The threshold A_c was here manually determined after calculating the energy-levels of tissue and blood for the particular scan.

4.4 Straight vessel phantoms

4.4.1 Methods

Parabolic flow in a rigid vessel was used to investigate the performance of the TO and TO-DB methods under laminar flow conditions, and to compare simulations with measurements. Simulations of channel RF-data were performed using the Field IIpro program (J. A. Jensen and Svendsen 1992; J. A. Jensen 1996b, 2014a). Non-pulsatile parabolic flow was simulated in a straight rigid-wall vessel with a radius of 6 mm and centered at a depth of 20 mm. The vessel was rotated to the angle θ , and the peak velocity of the flow was 0.5 m/s. The simulation used approximately 10 point scatterers per resolution cell randomly distributed and with amplitudes generated from a Gaussian distribution.

For measurements, the experimental scanner SARUS (J. A. Jensen, Holten-Lund, et al. 2013) was used to acquire channel RF data. The same setup as for simulations was employed. Constant parabolic flow was circulated in a flow rig system, where the radius of the tube was 6 mm. Volume flow was measured by a magnetic flow meter for reference. The PRF was reduced to 2 kHz to avoid reverberations in the water tank, and the volume flow was adjusted to match the peak velocity-to-PRF ratio in the simulations. The match of parameters in simulations and measurements allowed for direct comparison.

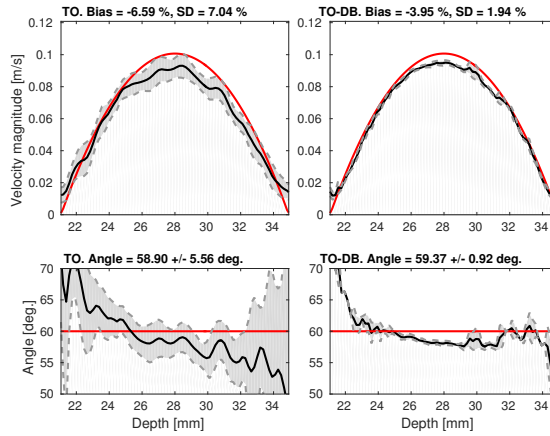


Figure 4.6: Measured velocity profiles for a straight vessel phantom at a 60° beam-to-flow angle. Velocity magnitude (top) and angles (bottom) for TO (left) and DB (right). Mean estimates are shown in black with ± 1 SD and true profiles are in red. From Paper III.

4.4.2 Results

Results for a beam-to-flow angle 60° are shown for simulations in Fig. 4.5 and for measurements in Fig. 4.6. The mean velocity magnitude and angles for the center line are shown in black with ± 1 SD, and the true velocities and angles are shown in red. Results for TO are shown in the left figures, while results for TO-DB are shown in the right figures. Accuracy and precision of velocity estimates were quantified with mean bias and mean SD relative to the true peak velocity. To avoid boundary effects, bias and SD were calculated within 90 % of the vessel radius. In simulations, the velocities were estimated accurately with a bias less than 2 % for both TO and TO-DB, and there was a reduction in SD from 5.7 % to 1.1 % when using TO-DB rather than only TO. The precision of angles was also improved, when applying TO-DB based on the TO estimates, while a high accuracy was maintained. The experimental results in Fig. 4.6 were in good agreement with simulations, only with a small increase in bias and SD for measurements compared to simulations. The wrong estimations close to the vessel walls were due to the echo-canceling filter, which removed all energy from blood and tissue.

Simulations were also performed for beam-to-flow angles from 30° to 90° , and the relative bias and SD are summarized in Fig. 4.7. SDs less than 2° for angles and 2 % for velocities were maintained at all beam-to-flow angles using TO-DB, while the SD of the angle for TO increased significantly, when the beam-to-flow angle was below 60° . Both TO and TO-DB estimated velocities with a bias less than 4 % for all angles. However, slightly larger biases on the velocities were obtained for TO-DB compared to TO at beam-to-flow angles above 60° .

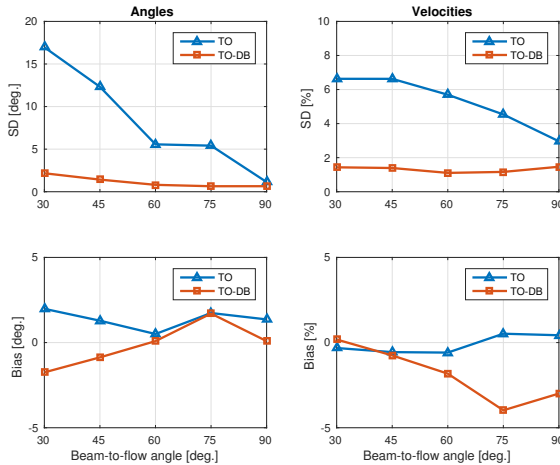


Figure 4.7: Results for simulated vessel phantoms at beam-to-flow angles from 30° to 90° . SD (top) and bias (bottom) for angles (left) and velocities (right). Red graphs show results for TO and blue graphs for TO-DB. From Paper III.

The 90° beam-to-flow angle was a challenging case for TO-DB. This was expected to be due to the low frequency content in the directional (transverse) signals. To increase the frequency content in the transverse direction, experiments were performed using larger steering angles and/or lower receive $F\#$. It was investigated by varying the maximum steering angle of the plane wave from 0° to 20° in steps of 5° and using three angles in each case except for 0° . The beam-to-flow angle was 90° . Two $F\#$ were tested: 0.8 and 1.6. The receive apodization in DB can be changed from a Hamming to a TO window, and both apodizations were also tested. Results are shown in Fig. 4.8.

For an $F\# = 0.8$, relative bias and SD were almost constant as a function of maximum steering angle. The difference between a TO and Hamming receive apodization was consistently 1-2 %. The TO apodization suppressed low frequency content and kept frequency components around the desired TO oscillation. However, the TO apodization for DB was not used for the experiments in the next sections, due to the relatively small improvement compared to a Hamming apodization, and to avoid a reduction in SNR due to TO filtering.

For a larger $F\#$, the dependency on maximum steering angle was large, and the bias reduced from -15 % to -5 %, when increasing the angle from 0° to 20° . In this case, the maximum steering angle had a larger impact on increasing the lateral frequency content.

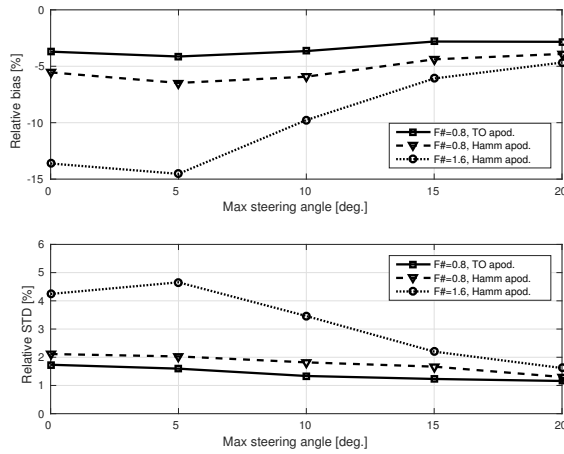


Figure 4.8: Relative bias (top) and SD (bottom) as a function of maximum steering angle of the emitted plane waves. For $F\# = 0.8$ and TO apodization in receive (solid line), $F\# = 0.8$ and Hamming apodization, and $F\# = 1.6$ and Hamming apodization.

4.5 CFD simulation of carotid bifurcation

4.5.1 Methods

A carotid bifurcation model was employed for investigation of complex flow conditions in a realistic vascular geometry. Swillens et al. (Swillens et al. 2009) has provided a computational fluid dynamics (CFD) dataset, which contains a bifurcation geometry of a healthy volunteer. An eccentric plaque is artificially inserted in the internal branch. Flow is simulated using the CFD-package Fluent for a cardiac cycle of 1 second in steps of 5 ms. An inlet velocity profile is applied at the common carotid artery. Rigid walls are assumed with no tissue movement. Swillens et al. also provide a framework (BioMMeda.ugent.be) for ultrasound simulations, where the CFD velocities are used for propagating scatterers and coupled to Field II. Spatial and temporal interpolation are handled by the framework for updating the scatterer positions according to the ultrasound simulation. The CFD dataset and the framework were used in this study.

4.5.2 Results

Vector flow images (VFI) from frames during peak systole and systolic deceleration are shown in Fig. 4.9 and 4.10. The reference CFD frames are shown to the left, where velocity vectors are overlaid on a color wheel map, which depends on both velocity magnitude and angle. The middle and right images show the ultrasound simulated estimates after TO and TO-DB processing, respectively. Visual inspection of the images reveal good agreement between the reference CFD images and estimated VFI frames. However, wrong

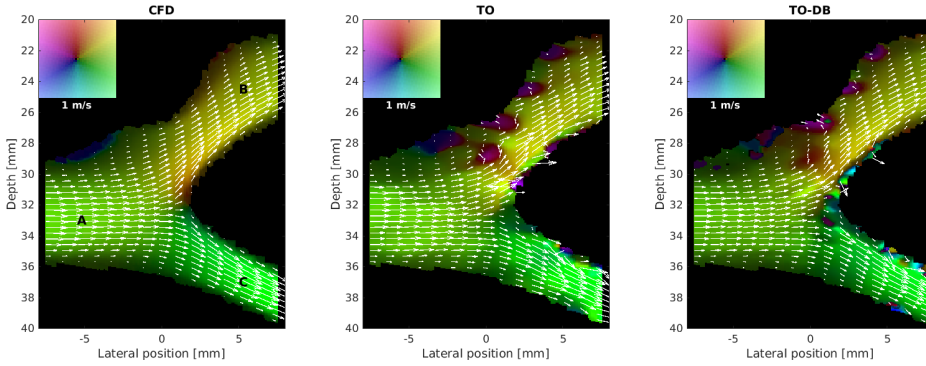


Figure 4.9: Simulation of flow in a carotid bifurcation model. Frames are shown at peak systole from the reference CFD model (left), estimated velocities using TO (middle), and estimated velocities using TO-DB (right). A, B and C indicate the common, internal, and external carotid artery, respectively. From Paper III.

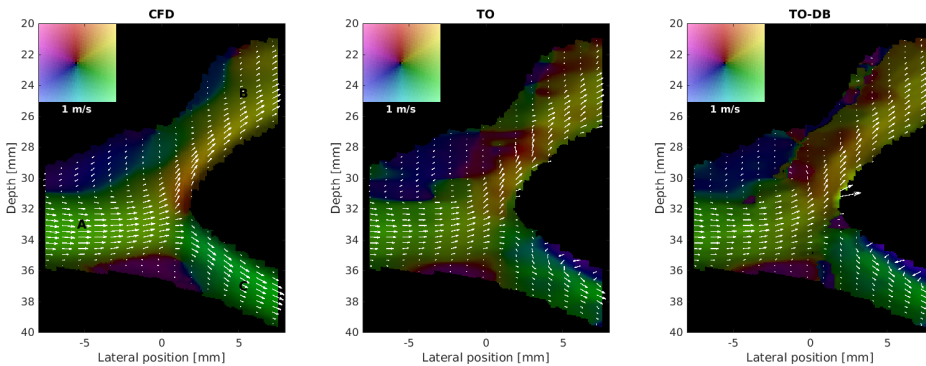


Figure 4.10: Simulation of flow in a carotid bifurcation model. Frames are shown at systolic deceleration from the reference CFD model (left), estimated velocities using TO (middle), and estimated velocities using TO-DB (right). From Paper III.

estimations were obtained in the internal carotid artery as shown in Fig. 4.9 at peak systole. This could be due to the low beam-to-flow angles, where TO also had the lowest precision according to the straight vessel simulations in Fig. 4.7. Furthermore, the TO-DB method cannot recover the angle, if the TO angle is estimated with an error more than $\pm\Delta\theta$.

Fig. 4.10 shows complex flow patterns during systolic deceleration, and two vortices are clearly visualized and defined using TO-DB. Furthermore, wrong TO angle estimates in the internal carotid artery around (5, 23) mm and (3, 29) mm were corrected with the TO-DB step.

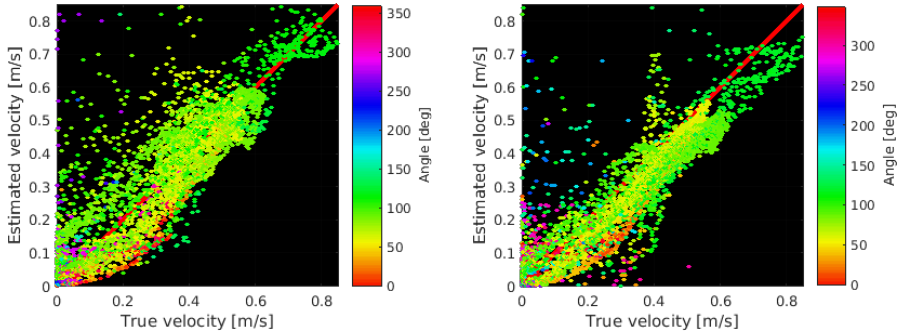


Figure 4.11: Scatter plots of true (CFD) velocities versus velocity estimates using TO (left) and TO-DB (right). Estimates are from peak systole, and the color encoding represents estimated angle. From Paper III.

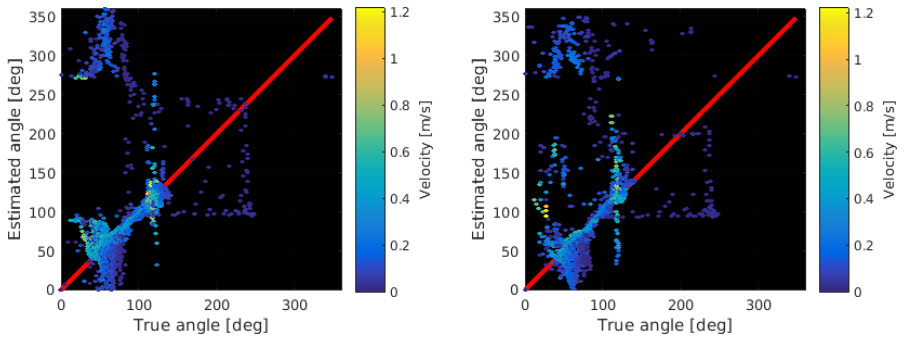


Figure 4.12: Scatter plots of true (CFD) angles versus angle estimates using TO (left) and TO-DB (right). Estimates are from peak systole, and the color encoding represents estimated velocity. From Paper III.

A more quantitative comparison between CFD and VFI is provided in scatter plots of estimated versus reference velocities and angles as shown in Fig. 4.11 and 4.12. Estimates at all spatial points from the frame at peak systole were used, and TO estimates are shown to the left and TO-DB to the right in the figures. The colors encode either estimated angle or velocity magnitude, and the straight red lines are the reference values. Linear regression of velocity magnitude gave a slope of 0.85 for TO-DB and 0.97 for TO, which indicated a larger underestimation of velocities when using TO-DB compared to TO. The spread of estimates along the linear regression line was quantified as the interquartile range, which was 11.8 cm/s for TO and 7.1 cm/s for TO-DB. The linear regression slope for the angles in Fig. 4.12 was 1.01 for both TO and TO-DB, while the angle spread was 6.7° for TO and 4.7° for TO-DB.

Fig. 4.12 also shows that true angles at 60° were wrongly estimated as angles about 300° . The angles corresponded to the wrong estimations in the internal carotid artery as shown in Fig. 4.9, which were not recovered by TO-DB. Furthermore, true angles at 120° were wrongly estimated as random angles, which corresponded to estimates near the vessel wall in the external carotid.

4.6 *In vivo* carotid bulb

4.6.1 Methods

Prior to an *in vivo* scan, intensity and temperature measurements were performed to assure compliance with FDA regulations (FDA 2008). Mechanical index (MI) and derated spatial-peak temporal average intensity ($I_{spta.3}$) were measured using the Acoustic Intensity Measurement System AIMS III (Onda Corp., Sunnyvale, CA, USA), an Onda HGL-0400 hydrophone, and the approach described in (J. A. Jensen, Rasmussen, et al. 2016). MI was measured to 1.25 and $I_{spta.3}$ to 267 mW/cm^2 for the sequence. This was within FDA limits, which are $MI = 1.9$ and $I_{spta.3} = 720 \text{ mW/cm}^2$. Transducer surface temperature rise was measured during 30 min for an excitation voltage of 50 V and was 18.6°C in still air and 6.3°C when attached to a phantom. The values are below the IEC limits of 27°C and 10°C , respectively (IEC 2015).

The *in vivo* scan was conducted on a 26-year old healthy male. The right carotid bulb was scanned in a longitudinal view. The scan sequence and equipment were the same as for simulations and flow rig measurements, and the PRF was 10 kHz. Data were acquired for 10 s using the SARUS scanner.

4.6.2 Results

Velocities were estimated from the acquired data at a frame rate of 300 frames/s, but the frame rate could have been increased to its maximum of 2000 frames/s. The corresponding B-mode images had a frame rate of 119 Hz. Frames from the *in vivo* scan at peak systole and late systole are shown in Fig. 4.13, which were processed using TO (left images) and TO-DB (right images). The shallow vessel was a part of the jugular vein with flow from left to right, while the deep vessel was the carotid bulb with the inlet of internal carotid artery leftmost. Both TO and TO-DB visualized a large vortex, which filled the carotid bulb at peak systole. Furthermore, a more streamlined flow with less angle spread was estimated in the deep part of the bulb, and the vortex with low velocities in its center at approximately (1, 22) mm could be better appreciated when using TO-DB. Laminar flow in the inlet of the internal carotid artery was estimated with an almost parabolic velocity profile using TO-DB. Similar angles and velocities were estimated during late systole using TO and TO-DB, however, TO estimated back-flow close to the vessel walls, which was not detected with TO-DB. It should be noted that velocities close to vessel walls are low and challenging to estimate.

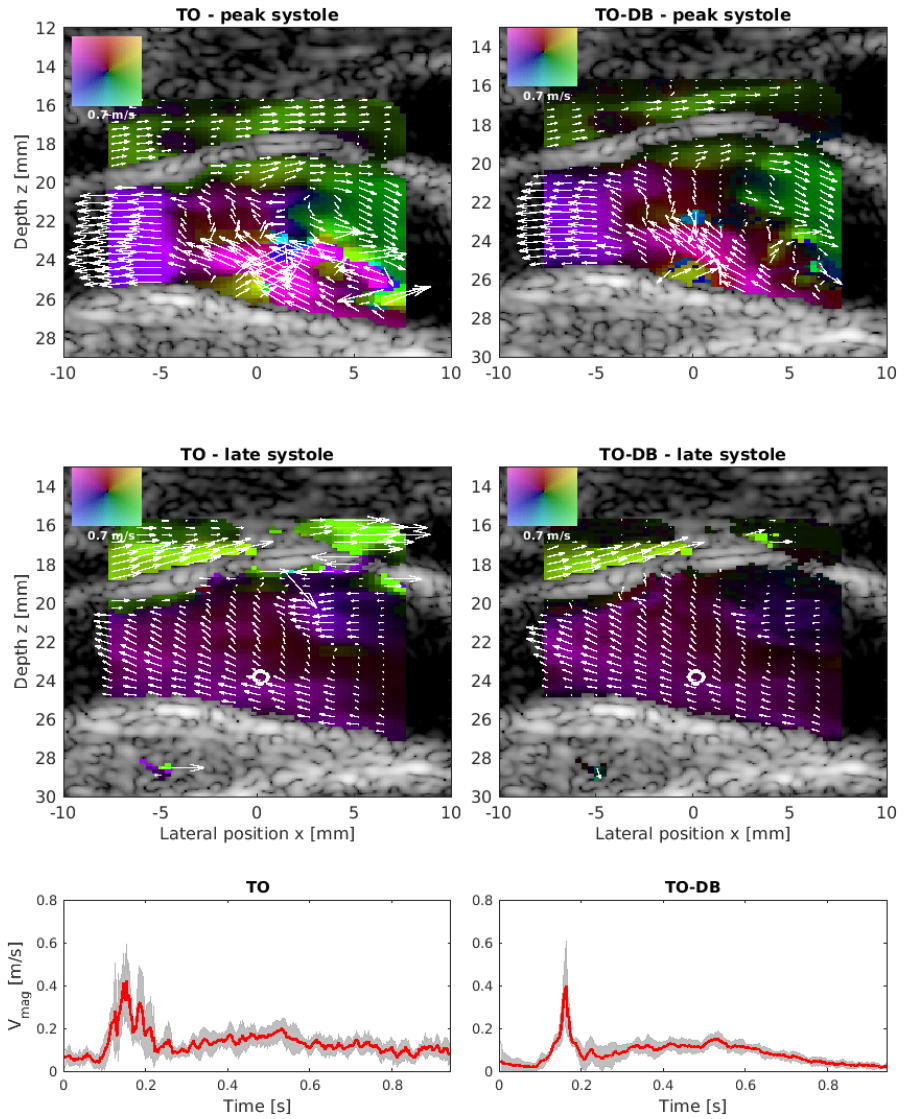


Figure 4.13: *In vivo* scan of the carotid bulb. VFI for frames at peak systole (top) and late systole (middle), and estimates using TO are in the left images while estimates using TO-DB are in the right images. The bottom figures show velocity magnitude at a single estimation point (white circle on VFI) after alignment of nine cardiac cycles. The mean \pm one SD is shown for TO (left) and TO-DB (right).

During the 10 s scan acquisition, nine cardiac cycles were detected. The alignment of the velocity magnitude profiles according to the cardiac cycle is shown in Fig. 4.13 (bottom) for TO (left) and TO-DB (right) for an estimation point indicated by the white circle in the bulb. The red curves are the mean estimates and the gray area is \pm one SD. The mean SD of the velocity magnitude was calculated to 14.1 % for TO and 8.8 % for TO-DB. The peak velocity was 0.4 m/s for both TO and TO-DB at the estimation point, while the velocities after peak systole quickly dropped for TO-DB. The velocities during diastole was 0.05 m/s lower for TO-DB than TO, where the angle changed to nearly 90° . For the *in vivo* scan presented in Paper III, the velocities were also estimated lower for TO-DB compared to TO, especially at peak systole where the velocity was 0.84 m/s for TO and 0.64 m/s for TO-DB. The differences in peak velocities may be related to the beam-to-flow angle, which was close to 90° . Any small angle errors can give an underestimation in the velocity magnitude, and as shown for the straight vessel phantoms in Section 4.4, the 90° beam-to-flow angle resulted in an underestimation of velocities for TO-DB.

4.7 Slow velocity flow

The TO-DB method for plane wave vector flow imaging was so far used for estimation of flow in the range 0.15 - 1 m/s, which is representative for flow in major vessels such as the carotid artery. However, blood flow velocities in the human body span a larger range from m/s in large arteries to mm/s in small vessels (J. A. Jensen 1996a). The TO-DB estimator should therefore also be investigated when applied for slower velocity flow estimation.

Plane wave imaging for slow velocity flow estimation has previously been investigated by Bercoff et al. (Bercoff et al. 2011) using Power Doppler imaging for the small vasculature present in the human thyroid. It was demonstrated that plane wave imaging had a larger sensitivity to slow velocity flow than line-by-line imaging, due to the high SNR and the availability of continuous data. It was also indicated that long plane wave sequences further increase the sensitivity compared to shorter sequences, because of an increase in SNR and lower side lobe levels for long sequences.

This section investigates the feasibility of applying the proposed TO-DB method for slow velocity flow estimation when using a longer sequence. The long sequence consisted of 21 plane waves and was identical to the sequence used for B-mode imaging described in Section 4.3. The sequence was interleaved with a short sequence, which consisted of three plane waves, to maintain a high limit of detectable velocities. A similar measurement setup as in Section 4.4 for straight vessels was used for an experiment of constant flow with a peak velocity of 4 cm/s. Flow was circulated in a tube with a diameter of 7 mm, the beam-to-flow angle was 90° , and the PRF was 10 kHz. After beamforming, 21 LRIs (one from each of the 21 plane waves) from the long sequence were combined to an HRI, while three LRIs were combined per HRI for the short sequence. For both sequences, 21 HRIs were then correlated for velocity estimation. Echo-canceling was performed for the

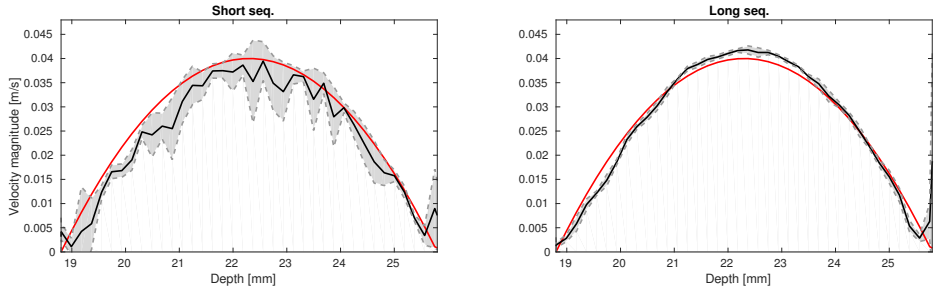


Figure 4.14: Slow velocity flow measurements. The velocity profile in the left image was obtained from the short sequence and the right image from the long sequence. From Paper V.

same time period (0.18 s) for the two sequences. Additional processing parameters were the same as listed in Table 4.2.

Fig. 4.14 shows the results. The short sequence (left figure) was capable of detecting the velocity profile, however, with a larger SD than the long sequence (right figure). The bias and SD were -6 % and 10 %, respectively, for the short sequence. For the long sequence, the SD was reduced by a factor of four to 2.5 % and the bias was reduced to 0.1 %. Since $v_{x,max}$ for the long sequence was 5.9 cm/s, the short sequence should be used whenever flow was above this threshold. The interleaved sequences would allow data to be processed in parallel and used with either of the sequences for fast and slow velocity estimation. Note that if a separate B-mode sequence cannot be included in the emission sequence, a compromise needs to be made for the receive gain.

The results indicated the advantages of having a long sequence with a higher sensitivity than a short sequence, because 21 rather than three plane waves were combined, thus, reducing side-lobe levels and improving contrast. Further investigations should be made to quantify the increase in sensitivity and to test the long sequence for slow velocity flow estimation in smaller vessels, where a high sensitivity is of importance. This would allow to find the limitations of the estimator and the sequence.

4.8 Discussion and summary

The suggested TO-DB method used a combination of TO and DB for 2-D vector flow imaging. The beamforming load was 4.6 times larger than for TO and seven times smaller than for conventional DB. Thus, TO-DB places itself between TO and conventional DB regarding beamforming load. The TO-DB method estimated flow angles and velocities accurately for constant flow in straight vessels at all investigated beam-to-flow angles, which were shown in Fig. 4.7. A constant SD less than 2 % for velocities and 2° for angles was also obtained. The TO-DB method was more precise than TO for especially low beam-to-flow angles, where TO had a SD larger than 6 % on the velocity magnitude and

larger than 10° on the angles. TO-DB underestimated velocities for beam-to-flow angles around 90° . The underestimation might be avoided by increasing the high frequency content in the directional signals, which helps to detect more accurately the lag between signals. A lower receive $F\#$ and/or larger steering of the emitted plane waves increases the high frequency content, and the impact on bias was shown in Fig. 4.8. An alternative is to compensate for the velocity bias at beam-to-flow angles close to 90° , which is possible since the bias on the angle is low and the SDs of both velocity magnitudes and angles are low.

A full version of DB with beamformation of lines in all directions was presented by Villagomez-Hoyos et al. (Villagomez-Hoyos, Stuart, Hansen, et al. 2016). They obtained angle biases below 1° and SDs around 1.5° in straight vessel phantoms, and estimated velocity magnitudes with a bias under 10 % bias and 5 % SD. Even though a direct comparison cannot be made due to different setups, it indicates that the results for TO-DB are close to the performance of DB.

Prior to the *in vivo* scan, intensities of the sequence were measured. The FDA limits on acoustic intensities are in general not an issue for plane wave imaging, because the lack of transmit focusing spreads the emitted energy over a large area. However, probe heating may be a limiting factor, since plane wave imaging uses all transducer elements to emit pulses in each transmit event. For flow estimation, where the PRF usually is high, it can significantly heat up the surface of the probe. Several factors impact the heating of the probe, e.g. the plane wave sequence, pulse length, excitation voltage, PRF, and the properties of the probe. The heating was also a limitation in this study, since the excitation voltage had to be reduced from 100 V to 50 V to ensure that heating did not exceed IEC requirements. Reducing PRF was not considered, as it would influence the performance of the velocity estimator negatively. The excitation voltage of 50 V resulted in acceptable SNR-levels and an imaging depth below 8 cm. However, if the excitation voltage and/or PRF could be increased, and the heating of the probe still could be kept within temperature requirements, it might improve the performance of plane wave VFI methods. Developments within transducer technology should address the heating issues, as it would allow plane wave flow imaging to utilize its full potential.

This chapter showed that the TO-DB method had improved performance in terms of accuracy and precision compared to the TO method. The TO-DB method approached the same accuracy as conventional DB, while maintaining a lower beamforming load. A single *in vivo* scan showed the feasibility and potential of the TO-DB method, but it should be followed up by several *in vivo* scans to further investigate its performance. This is the topic of the next chapter, where the accuracy and precision of the TO-DB VFI method is investigated for laminar and complex flow *in vivo* among ten healthy volunteers.

CHAPTER 5

In vivo study of plane wave vector flow imaging

This chapter continues the investigation of plane wave vector flow imaging from Chapter 4 by expanding the study to a number of volunteers. First, complex flow patterns are measured in an anthropomorphic flow phantom and the estimates are compared to a velocity field simulated from computational fluid dynamics. Second, the precision of vector flow imaging is investigated at several locations in the common carotid artery and bulb in a group of ten healthy volunteers. Third, examples of complex flow patterns *in vivo* are shown. For a further in-depth description of the study the reader is referred to Paper VI in the appendix.

5.1 Background and purpose

The imaging of both laminar and complex flow patterns is one of the main advantages of vector flow imaging (VFI). To establish the validity of a VFI estimator, it is important to investigate the precision and the accuracy not only in simulations but also *in vivo* under laminar and complex flow conditions.

Previously, the accuracy of vector flow methods has been investigated under laminar flow conditions in the common carotid artery by comparing peak systolic velocity (PSV) and volume flow with independent methods such as spectral Doppler and magnetic resonance angiography (MRA) (Hansen, Udesen, Oddershede, et al. 2009; Pedersen et al. 2012; Ekroll et al. 2014; Hansen, Møller-Sørensen, et al. 2015; Tortoli et al. 2015). However, for investigation of accuracy and precision under complex flow conditions, the following challenges arise: (1) neither spectral Doppler nor MRA has sufficient high spatial and temporal resolution to accurately capture complex flow patterns, when comparing to VFI methods; and (2) it requires data acquisition of at least two to three heart beats to evaluate the precision in terms of repeatability of velocity estimates, but this generates more transducer element data than most scanners can store.

In relation to (1), complex flow may be investigated in a realistic phantom study. Flow phantoms can be designed from anthropomorphic geometries by using novel fabrication processes, whereby complex flow patterns in a realistic vessel geometry and environment can be measured using ultrasound (Lai et al. 2013). Computational fluid dynamics (CFD) can then be used to simulate the velocity field from the same vessel geometry and boundary

conditions as the phantom measurement. The advantage is that CFD modelling is an independent method, and the simulated CFD velocities can be compared to the measured VFI estimates from the phantom. In relation to (2), 10 s scans can be performed and all element data stored using the experimental scanner SARUS, i.e. the precision of flow estimation methods may be evaluated from several heart beats.

The purpose of this study was to investigate the accuracy and precision of the TO-DB method under laminar and complex flow conditions in the carotid artery in ten volunteers. The TO-DB method is referred to as plane wave VFI in the rest of this chapter.

The approach was to evaluate:

- the accuracy under complex flow conditions by comparing plane wave VFI estimates obtained from an anthropomorphic phantom measurement to CFD simulated velocities derived from the same geometry,
- the precision *in vivo* by calculating the repeatability of the plane wave VFI estimates at several estimation points in the vessels.

5.2 Methods for experiments

Ten healthy volunteers were recruited (8 males and 2 females; mean BMI: 24 kg m^{-2} ; mean age: 32 years, range 25-52 years). VFI scans were conducted during a session in the morning and the MRA scan in the evening.

5.2.1 *In vivo* VFI scans

Plane wave VFI scans were performed using a linear array transducer (BK 8L2, BK Ultrasound, Herlev, Denmark) connected to the SARUS scanner. The same duplex sequence as described in Section 4.3 was employed. Each of the two scans listed below was recorded separately:

- a longitudinal scan at the right common carotid artery (CCA) 2-3 cm upstream of the bifurcation, and
- a longitudinal scan at the carotid bulb with the most optimal view of the bifurcation.

Transducer element RF data were acquired for a total of 10 s for each scan and were stored for further processing. Beamforming, echo-canceling, and velocity estimation were the same as described in Section 4.3 and are also detailed in Paper VI.

5.2.2 MRA scans

Anatomical MRA images were acquired for a volume covering the common carotid artery and the carotid bulb. The acquisition was made in parallel to a flow sequence, where through-plane velocities were measured in a cross-sectional plane of the CCA 2-3 cm

below the bifurcation. A retrospective ECG gated phase contrast sequence was applied, and the details of the sequence and processing of MRA data are described in details in Paper VI.

A 3-D geometry representing the carotid artery of one of the volunteers was used for producing a CFD model and a flow phantom as described below.

5.2.3 Flow phantom fabrication and scan

The anthropomorphic flow phantom matching the flow domain of the original scanned vessel was fabricated using stereolithography (Lai et al. 2013). A 3-D printed geometry of the vessel was used to create a wall-less phantom with a fluid domain identical to the original scanned vessel, and properties of the surrounding medium mimicking the properties of human tissue. Details on the phantom fabrication are given in Paper VI.

The phantom was connected to a flow system (CompuFlow 1000, Shelley Medical Imaging Technologies, Toronto, Canada) that circulated a blood-mimicking fluid. The CompuFlow system was set to generate a standard carotid artery waveform to mimic the flow in this artery. The transducer was placed on the phantom with the scan plane longitudinal to the bifurcation. Data were acquired for 10 s with the SARUS scanner using the same sequence and same parameters as for the *in vivo* scans.

5.2.4 CFD model

The vessel geometry was imported into Comsol Multiphysics (v5.2a, Comsol AB, Stockholm, Sweden). Flow fields were simulated based on parameters set to match those of the experimental set-up and the blood-mimicking fluid. A direct PARDISO solver (www.pardiso-project.org) was applied. A time-varying velocity waveform, which was obtained from the plane wave VFI phantom measurement at a velocity estimation point in the CCA, was imposed on the whole inlet plane with the assumption of fully developed parabolic flow. An outlet pressure of 0 Pa was set for the two exit branches representing the ICA and ECA, while a no-slip condition was set at the walls of the flow domain.

5.3 Methods for evaluation

5.3.1 Comparison between phantom VFI and CFD simulation

The geometries of the phantom VFI measurement and the CFD simulation had to be aligned before making any comparisons. First, the 2-D B-mode image from the VFI scan was used to manually segment the vessel. Then, the 3-D geometry from the CFD model was rotated and translated to the coordinate system of the VFI plane to align the geometries. This was performed manually by visual inspection of the geometries. The applied translation and rotation was saved in a transformation matrix to convert the CFD velocities into velocity components in the coordinate system corresponding to the VFI.

5.3.2 Precision of VFI *in vivo*

The VFI and B-mode datasets from the *in vivo* scans were imported into an in-house developed Matlab-based visualization tool, where the precision analysis was made. A video of the full 10 s acquisition was played and could be stopped at any frame. A medical doctor with experience in VFI evaluated each of the 2x10 scans by selecting evaluation points according to a defined procedure for:

- longitudinal scans of the CCA: one point in the center of the vessel and one point near the upper vessel wall
- longitudinal scans at the carotid bulb: a point in the center of a part of the CCA, near the upper vessel wall of the CCA, in the ECA, in the ICA, and the vortex in the carotid bulb.

An evaluation point was not selected, if a vessel or a vortex was not visible. For each selected evaluation point, the program automatically calculated the mean cardiac cycle based on the velocity estimates by using the autocorrelation function. The velocity magnitude and angle estimates were coherently aligned according to the cardiac period. 90 % of the cardiac period was used for the alignment to account for small deviations in heart rate. The standard deviation $\sigma(t)$ at time t in the cardiac cycle was calculated among the aligned velocity magnitude and angle estimates. The mean SD for each point was then

$$SD = \sqrt{\frac{1}{N_f} \sum_{t=1}^{N_f} \sigma(t)^2} \quad (5.1)$$

where N_f is the number of frames encompassing a cardiac cycle. The mean SD of velocity magnitude estimates was calculated relative to the peak velocity magnitude v_0 .

An example of coherently aligned estimates according to the cardiac period is shown in Fig. 5.1. The estimates were from an evaluation point close to the vessel wall of the CCA. It can be noticed that the angle naturally fluctuated randomly when very low velocities were present. The angles were much more stable when higher-velocity flow was present. The SD of the angles were therefore also calculated from (5.1) using frames N_f , where the velocity magnitude was above 10 % of the maximum velocity at the evaluation point.

5.4 Comparison between phantom VFI and CFD simulation

The VFI scan plane (segmented vessel) aligned with the CFD geometry is shown in Fig. 5.2. The segmented vessel from the VFI fitted generally well within the 3-D mesh of the CFD simulation. There was, however, about 0.5 to 1 mm misalignment in the external carotid artery (ECA) and at the outlet of the internal carotid artery (ICA).

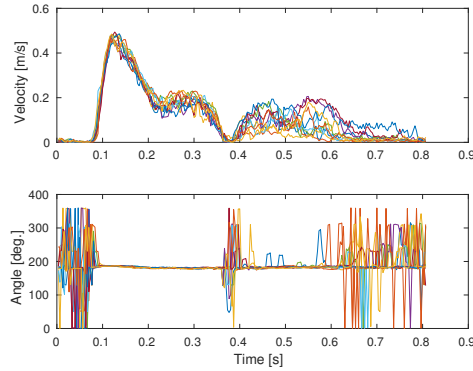


Figure 5.1: Velocities (top) and angles (bottom) for an evaluation point close to the vessel wall for one of the volunteers. Estimates were aligned to the cardiac cycle, and each coloured curve is for a cardiac cycle. From Paper VI.

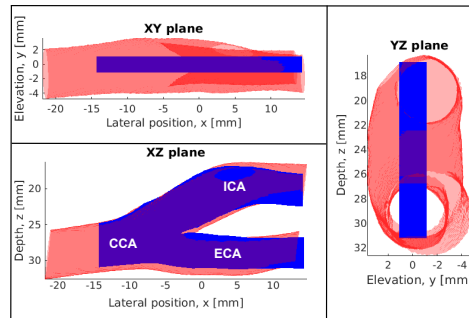


Figure 5.2: Alignment of the CFD vessel geometry (red) to the VFI scan plane (blue) of the segmented vessel. The elevation extent of the ultrasound beam is indicated by the width of the blue rectangle in the XY and YZ plane. From Paper VI.

A frame during systolic deceleration (0.32 s) is shown in Fig. 5.3 with estimates from the CFD simulation (left image) and VFI scan (right image). Generally, the VFI velocity field had the same patterns as the CFD simulation and the velocity magnitudes were at the same levels. Both the CFD and VFI showed a large vortex, which extended from the CCA into the ICA. Differences were obtained in the ECA, where lower velocity magnitudes were estimated with VFI than with CFD, and a small vortex was estimated within 1-2 mm for VFI and CFD.

Fig. 5.4 shows velocity profiles sampled at locations in the CCA, ICA, and ECA, and at three time instances during the pump cycle. The mean differences between CFD and VFI velocities were calculated across the vessels and relative to a peak velocity of

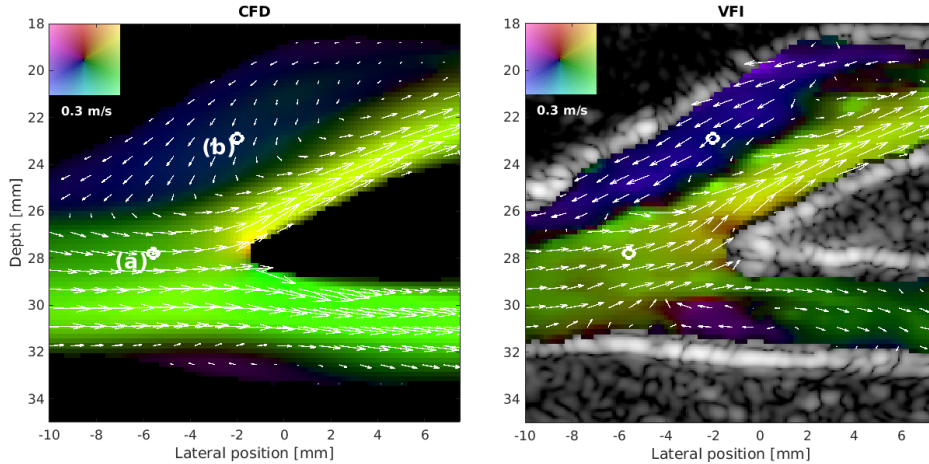


Figure 5.3: Velocity estimates from CFD simulation (left image) and VFI scan (right image). The frame was within systolic deceleration ($t = 0.32$ s). The white circles are estimation points (a) and (b) for the plots in Fig. 5.5. From Paper VI.

0.55 m/s. Mean differences were between -2 % and 6.8 % at the three time instances in the CCA, while the differences were between 2 % and 11.3 % in the ICA. The mean differences in the ECA were between 3.5 % and -20 %; the largest difference was at systolic deceleration ($t = 0.32$ s). The analysis reflects that the flow conditions in the CCA were close to the imposed inlet conditions, while the flow conditions were much more complex in the ECA and ICA, because the flow patterns changed though the bifurcation. The VFI-CFD misalignment of 0.5 - 1 mm in the ECA was also apparent from the velocity profiles.

Fig. 5.5 shows the velocity magnitude and angles as a function of time for an estimation point (a) in the CCA and (b) the vortex in the ICA. The location of the points were also indicated by the white circles in Fig. 5.3. The estimates from VFI were aligned to the pump cycle to find the mean and SD of the estimates during a pump cycle. Flow was mainly laminar in the CCA, where the mean difference between CFD and VFI was 6.6 % and the SD was 5 %. The angle changed drastically from 65° to around 200° at two time instances (at 0.13 s and 0.3 s) in the VFI measurements, which - in combination with a video sequence of the full acquisition - indicated the evolution of vortices at these two time instances. In the CFD simulation, a single vortex built up after 0.15 s. It was suspected that vessel wall movement in the phantom might be a reason for the different flow patterns between the VFI and CFD simulation during systole. The tissue velocities were therefore estimated by disabling the echo-canceling filter. The axial velocity component for a point on the proximal vessel wall is shown in Fig. 5.6 (top). For comparison, the velocity magnitude of blood flow at a point in the CCA is shown in Fig. 5.6 (bottom). Note the

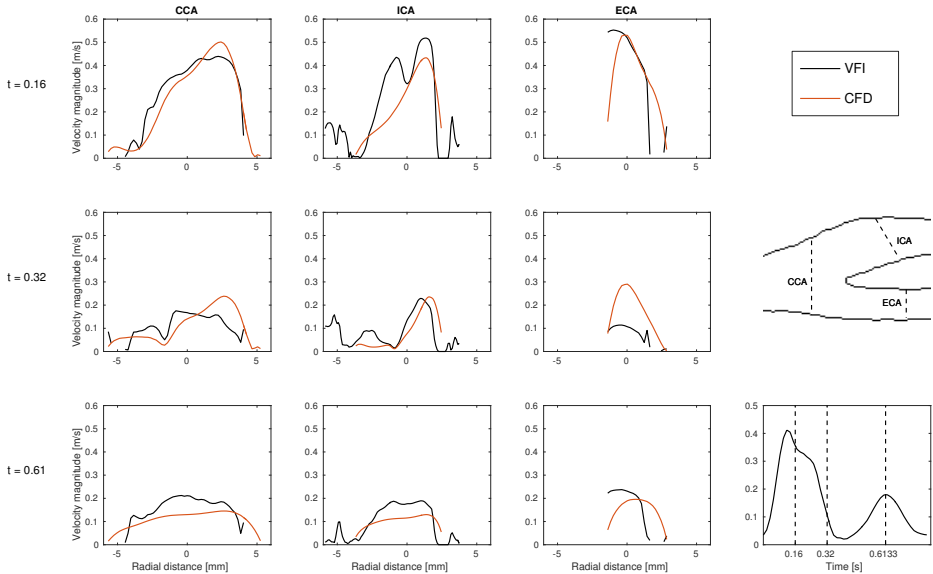


Figure 5.4: Comparison of velocity magnitude profiles at locations in the CCA (left column), ICA (middle column), and ECA (right column). Sampling was performed at $t = 0.16$ s (top row), $t = 0.32$ s (middle row), and $t = 0.61$ s (bottom row). Red profiles indicate CFD estimates and black VFI estimates. From Paper VI.

different scaling on the vertical axes in the figure: maximum vessel wall velocity was ± 2 mm/s and maximum blood flow velocity magnitude was 0.5 m/s. The largest movement of the vessel wall was in the systolic phase, where the wall moved towards the transducer. During systolic deceleration, the wall moved predominantly away from the transducer.

5.5 Precision of VFI *in vivo*

The results for mean SD of velocity magnitude estimates and angles calculated from (5.1) are shown for each volunteer in Fig. 5.7 from evaluations of CCA scans. Results are shown for the center of the CCA and near the upper vessel wall, and the dashed horizontal lines are the mean SDs among the volunteers. A high precision of the velocity magnitude was obtained in the center (mean SD was 4.4 %) and a slightly lower precision was obtained near the vessel wall (mean SD was 6.6 %). The angle estimates in the center of the CCA attained a precision of 10° , when using estimates throughout the whole cardiac cycle (dark blue bars in Fig. 5.7). The mean SD reduced to 7.5° , when excluding frames with low velocity flow (green bars in Fig. 5.7). Near the vessel wall, the mean SD among the volunteers was increased to 46° , when using estimates throughout the cardiac

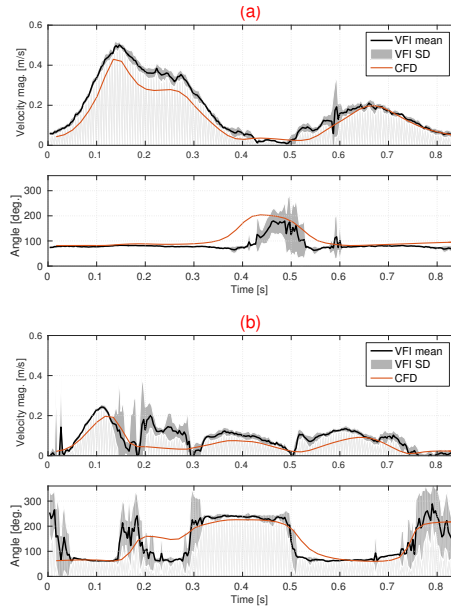


Figure 5.5: Velocity magnitude and angle estimates as a function of time during the cardiac cycle. Estimates for estimation point (a) in the CCA are shown in the two top images, and for point (b) in the ICA in the bottom images. The estimation points can be identified as white circles in Fig. 5.3. Black graphs show the mean VFI estimates, gray area is the SD of VFI estimates, and red graphs show CFD estimates. From Paper VI.

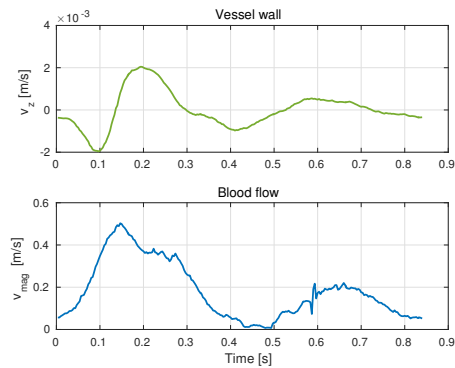


Figure 5.6: Axial velocities v_z of the proximal vessel wall are shown in the top figure. Velocity magnitude of blood flow in the CCA center is shown in the bottom figure. From Paper VI.

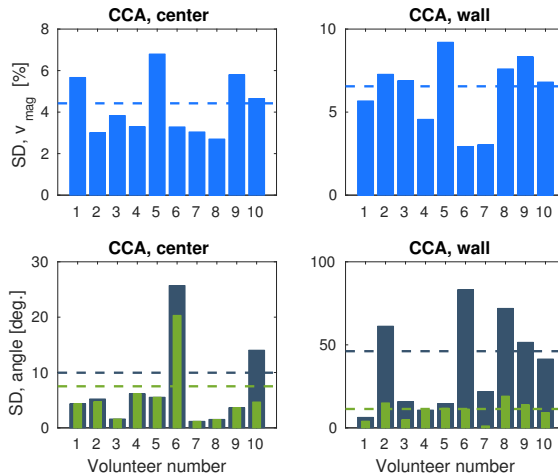


Figure 5.7: Mean SD of velocity magnitude (top) and angles (bottom) for each of the volunteers. Evaluation points in the center of the CCA (left) and close to the upper vessel wall (right) for scans of the CCA. The green bars are when excluding low velocity flow. Dashed line is the mean SD among volunteers. Note the different scaling on the vertical axes. From Paper VI.

cycle. The mean SD reduced to 11.4° , when excluding low velocity flow, and it shows that precise angles also can be obtained close to the vessel wall.

The measurement conditions *in vivo* were affected by physiological factors such as breathing, tissue and transducer movement, and heart rate variations. The very high precision in the CCA was approximately the same as the precision found in the phantom measurement, which indicated that the measurement conditions approached each other.

Results for evaluation points in the ICA, ECA and vortices are shown in Fig. 5.8. Velocity magnitude and angles were estimated with a higher precision in the ICA than the ECA: mean SD of the velocity magnitude was 9.4 % in the ICA and 16 % in the ECA. The mean SD of the angles was 13.2° in the ICA and 55° in the ECA, when excluding frames with low velocity flow. The ECA was a smaller vessel than the ICA and the flow patterns deviated from laminar flow conditions, which made it difficult for the plane wave VFI method to estimate angles precisely. Large fluctuations in the angles were also obtained for the vortices: the mean SD was 54° when calculating the precision during the short time span, where the vortices were present, which is shown with the green bars in Fig. 5.8. The precision for vortices was mainly affected by small variations in the time of development and disappearance of vortices, which is shown as an example in Fig. 5.9 for a vortex present from 0.33 s to 0.4 s. The 180° change in angles was not exactly repeatable from one cardiac cycle to the next one, which led to large variations in the

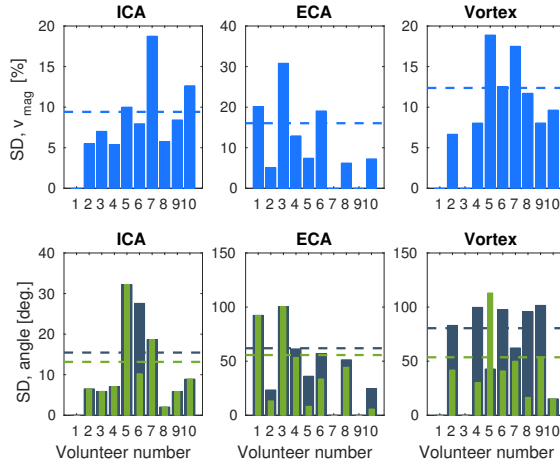


Figure 5.8: Mean SD of velocity magnitude (top) and angles (bottom) for each of the volunteers. Evaluation points in the ICA (left), ECA (middle), and vortex (right). The green bars are when excluding low velocity flow. Dashed line is the mean SD among volunteers. Note the different scaling on the vertical axes. From Paper VI.

angle estimates.

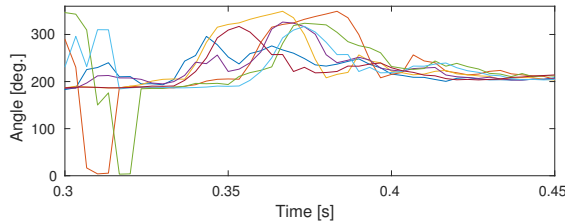


Figure 5.9: Angles for an evaluation point in a vortex, which was present from 0.33 s to 0.4 s. Estimates were aligned to the cardiac cycle, and each coloured curve is for a cardiac cycle. From Paper VI.

5.6 *In vivo* complex flow patterns

The carotid bulb scans on the ten volunteers showed interesting flow patterns with the presence of vortices in eight out of ten volunteers. Some vortices were very small and rapidly formed and disappeared, while others filled most of the carotid sinus. Fig. 5.10 shows two frames during systole for volunteer 8 with 10 ms between the frames. The high

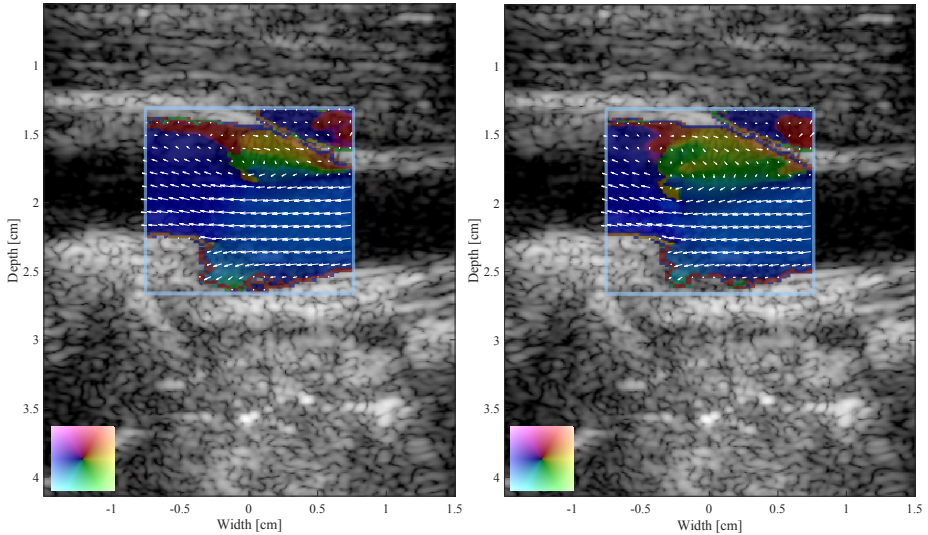


Figure 5.10: VFI of the carotid bulb for volunteer 8. A large vortex was created at the inlet of the ICA (left image) and it moved downstream (right image). The time between the two frames was 10 ms. From Paper VI.

frame rate of the VFI method captured the formation of a vortex initiated upstream in the carotid bulb and the increasing size as it moved downstream in the ICA. The same pattern was observed for volunteer 5 as shown in Fig. 5.11. This flow feature has previously been captured by synthetic aperture imaging (Villagomez-Hoyos et al. 2016) and plane wave imaging (Hansen, Udesen, Gran, et al. 2009).

5.7 Discussion and summary

The study showed that VFI measurements of laminar and complex flow patterns in a carotid bifurcation phantom were similar to the velocity field simulated using CFD. Mean differences between CFD and VFI for velocity magnitudes were within 7 % in the common carotid, but a mean difference of -20 % was obtained in the ECA. Among the ten scanned volunteers, the precision *in vivo* was highest in the center of the common carotid artery (standard deviation 4.4 % for velocity magnitudes) and lowest in the ECA and for vortices (standard deviation 16 % for velocity magnitudes).

A limitation of the phantom study was the manual alignment of the transducer scan plane and the CFD geometry. The alignment was not perfect as especially the ECA appeared more narrow and/or slightly translated vertically, which was also apparent from the velocity profiles in Fig. 5.4. Furthermore, the phantom material had slightly shrunken

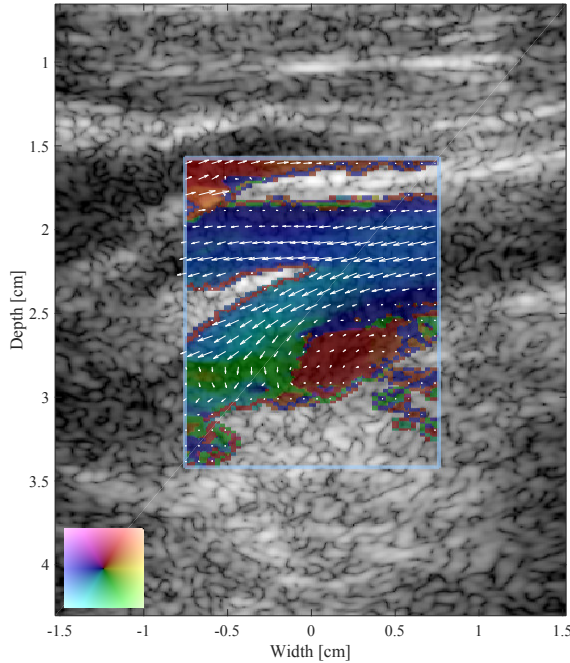


Figure 5.11: VFI of the carotid bulb for volunteer 5. A large vortex was formed and moved downstream in the ICA. From Paper VI.

during the time from initial fabrication to measurement, which may have affected the size of the vessels. An automatic procedure for alignment may improve the study, but it will require markers in an additional plane in order to avoid an ill-posed problem.

A limitation of the CFD simulation was that the vessel walls were assumed rigid. However, the vessel walls of the fabricated phantom moved during systole (axial velocities of ± 2 mm/s), which changed the flow pattern and may explain the differences in vortex development between measurement and CFD simulation. If vessel wall movement should be taken into account in the CFD simulation, fluid-structure interaction simulation models could be included (Swillens et al. 2010). This requires a much more complicated CFD model, which has yet to be developed. Another solution is to use additional freeze-thaw cycles during the phantom fabrication process to increase the stiffness of the material.

The CFD simulation should be considered an independent method to compare with VFI, and not the ground truth, since CFD is based on models and assumptions, which may not be entirely valid for the specific measurement. These include assumptions of the inlet and outlet boundary conditions. The temporal shape of the inlet profile for the simulation was obtained from the measurement, however, the spatial velocity profiles were assumed

parabolic and rotationally symmetric, which may not be the case for the measurement.

The study also used measurements of PSVs in the CCA of the ten volunteers and compared results for plane wave VFI, spectral Doppler and MRA. The methods and results are presented in detail in Paper VI, and in summary the results showed a mean difference of -0.17 m/s between plane wave VFI and MRA, and a mean difference of 0.07 m/s between plane wave VFI and spectral Doppler. The difference between plane wave VFI and MRA may be due to lower spatial and temporal resolution in MRA, where MRA data were averaged over 200 cardiac cycles, which effectively was a low-pass filtering of the data. In comparison to spectral Doppler, it is known that spectral Doppler has a positive bias due to spectral broadening, which was also reported in a study for plane wave vector Doppler (Tortoli et al. 2015).

The population size with ten volunteers in this study gave an indication of the precision of VFI estimates *in vivo*. Larger population studies with healthy volunteers and patients with cardiovascular diseases are needed to further establish the VFI technique and to reveal how vortices, turbulent flow and other complex flow patterns may provide new information to the clinician.

CHAPTER 6

Plane wave slow flow imaging in the human placenta

This chapter presents a separate study where plane wave imaging was applied clinically for estimating slow velocity flow in the small vasculature of the human placenta. The work presented was made in the final stage of the project and has not been fully finished yet. A description of the study, the proposed processing of data, and a few results from the study are presented in this chapter. The study was conducted during a research stay in Paris at Institut Langevin, ESPCI Paris, in collaboration with PhD student Marion Imbault, Post-doc Bruno-Felix Osmanski, MDs Edouard Lecarpentier and Vassilis Tsatsaris, and Prof. Mickael Tanter.

6.1 Background and purpose

The human placenta plays a crucial role during pregnancy. The organ provides oxygen and nutrients to the growing fetus and removes waste products from the fetus' blood. The placenta is attached to the wall of the uterus, while the umbilical cord of the fetus develops from it. An illustration of the placental blood circulation is shown in Fig. 6.1. Maternal arteries in the uterine wall branch into spiral arteries, which supply blood to the placenta. The large diameter of the arteries and relatively high pressure fills the intervillous space with maternal blood and bathes the fetal vessels in blood. The pulsatility of blood in the maternal arteries is dampened in the spiral arteries and provides the intervillous space with almost constant blood supply. The maternal blood in the intervillous space is a large pool of blood moving at very slow speeds, typically around 1 mm/s (Lecarpentier et al. 2016). The maternal blood exits through maternal veins.

On the fetal site, de-oxygenated fetal blood passes through the umbilical arteries to the placenta. The flow pulsates at a heart rate of two to three beats/sec. The umbilical arteries branch to form chorionic arteries, which in turn branch into smaller arteries. The branching creates fetal trees or villi, where the arterio-capillary-venous system brings fetal blood close to the maternal blood. Fetal blood has lost its pulsatility at this stage and returns in fetal veins, which are in close proximity to the arteries.

Placental dysfunction is a major cause of pregnancy complications. Pregnancy complications such as intrauterine growth restriction (IUGR) and preeclampsia are a result of decreased and impaired maternal blood flow to the placenta. It also affects the fetal blood

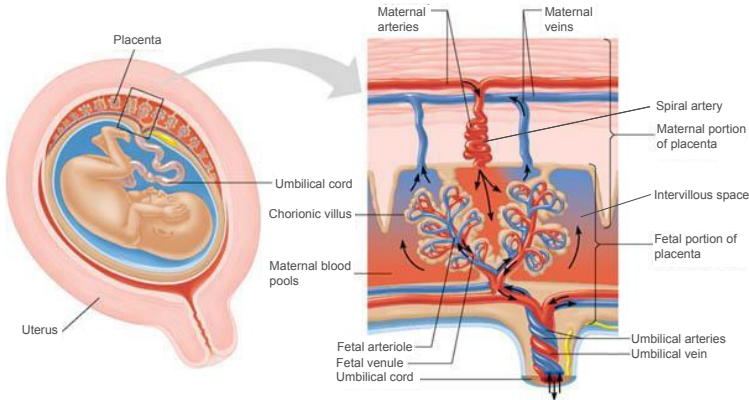


Figure 6.1: Illustration of the maternal and fetal blood flow circulation in the human placenta. Modified from (Marieb and Hoehn 2007).

flow, which shows an increased resistance to flow. Currently, fetal resistivity is measured on the umbilical cord or on main stem fetal arteries by using spectral Doppler at manually selected single locations (Babic et al. 2015). These measures have been correlated to pregnancy outcomes (Trudinger et al. 1985; Todros et al. 2011). Thus, single-location measurements on the umbilical cord are assumed to yield information about downstream fetal vessel resistivity. Quantification of the vascularization directly in the placenta may improve the prediction of IUGR and preeclampsia as it allows for a more direct evaluation of the vasculature (Yagel et al. 1999; Dar et al. 2010).

However, line-by-line ultrasound imaging is limited to imaging of only the largest vessels in the placenta due to its low sensitivity to slow velocity flow. There is furthermore no method to discriminate flow in the small fetal arteries from fetal veins and maternal flow, since continuous quantitative data are only obtained at a single location. This complicates the ability to measure the resistivity of the fetal arteries.

Fast plane wave imaging may be an interesting solution. Continuous data with hundreds of temporal samples can be obtained over a large field of view. Thereby, blood flow can be analysed with a high spatio-temporal resolution simultaneously at several locations and with enhanced sensitivity compared to line-by-line imaging (Mace et al. 2011). This study investigated (1) the feasibility of imaging the small vessels inside the placenta using plane wave imaging, and (2) an automatic approach for discriminating fetal arterial flow from maternal flow. This allows for mapping of the fetal arterial resistivity in several vessels within the placenta and in the entire imaging plane. Plane wave imaging has previously been used for enhancing the sensitivity to the small vessels in the placenta of pregnant rabbits, and a method for discriminating maternal and fetal blood flow was proposed (Osmanski et al. 2015). The uteroplacental circulation in rabbits

exhibits different anatomy and flow patterns from humans, and the same discrimination algorithm cannot be directly applied.

6.2 Data acquisition

Ten volunteers with normal pregnancy and one volunteer with IUGR pregnancy were enrolled in the study. The volunteers were selected among referred patients to the emergency pregnancy room at the Maternité Port-Royal Hospital in Paris, France. All volunteers were in their late second trimester or third trimester. Scans were performed by experienced obstetrician MD Edouard Lecarpentier.

An ultrasound scanner (Aixplorer v9, Supersonic Imagine, Aix en Provence, France) was equipped with a commercial linear array transducer (SL10-2; Supersonic Imagine) (center frequency 6.4 MHz, pitch 0.2 mm, 192 elements, bandwidth 80%, elevation focus 30 mm, 2-cycle excitation). Initially, the default line-by-line B-mode image and color-flow mapping on the scanner was used for orientation in the placenta and to find locations with fetal vessels. The MD selected 2-3 locations on the placenta where the probe was tried to be kept stationary while data for plane wave sequences were acquired. At each location, data for two plane wave sequences, (a) and (b), were acquired. The sequences are described below. Moreover, a plane wave data acquisition was performed with a view of the umbilical cord using a sequence (c). The volunteers were asked to hold their breath during each of the 1-2 s plane wave data acquisition.

The axial velocities in the largest fetal vessels can reach 6 cm/s, which imposed an effective f_{prf} of 1000 Hz to avoid aliasing. The maximum allowed f_{prf} according to the clinical protocol was 4000 Hz, which permitted using a four-angle plane wave sequence (-6° , -2° , 2° , 6°). Using all available storage space in the scanner, 1 s of element data were acquired with this setup for sequence (a). For sequence (b), the f_{prf} was lowered to 2000 Hz, which provided 2 s of acquired data. The longer data acquisition came in this case at the expense of a lower maximum detectable velocity of 3 cm/s, since the same four plane wave steering angles were used. For the scan of the umbilical cord (c), an unsteered plane wave at 0° was transmitted at $f_{prf} = 4000$ Hz and provided 1 s of data.

6.3 Data processing

6.3.1 Beamforming

Beamforming of RF element data was performed off-line using the BFT3 toolbox (Hansen, Hemmsen, and Jensen 2011) (spatial sampling interval $\lambda/5$, dynamic receive apodization with $F\# = 1$ and Tukey window of weight 0.5). An LRI was beamformed for each transmit event and an HRI was created from the four transmit events for the placenta sequences. The stack of HRI frames was denoted $I(x, z, t)$, where x is lateral position, z is depth, and t is time.

6.3.2 Echo-canceling

Tissue echo-canceling was performed using the singular value decomposition (SVD) filter proposed by Demené et al. (Demene, Deffieux, et al. 2015). The filter uses 2-D spatial and temporal coherence to separate blood from tissue signal, and the characteristics of the filter are similar to eigenvalue-based filters (Yu and Løvstakken 2010). The SVD decomposes a spatiotemporal matrix form of the ultrasound images $I(x, z, t)$ into separable time and space signals (singular vectors) weighted by singular values. Tissue signal is filtered by rejecting a number of singular values, which was 100 in this study. The filter also utilizes the large number of temporal samples provided by the continuous data. For this study, it was applied over 1000 temporal samples, which corresponded to 1 s.

6.3.3 Power Doppler

A Power Doppler image was obtained by integrating the energy of the echo-canceled image at each image point. The Power Doppler image represents the energy in the image after echo-canceling, and the intensity at each image point is proportional to the blood volume. No information on velocity magnitude and direction is obtained from the Power Doppler image, however, the advantage is the high sensitivity to slow velocity flow in small vessels. This is due to the use of the entire energy spectrum instead of only the mean frequency in the spectrum.

6.3.4 Velocity estimation

Velocity estimation was performed in the entire image throughout the acquisition. The phase-shift estimator was employed for estimating the axial velocity component $v_z(x, z, t)$. Each velocity estimate was calculated from 50 HRIs, and averaging was performed over the pulse length. The result was displayed on a color flow map.

6.3.5 Resistivity

The resistivity index (RI) was calculated at each image point as

$$RI(x, y) = \frac{\max_t(v_z(x, z, t)) - \min_t(v_z(x, z, t))}{\max_t(v_z(x, z, t))}. \quad (6.1)$$

The RI map was merged with the Power Doppler image using the color system hsv (hue, saturation, value) to display the RI values between 0 and 1 with a brightness according to the Power Doppler image (Demene, Pernot, et al. 2014).

6.3.6 Pulsatility

The pulsation, or heart rate, of the blood flow was also calculated at each image point. The heart rate was estimated directly from the velocity estimates by applying the Fourier transform to the time-varying velocity signal $v_z(x, z, t)$ at each image point. The frequency containing the maximum value in the spectrum was converted to beats/min and

used as an estimate of the heart rate. A heart rate map was constructed from estimates in the entire image.

6.3.7 Discrimination algorithm

The proposed algorithm for discriminating fetal arterial blood flow from maternal and fetal venous blood flow used information on the direction of axial velocities, RI, and heart rate. The following criteria were applied:

- Axial velocity direction towards the transducer,
- RI between 0.4 and 0.95,
- heart rate between 100 and 170 beats/min.

Image points, where the criteria were met, were classified as points belonging to fetal arteries.

The discrimination algorithm was designed based on the data set from one of the volunteers (Volunteer I). The obstetrician interpreted the acquired color flow map in terms of maternal and fetal blood flow. The velocity direction and the thresholds for RI were then determined empirically from consulting the expected venous and arterial flow in the data set. RIs above 0.95 were considered estimates from noise. The thresholds for the heart rate were based on the expected range of the fetal heart rate. The discrimination algorithm was applied for the other volunteers without modifications.

6.4 Results

6.4.1 Volunteers with normal pregnancy

Fig. 6.2 shows a screen dump from the Supersonic scanner, where the placenta of Volunteer I with normal pregnancy was scanned. The scanner used line-by-line imaging for the B-mode and color flow map, and the color map was in this example inverted (red is here towards the transducer and blue away from it). The volunteer had a thin fat layer (~ 1 cm). At depths from 1 to 1.5 cm, maternal (uterine) vessels ran parallel to the transducer surface, but the blood flow was poorly estimated, which might be due to the almost 90° beam-to-flow angle. The placenta was placed below a depth of 1.5 cm. The large black gap in the placenta, partly filled with blue color, was an opening of maternal arteries with blood supply into the intervillous space of the placenta. It is entitled a lacuna. Parts of fetal vessel were imaged below the lacuna, where a few vessels with blood flow in opposite directions ran parallel to each other.

Fig. 6.3 shows a color flow map processed using data from the plane wave sequence. Data were acquired at approximately the same location as in Fig. 6.2. A high sensitivity to the slow velocity blood flow was obtained with the plane wave data, where it was possible to estimate flow in the lacuna, flow in fetal vessels with a diameter of 1-2 mm (in

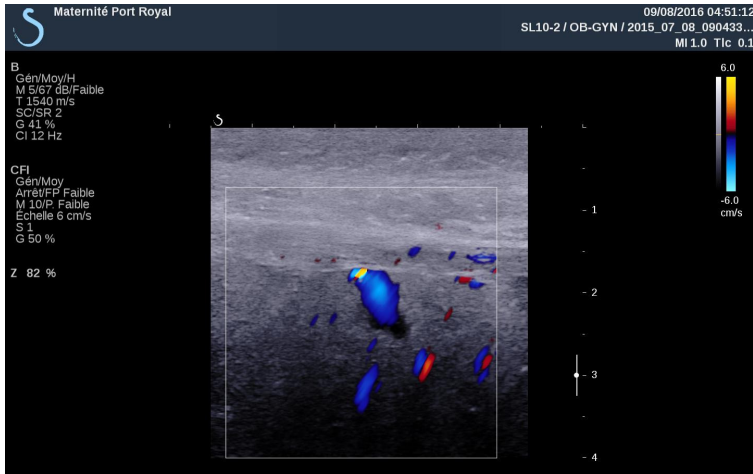


Figure 6.2: Screen dump from the Supersonic scanner. The placenta of volunteer I with normal pregnancy was scanned.

the bottom part of the image), and in small vessels around the lacuna. A big advantage with the plane wave data was that the time-varying velocity profile could be analysed at any image point. The Doppler spectrogram or directly the estimated velocities from the color flow map could be displayed. This is shown for four image points in Fig. 6.3. It revealed that slow non-pulsatile maternal flow exited the lacuna at a velocity of 1 cm/s, while pulsatile flow with a heart rate of 65 beats/min was estimated in a uterine (maternal) artery. Two closely situated vessels in the placenta contained flow in opposite directions: one with non-pulsatile and the other with pulsatile flow at a heart rate of 129 beats/min. It indicated the nature of the vessels: a fetal vein and fetal artery, respectively.

The continuously available velocity estimates at each image point were used for the discrimination algorithm, which was designed based on this volunteer. Maps of the axial velocity direction, heart rate, and RI are shown in Fig. 6.4. The transverse vessels at depths of 10-15 mm, lacuna, and vessels at $(x, z) = (-10, 25)$ mm and $(-3, 40)$ mm had heart rates about 65 beats/min, which indicated maternal blood flow. The remaining vessels had heart rates about 130 beats/min, which indicated fetal blood vessels. There were, however, also image points with heart rates above 200 beats/min, which might be affected by noise. The RI map in the image to the right in Fig. 6.4 illustrates that low RIs below 0.3 were obtained in the placenta for blood flow moving away from the transducer, when comparing to the left image (red velocities). RI above 0.4 were obtained in the remaining vessels. Image points with RI close to 1 contained random (noisy) signals.

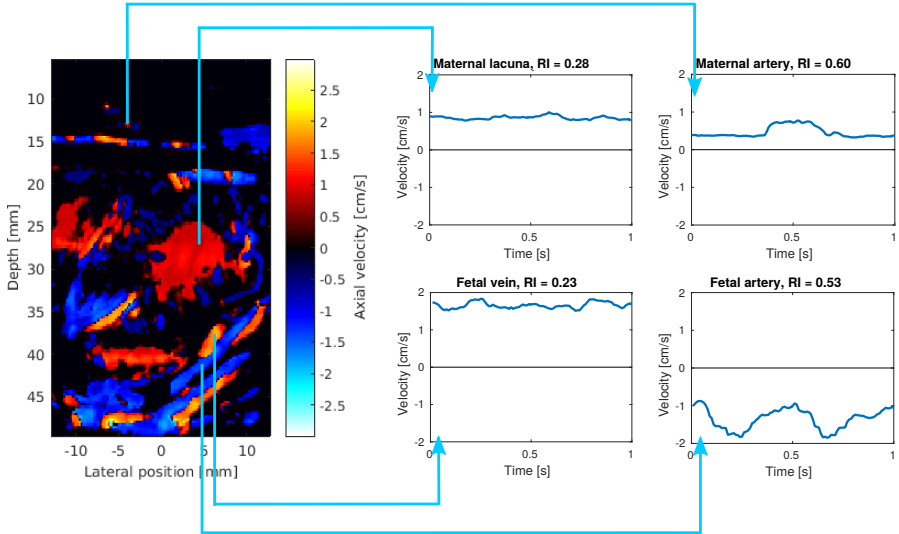


Figure 6.3: Color flow map of axial velocities measured using plane wave imaging for the placenta of volunteers I with normal pregnancy. Velocity profiles as a function of time can be extracted at any spatial position in the image, which are shown at four positions in the figures to the right: in a maternal lacuna, maternal artery, fetal vein, and fetal artery.

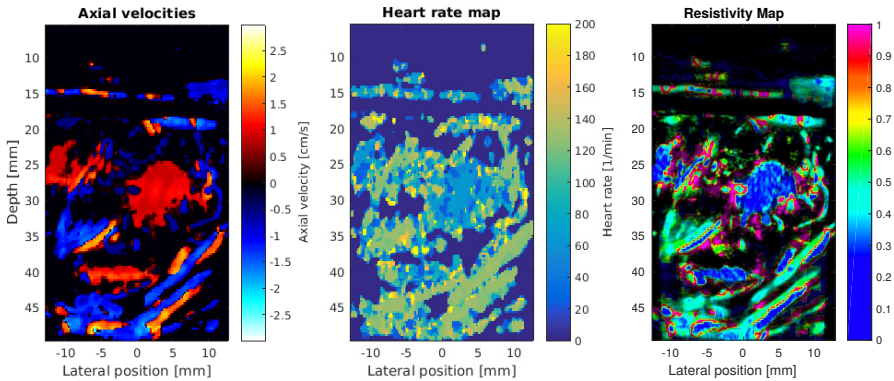


Figure 6.4: Color flow map of axial velocities (left), heart rate map (middle), and RI map (right) for volunteer I. The three maps were used in the discrimination algorithm.

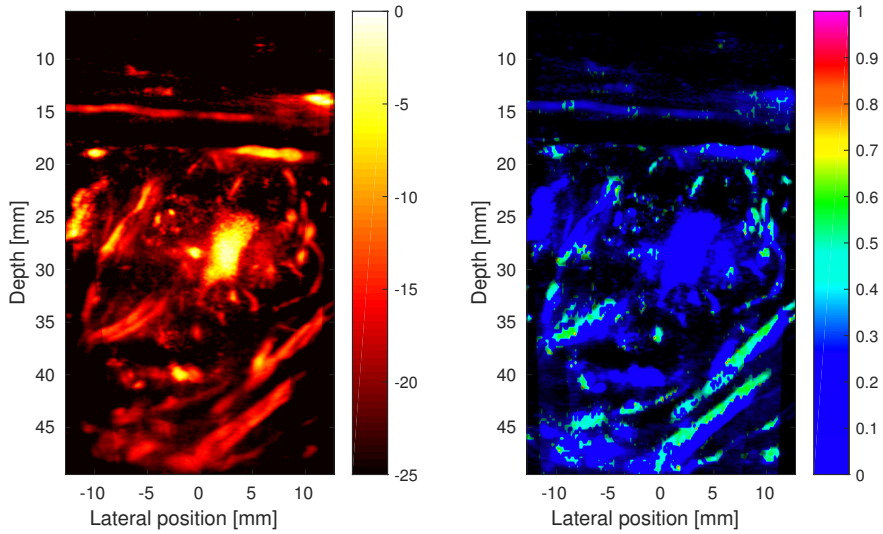


Figure 6.5: Power Doppler image (left) and the RI map of the fetal arteries after applying the discrimination algorithm (right) for volunteer I.

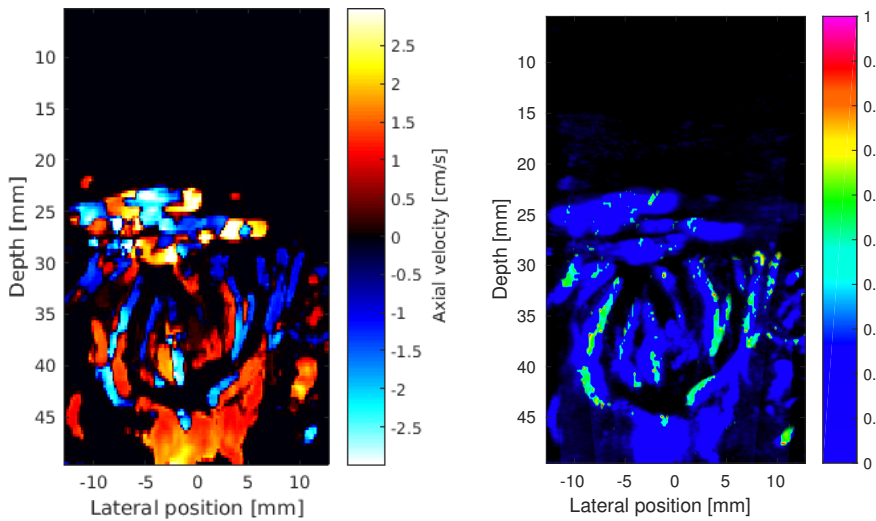


Figure 6.6: Color flow map of axial velocities (left) and RI map of the fetal arteries after applying the discrimination algorithm (right) for volunteer II with normal pregnancy.

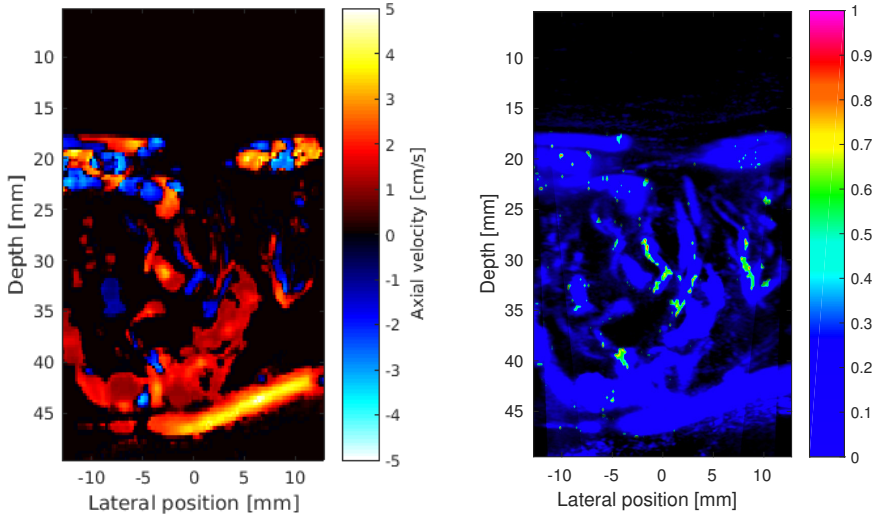


Figure 6.7: Color flow map of axial velocities (left) and RI map of the fetal arteries after applying the discrimination algorithm (right) for volunteer III with normal pregnancy.

Fig. 6.5 shows the Power Doppler image (left image) and the RI map after applying the proposed discrimination algorithm (right image). RI is shown for the fetal arteries with light blue/green colors, while the RI for the remaining vessels were set to zero and displayed with dark blue colors. Two large fetal arteries are displayed in the lower right part of the image, parts of vessels to the left of the lacuna, and small vessels above the lacuna. There are, however, image points in the bottom left part of the image, where the RI map looks scattered and noisy with no clear definition of vessels, which may be due to wrong discrimination. For the maternal vessels at 15 mm, some image points were also wrongly classified as belonging to fetal arteries. When calculating the mean ± 1 SD of the RI for the fetal arteries, the result was 0.47 ± 0.04 . For comparison, the RI of the umbilical artery was 0.75 for a scan of only the umbilical cord.

Color flow maps and RI map of discriminated fetal arteries are shown for two other volunteers in Fig. 6.6 and 6.7. Fig. 6.6 for volunteer II shows a fetal vessel tree below a depth of 30 mm, where small vessels with flow in opposite directions were aligned next to each other. Vessels at a depth of 25 mm were transverse to the ultrasound beam and were most likely maternal vessels. A few image points were also wrongly classified in the maternal vessels. An example of a scan, where it was more difficult to image the placental vasculature, is shown for volunteer III in Fig. 6.7. Quite few fetal vessels at depths from 25 to 40 mm were detected. Possible reasons for this are given in Section 6.5. In addition to the fetal vessels, large maternal vessels were detected at 20 mm depth and the umbilical vein at 45 mm depth.

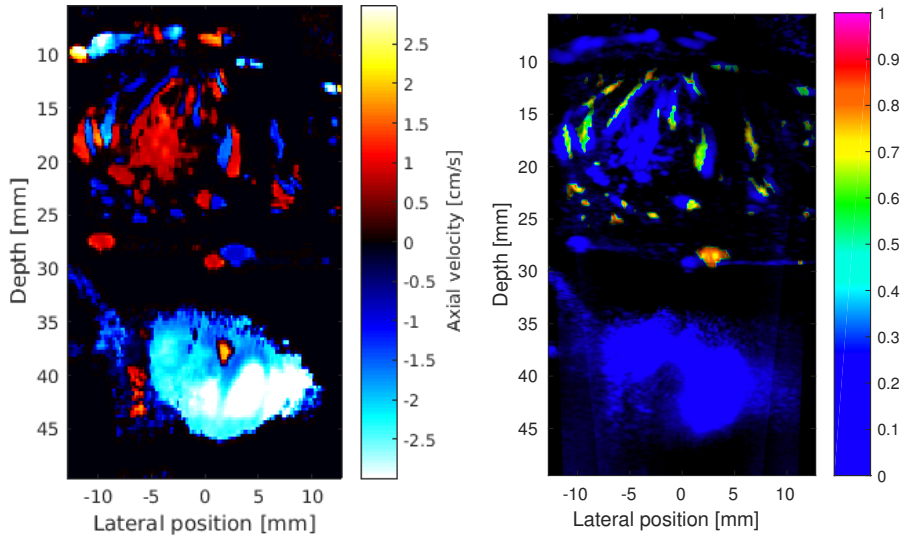


Figure 6.8: Color flow map of axial velocities (left) and RI map of the fetal arteries after applying the discrimination algorithm (right) for volunteer IV with IUGR pathology.

6.4.2 IUGR patient

One of the volunteers in the study had IUGR pathology. A scan of the placenta is shown in Fig. 6.8 with the color flow map and RI of discriminated fetal arteries. Fetal vessels in the placenta are shown at depths from 10-30 mm, while a part of the umbilical cord is shown below. The fetal arteries discriminated by the algorithm had either green-yellowish colors or orange colors. This corresponded to RI-values between 0.6 and 0.8, which was higher than for the scanned volunteers with normal pregnancy, which had RI-values between 0.4 and 0.6. Especially, a vessel at a depth of 30 mm and two small vessels at 10-15 mm depth had a RI of 0.8, while some vessels just below had a RI of 0.6. Thus, an advantage of the method used in this study was that resistivity was estimated in several vessels simultaneously, which revealed that some vessels had a larger resistivity than other vessels. The mean RI of all the discriminated fetal arteries was 0.68 ± 0.09 . RI on the umbilical artery in the image was in this case manually excluded, since the discrimination algorithm categorized it as a fetal artery.

A summary of the mean RI in the fetal arteries discriminated by the algorithm is shown in Table 6.1 for volunteer I-IV. The RI in the umbilical cord is shown for comparison, and it can be noted that the RI in fetal arteries was lower than in the umbilical cord for the volunteers. This was in agreement with other studies, which showed that the RI decreases along the fetal arterial tree and is lower in the fetal arteries compared to the umbilical cord (Yagel et al. 1999; Gordon et al. 2016).

Table 6.1: Mean \pm 1 SD of the RI for volunteer I-IV on the discriminated fetal arteries and the umbilical cord.

Volunteer	Pregnancy	Fetal arteries	Umbilical cord
I	Normal	0.47 ± 0.04	0.75
II	Normal	0.51 ± 0.06	0.68
III	Normal	0.55 ± 0.05	0.77
IV	IUGR	0.68 ± 0.09	0.87

6.5 Discussion and summary

The chapter showed representative examples of using plane wave imaging for slow velocity flow estimation inside the human placenta, and utilizing the continuously available data to discriminate fetal arterial flow from fetal venous flow and maternal flow. Thereby, maps of fetal artery resistivity were created. The fetal arterial resistivity was higher for a volunteer with IUGR pathology compared to volunteers with normal pregnancies (see Table 6.1). However, the acquired data for scans of the remaining volunteers should be fully processed and analysed to substantiate the observation. The study could also be improved by scanning more volunteers with IUGR pathology, which would make a statistical analysis possible. Furthermore, analysing data from the scans made at the other scan locations on the placenta of each volunteer would allow calculating the precision of the RI estimated according to the discrimination algorithm.

The calculation of RI was very sensitive to random fluctuations of velocities. A solution could be to acquire data over a number of heart cycles and then average the velocity estimates after alignment to the heart cycle. This would reduce the random fluctuations and improve the robustness of RI estimates and the discrimination algorithm. It was, however, not possible with the used scanner due to hardware limitations.

A thick fat layer limited the applicability of the plane wave imaging method. A fat layer of more than about 3 cm made it very difficult to image blood vessels inside the placenta. The linear probe had a small footprint and was challenging to use for abdominal imaging, which was a compromise between the pulse center frequency, field-of-view, and imaging depth. Few fetal vessels were imaged in the scan of volunteer III (see Fig. 6.7), and the low quality with very few detected vessels in the placenta for some of the volunteers might be due to either the fat layer, difficulties in getting a good view of the placental vasculature, or tissue movement. The tissue motion was tried to be minimized by asking the volunteer to hold her breath, but movement by the fetus could not be avoided.

Another limitation of the study was that there was no way to directly validate the discrimination algorithm *in vivo*. A simple phantom with vessels mimicking flow in a fetal artery and vein might be valuable for testing the algorithm and substantiating the applied thresholds for RI. Especially the RI threshold of 0.4 for differentiating pulsatile flow from

non-pulsatile flow was a critical choice and should be better justified. An *ex vivo* placental perfusion model could also be interesting for validation (Gordon et al. 2016), but it is a cumbersome study, and organ preservation and blood perfusion are severe challenges to be solved.

The discrimination algorithm used a number of assumptions about the flow. The assumption of pulsating fetal arterial flow moving towards the transducer was reasonable for nine of the volunteers, which all had an anterior placenta position (attached to the front of uterine wall). For the two volunteers with a posterior placenta (to the back of uterine wall), pulsating fetal flow moved in both directions. This has to be taken into account in the algorithm.

The study of the placenta in pregnant rabbits (Osmanski et al. 2015) showed increased sensitivity to slow velocity flow, when using fast plane wave imaging compared to line-by-line imaging. Although the line-by-line image in Fig. 6.2 cannot be directly compared to the plane wave image in Fig. 6.3, the plane wave image indicated a high sensitivity to flow in small vessels, which had diameters down to 1 mm. The high sensitivity for plane wave imaging was related to the focusing and the echo-canceling, which used spatiotemporal information from a large number of HRIs (Demene, Deffieux, et al. 2015).

The sensitivity may be further improved by emitting more than the four plane waves, which will increase the contrast and the amount of blood energy available for velocity estimation. A longer sequence requires, however, that compromises on the maximum detectable velocity are made. A longer sequence would be an advantage for estimating the very slow maternal blood flow pool inside the placenta, which may provide valuable information about the placental circulation and dysfunction.

It would also be interesting to estimate 2-D vector flow in the vessels in the placenta, which would reveal the full velocity magnitude independent from the beam-to-flow angle. However, vector flow estimation in small vessels is challenging, and the energy left for blood flow estimation should be maximized using appropriate tissue echo-canceling. The use of other echo-canceling filters or further improvements for the SVD filter could be performed regarding the number of temporal samples and rejected singular values.

CHAPTER 7

Vector velocity volume flow estimation

In clinics, volume flow is commonly used as a quantitative flow measure. This chapter investigates a method for vector velocity volume flow estimation and its sources of error. The method was applied clinically on patients undergoing dialysis. Line-by-line imaging was used for data acquisition, but plane waves or other parallel imaging techniques could also be applied. The work was performed as a master project, and a journal paper expanding on the topic was written during the PhD project. An overview of the findings is presented in this chapter, and for a further in-depth description of the study the reader is referred to Paper VII in the appendix.

7.1 Introduction

The quantification of volume flow through a vessel is often used in the clinic to evaluate the pathological state of the vascular system. In the specific case of an arteriovenous fistula (AVF) in patients undergoing dialysis, the function of the vessel is monitored by measuring volume flow (Wiese and Nonnast-Daniel 2004; Whittier 2009). The referential method for measuring volume flow in AVFs is the ultrasound dilution technique (UDT) (Krivitski 1995), which is an indirect and invasive method performed during dialysis. Ultrasound provides a direct, real-time, and non-invasive method for quantifying volume flow (Schwarz et al. 2003; Hansen et al. 2014). However, AVFs are irregular and superficial vessels, which are difficult to scan, and this may introduce different sources of error.

The most widely available methods for ultrasound volume flow estimation use either a single-point Doppler estimation of the peak velocity or measurement of velocities at several points along the vessel diameter. While the first method assumes a certain shape of the velocity profile, the latter method directly measures the actual in-plane velocity profile (Ricci et al. 2013). Several authors have documented the errors associated with the methods (Gill 1985; Burns 1992). A major limitation is the measurement of 1-D velocities, because the beam-to-flow angle has to be determined manually, and it has shown to be the most dominant source of error in volume flow estimation (Picot and Embree 1994).

Volume flow estimation based on 2-D VFI is an attractive solution, since a spatial

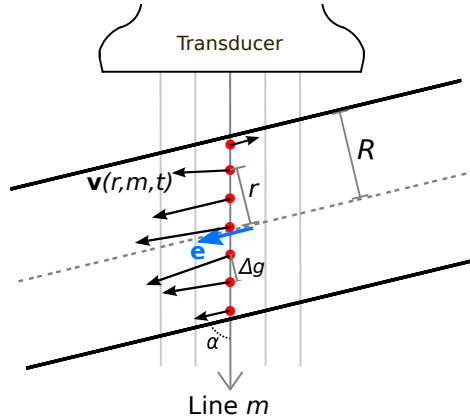


Figure 7.1: Volume flow estimation along line m . The velocity vector $\mathbf{v}(r, m, t)$ is sampled at a radial and perpendicular distance r from the center axis. The beam-to-flow angle is α , and \mathbf{e} is a unit vector normal to the cross-sectional vessel area. From Paper VII.

and temporal variation in the beam-to-flow angle can be handled automatically. As for the Doppler-based methods, VFI estimates are only obtained in one scan plane along the vessel, and assumptions of the flow and vessel have to be made to calculate the volume flow. The purpose of this study was to investigate the sources of error for a volume flow estimator based on VFI. The errors were investigated in a theoretical model and *in vivo* for AVFs in hemodialysis patients.

7.2 Volume flow estimation

For this study, VFI estimates were obtained in a scan plane along the vessel using line-by-line imaging and the TO approach. However, other VFI techniques and/or parallel imaging could also have been used for the volume flow estimation. Three assumptions were made: It was assumed that flow was axisymmetric, the cross-sectional area of the vessel was circular, and that velocities were sampled along a diameter of the vessel. The volume flow Q of a fluid crossing a circular surface S is:

$$Q(t) = \int_S \mathbf{v}(\mathbf{x}, t) \cdot \mathbf{e} \, dS, \quad (7.1)$$

where \mathbf{v} is the velocity vector at position \mathbf{x} with respect to an arbitrary origin, t is time, \mathbf{e} is a unit vector normal to the surface S , and \cdot is the dot product operator.

Each VFI frame was constructed using line-by-line imaging of M parallel lines. The 2-D vector velocity estimate $\mathbf{v}(r, m, t)$ represents the velocity magnitude and direction for a point along line m and at a perpendicular distance r from the center axis of the vessel,

see Fig. 7.1. The volume flow at line number m is then estimated as

$$Q(m, t) = \pi \int_{-R}^R \mathbf{v}(r, m, t) \cdot \mathbf{e} |r| dr, \quad (7.2)$$

which corresponds to a rotation of the vector velocity profile around the vessel axis. R is the radius of the vessel, and the projection of \mathbf{v} onto \mathbf{e} ensures that flow is normal to the cross-sectional area. The volume flow estimator handles laminar flow along the vessel as well as cases with varying flow angles. For a finite number, N , of velocity estimates inside the vessel, a summation of discrete values is used

$$Q(m, t) = \pi \Delta g^2 \sum_{n=-N/2}^{N/2} \mathbf{v}(n, m, t) \cdot \mathbf{e} |n|, \quad (7.3)$$

where Δg is the radial distance between velocity estimation points, and $r = n\Delta g$. The equation can be considered a sum of volume flows through semi-annular rings, which each have an area of $\pi \Delta g^2 |n|$ and an associated velocity magnitude $\mathbf{v}(n, m, t) \cdot \mathbf{e}$. The mean volume flow for a scan sequence is found by averaging the estimates over a number of scan lines and over a number of frames N_f . For pulsatile flow, the averaging should be over frames for a whole number of cardiac cycles.

7.3 Sources of error

Five sources of error, which affected the accuracy of volume flow estimation, were investigated. An illustration of the error sources is shown in Fig. 7.2 and described in the following:

- A. The spatial resolution of the measured velocity profile depends on the distance, Δg , between velocity estimation points. Δg is primarily determined by the emitted pulse length. The number of velocity samples inside the vessel is related to the size of semi-annular rings, which impacts the accuracy of the volume flow estimates.
- B. The radius of the vessel used for volume flow estimation, r_Q , which is often estimated by measuring directly on the B-mode image or by using a blood-tissue discriminator.
- C. The ultrasound beam may intersect the vessel at an off-axis distance d_{off} from the center line, since it is challenging for the examiner to align the scan plane with the vessel's center line. This error source has previously been investigated (Picot and Embree 1994) and was included here for completeness.
- D. The cross-sectional blood vessel area is often elliptical rather than circular. The volume flow is underestimated by a factor proportional to the ratio of the elliptical

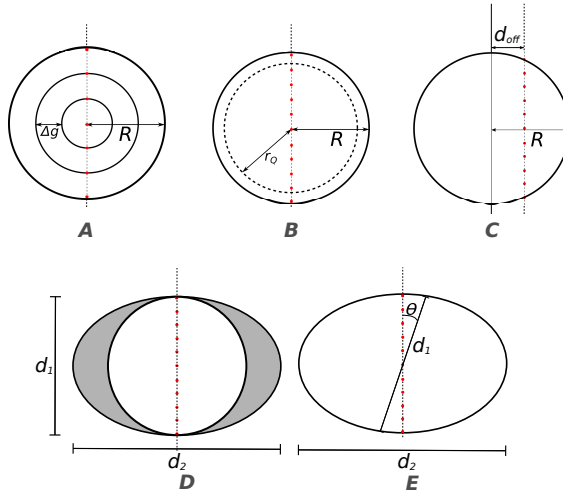


Figure 7.2: Illustration of error sources affecting volume flow estimation: (A) the distance between velocity estimates Δg , (B) the vessel radius, r_Q , used for volume flow estimation, (C) beam off-axis, (D) elliptic versus circular cross-section, and (E) non-perpendicular diameters. From Paper VII.

diameters, d_2/d_1 , when the vessel area is assumed circular (Picot and Embree 1994).

- E. The diameters d_1 and d_2 measured along the major and minor axes of the ellipse should be perpendicular to each other. An error in locating the perpendicular diameters, e.g. d_1 is measured at an angle θ from the minor axis, results in an incorrect estimate of the vessel area.

7.4 Theoretical analysis

7.4.1 Methods

The effects of error sources in volume flow estimation were investigated theoretically using a numerical implementation of the Womersley-Evans model for pulsatile flow (Womersley 1955; Evans 1982). The Womersley-Evans model decomposed the flow pattern of pulsatile flow into sinusoidal components, which were added to attain velocity profiles in time and space. The velocity profiles were then used in the volume flow estimator for investigating error sources A, B, C, and E. A number of parameters was varied in the analysis, including Δg , vessel radius for volume flow estimation r_Q , off-axis distance d_{off} , and angle θ of a non-perpendicular diameter d_1 .

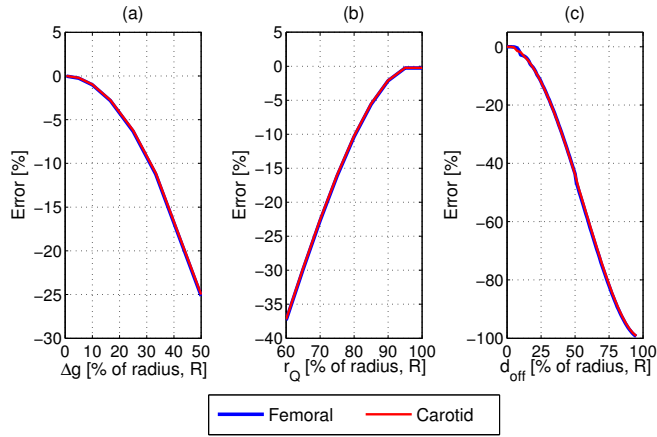


Figure 7.3: Volume flow errors calculated as deviation of average volume flow for a femoral (blue) and carotid (red) waveform. In (a) as a function of distance between velocity estimation points, Δg ; in (b) for vessel radius, r_Q ; and in (c) for a beam being off the vessel axis by the distance, d_{off} . All distances are expressed as a percentage of the radius, R . From Paper VII.

A carotid and a femoral waveform were created for the study. Mean temporal velocity of the flow was set to 0.15 m/s, the heart rate was 62 min^{-1} , and Womersley's number was 1.05. The vessel radius was normalized, and Δg was fixed at 0.05. Volume flow was calculated from (7.3) for a number of time steps using the generated velocity magnitudes and Δg . The true volume flow was calculated from the spatial average velocity and multiplying with the cross-sectional vessel area.

7.4.2 Results

The error in volume flow estimation as a function of the distance between velocity estimation points, Δg , is shown in Fig. 7.3(a) for the carotid (red) and femoral (blue) waveform. A decreased spatial resolution of velocity estimates increased the area of each semi-annular ring and, thus, the weight applied to each velocity estimate. The same trend with an increase in volume flow error for a larger Δg was obtained for the two waveforms. Temporally averaged estimates were used, and the mean volume flow during a cardiac cycle was important, rather than the temporal variations during a cycle for the femoral and carotid waveforms.

Fig. 7.3(b) shows the volume flow error, when reducing the radius used for volume flow estimation, $r_Q < R$. This corresponded to excluding velocity estimates close to the vessel boundary, where the weight function $|n|$ had large values. At least 85% of the vessel radius should be identified to achieve less than 5% volume flow error.

The impact of displacing the transducer off the vessel axis by a distance d_{off} relative

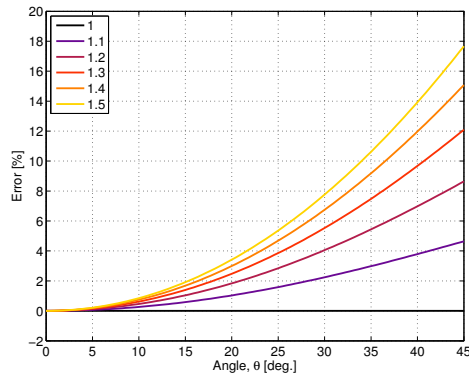


Figure 7.4: Volume flow errors for non-perpendicular diameters in elliptic vessels. The diameter d_1 was measured at angles θ from 0° to 45° from the minor axis. Each graph is for a specific elliptic geometry, d_2/d_1 . From Paper VII.

to the vessel center is shown in Fig. 7.3(c). The graphs in the figure have the characteristic shapes of a sigmoid curve. An off-axis distance of 30%, which corresponded to 1-2 mm in a typical AVF, resulted in 17% volume flow error.

Fig. 7.4 shows the effects of not measuring d_1 and d_2 perpendicularly. The angle θ was measured between d_1 and the minor axis, and the velocity profile was measured along the minor axis of the ellipse. Each of the curves in Fig. 7.4 corresponded to a specific elliptic geometry - the ellipticity d_2/d_1 . The result showed that volume flow in general was overestimated with more than 5% for an ellipticity larger than 1.2 and $\theta > 20^\circ$.

7.5 Clinical scans

7.5.1 Methods

The effects of error sources C and D on volume flow were also investigated in twenty patients with AVFs. The scans were performed as part of a related study (Hansen et al. 2014) by an experienced radiologist using an UltraView 800 scanner (BK Ultrasound, Herlev, Denmark) and a 9 MHz linear array transducer. Each AVF was B-mode scanned with a cross-sectional view for orientation purposes, and the radiologist measured two perpendicular diameters, d_1 and d_2 , in each vessel. The AVF was then scanned longitudinally to record TO VFI estimates in a plane along the vessel. Data were recorded for 15 s with a frame rate of 15 Hz. The average volume flow during a scan sequence was calculated off-line in the central part of the scan region. UDT measurements of volume flow were performed for comparison using a Transonic HD03 Flow-QC Hemodialysis Monitor (Transonic Systems Inc., Ithaca, NY, USA).

7.5.2 Results

The measurement of vessel ellipticity d_2/d_1 for all twenty patients gave an indication of how elliptical the cross-sectional AVFs were. The mean \pm one standard deviation (SD) of d_2/d_1 was 1.086 ± 0.105 , i.e. d_2 on average was 8.6% larger than d_1 . The smallest d_2/d_1 was 0.965, while the largest was 1.426.

Initially, mean volume flow was calculated by assuming a circular vessel area with $R = d_1/2$. Then, it was calculated by assuming an elliptical vessel area by including d_2 . The volume flow error with respect to UDT reduced for all patients, except two, when using elliptical rather than circular vessel areas. Paper VII in the appendix shows the results for each of the patients. Averaging over all twenty patients, the volume flow error relative to UDT reduced from $31.2 \pm 14.1\%$ to $27.4 \pm 16.4\%$.

Beam-vessel intersection was also investigated by using VFI data and the B-mode images. The actual vessel diameter, $d_{scanner}$, was determined as the average width of the measured VFI velocity profiles and was compared to the diameter d_1 on a B-mode image for each patient. For half of the patients, $d_{scanner}$ was smaller than d_1 , which indicated that the transducer was displaced. An off-axis distance relative to d_2 was calculated based on the elliptical dimensions of the fistula. The mean \pm one SD of the off-axis distances for the patients was 0.15 ± 0.08 cm. This corresponded to $28.5 \pm 11.3\%$ relative to the semi-major axis $d_2/2$. Thus, even though the scans were performed carefully by an experienced radiologist, it was difficult to scan with the beam in the center of a vessel.

The volume flow errors corresponding to off-axis distances were quantified theoretically in Fig. 7.3(c). Based on the off-axis distances for each patient and a corresponding theoretical correction factor, the volume flow estimates were corrected. This is further explained in Paper VII in the appendix. The volume flow error relative to UDT and averaged over all patients reduced to $24.3 \pm 16.2\%$, when compensating for the beam being off-axis. An important limitation of the off-axis correction was the measurement of $d_{scanner}$, which was affected by the echo-canceling filter, side lobes, and a variation of the vessel diameter as a function of time.

The volume flow estimator used angle-independent vector velocities, which were an advantage compared to using 1-D velocities, because it eliminated the error source related to compensating for the beam-to-flow angle. A volume flow estimator based on plane wave imaging may further improve the volume flow estimation, because the high frame rate and continuous data provide vector velocities with higher precision and accuracy than line-by-line imaging. The sources of error, which were investigated in this study, also apply for a volume flow estimator based on plane wave imaging and should be taken into consideration.

CHAPTER 8

Project Conclusion and Perspectives

The thesis investigated and further developed methods for plane wave B-mode imaging and flow estimation with the objective of overcoming issues related to low frame rates and 1-D velocity estimation, which are major limitations in conventional ultrasound systems. The work started with a study of high-quality plane wave imaging at a high frame rate, went on to fast 2-D vector flow estimation of laminar and complex flow in large vessels, and finally to clinical applications of estimating slow velocity flow and volume flow.

In Chapter 3, the compromise between image quality and frame rate was addressed. The importance of using a $\lambda/2$ -pitch transducer to avoid grating lobe artifacts from a λ -pitch transducer was demonstrated by showing the direct impact on image quality and frame rate. It was shown that the best image quality for a specific $\lambda/2$ -pitch transducer was attained close to the transducer (to a depth of 66λ), where large steering angles of 20° were advantageous in combination with only 21 emissions. For a λ -pitch transducer, 61 emissions were needed to (partly) suppress grating lobe artifacts. For deeper regions (below 66λ), 21 emissions were optimal for both transducers. The chapter showed that good control over the transmit field resulted in images of high quality and high frame rates, but further investigations are needed to reveal why the image quality for measurements was worse than for simulations. It indicates that there still are factors which impact the image quality in plane wave imaging. This understanding is important not only for B-mode imaging, but also for flow estimation and design of emissions sequences.

A plane wave 2-D vector flow method based on transverse oscillation and directional beamforming was developed and investigated. It was shown in simulations and measurements in Chapter 4 that the method estimated angles with a bias and standard deviation less than 2° , and velocity magnitude with a bias and standard deviation less than 4 % and 2 %, respectively. The accuracy and precision of the vector flow method was also investigated under laminar and complex flow conditions in the carotid artery in ten healthy volunteers. Chapter 5 presented the results, where the mean standard deviation in the common carotid artery was 4.4 % for velocity magnitude estimates aligned to the heart cycle. The largest standard deviations were obtained in the external branch and for vortices (16 % for velocity magnitude). Complex flow patterns measured in an anthropomorphic flow phantom showed good agreement with a CFD simulated velocity field.

The comparison between measured vector flow and CFD simulations should be performed on additional anthropomorphic phantoms with different degrees of stenosis to further establish the vector flow method's validity for complex flow quantification. A full understanding of the complex flow dynamics will, however, only be achieved if the

full 3-D velocity information is available at a high frame rate. This may be feasible by expanding the proposed vector flow method to 3-D by using a matrix transducer array. Furthermore, the 2-D vector flow method should be used in larger studies by including patients with cardiovascular diseases to investigate which flow patterns and features may be related to the diseases. This may give the clinicians a new tool for assessing the health of blood vessels. The larger patient studies will require an implementation of the 2-D vector flow method on a clinical ultrasound scanner, which may have to use the system's graphical processing unit to handle the computational burden of the method.

While the vector flow method was developed for high velocity flow in large vessels, the focus of Chapter 6 was shifted towards applying plane wave imaging for slow flow velocity estimation in the human placenta. It was shown that plane wave imaging could image the small vasculature with high sensitivity. Velocity estimation was performed everywhere in the image throughout the data acquisition, which made it possible to map the vessel resistivity in several fetal arteries. Potentially, this may provide new insight about placental dysfunction at the fetal arterial level at an early stage. Finally, Chapter 7 used vector flow imaging for estimating volume flow in arteriovenous fistulas of dialysis patients. The assumptions of circular rather than elliptical vessels and the ultrasound beam being off-axis were important sources of error, and it was shown that the volume flow error relative to the referential method reduced, when compensating for the errors. While volume flow estimation is a commonly used quantitative flow measure, other flow-derived measures such as wall shear stress, pressure gradient estimation, and stenosis degree may also be used for assessment of cardiovascular diseases. The measures can benefit from using the accurate 2-D angle-independent vector velocities estimated from fast plane wave imaging.

Bibliography

References from Chapter 1

- Demene, C., T. Deffieux, M. Pernot, B.-F. Osmanski, V. Biran, J.-L. Gennisson, L.-A. Sieu, A. Bergel, S. Franqui, J.-M. Correas, I. Cohen, O. Baud, and M. Tanter (2015). “Spatiotemporal clutter filtering of ultrafast ultrasound data highly increases Doppler and fUltrasound sensitivity”. In: *IEEE Trans. Med. Imag.* 34.11, pp. 2271–2285. DOI: 10.1109/TMI.2015.2428634 (cit. on p. 2).
- Hansen, K. L., J. Udesen, F. Gran, J. A. Jensen, and M. B. Nielsen (2009). “In-vivo examples of flow patterns with the fast vector velocity ultrasound method”. In: *Ultraschall in Med.* 30, pp. 471–476 (cit. on p. 3).
- Jensen, J. A., S. I. Nikolov, A. Yu, and D. Garcia (2016). “Ultrasound Vector Flow Imaging II: Parallel Systems”. In: *IEEE Trans. Ultrason., Ferroelec., Freq. Contr.* 63.11, pp. 1722–1732. DOI: 10.1109/TUFFC.2016.2598180 (cit. on p. 3).
- Jensen, J. A., S. Nikolov, K. L. Gammelmark, and M. H. Pedersen (2006). “Synthetic Aperture Ultrasound Imaging”. In: *Ultrasonics* 44, e5–e15 (cit. on p. 2).
- Kruskal, J. B., P. A. Newman, L. G. Sammons, and R. A. Kane (2004). “Optimizing Doppler and Color Flow US: Application to Hepatic Sonography”. In: *Radiographics* 24.3, pp. 657–675 (cit. on p. 3).
- Stewart, S. F. C. (2001). “Effects of transducer, velocity, Doppler angle, and instrument settings on the accuracy of color Doppler ultrasound”. In: *Ultrasound Med. Biol.* 27.4, pp. 551–564. DOI: 10.1016/S0301-5629(01)00357-X (cit. on p. 3).
- Tanter, M. and M. Fink (2014). “Ultrafast imaging in biomedical ultrasound”. In: *IEEE Trans. Ultrason., Ferroelec., Freq. Contr.* 61.1, pp. 102–119. DOI: 10.1109/TUFFC.2014.6689779 (cit. on p. 2).
- WHO (2015). *Cardiovascular diseases (CVDs)*. URL: <http://www.who.int/mediacentre/factsheets/fs317/en/> (cit. on p. 1).

References from Chapter 2

- Anderson, M. E. (1998). “Multi-dimensional velocity estimation with ultrasound using spatial quadrature”. In: *IEEE Trans. Ultrason., Ferroelec., Freq. Contr.* 45, pp. 852–861 (cit. on p. 18).

- Basarab, A., P. Gueth, H. Liebgott, and P. Delachartre (2009). "Phase-based block matching applied to motion estimation with unconventional beamforming strategies". In: *IEEE Trans. Ultrason., Ferroelec., Freq. Contr.* 56.5, pp. 945–957 (cit. on p. 19).
- Bercoff, J., S. Chaffai, M. Tanter, L. Sandrin, S. Catheline, M. Fink, J. Gennisson, and M. Meunier (2003). "In vivo breast tumor detection using transient elastography". In: *Ultrasound Med. Biol.* 29.10, pp. 1387–1396. DOI: 10.1016/S0301-5629(03)00978-5 (cit. on p. 10).
- Bercoff, J., G. Montaldo, T. Loupas, D. Savery, F. Meziere, M. Fink, and M. Tanter (2011). "Ultrafast Compound Doppler Imaging: providing Full Blood Flow Characterization". In: *IEEE Trans. Ultrason., Ferroelec., Freq. Contr.* 58.1, pp. 134–147. DOI: 10.1109/TUFFC.2011.1780 (cit. on pp. 14, 21).
- Bercoff, J., M. Tanter, and M. Fink (2004). "Supersonic shear imaging: A new technique for soft tissue elasticity mapping". In: *IEEE Trans. Ultrason., Ferroelec., Freq. Contr.* 51.4, pp. 396–409. DOI: 10.1109/TUFFC.2004.1295425 (cit. on p. 11).
- Bohs, L. N., B. J. Geiman, S. M. Breit, and G. E. Trahey (1998). "Ensemble tracking for 2D vector velocity measurement: experimental and initial clinical results". In: *IEEE Trans. Ultrason., Ferroelec., Freq. Contr.* 45, pp. 912–924 (cit. on p. 18).
- Bonnefous, O. and P. Pesqué (1986). "Time Domain Formulation of Pulse-Doppler Ultrasound and Blood Velocity Estimation by Cross Correlation". In: *Ultrasound Imaging* 8, pp. 73–85. DOI: 10.1016/0161-7346(86)90001-5 (cit. on p. 15).
- Capineri, L., M. Scabia, and L. Masotti (2002). "A Doppler system for dynamic vector velocity maps". In: *Ultrasound Med. Biol.* 28.2, pp. 237–248 (cit. on p. 16).
- Cheng, J. and J. Lu (2006). "Extended high-frame rate imaging method with limited-diffraction beams". In: *IEEE Trans. Ultrason., Ferroelec., Freq. Contr.* 53.5, pp. 880–899. DOI: 10.1109/TUFFC.2006.1632680 (cit. on p. 10).
- Correia, M., J. Provost, M. Tanter, and M. Pernot (2016). "4D ultrafast ultrasound flow imaging: in vivo quantification of arterial volumetric flow rate in a single heartbeat". In: *Phys. Med. Biol.* 61.23, pp. L48–L61 (cit. on p. 17).
- Couture, O., M. Fink, and M. Tanter (2012). "Ultrasound Contrast Plane Wave Imaging". In: *IEEE Trans. Ultrason., Ferroelec., Freq. Contr.* 59.12, pp. 2676–2683. DOI: 10.1109/tuffc.2012.2508 (cit. on p. 11).
- Delannoy, B., R. Torguet, C. Bruneel, E. Bridoux, J. M. Rouvaen, and H. Lasota (1979). "Acoustical image reconstruction in parallel-processing analog electronic systems". In: *J. Applied Phys.* 50.5, pp. 3153–3159. DOI: <http://scitation.aip.org/content/aip/journal/jap/50/5/10.1063/1.326397> (cit. on p. 10).
- Dotti, D., E. Gatti, V. Svelto, A. Uggè, and P. Vidali (1976). "Blood flow measurements by ultrasound correlation techniques". In: *Energia Nucleare* 23.11, pp. 571–575 (cit. on p. 15).
- Dunmire, B., K. W. Beach, K.-H. Labs., M. Plett, and D. E. Strandness (2000). "Cross-beam vector Doppler ultrasound for angle independent velocity measurements". In: *Ultrasound Med. Biol.* 26, pp. 1213–1235 (cit. on p. 16).

- Ekroll, I. K., T. Dahl, H. Torp, and L. Løvstakken (2014). “Combined Vector Velocity and Spectral Doppler Imaging for Improved Imaging of Complex Blood Flow in the Carotid Arteries”. In: *Ultrasound Med. Biol.* 40.7, pp. 1629–1640 (cit. on p. 14).
- Ekroll, I. K., A. Swillens, P. Segers, T. Dahl, H. Torp, and L. Lovstakken (2013). “Simultaneous quantification of flow and tissue velocities based on multi-angle plane wave imaging”. In: *IEEE Trans. Ultrason., Ferroelec., Freq. Contr.* 60.4, pp. 727–738 (cit. on p. 17).
- Evans, D. H. and W. N. McDicken (2000). *Doppler Ultrasound, Physics, Instrumentation, and Signal Processing*. New York: John Wiley & Sons (cit. on p. 13).
- Fadnes, S., I. K. Ekroll, S. A. Nytnes, H. Torp, and L. Løvstakken (2015). “Robust Angle-Independent Blood Velocity Estimation Based on Dual-Angle Plane Wave Imaging”. In: *IEEE Trans. Ultrason., Ferroelec., Freq. Contr.* 62.10, pp. 1757–1767. DOI: 10.1109/tuffc.2015.007108 (cit. on p. 18).
- Fadnes, S., S. A. Nytnes, H. Torp, and L. Lovstakken (2014). “Shunt Flow Evaluation in Congenital Heart Disease Based on Two-Dimensional Speckle Tracking”. In: *Ultrasound Med. Biol.* 40.10, pp. 2379–2391. DOI: 10.1016/j.ultrasmedbio.2014.03.029 (cit. on p. 18).
- Fahrbach, K. (1970). “Ein Beitrag Zur Blutgeschwindigkeitsmessung unter Anwendung des Dopplereffektes”. In: *Elektromedizin* 15.1, pp. 26–36 (cit. on p. 16).
- Fink, M. (1992). “Time Reversal of Ultrasonic Fields-Part I: Basic Principles”. In: *IEEE Trans. Ultrason., Ferroelec., Freq. Contr.* 39.5, pp. 555–566 (cit. on p. 9).
- Flaherty, J. J., K. R. Erikson, and V. M. Lund (1967). *Synthetic Aperture Ultrasound Imaging Systems*. United States Patent, US 3,548,642. United States Patent, US 3,548,642, 1967, Published 22 Dec 1970 (cit. on p. 9).
- Flynn, J., R. Daigle, L. Pflugrath, P. Kaczkowski, and K. Linkhart (2011). “Estimation and display for vector Doppler imaging using planewave transmissions”. In: *Proc. IEEE Ultrason. Symp.* Pp. 413–418 (cit. on p. 17).
- Foster, S. G., P. M. Embree, and W. D. O’Brien (1990). “Flow Velocity Profile via Time-Domain Correlation: Error Analysis and Computer Simulation”. In: *IEEE Trans. Ultrason., Ferroelec., Freq. Contr.* 37, pp. 164–175 (cit. on p. 16).
- Fox, M. D. (1978). “Multiple crossed-beam ultrasound Doppler velocimetry”. In: *IEEE Trans. Son. Ultrason.* SU-25, pp. 281–286 (cit. on p. 17).
- Gammelmark, K. L. and J. A. Jensen (2003). “Multielement Synthetic Transmit Aperture Imaging using Temporal Encoding”. In: *IEEE Trans. Med. Imag.* 22.4, pp. 552–563 (cit. on p. 11).
- Garcia, D., J. C. del Alamo, D. Tanne, R. Yotti, C. Cortina, E. Bertrand, J. C. Antoranz, E. Perez-David, R. Rieu, F. Fernandez-Aviles, and J. Bermejo (2010). “Two-dimensional intraventricular flow mapping by digital processing conventional color-Doppler echocardiography images”. In: *IEEE Trans. Med. Imag.* 29.10, pp. 1701–1713 (cit. on p. 16).

- Hansen, K. L., J. Udesen, F. Gran, J. A. Jensen, and M. B. Nielsen (2009). “In-vivo examples of flow patterns with the fast vector velocity ultrasound method”. In: *Ultraschall in Med.* 30, pp. 471–476 (cit. on p. 18).
- Hasegawa, H. and H. Kanai (2008). “Simultaneous Imaging of Artery-Wall Strain and Blood Flow by High Frame Rate Acquisition of RF Signals”. In: *IEEE Trans. Ultrason., Ferroelec., Freq. Contr.* 55.12, pp. 2626–2639. DOI: 10.1109/TUFFC.2008.978 (cit. on p. 11).
- Holbek, S., C. Ewertsen, H. Bouzari, M. J. Pihl, K. L. Hansen, M. B. Stuart, M. B. Nielsen, and J. A. Jensen (2017). “Ultrasonic 3-D vector flow method for quantitative in vivo peak velocity and flow rate estimation”. In: *IEEE Trans. Ultrason., Ferroelec., Freq. Contr.* 64.3, pp. 544–554 (cit. on p. 19).
- Jensen, J. A. (1996). *Estimation of Blood Velocities Using Ultrasound: A Signal Processing Approach*. New York: Cambridge University Press (cit. on pp. 13, 17).
- (2001). “A New Estimator for Vector Velocity Estimation”. In: *IEEE Trans. Ultrason., Ferroelec., Freq. Contr.* 48.4, pp. 886–894 (cit. on p. 19).
- (2003). “Directional velocity estimation using focusing along the flow direction: I: Theory and simulation”. In: *IEEE Trans. Ultrason., Ferroelec., Freq. Contr.* 50, pp. 857–872 (cit. on p. 20).
- (2015). “Improved Vector Velocity Estimation using Directional Transverse Oscillation”. In: *Proc. IEEE Ultrason. Symp. IEEE*, pp. 1–4. DOI: 10.1109/ULTSYM.2015.0011 (cit. on p. 19).
- Jensen, J. A. and R. Bjerngaard (2003). “Directional velocity estimation using focusing along the flow direction: II: Experimental investigation”. In: *IEEE Trans. Ultrason., Ferroelec., Freq. Contr.* 50, pp. 873–880 (cit. on p. 20).
- Jensen, J. A., A. H. Brandt, and M. B. Nielsen (2015). “Convex Array Vector Velocity Imaging Using Transverse Oscillation and Its Optimization”. In: *IEEE Trans. Ultrason., Ferroelec., Freq. Contr.* 62.12, pp. 2043–2053. DOI: 10.1109/TUFFC.2015.006970 (cit. on p. 19).
- Jensen, J. A., O. Holm, L. J. Jensen, H. Bendsen, H. M. Pedersen, K. Salomonsen, J. Hansen, and S. Nikolov (1999). “Experimental ultrasound system for real-time synthetic imaging”. In: *Proc. IEEE Ultrason. Symp.* Vol. 2, pp. 1595–1599. DOI: 10.1109/ULTSYM.1999.849300 (cit. on p. 11).
- Jensen, J. A. and P. Munk (1998). “A New Method for Estimation of Velocity Vectors”. In: *IEEE Trans. Ultrason., Ferroelec., Freq. Contr.* 45.3, pp. 837–851 (cit. on p. 18).
- Jensen, J. A. and S. I. Nikolov (2004). “Directional Synthetic Aperture Flow Imaging”. In: *IEEE Trans. Ultrason., Ferroelec., Freq. Contr.* 51, pp. 1107–1118 (cit. on p. 20).
- Jensen, J. A., S. I. Nikolov, A. Yu, and D. Garcia (2016). “Ultrasound Vector Flow Imaging II: Parallel Systems”. In: *IEEE Trans. Ultrason., Ferroelec., Freq. Contr.* 63.11, pp. 1722–1732. DOI: 10.1109/TUFFC.2016.2598180 (cit. on pp. 12, 13, 21).
- Jensen, J. A., S. Nikolov, K. L. Gammelmark, and M. H. Pedersen (2006). “Synthetic Aperture Ultrasound Imaging”. In: *Ultrasonics* 44, e5–e15 (cit. on p. 9).

- Jensen, J. A. and N. Oddershede (2006). “Estimation of velocity vectors in synthetic aperture ultrasound imaging”. In: *IEEE Trans. Med. Imag.* 25, pp. 1637–1644 (cit. on p. 20).
- Karaman, M., P. C. Li, and M. O’Donnell (1995). “Synthetic aperture imaging for small scale systems”. In: *IEEE Trans. Ultrason., Ferroelec., Freq. Contr.* 42, pp. 429–442 (cit. on p. 9).
- Kasai, C., K. Namekawa, A. Koyano, and R. Omoto (1985). “Real-Time Two-Dimensional Blood Flow Imaging using an Autocorrelation Technique”. In: *IEEE Trans. Son. Ultrason.* 32.3, pp. 458–463 (cit. on p. 15).
- Kortbek, J. and J. A. Jensen (2006). “Estimation of velocity vector angles using the directional cross-correlation method”. In: *IEEE Trans. Ultrason., Ferroelec., Freq. Contr.* 53, pp. 2036–2049 (cit. on p. 20).
- Lenge, M., A. Ramalli, P. Tortoli, C. Cachard, and H. Liebgott (2015). “Plane-Wave Transverse Oscillation for High-Frame-Rate 2-D Vector Flow Imaging”. In: *IEEE Trans. Ultrason., Ferroelec., Freq. Contr.* 62.12, pp. 2126–2137 (cit. on p. 19).
- Liebgott, H. (2010). “Fourier domain beamforming for transverse-oscillations”. In: *Proc. IEEE Ultrason. Symp.* Pp. 1755–1758 (cit. on p. 18).
- Liebgott, H., A. Basarab, P. Gueth, C. Cachard, and P. Delachartre (2008). “Lateral RF image synthesis using a synthetic aperture imaging technique.” In: *IEEE Trans. Ultrason., Ferroelec., Freq. Contr.* 55.9, pp. 2097–2103 (cit. on p. 19).
- Liebgott, H., J. Wilhjelm, J. A. Jensen, D. Vray, and P. Delachartre (2007). “PSF dedicated to estimation of displacement vectors for tissue elasticity imaging with ultrasound”. In: *IEEE Trans. Ultrason., Ferroelec., Freq. Contr.* 54.4, pp. 746–756 (cit. on p. 19).
- Lockwood, G. R. and F. Foster (1995). “Design of sparse array imaging systems”. In: *Proc. IEEE Ultrason. Symp.* Pp. 1237–1243 (cit. on p. 9).
- Lockwood, G. R., J. R. Talman, and S. S. Brunke (1998). “Real-time 3-D ultrasound imaging using sparse synthetic aperture beamforming”. In: *IEEE Trans. Ultrason., Ferroelec., Freq. Contr.* 45, pp. 980–988 (cit. on p. 9).
- Lu, J. Y. (1997). “2D and 3D high frame rate imaging with limited diffraction beams”. In: *IEEE Trans. Ultrason., Ferroelec., Freq. Contr.* 44, pp. 839–855 (cit. on p. 10).
- (1998). “Experimental study of high frame rate imaging with limited diffraction beams”. In: *IEEE Trans. Ultrason., Ferroelec., Freq. Contr.* 45, pp. 84–97 (cit. on p. 10).
- Lu, J., J. Cheng, and J. Wang (2006). “High Frame Rate Imaging System for Limited Diffraction Array Beam Imaging with Square-Wave Aperture Weightings”. In: *IEEE Trans. Ultrason., Ferroelec., Freq. Contr.* 53.10, pp. 1796–1812 (cit. on p. 11).
- Mace, E., G. Montaldo, I. Cohen, M. Baulac, M. Fink, and M. Tanter (2011). “Functional ultrasound imaging of the brain”. In: *Nature methods* 8.8, pp. 662–664. DOI: 10.1038/nmeth.1641 (cit. on pp. 11, 21).
- Montaldo, G., M. Tanter, J. Bercoff, N. Benech, and M. Fink (2009). “Coherent plane-wave compounding for very high frame rate ultrasonography and transient elastog-

- raphy". In: *IEEE Trans. Ultrason., Ferroelec., Freq. Contr.* 56.3, pp. 489–506. DOI: 10.1109/TUFFC.2009.1067 (cit. on p. 10).
- Namekawa, K., C. Kasai, M. Tsukamoto, and A. Koyano (1982). "Realtime bloodflow imaging system utilizing autocorrelation techniques". In: *Ultrasound '82*. Ed. by R. Lerski and P. Morley. New York: Pergamon Press, pp. 203–208 (cit. on p. 14).
- Newhouse, V. L., D. Censor, T. Vontz, J. A. Cisneros, and B. B. Goldberg (1987). "Ultrasound Doppler probing of flows transverse with respect to beam axis". In: *IEEE Trans. Biomed. Eng.* BME-34, pp. 779–788 (cit. on p. 16).
- Nikolov, S. I. and J. A. Jensen (2001). "Velocity estimation using synthetic aperture imaging". In: *Proc. IEEE Ultrason. Symp.* Pp. 1409–1412 (cit. on pp. 12, 16).
- (2002). "Virtual ultrasound sources in high-resolution ultrasound imaging". In: *Proc. SPIE - Progress in biomedical optics and imaging*. Vol. 3, pp. 395–405 (cit. on p. 9).
- (2003). "In-vivo Synthetic Aperture Flow Imaging in Medical Ultrasound". In: *IEEE Trans. Ultrason., Ferroelec., Freq. Contr.* 50.7, pp. 848–856 (cit. on pp. 11, 16).
- O'Donnell, M. and L. J. Thomas (1992). "Efficient synthetic aperture imaging from a circular aperture with possible application to catheter-based imaging". In: *IEEE Trans. Ultrason., Ferroelec., Freq. Contr.* 39, pp. 366–380 (cit. on p. 9).
- Ohtsuki, S. and M. Tanaka (2006). "The Flow Velocity Distribution from the Doppler Information on a Plane in Three-Dimensional Flow". In: *J. of Visualization* 9.1, pp. 69–82 (cit. on p. 16).
- Osmanski, B.-F., G. Montaldo, and M. Tanter (2015). "Out-of-plane Doppler imaging based on ultrafast plane wave imaging". In: *IEEE Trans. Ultrason., Ferroelec., Freq. Contr.* 62.4, pp. 625–636. DOI: 10.1109/TUFFC.2014.006575 (cit. on p. 16).
- Pedersen, M. H., K. L. Gammelmark, and J. A. Jensen (2007). "In-vivo evaluation of convex array synthetic aperture imaging". In: *Ultrasound Med. Biol.* 33, pp. 37–47 (cit. on p. 11).
- Peronneau, P., J.-P. Bournat, A. Bugnon, A. Barbet, and M. Xhaard (1974). "Theoretical and practical aspects of pulsed Doppler flowmetry real-time application to the measure of instantaneous velocity profiles in vitro and in vivo". In: *Cardiovascular applications of ultrasound*. Ed. by R. Reneman. North Holland Publishing, pp. 66–84 (cit. on p. 16).
- Phillips, P. J., A. P. Kadi, and O. T. von Ramm (1995). "Feasibility study for a two-dimensional diagnostic ultrasound velocity mapping system". In: *Ultrasound Med. Biol.* 21.2, pp. 217–229 (cit. on p. 16).
- Pihl, M. J. and J. A. Jensen (2014). "A Transverse Oscillation Approach for Estimation of Three-Dimensional Velocity Vectors. Part I: Concept and Simulation Study". In: *IEEE Trans. Ultrason., Ferroelec., Freq. Contr.* 61, pp. 1599–1607 (cit. on p. 19).
- Pihl, M. J., M. B. Stuart, B. G. Tomov, M. F. Rasmussen, and J. A. Jensen (2014). "A Transverse Oscillation Approach for Estimation of Three-Dimensional Velocity Vectors. Part II: Experimental Validation". In: *IEEE Trans. Ultrason., Ferroelec., Freq. Contr.* 51.10, pp. 1608–1618 (cit. on p. 19).
- Prine, D. W. (1972). "Synthetic Aperture Ultrasonic Imaging". In: *Proceedings of the Engineering Applications of Holography Symposium*, pp. 287–294 (cit. on p. 9).

- Provost, J., C. Papadacci, J. E. Arango, M. Imbault, M. Fink, J. L. Gennisson, M. Tanter, and M. Pernot (2014). “3-D ultrafast ultrasound imaging in vivo”. In: *Phys. Med. Biol.* 59.19, pp. L1–L13 (cit. on p. 17).
- Ricci, S., L. Bassi, and P. Tortoli (2014). “Real-time vector velocity assessment through multigate Doppler and plane waves”. In: *IEEE Trans. Ultrason., Ferroelec., Freq. Contr.* 61.2, pp. 314–324 (cit. on p. 17).
- Salles, S., A. J. Y. Chee, D. Garcia, A. C. H. Yu, D. Vray, and H. Liebgott (2015). “2-D arterial wall motion imaging using ultrafast ultrasound and transverse oscillations”. In: *IEEE Trans. Ultrason., Ferroelec., Freq. Contr.* 62.6, pp. 1047–1058. DOI: 10.1109/TUFFC.2014.006910 (cit. on p. 19).
- Sandrin, L., S. Catheline, M. Tanter, X. Hennequin, and M. Fink (1999). “Time-resolved pulsed elastography with ultrafast ultrasonic imaging”. In: *Ultrason. Imaging* 21.4, pp. 259–272 (cit. on pp. 10, 11).
- Sandrin, L., S. Manneville, and M. Fink (2001). “Ultrafast two-dimensional ultrasonic speckle velocimetry: A tool in flow imaging”. In: *Appl. Phys. Lett.* 78.8, pp. 1155–1157 (cit. on p. 18).
- Sandrin, L., M. Tanter, S. Catheline, and M. Fink (2002). “Shear modulus imaging with 2-D transient elastography”. In: *IEEE Trans. Ultrason., Ferroelec., Freq. Contr.* 49.4, pp. 426–435. DOI: 10.1109/58.996560 (cit. on p. 11).
- Saris, A. E. C. M., H. H. G. Hansen, S. Fekkes, M. M. Nillesen, M. C. M. Rutten, and C. L. de Korte (2016). “A Comparison Between Compounding Techniques Using Large Beam-Steered Plane Wave Imaging for Blood Vector Velocity Imaging in a Carotid Artery Model”. In: *IEEE Trans. Ultrason., Ferroelec., Freq. Contr.* 63.11, pp. 1758–1771. DOI: 10.1109/TUFFC.2016.2606565 (cit. on p. 18).
- Shattuck, D. P., M. D. Weinshenker, S. W. Smith, and O. T. von Ramm (1984). “Explososcan: A parallel processing technique for high speed ultrasound imaging with linear phased arrays”. In: *J. Acoust. Soc. Am.* 75, pp. 1273–1282 (cit. on p. 10).
- Smith, S. W., H. G. Pavy, and O. T. von Ramm (1991). “High speed ultrasound volumetric imaging system – Part I: Transducer design and beam steering”. In: *IEEE Trans. Ultrason., Ferroelec., Freq. Contr.* 38, pp. 100–108 (cit. on p. 10).
- Tanter, M., J. Bercoff, L. Sandrin, and M. Fink (2002). “Ultrafast compound imaging for 2-D motion vector estimation: application to transient elastography”. In: *IEEE Trans. Ultrason., Ferroelec., Freq. Contr.* 49, pp. 1363–1374 (cit. on pp. 10, 17).
- Tanter, M. and M. Fink (2014). “Ultrafast imaging in biomedical ultrasound”. In: *IEEE Trans. Ultrason., Ferroelec., Freq. Contr.* 61.1, pp. 102–119. DOI: 10.1109/TUFFC.2014.6689779 (cit. on p. 11).
- Tortoli, P., G. Bambi, and S. Ricci (2006). “Accurate Doppler angle estimation for vector flow measurements”. In: *IEEE Trans. Ultrason., Ferroelec., Freq. Contr.* 53.8, pp. 1425–1431 (cit. on p. 16).
- Tortoli, P., L. Bassi, E. Boni, A. Dallai, F. Guidi, and S. Ricci (2009). “ULA-OP: An Advanced Open Platform for Ultrasound Research”. In: *IEEE Trans. Ultrason., Ferroelec., Freq. Contr.* 56.10, pp. 2207–2216 (cit. on p. 11).

- Trahey, G. E., J. W. Allison, and O. T. von Ramm (1987). "Angle independent ultrasonic detection of blood flow". In: *IEEE Trans. Biomed. Eng.* BME-34.12, pp. 965–967 (cit. on p. 17).
- Tsang, I. K. H., B. Y. S. Yiu, and A. C. H. Yu (2009). "A least-squares vector flow estimator for synthetic aperture imaging". In: *Proc. IEEE Ultrason. Symp.* Pp. 1387–1390 (cit. on p. 17).
- Udesen, J., F. Gran, K. L. Hansen, J. A. Jensen, C. Thomsen, and M. B. Nielsen (2008). "High Frame-Rate Blood Vector Velocity Imaging Using Plane Waves: simulations and preliminary experiments". In: *IEEE Trans. Ultrason., Ferroelec., Freq. Contr.* 55.8, pp. 1729–1743 (cit. on p. 18).
- Udesen, J., F. Gran, and J. A. Jensen (2005). "Fast Color Flow Mode Imaging Using Plane Wave Excitation and Temporal Encoding". In: *Proc. SPIE Med. Imag.* Vol. 5750, pp. 427–436 (cit. on p. 20).
- Udesen, J. and J. A. Jensen (2006). "Investigation of Transverse Oscillation Method". In: *IEEE Trans. Ultrason., Ferroelec., Freq. Contr.* 53, pp. 959–971 (cit. on p. 19).
- Udesen, J., M. B. Nielsen, K. R. Nielsen, and J. A. Jensen (2007). "Examples of in-vivo blood vector velocity estimation". In: *Ultrasound Med. Biol.* 33, pp. 541–548 (cit. on p. 19).
- Vappou, J., J. Luo, and E. E. Konofagou (2010). "Pulse Wave Imaging for Noninvasive and Quantitative Measurement of Arterial Stiffness In Vivo". In: *Am. J. Hypertens.* 23.4, pp. 393–398. DOI: 10.1038/ajh.2009.272 (cit. on p. 11).
- Varray, F. and H. Liebgott (2013). "An alternative method to classical beamforming for transverse oscillation images: Application to elastography". In: *IEEE 10th Int. Symp. Biomedical Imaging*, pp. 716–719. DOI: 10.1109/ISBI.2013.6556575 (cit. on p. 18).
- Villagomez-Hoyos, C. A., M. B. Stuart, K. L. Hansen, M. B. Nielsen, and J. A. Jensen (2016). "Accurate Angle Estimator for High Frame Rate 2-D Vector Flow Imaging". In: *IEEE Trans. Ultrason., Ferroelec., Freq. Contr.* 63.6, pp. 842–853 (cit. on p. 20).
- von Ramm, O. T., S. W. Smith, and H. G. Pavy (1991). "High speed ultrasound volumetric imaging system – Part II: Parallel processing and image display". In: *IEEE Trans. Ultrason., Ferroelec., Freq. Contr.* 38, pp. 109–115 (cit. on p. 10).
- Wigen, M. and L. Løvstakken (2016). "In vivo three-dimensional intra-cardiac vector flow imaging using a 2D matrix array transducer". In: *Proc. IEEE Ultrason. Symp.* Pp. 1–4 (cit. on p. 18).
- Yiu, B. Y., S. S. Lai, and A. C. Yu (2014). "Vector projectile imaging: time-resolved dynamic visualization of complex flow patterns." In: *Ultrasound Med. Biol.* 40.9, pp. 2295–2309 (cit. on p. 17).

References from Chapter 3

- Bercoff, J., G. Montaldo, T. Loupas, D. Savery, F. Meziere, M. Fink, and M. Tanter (2011). “Ultrafast Compound Doppler Imaging: providing Full Blood Flow Characterization”. In: *IEEE Trans. Ultrason., Ferroelec., Freq. Contr.* 58.1, pp. 134–147. DOI: 10.1109/TUFFC.2011.1780 (cit. on p. 24).
- Coello, C. A. C., G. B. Lamont, and D. A. V. Veldhuizen (2007). “Basic Concepts”. In: *Evolutionary Algorithms for Solving Multi-Objective Problems*. Springer (cit. on p. 26).
- Deb, K. (2005). “Multi-objective optimization”. In: *Search methodologies*. Springer (cit. on p. 26).
- Denarie, B., T. A. Tangen, I. K. Ekroll, N. Rolim, H. H. Torp, T. Bjastad, and L. Løvsstakken (2013). “Coherent Plane Wave Compounding for Very High Frame Rate Ultrasonography of Rapidly Moving Targets”. In: *IEEE Trans. Ultrason., Ferroelec., Freq. Contr.* 32.7, pp. 1265–1276 (cit. on p. 24).
- Ekroll, I. K., A. Swillens, P. Segers, T. Dahl, H. Torp, and L. Lovstakken (2013). “Simultaneous quantification of flow and tissue velocities based on multi-angle plane wave imaging”. In: *IEEE Trans. Ultrason., Ferroelec., Freq. Contr.* 60.4, pp. 727–738 (cit. on p. 24).
- FDA (2008). *Information for Manufacturers Seeking Marketing Clearance of Diagnostic Ultrasound Systems and Transducers*. Tech. rep. Center for Devices, Radiological Health, United States Food, and Drug Administration (cit. on p. 32).
- Haller, M. I. and B. T. Khuri-Yakub (1996). “A surface micromachined electrostatic ultrasonic air transducer”. In: *IEEE Trans. Ultrason., Ferroelec., Freq. Contr.* 43.1, pp. 1–6 (cit. on p. 35).
- Hansen, K. L., J. Udesen, F. Gran, J. A. Jensen, and M. B. Nielsen (2009). “In-vivo examples of flow patterns with the fast vector velocity ultrasound method”. In: *Ultraschall in Med.* 30, pp. 471–476 (cit. on p. 24).
- Hasegawa, H. and C. L. de Korte (2016). “Impact of element pitch on synthetic aperture ultrasound imaging”. In: *J. Med. Ultrason.* Pp. 1–9. DOI: 10.1007/s10396-016-0700-6 (cit. on p. 34).
- IEC (2015). *Medical electrical equipment - Part 2-37: Particular requirements for the basic safety and essential performance of ultrasonic medical diagnostic and monitoring equipment*. Tech. rep. IEC 60601-2-37. Edition 2.1 2015-06. International Electrotechnical Commission (cit. on p. 32).
- Jensen, J. A. (1996). “Field: A Program for Simulating Ultrasound Systems”. In: *Med. Biol. Eng. Comp.* 10th Nordic-Baltic Conference on Biomedical Imaging, Vol. 4, Supplement 1, Part 1, pp. 351–353 (cit. on p. 25).
- Jensen, J. A., H. Holtén-Lund, R. T. Nilsson, M. Hansen, U. D. Larsen, R. P. Domsten, B. G. Tomov, M. B. Stuart, S. I. Nikolov, M. J. Pihl, Y. Du, J. H. Rasmussen, and M. F. Rasmussen (2013). “SARUS: A Synthetic Aperture Real-time Ultrasound System”. In: *IEEE Trans. Ultrason., Ferroelec., Freq. Contr.* 60.9, pp. 1838–1852 (cit. on p. 31).

- Jensen, J. A. and S. I. Nikolov (2004). “Directional Synthetic Aperture Flow Imaging”. In: *IEEE Trans. Ultrason., Ferroelec., Freq. Contr.* 51, pp. 1107–1118 (cit. on p. 24).
- Jensen, J. A. and N. B. Svendsen (1992). “Calculation of Pressure Fields from Arbitrarily Shaped, Apodized, and Excited Ultrasound Transducers”. In: *IEEE Trans. Ultrason., Ferroelec., Freq. Contr.* 39, pp. 262–267 (cit. on p. 25).
- Montaldo, G., M. Tanter, J. Bercoff, N. Bencech, and M. Fink (2009). “Coherent plane-wave compounding for very high frame rate ultrasonography and transient elastography”. In: *IEEE Trans. Ultrason., Ferroelec., Freq. Contr.* 56.3, pp. 489–506. DOI: 10.1109/TUFFC.2009.1067 (cit. on pp. 23, 24).
- Moshavegh, R., J. Jensen, C. A. Villagomez-Hoyos, M. B. Stuart, M. C. Hemmsen, and J. A. Jensen (2016). “Optimization of synthetic aperture image quality”. In: *Proc. SPIE Med. Imag.* Vol. 9790, pages (cit. on p. 34).
- Nikolov, S. I. and J. A. Jensen (2003). “In-vivo Synthetic Aperture Flow Imaging in Medical Ultrasound”. In: *IEEE Trans. Ultrason., Ferroelec., Freq. Contr.* 50.7, pp. 848–856 (cit. on p. 24).
- Oddershede, N. and J. A. Jensen (2007). “Effects influencing focusing in synthetic aperture vector flow imaging”. In: *IEEE Trans. Ultrason., Ferroelec., Freq. Contr.* 54.9, pp. 1811–1825 (cit. on p. 25).
- Ranganathan, K. and W. F. Walker (2007). “Cystic Resolution: A Performance Metric for Ultrasound Imaging Systems”. In: *IEEE Trans. Ultrason., Ferroelec., Freq. Contr.* 54.4, pp. 782–792. DOI: 10.1109/TUFFC.2007.311 (cit. on p. 26).
- Stuart, M. B., J. Jensen, T. Di Ianni, and J. A. Jensen (2015). “Image quality degradation from transmit delay profile quantization”. In: *Proc. IEEE Ultrason. Symp.* Pp. 1–4. DOI: 10.1109/ULTSYM.2015.0126 (cit. on p. 36).
- Yiu, B. Y. S. and A. C. H. Yu (2013). “High-frame-rate ultrasound color-encoded speckle imaging of complex flow dynamics”. In: *Ultrasound Med. Biol.* 39.6, pp. 1015–1025 (cit. on p. 24).

References from Chapter 4

- Bercoff, J., G. Montaldo, T. Loupas, D. Savery, F. Meziere, M. Fink, and M. Tanter (2011). “Ultrafast Compound Doppler Imaging: providing Full Blood Flow Characterization”. In: *IEEE Trans. Ultrason., Ferroelec., Freq. Contr.* 58.1, pp. 134–147. DOI: 10.1109/TUFFC.2011.1780 (cit. on p. 54).
- Bonnefous, O. and P. Pesqué (1986). “Time Domain Formulation of Pulse-Doppler Ultrasound and Blood Velocity Estimation by Cross Correlation”. In: *Ultrason. Imaging* 8, pp. 73–85. DOI: 10.1016/0161-7346(86)90001-5 (cit. on p. 42).
- Ekroll, I. K., A. Swillens, P. Segers, T. Dahl, H. Torp, and L. Lovstakken (2013). “Simultaneous quantification of flow and tissue velocities based on multi-angle plane wave imaging”. In: *IEEE Trans. Ultrason., Ferroelec., Freq. Contr.* 60.4, pp. 727–738 (cit. on p. 39).

- Fadnes, S., I. K. Ekroll, S. A. Nyenes, H. Torp, and L. Løvstakken (2015). “Robust Angle-Independent Blood Velocity Estimation Based on Dual-Angle Plane Wave Imaging”. In: *IEEE Trans. Ultrason., Ferroelec., Freq. Contr.* 62.10, pp. 1757–1767. DOI: 10.1109/tuffc.2015.007108 (cit. on p. 39).
- FDA (2008). *Information for Manufacturers Seeking Marketing Clearance of Diagnostic Ultrasound Systems and Transducers*. Tech. rep. Center for Devices, Radiological Health, United States Food, and Drug Administration (cit. on p. 52).
- Foster, S. G., P. M. Embree, and W. D. O’Brien (1990). “Flow Velocity Profile via Time-Domain Correlation: Error Analysis and Computer Simulation”. In: *IEEE Trans. Ultrason., Ferroelec., Freq. Contr.* 37, pp. 164–175 (cit. on p. 43).
- Hoeks, A. P. G., M. Hennerici, and R. S. Reneman (1991). “Spectral composition of Doppler signals”. In: *Ultrasound Med. Biol.* 17, pp. 751–760 (cit. on p. 45).
- IEC (2015). *Medical electrical equipment - Part 2-37: Particular requirements for the basic safety and essential performance of ultrasonic medical diagnostic and monitoring equipment*. Tech. rep. IEC 60601-2-37. Edition 2.1 2015-06. International Electrotechnical Commission (cit. on p. 52).
- Jensen, J. A. (1996a). *Estimation of Blood Velocities Using Ultrasound: A Signal Processing Approach*. New York: Cambridge University Press (cit. on p. 54).
- (1996b). “Field: A Program for Simulating Ultrasound Systems”. In: *Med. Biol. Eng. Comp.* 10th Nordic-Baltic Conference on Biomedical Imaging, Vol. 4, Supplement 1, Part 1, pp. 351–353 (cit. on p. 46).
- (2001). “A New Estimator for Vector Velocity Estimation”. In: *IEEE Trans. Ultrason., Ferroelec., Freq. Contr.* 48.4, pp. 886–894 (cit. on p. 42).
- (2014a). “A Multi-threaded Version of Field II”. In: *Proc. IEEE Ultrason. Symp. IEEE*, pp. 2229–2232 (cit. on p. 46).
- (2014b). “Comparison of Vector Velocity Imaging using Directional Beamforming and Transverse Oscillation for a Convex Array Transducer”. In: *Proc. SPIE Med. Imag.* Vol. 9040, pages. DOI: 10.1117/12.2043701 (cit. on p. 39).
- (2016). “Directional Transverse Oscillation Vector Flow Estimation”. In: *IEEE Trans. Ultrason., Ferroelec., Freq. Contr.* 63, Submitted (cit. on p. 42).
- Jensen, J. A., H. Holten-Lund, R. T. Nilsson, M. Hansen, U. D. Larsen, R. P. Domsten, B. G. Tomov, M. B. Stuart, S. I. Nikolov, M. J. Pihl, Y. Du, J. H. Rasmussen, and M. F. Rasmussen (2013). “SARUS: A Synthetic Aperture Real-time Ultrasound System”. In: *IEEE Trans. Ultrason., Ferroelec., Freq. Contr.* 60.9, pp. 1838–1852 (cit. on p. 46).
- Jensen, J. A. and N. Oddershede (2006). “Estimation of velocity vectors in synthetic aperture ultrasound imaging”. In: *IEEE Trans. Med. Imag.* 25, pp. 1637–1644 (cit. on pp. 39, 43).
- Jensen, J. A., M. F. Rasmussen, M. J. Pihl, S. Holbek, C. A. Villagomez-Hoyos, D. P. Bradway, M. B. Stuart, and B. G. Tomov (2016). “Safety Assessment of Advanced Imaging Sequences, I: Measurements”. In: *IEEE Trans. Ultrason., Ferroelec., Freq. Contr.* 63.1, pp. 110–119 (cit. on p. 52).

- Jensen, J. A. and N. B. Svendsen (1992). "Calculation of Pressure Fields from Arbitrarily Shaped, Apodized, and Excited Ultrasound Transducers". In: *IEEE Trans. Ultrason., Ferroelec., Freq. Contr.* 39, pp. 262–267 (cit. on p. 46).
- Jensen, J., M. B. Stuart, and J. A. Jensen (2015). "High Frame Rate Vector Velocity Estimation using Plane Waves and Transverse Oscillation". In: *Proc. IEEE Ultrason. Symp.* Pp. 1–4. DOI: 10.1109/ultsym.2015.0423 (cit. on p. 45).
- Lenge, M., A. Ramalli, P. Tortoli, C. Cachard, and H. Liebgott (2015). "Plane-Wave Transverse Oscillation for High-Frame-Rate 2-D Vector Flow Imaging". In: *IEEE Trans. Ultrason., Ferroelec., Freq. Contr.* 62.12, pp. 2126–2137 (cit. on p. 39).
- Salles, S., A. J. Y. Chee, D. Garcia, A. C. H. Yu, D. Vray, and H. Liebgott (2015). "2-D arterial wall motion imaging using ultrafast ultrasound and transverse oscillations". In: *IEEE Trans. Ultrason., Ferroelec., Freq. Contr.* 62.6, pp. 1047–1058. DOI: 10.1109/TUFFC.2014.006910 (cit. on p. 41).
- Swillens, A., L. Løvstakken, J. Kips, H. Torp, and P. Segers (2009). "Ultrasound simulation of complex flow velocity fields based on computational fluid dynamics". In: *IEEE Trans. Ultrason., Ferroelec., Freq. Contr.* 56.3, pp. 546–556. DOI: 10.1109/TUFFC.2009.1071 (cit. on p. 49).
- Udesen, J., F. Gran, K. L. Hansen, J. A. Jensen, C. Thomsen, and M. B. Nielsen (2008). "High Frame-Rate Blood Vector Velocity Imaging Using Plane Waves: simulations and preliminary experiments". In: *IEEE Trans. Ultrason., Ferroelec., Freq. Contr.* 55.8, pp. 1729–1743 (cit. on p. 39).
- Udesen, J., F. Gran, and J. A. Jensen (2005). "Fast Color Flow Mode Imaging Using Plane Wave Excitation and Temporal Encoding". In: *Proc. SPIE Med. Imag.* Vol. 5750, pp. 427–436 (cit. on p. 39).
- Udesen, J. and J. A. Jensen (2006). "Investigation of Transverse Oscillation Method". In: *IEEE Trans. Ultrason., Ferroelec., Freq. Contr.* 53, pp. 959–971 (cit. on pp. 39, 45).
- Varray, F. and H. Liebgott (2013). "An alternative method to classical beamforming for transverse oscillation images: Application to elastography". In: *IEEE 10th Int. Symp. Biomedical Imaging*, pp. 716–719. DOI: 10.1109/ISBI.2013.6556575 (cit. on p. 41).
- Villagomez-Hoyos, C. A. (2016). "Synthetic Aperture Vector Flow Imaging". PhD thesis. Technical University of Denmark. URL: <http://findit.dtu.dk/en/catalog/2347162876> (cit. on p. 45).
- Villagomez-Hoyos, C. A., M. B. Stuart, T. Bechsgaard, M. B. Nielsen, and J. A. Jensen (2016). "High frame rate synthetic aperture vector flow imaging for transthoracic echocardiography". In: *Proc. SPIE Med. Imag.* (Cit. on p. 45).
- Villagomez-Hoyos, C. A., M. B. Stuart, K. L. Hansen, M. B. Nielsen, and J. A. Jensen (2016). "Accurate Angle Estimator for High Frame Rate 2-D Vector Flow Imaging". In: *IEEE Trans. Ultrason., Ferroelec., Freq. Contr.* 63.6, pp. 842–853 (cit. on p. 56).
- Yiu, B. Y., S. S. Lai, and A. C. Yu (2014). "Vector projectile imaging: time-resolved dynamic visualization of complex flow patterns." In: *Ultrasound Med. Biol.* 40.9, pp. 2295–2309 (cit. on p. 39).

References from Chapter 5

- Ekroll, I. K., T. Dahl, H. Torp, and L. Løvstakken (2014). “Combined Vector Velocity and Spectral Doppler Imaging for Improved Imaging of Complex Blood Flow in the Carotid Arteries”. In: *Ultrasound Med. Biol.* 40.7, pp. 1629–1640 (cit. on p. 57).
- Hansen, K. L., H. Møller-Sørensen, J. Kjaergaard, M. B. Jensen, J. T. Lund, M. M. Pedersen, J. B. Olesen, J. A. Jensen, and M. B. Nielsen (2015). “Vector Flow Imaging Compared with Conventional Doppler Ultrasound and Thermodilution for Estimation of Blood Flow in the Ascending Aorta”. In: *Ultrasonic Imaging*, pp. 1–16. DOI: 10.1177/0161734615620137 (cit. on p. 57).
- Hansen, K. L., J. Udesen, F. Gran, J. A. Jensen, and M. B. Nielsen (2009). “In-vivo examples of flow patterns with the fast vector velocity ultrasound method”. In: *Ultraschall in Med.* 30, pp. 471–476 (cit. on p. 67).
- Hansen, K. L., J. Udesen, N. Oddershede, L. Henze, C. Thomsen, J. A. Jensen, and M. B. Nielsen (2009). “In vivo comparison of three ultrasound vector velocity techniques to MR phase contrast angiography”. In: *Ultrasonics* 49, pp. 659–667 (cit. on p. 57).
- Lai, S. S. M., B. Y. S. Yiu, A. K. K. Poon, and A. C. H. Yu (2013). “Design of Anthropomorphic Flow Phantoms Based on Rapid Prototyping of Compliant Vessel Geometries”. In: *Ultrasound Med. Biol.* 39.9, pp. 1654–1664 (cit. on pp. 57, 59).
- Pedersen, M. M., M. J. Pihl, P. Haugaard, J. M. Hansen, K. L. Hansen, M. B. Nielsen, and J. A. Jensen (2012). “Comparison of Real-Time In Vivo Spectral and Vector Velocity Estimation”. In: *Ultrasound Med. Biol.* 38.1, pp. 145–151 (cit. on p. 57).
- Swillens, A., J. Degroote, J. Vierendeels, L. Løvstakken, and P. Segers (2010). “A simulation environment for validating ultrasonic blood flow and vessel wall imaging based on fluid-structure interaction simulations: Ultrasonic assessment of arterial distension and wall shear rate”. In: *Medical Physics* 37.8, pp. 4318–4330. DOI: 10.1118/1.3462592 (cit. on p. 68).
- Tortoli, P., M. Lenge, D. Righi, G. Ciuti, H. Liebgott, and S. Ricci (2015). “Comparison of carotid artery blood velocity measurements by vector and standard Doppler approaches”. In: *Ultrasound Med. Biol.* 41.5, pp. 1354–1362. DOI: 10.1016/j.ultrasmedbio.2015.01.008 (cit. on pp. 57, 69).
- Villagomez-Hoyos, C. A., M. B. Stuart, K. L. Hansen, M. B. Nielsen, and J. A. Jensen (2016). “Accurate Angle Estimator for High Frame Rate 2-D Vector Flow Imaging”. In: *IEEE Trans. Ultrason., Ferroelec., Freq. Contr.* 63.6, pp. 842–853 (cit. on p. 67).

References from Chapter 6

- Babic, I., Z. M. Ferraro, K. Garbedian, A. Oulette, C. G. Ball, F. Moretti, and A. Gruslin (2015). “Intraplacental villous artery resistance indices and identification of placenta-mediated diseases”. In: *J. Perinatol.* 35.10, pp. 793–798. DOI: 10.1038/jp.2015.85 (cit. on p. 72).

- Dar, P., J. Gebb, L. Reimers, P. S. Bernstein, C. Chazotte, and I. R. Merkatz (2010). "First-trimester 3-dimensional power Doppler of the uteroplacental circulation space: a potential screening method for preeclampsia". In: *Am. J. Obstet. Gynecol.* 203.3, 238.e1–238.e7. DOI: 10.1016/j.ajog.2010.06.006 (cit. on p. 72).
- Demene, C., T. Deffieux, M. Pernot, B.-F. Osmanski, V. Biran, J.-L. Gennisson, L.-A. Sieu, A. Bergel, S. Franqui, J.-M. Correas, I. Cohen, O. Baud, and M. Tanter (2015). "Spatiotemporal clutter filtering of ultrafast ultrasound data highly increases Doppler and fUltrasound sensitivity". In: *IEEE Trans. Med. Imag.* 34.11, pp. 2271–2285. DOI: 10.1109/TMI.2015.2428634 (cit. on pp. 74, 82).
- Demene, C., M. Pernot, V. Biran, M. Alison, M. Fink, O. Baud, and M. Tanter (2014). "Ultrafast Doppler reveals the mapping of cerebral vascular resistivity in neonates". In: *J. Cerebr. Blood F. Met.* 34.6, pp. 1009–1017. DOI: 10.1038/jcbfm.2014.49 (cit. on p. 74).
- Gordon, Z., L. Glaubach, D. Elad, U. Zaretsky, and A. J. Jaffa (2016). "Ex Vivo Human Placental Perfusion Model for Analysis of Fetal Circulation in the Chorionic Plate". In: *J. Ultrasound Med.* 35.3, pp. 553–560. DOI: 10.7863/ultra.15.04080 (cit. on pp. 80, 82).
- Hansen, J. M., M. C. Hemmsen, and J. A. Jensen (2011). "An object-oriented multi-threaded software beamformation toolbox". In: *Proc. SPIE Med. Imag.* Vol. 7968, pages. DOI: 10.1117/12.878178 (cit. on p. 73).
- Lecarpentier, E., M. Bhatt, G. I. Bertin, B. Deloison, L. J. Salomon, P. Deloron, T. Fournier, A. I. Barakat, and V. Tsatsaris (2016). "Computational Fluid Dynamic Simulations of Maternal Circulation: Wall Shear Stress in the Human Placenta and Its Biological Implications". In: *Plos One* 11.1, e0147262. DOI: 10.1371/journal.pone.0147262 (cit. on p. 71).
- Mace, E., G. Montaldo, I. Cohen, M. Baulac, M. Fink, and M. Tanter (2011). "Functional ultrasound imaging of the brain". In: *Nature methods* 8.8, pp. 662–664. DOI: 10.1038/nmeth.1641 (cit. on p. 72).
- Marieb, E. N. and K. N. Hoehn (2007). *Human anatomy and physiology*. 7th ed. Pearson Education, Inc. (cit. on p. 72).
- Osmanski, B., E. Lecarpentier, G. Montaldo, V. Tsatsaris, P. Chavatte-Palmer, and M. Tanter (2015). "Discriminative imaging of maternal and fetal blood flow within the placenta using ultrafast ultrasound". In: *Scientific Reports* 5.13394, pp. 1–10. DOI: 10.1038/srep13394 (cit. on pp. 72, 82).
- Todros, T., E. Piccoli, A. Rolfo, S. Cardaropoli, C. Guiot, P. Gaglioti, M. Oberto, E. Vasario, and I. Caniggia (2011). "Review: Feto-placental vascularization: A multifaceted approach". In: *Placenta* 32.2, pp. 165–169. DOI: 10.1016/j.placenta.2010.12.020 (cit. on p. 72).
- Trudinger, B. J., W. B. Giles, C. M. Cook, J. Bombardieri, and L. Collins (1985). "Fetal umbilical artery flow velocity waveforms and placental resistance: clinical significance". In: *Br. J. Obstet. Gynaecol.* 92.1, pp. 23–30. DOI: 10.1111/j.1471-0528.1985.tb01044.x (cit. on p. 72).

- Yagel, S., E. Anteby, O. Shen, S. Cohen, Z. Friedman, and R. Achiron (1999). “Simultaneous multigate spectral Doppler imaging of the umbilical artery and placental vessels: novel ultrasound technology”. In: *Ultrasound Obstet. Gyn.* 14.4, pp. 256–261. DOI: 10.1046/j.1469-0705.1999.14040256.x (cit. on pp. 72, 80).
- Yu, A. C. H. and L. Løvstakken (2010). “Eigen-based clutter filter design for ultrasound color flow imaging: a review”. In: *IEEE Trans. Ultrason., Ferroelec., Freq. Contr.* 57.5, pp. 1096–1111. DOI: 10.1109/TUFFC.2010.1521 (cit. on p. 74).

References from Chapter 7

- Burns, P. N. (1992). “Measuring volume flow with Doppler ultrasound: An old nut”. In: *Ultrasound Obstet. Gyn.* 2.4, pp. 238–241. DOI: 10.1046/j.1469-0705.1992.02040237-2.x (cit. on p. 83).
- Evans, D. H. (1982). “Some aspects of the relationship between instantaneous volumetric blood flow and continuous wave Doppler ultrasound recordings III”. In: *Ultrasound Med. Biol.* 8, pp. 617–623 (cit. on p. 86).
- Gill, R. W. (1985). “Measurement of blood flow by ultrasound: Accuracy and sources of error”. In: *Ultrasound Med. Biol.* 11, pp. 625–641 (cit. on p. 83).
- Hansen, P. M., J. B. Olesen, M. J. Pihl, T. Lange, S. Heerwagen, M. M. Pedersen, M. Rix, L. Lønn, J. A. Jensen, and M. B. Nielsen (2014). “Volume Flow in Arteriovenous Fistulas using Vector Velocity Ultrasound”. In: *Ultrasound Med. Biol.* 40.11, pp. 2707–2714 (cit. on pp. 83, 88).
- Krivitski, N. M. (1995). “Theory and validation of access flow measurement by dilution technique during hemodialysis”. In: *Kidney Int.* 48.1, pp. 244–250 (cit. on p. 83).
- Picot, P. A. and P. M. Embree (1994). “Quantitative volume flow estimation using velocity profiles”. In: *IEEE Trans. Ultrason., Ferroelec., Freq. Contr.* 41, pp. 340–345 (cit. on pp. 83, 85, 86).
- Ricci, S., M. Cinthio, Å. Ahlgren, and P. Tortoli (2013). “Accuracy and Reproducibility of a Novel Dynamic Volume Flow Measurement Method”. In: *Ultrasound Med. Biol.* 39.10, pp. 1903–1914 (cit. on p. 83).
- Schwarz, C., C. Mitterbauer, M. Boczula, T. Maca, M. Funovics, G. Heinze, M. Lorenz, J. Kovarik, and R. Oberbauer (2003). “Flow monitoring: Performance characteristics of ultrasound dilution versus color Doppler ultrasound compared with fistulography”. In: *Am. J. Kidney Dis.* 42.3, pp. 539–545. DOI: 10.1016/s0272-6386(03)00786-8 (cit. on p. 83).
- Whittier, W. L. (2009). “Surveillance of hemodialysis vascular access”. In: *Seminars in Interventional Radiology* 26.2, pp. 130–138. DOI: 10.1055/s-0029-1222457 (cit. on p. 83).
- Wiese, P. and B. Nonnast-Daniel (2004). “Colour Doppler ultrasound in dialysis access”. In: *Nephrol. Dial. Transpl.* 19.8, pp. 1956–1963. DOI: 10.1093/ndt/gfh244 (cit. on p. 83).

Womersley, J. R. (1955). "Oscillatory motion of a viscous liquid in a thin-walled elastic tube. I: The linear approximation for long waves". In: *Phil. Mag.* 46, pp. 199–221 (cit. on p. 86).

Optimized Plane Wave Imaging for Fast and High-Quality Ultrasound Imaging

Jonas Jensen, Matthias Bo Stuart, and Jørgen Arendt Jensen

IEEE Trans. Ultrason., Ferroelec., Freq. Contr., vol. 63, no. 11, p. 1922 – 1934,
November 2016.

Optimized Plane Wave Imaging for Fast and High-Quality Ultrasound Imaging

Jonas Jensen, Matthias Bo Stuart, and Jørgen Arendt Jensen, *Fellow, IEEE*

Abstract—This paper presents a method for optimizing parameters affecting the image quality in plane wave imaging. More specifically, the number of emissions and steering angles is optimized to attain the best images with the highest frame rate possible. The method is applied to a specific problem, where image quality for a λ -pitch transducer is compared with a $\lambda/2$ -pitch transducer. Grating lobe artifacts for λ -pitch transducers degrade the contrast in plane wave images, and the impact on frame rate is studied. Field II simulations of plane wave images are made for all combinations of the parameters, and the optimal setup is selected based on Pareto optimality. The optimal setup for a simulated 4.1-MHz λ -pitch transducer uses 61 emissions and a maximum steering angle of 20° for depths from 0 to 60 mm. The achieved lateral full-width at half-maximum (FWHM) is 1.5λ and the contrast is -29 dB for a scatterer at 9 mm (24λ). Using a $\lambda/2$ -pitch transducer and only 21 emissions within the same angle range, the image quality is improved in terms of contrast, which is -37 dB. For imaging in regions deeper than 25 mm (66λ), only 21 emissions are optimal for both the transducers, resulting in a -36 dB contrast at 34 mm (90λ). Measurements are performed using the experimental SARUS scanner connected to a λ -pitch and $\lambda/2$ -pitch transducer. A wire phantom and a tissue mimicking phantom containing anechoic cysts are scanned and show the performance using the optimized sequences for the transducers. FWHM is 1.6λ and contrast is -25 dB for a wire at 9 mm using the λ -pitch transducer. For the $\lambda/2$ -pitch transducer, contrast is -29 dB. *In vivo* scans of the carotid artery of a healthy volunteer show improved contrast and present fewer artifacts, when using the $\lambda/2$ -pitch transducer compared with the λ -pitch. It is demonstrated with a frame rate, which is three times higher for the $\lambda/2$ -pitch transducer.

Index Terms—Medical ultrasound, ultrasonic imaging, plane wave imaging.

I. INTRODUCTION

CONVENTIONAL medical ultrasound images are acquired sequentially one image line at a time, which result in a limited frame rate and only an optimal focus at one depth. An alternative imaging method, which solves these issues, is synthetic aperture (SA) imaging using either spherical or plane wave emissions [1]. By using emissions with the wide areas of insonification, a low-resolution (LR) image is created for each emission; however, each LR image has low contrast [2]. To regain contrast, a number of LR images are combined to high-resolution (HR) images. There is, thus, a tradeoff between image quality and frame rate, but—as is

shown in this paper—good image quality can be attained with more than 200 frames/s. Images with dynamic transmit and receive focusing are generated in SA imaging, and any beam and focusing can be synthesized, while keeping the frame rate high. SA using spherical waves has been investigated for the excitation of multielement subapertures by O'Donnell and Thomas [3], Karaman *et al.* [4], [5], and Nikolov *et al.* [6] and for sparse SA systems by Lockwood *et al.* [7]. Tanter *et al.* [8], [9] and Lu [10] have made extensive research on plane wave imaging and its applications. Compared with conventional imaging, SA/plane wave imaging has shown to improve anatomical imaging [11], [12], flow estimation [13]–[19], elastography [8], and imaging of contrast agents [20]. In all of the applications, it is important to use as few emissions as possible to keep the frame rate high and still obtain high-quality images useful for the imaging of moving structures, for fast flow estimation, and for image segmentation. Therefore, the optimization of the imaging and transducer parameters should be performed to obtain the best tradeoff between frame rate and image quality. Specifically, for plane-wave imaging, the choice of maximum steering angle and number of emissions have a significant impact on the image quality, and Montaldo *et al.* [12] showed how to achieve images comparable with line-by-line imaging.

In addition to the number of emissions and steering angles, the transducer pitch relative to the wavelength λ should be considered. The spatial sampling of a transducer aperture into array elements with λ -pitch results in the aliasing of spatial frequencies. An unfocused emission from a transducer with a pitch equal to or larger than λ generates grating lobes in the emitted field within the image plane. It introduces artifacts in the beamformed image. Grating lobe artifacts can be suppressed by increasing the number of emissions at different steering angles at the cost of frame rate. However, a $\lambda/2$ -pitch transducer does not generate grating lobes and can, therefore, potentially increase the frame rate without compromising the image quality.

Small parts SA/plane-wave imaging in related work [11]–[20] has so far been conducted with commercially available λ -pitch transducers, which are actually intended for line-by-line imaging with no steering. The pitch size is a compromise between having a high center frequency and a wide aperture to get a large field of view for small parts imaging, and the limitation of 192–256 channels in commercial scanners. Therefore, a transducer with the same aperture size and a pitch around $\lambda/2$ can only be obtained by using more channels, a lower center frequency, or not sampling all elements.

Manuscript received May 8, 2016; accepted July 11, 2016. Date of publication July 18, 2016; date of current version November 1, 2016. This work was supported in part by the Danish National Advanced Technology Foundation under Grant 82-2012-4 and in part by BK Ultrasound Aps.

The authors are with the Center for Fast Ultrasound Imaging, Department of Electrical Engineering, Technical University of Denmark, DK-2800 Kgs. Lyngby, Denmark (e-mail: jonjensen@elektro.dtu.dk; mbs@elektro.dtu.dk; jaj@elektro.dtu.dk).

Digital Object Identifier 10.1109/TUFFC.2016.2591980

The key question is how to optimize all these parameters and at the same time balance frame rate and image quality. This paper presents a method for optimizing the number of plane wave emissions and maximum steering angles to obtain high-quality images in terms of resolution and contrast. It is a general design approach and can be applied for any transducer and imaging depth. The method is applied for a λ -pitch and $\lambda/2$ -pitch transducer, and it is shown how the frame rate can be increased without the loss of image quality by using a $\lambda/2$ -pitch transducer rather than a λ -pitch transducer. A preliminary version of the method has been presented in a conference publication [21], and this paper expands on the optimization procedure and presents an *in vivo* example.

In Section II, the emitted field for the plane wave propagation is considered. In Section III, metrics for evaluating the image quality are described, and the optimization method is presented. Section IV describes the simulations and implementation on the experimental scanner SARUS. The results from simulations, phantom measurements, and an *in vivo* scan of the carotid artery are presented in Section V. Discussion and conclusion follow in Sections VI and VII.

II. PLANE WAVE PROPAGATION

The first step in the optimization of plane wave images is to ensure the propagation of a plane wave is as desired. This includes an emitted field without grating lobes and edge waves. The angular response of the transducer elements determines the range in which plane waves can be steered, and for which acceptance angle the received responses should be used. It is transducer-dependent, and is therefore investigated through simulations and measurements in this section.

A. Grating Lobes and Edge Waves

The periodic nature of a transducer array, where the aperture is sampled into array elements, results in a beam pattern in the far field with the first grating lobe at an angle

$$\theta_g = \arcsin(\lambda/p + \sin(\theta_s)) \quad (1)$$

where λ is the wavelength, p is the transducer pitch, and θ_s is the steering angle of the beam off the center axis [22]. With a pitch of λ as for most commercial linear transducers, steering a plane wave -10° generates a grating lobe at 57° . This is shown in Fig. 1, where the top image shows the simulated emitted field for a fixed time using a λ -pitch array with no transmit apodization. A stream of energy behind the wave front is built up and travels in a direction 57° off axis [Fig. 1 (red arrow)]. The grating lobe has amplitudes around -25 dB relative to the main lobe, and the large spatial extent of the grating lobe in the near field results in artifacts. A pitch of half a wavelength is more desirable, because grating lobes are moved outside the imaging plane even for steered wave fronts, as shown in Fig. 1 (center image). The edge waves are the spherical waves, which are generated by the transducer edges. They can be suppressed in the emitted field by the use of apodization in transmit, and a Tukey apodization (weight 0.5) is efficient for this, as shown in the bottom image [15].

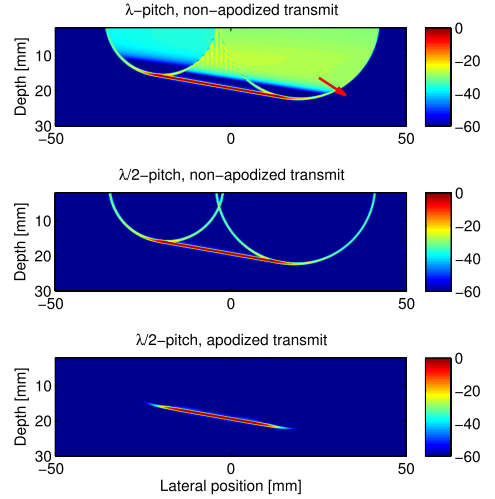


Fig. 1. Field II simulation of the emitted field, when a plane wave is emitted at -10° . For a λ -pitch array with no apodization in transmit (top image), $\lambda/2$ -pitch array (center image), and $\lambda/2$ -pitch array with Tukey (weight 0.5) window as transmit apodization (bottom image). Red arrow: direction of grating lobe propagation.

B. Angular Response of Elements

Every element has a directivity pattern, which determines the element's acceptance angle. This angle is related to how much an emitted plane can be steered, and to the minimum receive F -number used for beamforming. The angular response of the transducer elements is, therefore, investigated through simulations and measurements, and the results are used when optimizing the image quality. A model in [23] based on SNR considerations was used to determine the opening angle of a virtual source, and it is used in this paper to investigate the element acceptance angle. The amplitude drop and the phase error for emitted wave signals measured at different positions on an arc are used to determine whether the signals are valuable in an SNR sense. For an m -cycle pulsed wave of amplitude k , this is the case, when

$$\frac{1 - k^2}{2k} \leq \left(1 - \frac{\Delta\theta}{2\pi m}\right) \cos(\Delta\theta) - \frac{1}{2\pi m} \sin(\Delta\theta) \quad (2)$$

where $\Delta\theta$ is the phase error in radians between two signals [23]. The acceptance angle is at equality between the left-hand side (LHS) and right-hand side (RHS) of (2).

The emitted pressure field was simulated using the Field II program [24], [25]. A $\lambda/2$ -pitch transducer with parameters, as listed in Table I, was simulated, and this transducer will be used for imaging by emulating a pitch of λ and $\lambda/2$, as described in Section IV. A single element was excited in the simulations, and both a hard and soft baffle condition for the aperture were applied to determine which boundary condition for the aperture radiation is most appropriate [22]. The hard baffle condition assumes a rigid mounting, while

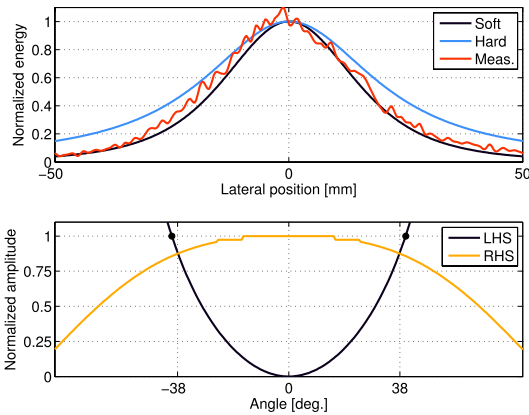


Fig. 2. Top: energy of the emitted field, when the center element is excited. The red curve is measured with a hydrophone, black and blue curves are simulations using a soft and hard baffle condition, respectively. Bottom: the LHS and RHS of (2) using simulation points on an arc 38 mm from the transducer.

the pressure on the baffle surface is assumed to be zero for the soft baffle condition. It is taken into account by a cos-factor in the radiation pattern [22]. The pressure field was also measured using an Onda HGL-0085 hydrophone, which has an acceptance angle $>150^\circ$ [26]. It was connected to the experimental scanner SARUS [27] and an in-house intensity measurement framework was used [28]. Each of the transducer elements was excited, one at a time, and the hydrophone scanned along the transducer 38 mm from the transducer surface (at the elevation focus).

Fig. 2 (top) shows the energy of the emitted field for the center element as a function of lateral position at the elevation focus. The red curve is the measured response, the blue curve is the simulation using a hard baffle condition, and the black curve is simulated using a soft baffle condition. The average error between simulation and measurement is 10.3% and 5.1%, when using the hard and soft baffle conditions, respectively, and the soft baffle condition is, therefore, used for the following simulations.

The good agreement between simulation and measurement allows using the simulated field for the further investigation of the acceptance angle. Since the energy of the emitted pressure drops by $1/r^2$, where r is the radial distance to the element, the emitted field should be calculated at a constant radial distance to properly estimate acceptance angle. The emitted pressure field was simulated for points on an arc at $r = 38$ mm from the center element, and the amplitude drop with respect to maximum amplitude on the arc and the phase error with respect to expected phase were estimated. The LHS and the RHS of (2) were then applied, and the result is shown in Fig. 2 (bottom). It shows that the acceptance angle is $\pm 38^\circ$ giving an F -number of 0.64. If only the amplitude drop k was taken into account and phase errors were assumed to be zero, (2) would reduce to $(1 - k^2)/2k \leq 1$. It gives an acceptance angle of $\pm 40^\circ$, which is shown in Fig. 2 (black dots).

III. OPTIMIZATION OF IMAGE QUALITY

This section presents performance metrics for evaluating the image quality, which are used for optimization of plane wave images.

A. Evaluation of Image Quality

Three performance measures for evaluating the image quality of the plane wave ultrasound images are used in this paper: the detail resolution, contrast resolution, and contrast-to-noise ratio (CNR). The detail resolution is quantified as the -6 dB width of the main lobe of the point-spread-function (PSF), i.e., the full-width at half-maximum (FWHM). It should be measured in the axial and lateral directions and is determined by the bandwidth of the system and the size of the aperture (F -number). Lateral FWHM is also dependent on the maximum steering angle of the emitted plane wave. The contrast resolution of a PSF is assessed through the cystic resolution, which describes the ability to detect an anechoic cyst in a uniform scattering medium. It quantifies the clutter energy outside the main lobe of the PSF and has been defined in [29] to be quantified as the ratio of the energy outside a circular region of radius R to the total PSF energy

$$\text{Contrast}(R) = \sqrt{\frac{E_{\text{out}}(R)}{E_{\text{total}}}} \quad (3)$$

where E_{out} is the PSF energy outside a circular region with radius R centered at the peak of the PSF and E_{total} is the total energy. To get a single number, one either determines the relative energy for a fixed radius R , or determines the required radius to observe a cyst at a fixed relative energy. In this paper, contrast is presented as the relative energy for a fixed radius of 2.5λ and $R_{2.5\lambda}$.

The CNR is used to quantify the image quality of a cyst, where the scattering level is different from the background

$$\text{CNR} = \frac{\mu_s - \mu_c}{\sqrt{\sigma_s^2 + \sigma_c^2}} \quad (4)$$

μ_c and μ_s are the mean intensities of envelope-detected signals from a region inside a cyst and a region of speckle, respectively, while σ_c^2 and σ_s^2 are the corresponding variances. The cyst and speckle regions are of the same size and at the same depth.

B. Method for the Optimization of Image Quality

The presented method for optimizing image quality relies on the theory of Pareto optimality [30], [31]. The theory is applicable for multiobjective optimization problems, where two or more objectives are to be optimized, and the aim is to find good compromises rather than a single optimum solution. The set of compromise solutions are known as Pareto optimal solutions and constitute a tradeoff between the objectives.

A solution $\mathbf{x} = \{x_1, x_2\}$ is Pareto optimal, if there exists no other \mathbf{x}' for which $\mathbf{v} = F(\mathbf{x}')$ dominates $\mathbf{u} = F(\mathbf{x})$, where F is the objective function. A set of objectives \mathbf{v} is dominating another set of objectives \mathbf{u} (written $\mathbf{v} \leq \mathbf{u}$) if \mathbf{v} is no worse than \mathbf{u} in all objectives, and \mathbf{v} is strictly better than \mathbf{u} in at

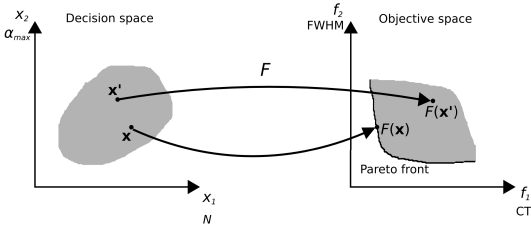


Fig. 3. Illustration of the decision space containing the independent variables x_1 and x_2 , and the objective space with the dependent variables F_1 and F_2 . For the current optimization problem, the number of emissions N and max steering angle α_{\max} are used in the decision space, while contrast and FWHM are the objectives. Black curve: Pareto front for a minimization problem.

least one objective. Thus, a Pareto optimal solution is defined as

$$\mathcal{P}^* := \{\mathbf{x} \mid \nexists \mathbf{x}' : F(\mathbf{x}') \leq F(\mathbf{x})\}. \quad (5)$$

All Pareto optimal solutions are collectively called the Pareto front. An example of a Pareto front is shown in Fig. 3 as the black curve in the objective space.

The Pareto front is interesting for optimization purposes, because it represents solutions where it is impossible to improve one of the variables without worsening the other. Thereby, attention can be restricted only to solutions that are Pareto optimal, wherein tradeoffs can be made, rather than considering all the solutions.

For the current optimization problem, the purpose is to optimize plane wave images for small parts imaging in a sector directly below the transducer. It corresponds to the imaged region in line-by-line imaging with no steering of the beam. Point targets are simulated individually at 9, 20, 34, 44, and 60 mm depth placed in a grid along the center line and 10 mm laterally. The independent variables to optimize are the number of plane wave emissions, N , and the maximum steering angle, α_{\max} . The image quality is evaluated with respect to the lateral FWHM and contrast, which are thereby the dependent variables (or objectives). The objective function F is the mapping of N and α_{\max} to FWHM and contrast. An automatic approach in MATLAB is used to construct a Pareto front for each point target by using several \mathbf{x} (i.e., all combinations of N and α_{\max} for a given image of the point target) and calculating the corresponding FWHM and contrast. Special attention is drawn to the knee-point solution on the Pareto front, because it represents a good tradeoff between FWHM and contrast. Pareto optimal solutions and knee-point solutions will be considered for each point target to include depth dependence. It is required that image quality in terms of contrast and FWHM is improved or comparable with conventional line-by-line imaging. This is explained in more detail in Section V-A.

IV. METHODS FOR SIMULATIONS AND EXPERIMENTS

This section describes the simulation method and how the imaging approach has been implemented on the experimental

TABLE I
PARAMETERS USED FOR SIMULATION AND MEASUREMENTS

Parameter	λ -pitch transducer	$\lambda/2$ -pitch transducer
Number of elements	96	192
Center frequency f_0	4.1 MHz	4.1 MHz
Wavelength λ	0.376 mm	0.376 mm
Element pitch	0.4 mm (1.06λ)	0.2 mm (0.53λ)
Element height	6 mm	6 mm
Elevation focus	38 mm	38 mm
Cycles m in emitted pulse	1	1
Transmit apodization	Tukey (weight 0.5)	Tukey (weight 0.5)
Receive apodization	Hamming	Hamming
Receive F-number	1	1
Max angle	$\pm 38^\circ$	$\pm 38^\circ$

scanner SARUS. Measurements have been conducted on phantoms and *in vivo* on a healthy volunteer.

A. Simulations

The simulations of RF data were performed in Field II using two transducers with parameters, as listed in Table I. The transducer pitches were 1.06λ and 0.53λ , respectively, due to the experimental equipment available, but are still referred to as λ and $\lambda/2$ -pitch. The $\lambda/2$ -pitch transducer has twice as many elements as the λ -pitch transducer to obtain the same aperture width. Ten point targets were simulated at axial distances 9 mm (24λ), 20 mm (53λ), 34 mm (90λ), 44 mm (117λ), and 60 mm (160λ) and placed along the center line of the transducer and 10 mm (27λ) laterally. The depths correspond to wire positions in a scanned phantom. A Tukey apodization (weight 0.5) on the active transmit aperture was applied to reduce artifacts from the edge waves. The receive F-number was set to 1, which was in accordance with the investigated angular response of the elements (see Section II-B). Plane wave emissions uniformly distributed between maximum steering angles of -38° and $+38^\circ$ were simulated. The smallest angle step was 0.25° . Received signals from all elements were stored for each emission and beam formation was performed using the BFT3 toolbox [32]. The beamformed LR images were subsequently combined to HR images by the summation of IQ-data and using all the combinations of α_{\max} and N .

Conventional line-by-line imaging with dynamic receive focusing was also simulated using the $\lambda/2$ -pitch transducer, 129 focused emissions with 64 active elements, and an F-number of 2 in transmit. The same transmit and receive apodization was used as for plane wave imaging.

B. Measurement Setup

A B-mode imaging sequence was implemented on the experimental scanner SARUS [27] using the parameters listed in Table I. An interleaved sequence with emissions for the $\lambda/2$ -pitch and λ -pitch transducers was used with a pulse repetition frequency of 5 kHz. A linear array transducer was employed and has the same parameters as the $\lambda/2$ -pitch transducer in Table I. By exciting the first and second element simultaneously, the third and fourth element simultaneously,

and so forth, a λ -pitch transducer with 96 elements is emulated in transmit. For receive, stored channel data from element one and two, three and four, and so on were averaged to emulate the λ -pitch transducer. A water tank phantom containing five wires was scanned and the speed of sound was set according to the water temperature. A multitissue contrast phantom containing anechoic cysts (Model 040GSE, CIRS Inc., Virginia, USA) with tissue attenuation of 0.5 dB/(cm·MHz) was also scanned.

C. Intensity and Temperature Measurement Setup

The intensity and the mechanical index (MI) were measured for the *in vivo* sequence using the Acoustic Intensity Measurement System AIMS III (Onda, Sunnyvale, CA, USA) with an Onda HGL-0400 hydrophone. It was connected to the SARUS scanner, and an in-house intensity measurement framework was used [28].

Transducer surface temperature rise was measured with the probe in contact with the multitissue contrast phantom and a thermocouple attached to the probe surface. The sequence was run for 30 min with an excitation voltage of 100 V.

D. In Vivo Measurement Setup

The SARUS scanner and a commercial transducer were used with the same imaging sequence as for the phantom measurements. The pulse repetition frequency was 5 kHz, the maximum steering angle α_{\max} was 22°, and the number of emissions N was 89. A cross-sectional scan of a straight part of the right common carotid artery was performed on a healthy volunteer; 3 s of data were acquired, giving 90 frames of HR images.

V. RESULTS

This section presents simulation results from the optimization study, results from phantom measurements, intensity measurements, and an *in vivo* scan.

A. Simulation Results

1) *Optimization*: The proposed optimization procedure is applied separately for each of the ten point targets simulated with the λ -pitch and $\lambda/2$ -pitch transducers. In the following, results are shown for a point target at 34 mm simulated with the λ -pitch transducer. It provides as an example of the procedure and its results.

Lateral FWHM and the contrast of HR images with all the combinations of α_{\max} and N for the point target at 34 mm depth are shown in Fig. 4 (left) and (right), respectively. Axial FWHM was approximately λ in all cases. There is an asymptotic behavior of lateral FWHM when increasing α_{\max} , and the same for the contrast when increasing N . The number of considered HR images has been limited by requiring an improvement in FWHM when increasing α_{\max} , and an improvement in contrast when increasing N . Here, an improvement of 2.5% in FWHM was required when steering 2° more, and an improvement of 1% in contrast when using four more emissions. Local extrema were thus allowed.

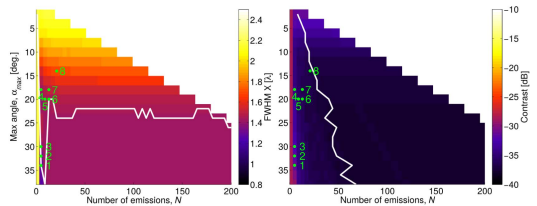


Fig. 4. Image quality of a point target at 34 mm for all the combinations of N and α_{\max} using the λ -pitch transducer. Left: FWHM. Right: contrast. White curves: borderlines, where increasing α_{\max} more will not give an improvement in FWHM as required, and increasing N will not improve CT. Green dots: Pareto optimal solutions, which can be identified in Fig. 5.

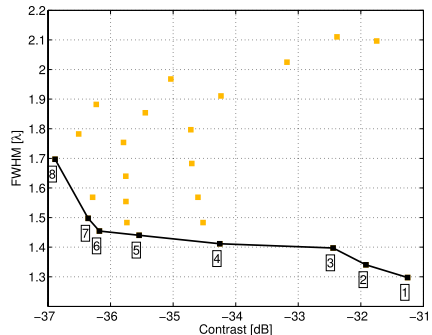


Fig. 5. Scatter plot of FWHM-contrast pairs from the simulated images at 34 mm for the λ -pitch transducer. Black squares: Pareto optimal solutions. Black curve: Pareto front. The eight labeled Pareto solutions can also be identified in Fig. 4.

The borderlines, where the requirements are no longer fulfilled, are shown in Fig. 4 (white curves). Other values and requirements could also have been used, e.g., cutoff at a threshold or at a specified image quality.

The results in Fig. 4 of FWHM and contrast from the λ -pitch transducer are used to construct the scatter plot, as shown in Fig. 5. A Pareto front is also constructed based on the criteria of minimizing FWHM and contrast, as explained in Section III-B. The eight resulting Pareto solutions are labeled 1–8 and can also be identified with corresponding N and α_{\max} in Fig. 4 (green dots).

The proposed optimization method does not result in a final optimal setup to use for all depths. However, a Pareto front is generated for each of the simulated point targets, and attention should, therefore, be drawn to all solutions on the Pareto front for the individual point targets. It is accommodated by plotting the maximum steering angles and the number of emissions corresponding to the Pareto optimal solutions. It is shown for point targets along the center line of the transducer in Fig. 6. The figures give an overview of the Pareto optimal solutions in addition to the knee-point solutions from the Pareto front (marked with asterisks). The Pareto optimal solutions for point targets at 34, 44, and 60 mm are mainly placed in the bottom-left corner of the figures, i.e., $10^\circ \leq \alpha_{\max} \leq 20^\circ$

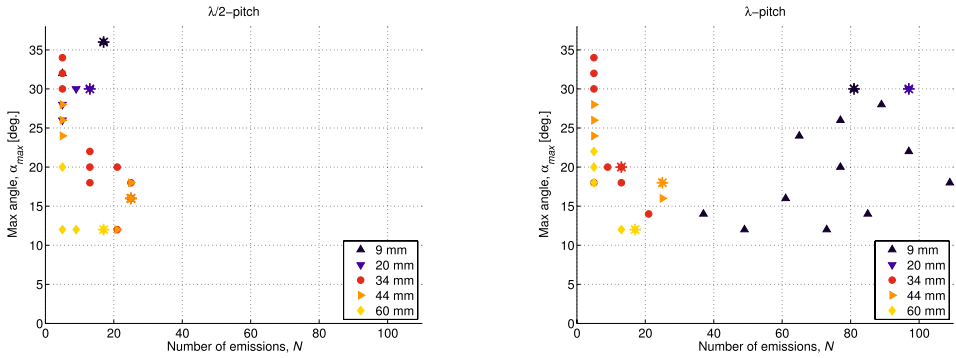


Fig. 6. Maximum steering angles α_{\max} and the number of emissions N corresponding to Pareto optimal solutions on the Pareto fronts are shown for each depth along the centerline for the $\lambda/2$ -pitch (left) and λ -pitch transducer (right). Knee-point solution from the Pareto fronts are marked with asterisks. Knee points for 34 and 44 mm are on the top of each other in the left figure.

and $10 \leq N \leq 20$. Closer to the transducer, a larger α_{\max} and the same number of emissions are beneficial for the $\lambda/2$ -pitch transducer, but for the λ -pitch transducer, the number of emissions is higher ($N > 60$).

Fig. 6 reveals in which angle span and emission span the Pareto optimal solutions are for the different depths. Tradeoffs can then be made among the setups by considering FWHM and contrast for the different combinations of α_{\max} and N . A setup of $\alpha_{\max} = 20^\circ$ and $N = 21$ for both transducers would result in similar image quality for regions deeper than 25 mm (66 λ), e.g., the contrast is 36 dB at 34 mm. A setup for the $\lambda/2$ -pitch transducer could be $\alpha_{\max} = 36^\circ$ and $N = 19$, which is at the top-right corner of the points in Fig. 6 (left). However, within this angle span, almost half of the emissions would be outside the optimal $\pm 20^\circ$ span for scatterers deeper than 30 mm, thereby not having $N = 21$. Either N can be doubled, or if a 0.4 λ reduction in FWHM can be accepted at 9 mm, α_{\max} can be set to 20° and $N = 21$. The 9-mm case with large α_{\max} is studied in more detail in Section V-A2. The contrast at 9 mm is -37 dB and FWHM = 1.5 λ using this setup, as shown in Fig. 7 (left). To balance frame rate and image quality at depths from 0–60 mm for the λ -pitch transducer, a single setup of 61 emissions and $\alpha_{\max} = 20^\circ$ is suggested. It gives a contrast of -29 dB at 9 mm. If only 21 emissions were used, the contrast would degrade by 15 dB and the image quality would be worse than line-by-line imaging. This is mainly due to grating lobe artifacts. Using 61 (λ -pitch) rather than 21 emissions ($\lambda/2$ -pitch) improves contrast by 1–2 dB in regions deeper than 30 mm. The chosen setups also give acceptable image quality for point targets at 10 mm laterally [see Fig. 7 (right)]. The focal point for line-by-line imaging is at 25 mm (F -number of 2 in transmit), thus, the minimum values of FWHM and contrast are attained around this depth.

Note that the Pareto optimal solutions at 30–60 mm can still be obtained by combining only the LR images corresponding to a Pareto optimal setup [e.g., $\alpha_{\max} = 12^\circ$ and $N = 17$ for (0 and 60) mm λ -pitch]. This can be done for each depth when

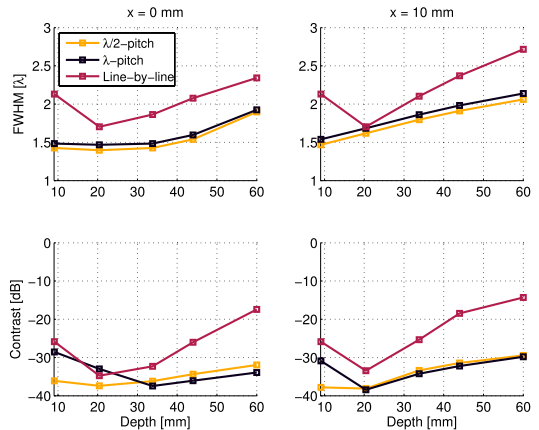


Fig. 7. FWHM (top) and contrast (bottom) for scatterers at 9–60 mm depth along center line, $x = 0$ mm (left) and along $x = 10$ mm (right). Simulations using a $\lambda/2$ -pitch transducer (yellow), λ -pitch transducer (black), and line-by-line imaging (red). The setup is $\alpha_{\max} = 20^\circ$ and $N = 21$ ($\lambda/2$ -pitch) and $N = 61$ (λ -pitch).

forming the HR images. Examples of simulated PSFs for the λ -pitch and $\lambda/2$ -pitch transducers are shown in Fig. 8 with a dynamic range of 60 dB, $\alpha_{\max} = 20^\circ$, and $N = 21$. Due to the grating lobes in the emitted field for the λ -pitch transducer, the image contains artifacts to a depth of 25 mm below the PSFs and off to the sides.

2) *Element Pitch*: The simulations show that the λ and $\lambda/2$ -pitch transducers can obtain similar image quality with contrast < -30 dB for depths higher than 25 mm using the same setups. The challenge is to obtain acceptable contrast closer to the transducer, where the $\lambda/2$ -pitch transducer has a 10–15 dB better contrast than the λ -pitch transducer. Fig. 9 shows contrast for a point target at 9 mm for all the combinations of N and α_{\max} , and FWHM is shown for $N = 21$. For λ -pitch, contrast can only be improved to less than -30 dB using a relative small α_{\max} around 10° , while the $\lambda/2$ -pitch

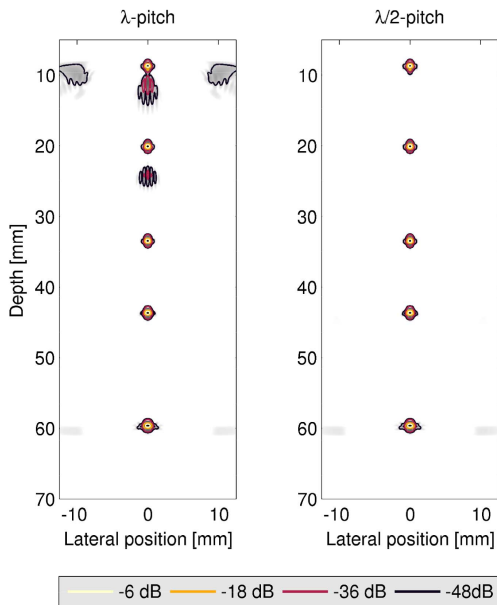


Fig. 8. Simulated PSFs using a λ -pitch (left) and $\lambda/2$ -pitch transducer (right). Maximum steering angle is 20° and 21 emissions are used. Dynamic range is 60 dB.

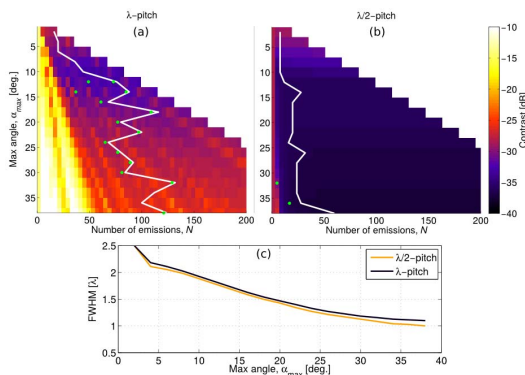


Fig. 9. Image quality of a point target at 9 mm for all the combinations of N and α_{\max} . (a) and (b) Contrast is shown for (a) λ -pitch transducer and (b) $\lambda/2$ -pitch transducer. FWHM is shown in (c) for $N = 21$. White curves: borderlines. Green dots: Pareto optimal solutions.

attains contrast < -30 dB for larger angles. Increasing α_{\max} from 20° to 38° improves FWHM by 0.4λ for both transducers, and does not improve the contrast for $\lambda/2$ -pitch. This combination could be interesting for very shallow imaging.

The influence of element pitch on contrast is shown in Fig. 10. Contrast is shown as a function of N for several pitch-sizes using $\alpha_{\max} = 20^\circ$. The point target is at 9 mm depth, where image quality is affected by grating lobes.

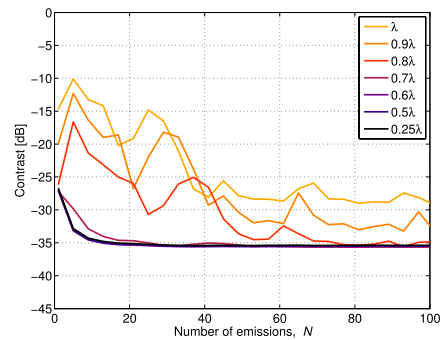


Fig. 10. Contrast as a function of N for several pitch-sizes. A point target was simulated at 9 mm depth and α_{\max} was 20° .

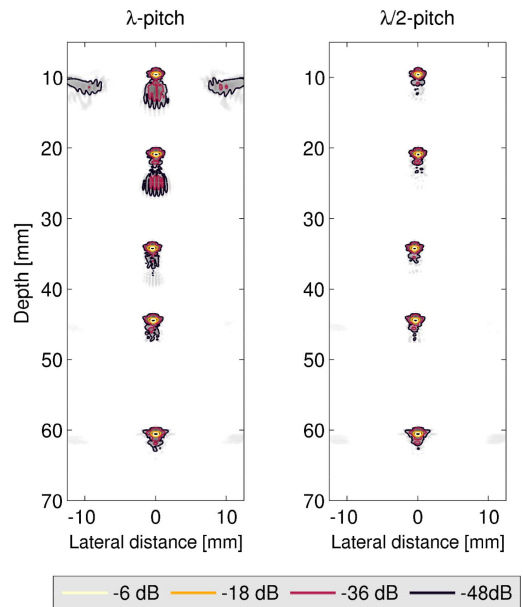


Fig. 11. Measured B -mode image of the wire phantom using the λ -pitch transducer (left) and the $\lambda/2$ -pitch transducer (right), and 21 emissions with $\alpha_{\max} = 20^\circ$. The dynamic range is 60 dB.

The curves for pitch $0.25 - 0.6\lambda$ are on the top of each other, indicating similar performance, while a 0.7λ -pitch performs slightly worse for a low number of emissions. Pitches of 0.8 and 0.9λ give CT-levels in-between the levels of a $\lambda/2$ -pitch and λ -pitch transducer.

B. Experimental Results

A scan of the wire phantom is shown in Fig. 11 for the λ -pitch and $\lambda/2$ -pitch transducers. The optimized setup for the $\lambda/2$ -pitch transducer is used ($N = 21$ and $\alpha_{\max} = 20^\circ$). For the λ -pitch transducer, off-axis energy lobes and artifacts

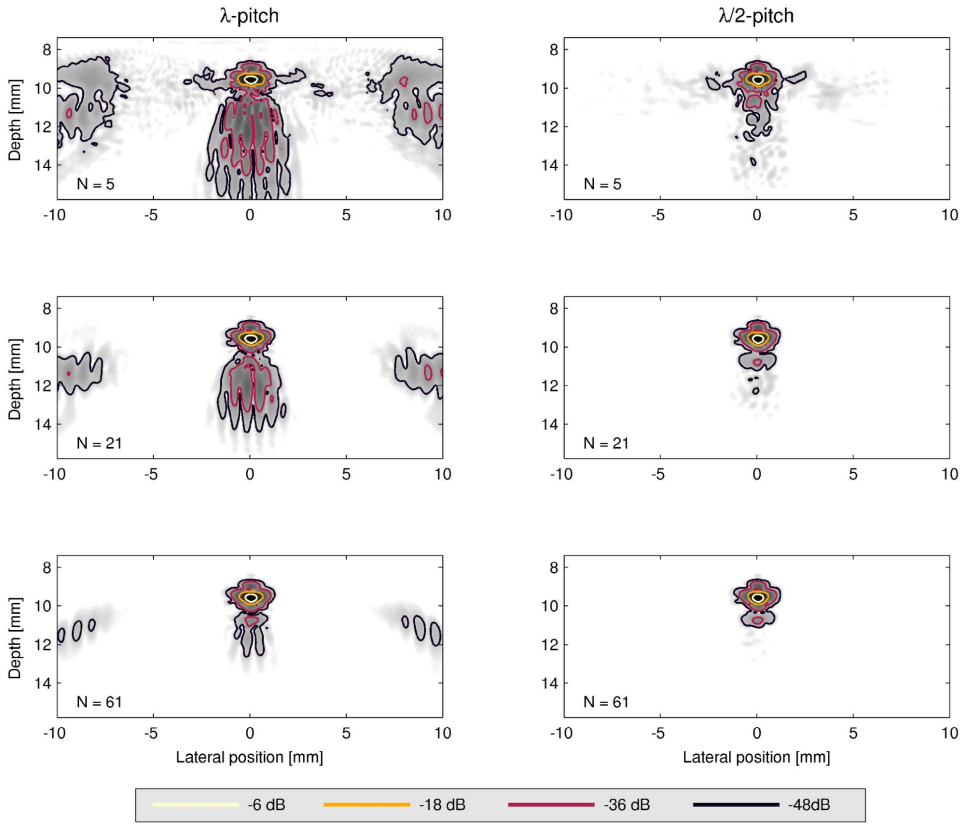


Fig. 12. Measured PSFs at 9 mm depth. Figures in the left column are for the λ -pitch transducer and in the right column for the $\lambda/2$ -pitch transducer. The number of emissions, N , is 5 (top), 21 (center), and 61 (bottom). The maximum steering angle is 20° , and the images have a dynamic range of 60 dB.

below the wires at 9 and 20 mm degrade the image quality compared with using the $\lambda/2$ -pitch transducer.

The measured PSF at a depth of 9 mm is shown in Fig. 12, where the number of emissions has been varied for the λ -pitch (left images) and $\lambda/2$ -pitch transducer (right images). For the $\lambda/2$ -pitch transducer, no or negligible grating lobe artifacts are present even for a low number of emissions, while increasing the number of emissions for the λ -pitch transducer only partly reduces the artifacts. Contrast is quantified as a function of N for the PSFs at 9 and 34 mm in Fig. 13, where $\alpha_{\max} = 20^\circ$. Measurements are in accordance with simulations for the λ -pitch transducer at 9 mm, and the same trend for the curves of measurement and simulation is obtained for the other cases. However, there is an 8–10 dB difference between simulations and measurements for the $\lambda/2$ -pitch transducer at 9 mm and for both transducers at 34 mm. This is primarily because of additional clutter just behind the measured PSF, which is discussed in Section VI.

In Fig. 14, measurements of the cyst phantom are shown. A similar degraded image quality, as in Fig. 12, is observed for the cyst at 17 mm, when using the λ -pitch transducer and

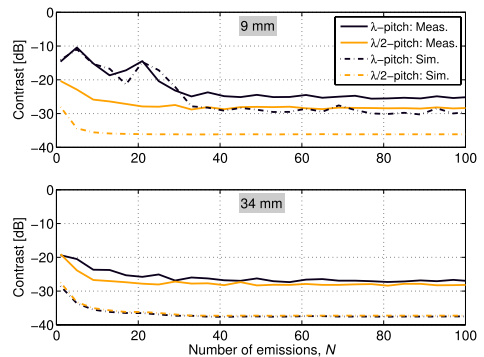


Fig. 13. Contrast as a function of the number of emissions N for $\alpha_{\max} = 20^\circ$. For a PSF at 9 mm (top) and at 34 mm (bottom). Contrast is shown for the λ and $\lambda/2$ -pitch transducers for simulated and measured data.

21 emissions (left image). This should be compared with using 61 emissions (center image) and the $\lambda/2$ -pitch transducer using 21 emissions (right image). Similar image quality is

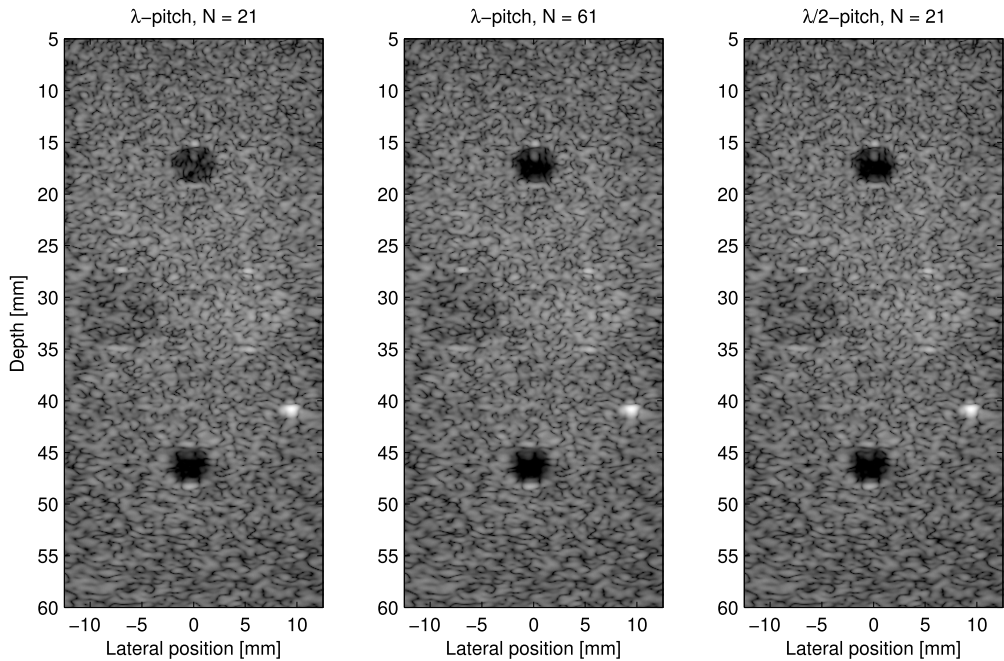


Fig. 14. Plane wave imaging of an anechoic cyst embedded in a tissue mimicking phantom. The left and center images are for the λ -pitch transducer and the right image is for the $\lambda/2$ -pitch transducer. The number of emissions, N , is 21, 61, and 21 for the three figures, respectively. The maximum steering angle is 20° .

TABLE II
CNR FOR THE CYSTS IN FIG. 14

Depth of cyst	λ , $N = 21$	λ , $N = 61$	$\lambda/2$, $N = 21$
17 mm	1.54	1.62	1.67
47 mm	2.10	2.08	2.05

obtained in deeper regions. CNR for the cysts is shown in Table II.

C. Intensities and Temperatures

The derated spatial peak, temporal average intensity $I_{spta,3}$, was measured to be 92.5 mW/cm^2 for the *in vivo* scan sequence, and the derated MI was 1.03. This is within FDA limits, which are 720 mW/cm^2 and 1.9. The transducer surface temperature rise was measured to be $7.5 \text{ }^\circ\text{C}$ for an excitation voltage of 100 V and 30 min of scan. This is within IEC limits of $10 \text{ }^\circ\text{C}$ temperature rise for 30 min scan.

D. In Vivo Results

Cross-sectional scans of the carotid artery on a healthy volunteer are shown in Figs. 15 and 16 using 21 and 61 emissions, respectively. The images are taken from frame 28 in the accompanying videos [14]. The image quality is degraded for the λ -pitch transducer, due to clutter from grating lobe artifacts appearing inside the vessel lumen. This is especially apparent when using 21

emissions. In the video [14] for the λ -pitch transducer, it looks like a valve is moving in the bottom-left corner of the artery lumen. This is, however, an artifact that might arise from a combination of vessel wall movement and the grating lobe artifacts generated by the transducer.

The image quality is improved when using 61 emissions with the λ -pitch transducer. However, there is still clutter inside the vessel, which is significantly reduced on the image for the $\lambda/2$ -pitch transducer. The increased amount of clutter in images by the λ -pitch transducer could in the worst case lead to a false positive diagnosis, if the medical doctor interpreted the clutter as being related to a plaque in the vessel.

VI. DISCUSSION

High-quality plane wave imaging requires precise calculation of delays in beamforming, good interpolation, and appropriate selection of receive F -number, plane wave steering angles, and number of emissions. It will reduce sidelobe levels and enhance contrast in the image. Good control over the emitted plane wave front should be ensured using, e.g., a $\lambda/2$ -pitch array to avoid grating lobes, which would otherwise result in artifacts outside the main response of the PSF. An optimization method was used to select the steering angles and number of emissions for imaging with a λ and $\lambda/2$ -pitch array. The method can be applied for any transducer and imaging region, and it reduces the number of possible setups, so the user only has to make decisions among Pareto

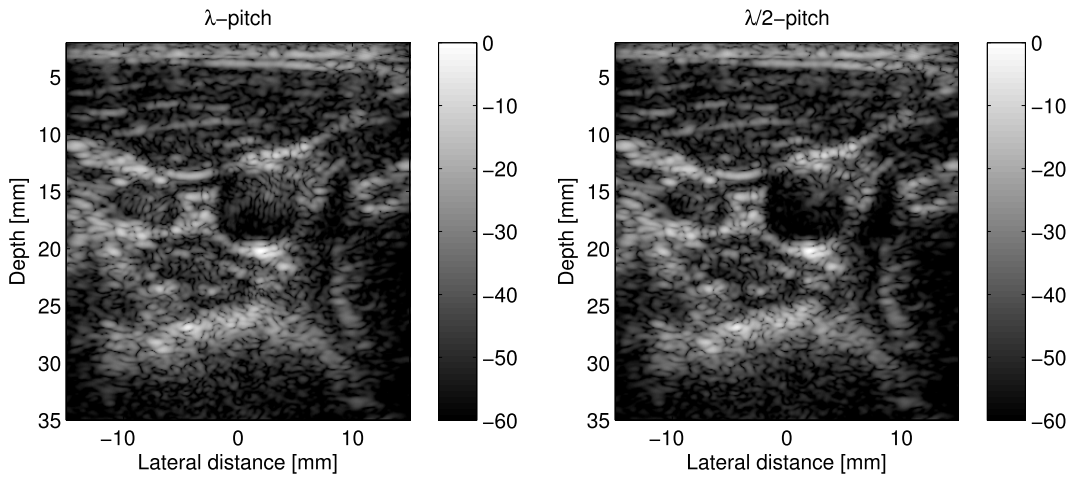



Fig. 15. *In vivo* cross-sectional images of the carotid artery using 21 emissions and $\alpha_{\max} = 20^\circ$. For the λ -pitch transducer (left) and $\lambda/2$ -pitch transducer (right). The video sequence is included here .

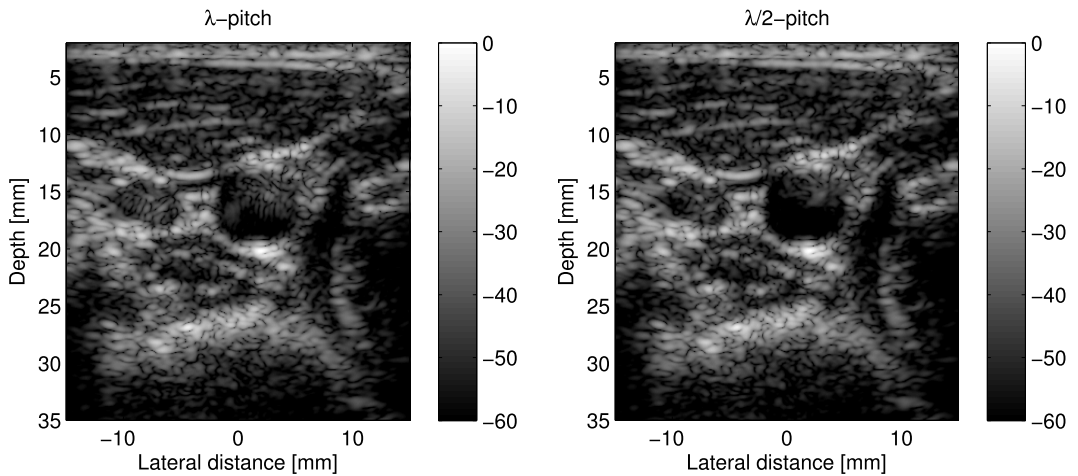



Fig. 16. *In vivo* cross-sectional images of the carotid artery using 61 emissions and $\alpha_{\max} = 20^\circ$. For the λ -pitch transducer (left) and $\lambda/2$ -pitch transducer (right). The video sequence is included here .

optimal setups.

The optimization study showed that the best image quality for a $\lambda/2$ -pitch transducer could be attained close to the transducer surface, where a large steering of the plane wave was advantageous using 21 emissions. If the pulse repetition frequency is 5 kHz, the sequence produces 238 frames/s. However, the λ -pitch did not provide a contrast resolution as good as line-by-line imaging, unless the number of emissions was increased to 61. For higher depths for both transducers, the region of overlap for emitted plane waves is restricted to smaller steering angles, which limits the obtainable resolution and contrast. The resulting image qualities obtained for the λ and $\lambda/2$ -pitch transducers are similar in regions deeper

than 25 mm. In a study by Montaldo *et al.* [12], a good compromise was found between contrast and frame rate for a λ -pitch array using $N = 45$ and $\alpha_{\max} = 11^\circ$. This was at the expense of a reduced FWHM and by allowing edge waves from an unapodized transmit array. Another challenge in plane wave and SA imaging can be intermission motion of tissue, especially when a high number of emissions are used for each HR image. This can, however, be compensated for [33] and [34].

The comparison between the measurement and simulation of the emitted field for a single-element emission resulted in a smaller error, when using a soft baffle condition in the simulations compared with using a hard baffle. The

boundary condition depends on which transducer is used and the medium. Delannoy *et al.* [35] found good agreement with the soft baffle condition for a transducer held in air against a tissue boundary, while Pesque and Fink [36] found an intermediate result between the two conditions. If only amplitude is considered for acceptance angle estimation, the angle is $\pm 40^\circ$, while it reduces to $\pm 38^\circ$, when phase errors also are taken into consideration. For beamformation, it is important to consider both amplitude drop and phase errors of the signals, because including signals out of phase for beamforming can deteriorate the image [23]. For transmission, steering plane waves more than $\pm 38^\circ$ will not lead to the expected plane wavefront and not improve the image quality.

Measurements on the wire phantom confirmed findings from the simulations. However, the HR images contained clutter behind the wire even for the $\lambda/2$ -pitch transducer, which was not in accordance with simulations. It resulted in a degraded contrast for measurements compared with simulations, as shown in Fig. 13. The clutter behind the wire can be due to a long impulse response of the transducer. It can also be related to artifacts arising from quantization of the transmit delay profile at 70 MHz [37], which is an ongoing investigation. Quantization effects vary with element pitch, and contrast for the λ -pitch transducer can be affected by both spatial and temporal quantization effects. Field II uses continuous time simulation for the impulse responses, thus, eliminating transmit quantization effects. The two peaks in Fig. 13 for the 9-mm λ -pitch case are also interesting, because it shows that using more emission angles not necessarily improves contrast. Location of grating lobe artifacts on the LR images vary with steering angle and changes the region of overlap of artifacts among LR images.

The illustration of the PSF in Fig. 12 includes a case of using only five emissions, which would be too few for a *B*-mode image, but it is a realistic number for flow estimation [38]. However, the contrast is clearly degraded for the λ -pitch transducer, and the peak amplitude of the artifacts is around -22 dB, which is undesirable and will give false flow velocities, if the vessel wall is moving. In particular, it is a challenge in small parts imaging, because the λ -pitch transducer gives artifacts at depths from 0–25 mm, which is the region of interest. It has been shown in this paper, that high-quality images with good resolution and contrast can be made with $\lambda/2$ -pitch transducers at a very high frame rate. This is important, e.g., for vector velocity estimation, where the standard deviation of the velocity estimates is related to the frame rate [23].

Using a transducer pitch of $\lambda/2$ comes at the expense of having twice as many channels compared with λ -pitch, if the aperture width has to be maintained. Another consideration is the transducer kerf, which is limited by the manufacturing process for piezo transducers. The total kerf area and the inactive material are thereby doubled for a $\lambda/2$ -pitch compared with a λ -pitch transducer. It results in an emitted field of reduced energy. This can be compensated for by having even more elements and/or use capacitive micromachined ultrasonic transducers [39], which allows a smaller kerf. Another compromise could be a pitch around $0.6\text{--}0.7\lambda$,

which gives an acceptable image quality at 10 mm depth (see Fig. 10).

Recently, image quality in SA imaging was investigated using a $\lambda/2$ -pitch transducer, and slightly improved contrast was obtained for the same number of emissions when using $\lambda/2$ -pitch rather than λ -pitch [40]. Other methods for avoiding grating lobes in SA/plane wave imaging have previously been proposed. They are based on sparse aperture techniques and special apodizations of the array [7], [41], or modulating receive beams [42]. A disadvantage with these methods is the reduced transmitted energy, and that the transmit grating lobes are not always avoided. By using $\lambda/2$ -pitch arrays as suggested in this paper, the sampling theorem is fulfilled and grating lobes are completely avoided.

VII. CONCLUSION

A method has been suggested for the optimization of the steering angles and the number of emissions for plane wave imaging, where at the same time frame rate and image quality are balanced. The method was applied for the λ -pitch and $\lambda/2$ -pitch transducers, and image quality and frame rate were compared for simulations, phantom measurements, and *in vivo* scans. Image quality was degraded to a depth of 25 mm for a λ -pitch compared with $\lambda/2$ -pitch transducer, because grating lobes in the emitted field for the λ -pitch transducer resulted in artifacts in the beamformed image. Grating lobes were avoided for the $\lambda/2$ -pitch transducer, and therefore, fewer emissions were needed to obtain the same or even better image quality. The optimization study showed that the number of emissions could be decreased from 61 to 21 by using a $\lambda/2$ -pitch rather than a λ -pitch transducer. Thus, with a pulse repetition frequency of 5 kHz, more than 200 frames/s are obtained. The achieved FWHM was 1.5λ and the contrast at $R_{2.5\lambda}$ was -37 dB for a point target at 9 mm. For imaging in regions deeper than 25 mm, only 21 emissions were optimal for both transducers, resulting in -36 dB contrast at 34 mm. Wire and cyst phantom measurements confirmed trends from the simulation study. *In vivo* scans showed improved contrast, and fewer artifacts were observed for a cross-sectional view of the carotid artery, when using the $\lambda/2$ -pitch transducer.

REFERENCES

- [1] J. J. Flaherty, K. R. Erikson, and V. M. Lund, "Synthetic aperture ultrasonic imaging systems," U.S. Patent 3548642, Dec. 22, 1970.
- [2] J. A. Jensen, S. I. Nikolov, K. L. Gammelmark, and M. H. Pedersen, "Synthetic aperture ultrasound imaging," *Ultrasonics*, vol. 44, pp. e5–e15, Dec. 2006.
- [3] M. O'Donnell and L. J. Thomas, "Efficient synthetic aperture imaging from a circular aperture with possible application to catheter-based imaging," *IEEE Trans. Ultrason., Ferroelectr., Freq. Control*, vol. 39, no. 3, pp. 366–380, May 1992.
- [4] M. Karaman, P.-C. Li, and M. O'Donnell, "Synthetic aperture imaging for small scale systems," *IEEE Trans. Ultrason., Ferroelectr., Freq. Control*, vol. 42, no. 3, pp. 429–442, May 1995.
- [5] M. Karaman and M. O'Donnell, "Subaperture processing for ultrasonic imaging," *IEEE Trans. Ultrason., Ferroelectr., Freq. Control*, vol. 45, no. 1, pp. 126–135, Jan. 1998.
- [6] S. Nikolov, K. Gammelmark, and J. A. Jensen, "Recursive ultrasound imaging," in *Proc. IEEE Ultrason. Symp.*, vol. 2, Oct. 1999, pp. 1621–1625.

- [7] G. R. Lockwood, J. R. Talman, and S. S. Brunke, "Real-time 3-D ultrasound imaging using sparse synthetic aperture beamforming," *IEEE Trans. Ultrason., Ferroelectr., Freq. Control*, vol. 45, no. 4, pp. 980–988, Jul. 1998.
- [8] M. Tanter, J. Bercoff, L. Sandrin, and M. Fink, "Ultrafast compound imaging for 2-D motion vector estimation: Application to transient elastography," *IEEE Trans. Ultrason., Ferroelectr., Freq. Control*, vol. 49, no. 10, pp. 1363–1374, Oct. 2002.
- [9] M. Tanter and M. Fink, "Ultrafast imaging in biomedical ultrasound," *IEEE Trans. Ultrason., Ferroelectr., Freq. Control*, vol. 61, no. 1, pp. 102–119, Jan. 2014.
- [10] J.-Y. Lu, "2D and 3D high frame rate imaging with limited diffraction beams," *IEEE Trans. Ultrason., Ferroelectr., Freq. Control*, vol. 44, no. 4, pp. 839–856, Jul. 1997.
- [11] K. L. Gammelmark and J. A. Jensen, "Multielement synthetic transmit aperture imaging using temporal encoding," *IEEE Trans. Med. Imag.*, vol. 22, no. 4, pp. 552–563, Apr. 2003.
- [12] G. Montaldo, M. Tanter, J. Bercoff, N. Benceh, and M. Fink, "Coherent plane-wave compounding for very high frame rate ultrasonography and transient elastography," *IEEE Trans. Ultrason., Ferroelectr., Freq. Control*, vol. 56, no. 3, pp. 489–506, Mar. 2009.
- [13] S. I. Nikolov and J. A. Jensen, "In-vivo synthetic aperture flow imaging in medical ultrasound," *IEEE Trans. Ultrason., Ferroelectr., Freq. Control*, vol. 50, no. 7, pp. 848–856, Jul. 2003.
- [14] A. J. Jensen and S. I. Nikolov, "Directional synthetic aperture flow imaging," *IEEE Trans. Ultrason., Ferroelectr., Freq. Control*, vol. 51, no. 9, pp. 1107–1118, Sep. 2004.
- [15] J. Udesen, F. Gran, K. L. Hansen, J. A. Jensen, C. Thomsen, and M. B. Nielsen, "High frame-rate blood vector velocity imaging using plane waves: Simulations and preliminary experiments," *IEEE Trans. Ultrason., Ferroelectr., Freq. Control*, vol. 55, no. 8, pp. 1729–1743, Aug. 2008.
- [16] K. L. Hansen, J. Udesen, F. Gran, J. A. Jensen, and M. B. Nielsen, "In-vivo examples of flow patterns with the fast vector velocity ultrasound method," *Ultraschall Med.*, vol. 30, no. 5, pp. 471–476, 2009.
- [17] J. Bercoff *et al.*, "Ultrafast compound Doppler imaging: Providing full blood flow characterization," *IEEE Trans. Ultrason., Ferroelectr., Freq. Control*, vol. 58, no. 1, pp. 134–147, Jan. 2011.
- [18] I. K. Ekroll, A. Swillems, P. Segers, T. Dahl, H. Torp, and L. Lovstakken, "Simultaneous quantification of flow and tissue velocities based on multi-angle plane wave imaging," *IEEE Trans. Ultrason., Ferroelectr., Freq. Control*, vol. 60, no. 4, pp. 727–738, Apr. 2013.
- [19] B. Y. Yiu, S. S. Lai, and A. C. Yu, "Vector projectile imaging: Time-resolved dynamic visualization of complex flow patterns," *Ultrasound Med. Biol.*, vol. 40, no. 9, pp. 2295–2309, Sep. 2014.
- [20] O. Couture, M. Fink, and M. Tanter, "Ultrasound contrast plane wave imaging," *IEEE Trans. Ultrason., Ferroelectr., Freq. Control*, vol. 59, no. 12, pp. 2676–2683, Dec. 2012.
- [21] J. Jensen, M. B. Stuart, and J. A. Jensen, "Increased frame rate for plane wave imaging without loss of image quality," in *Proc. IEEE Ultrason. Symp.*, Oct. 2015, pp. 1–4.
- [22] T. L. Szabo, *Diagnostic Ultrasound Imaging: Inside Out*, 2nd ed. Oxford, U.K.: Elsevier, 2014.
- [23] N. Oddershede and J. A. Jensen, "Effects influencing focusing in synthetic aperture vector flow imaging," *IEEE Trans. Ultrason., Ferroelectr., Freq. Control*, vol. 54, no. 9, pp. 1811–1825, Sep. 2007.
- [24] J. A. Jensen and N. B. Svendsen, "Calculation of pressure fields from arbitrarily shaped, apodized, and excited ultrasound transducers," *IEEE Trans. Ultrason., Ferroelectr., Freq. Control*, vol. 39, no. 2, pp. 262–267, Mar. 1992.
- [25] J. A. Jensen, "Field: A program for simulating ultrasound systems," *Med. Biol. Eng. Comput.*, vol. 34, suppl. 1, pt. 1, pp. 351–353, 1996.
- [26] Onda, "HGL hydrophones datasheet," Onda Corp., Sunnyvale, CA, USA, Tech. Rep. 090917, 2009.
- [27] J. A. Jensen *et al.*, "SARUS: A synthetic aperture real-time ultrasound system," *IEEE Trans. Ultrason., Ferroelectr., Freq. Control*, vol. 60, no. 9, pp. 1838–1852, Sep. 2013.
- [28] J. A. Jensen *et al.*, "Safety assessment of advanced imaging sequences I: Measurements," *IEEE Trans. Ultrason., Ferroelectr., Freq. Control*, vol. 63, no. 1, pp. 110–119, Jan. 2016.
- [29] K. Ranganathan and W. F. Walker, "Cystic resolution: A performance metric for ultrasound imaging systems," *IEEE Trans. Ultrason., Ferroelectr., Freq. Control*, vol. 54, no. 4, pp. 782–792, Apr. 2007.
- [30] K. Deb, "Multi-objective optimization," in *Search Methodologies*. New York, NY, USA: Springer, 2005.
- [31] C. A. C. Coello, G. B. Lamont, and D. A. van Veldhuizen, *Evolutionary Algorithms for Solving Multi-Objective Problems*. New York, NY, USA: Springer, 2007.
- [32] J. M. Hansen, M. C. Hemmsen, and J. A. Jensen, "An object-oriented multi-threaded software beamformation toolbox," *Proc. SPIE*, vol. 7968, p. 79680Y, Mar. 2011.
- [33] B. Denarie *et al.*, "Coherent plane wave compounding for very high frame rate ultrasonography of rapidly moving targets," *IEEE Trans. Med. Imag.*, vol. 32, no. 7, pp. 1265–1276, Jul. 2013.
- [34] K. L. Gammelmark and J. A. Jensen, "2-D tissue motion compensation of synthetic transmit aperture images," *IEEE Trans. Ultrason., Ferroelectr., Freq. Control*, vol. 61, no. 4, pp. 594–610, Apr. 2014.
- [35] B. Delannoy, H. Lasota, C. Bruneel, R. Torguet, and E. Bridoux, "The infinite planar baffles problem in acoustic radiation and its experimental verification," *J. Appl. Phys.*, vol. 50, no. 8, pp. 5189–5195, 1979.
- [36] P. Pesque and M. Fink, "Effect of the planar baffle impedance in acoustic radiation of a phased array element theory and experimentation," in *Proc. IEEE Ultrason. Symp.*, Nov. 1984, pp. 1034–1038.
- [37] M. B. Stuart, J. Jensen, T. Di Ianni, and J. A. Jensen, "Image quality degradation from transmit delay profile quantization," in *Proc. IEEE Ultrason. Symp.*, Oct. 2015, pp. 1–4.
- [38] J. Jensen, M. B. Stuart, and J. A. Jensen, "High frame rate vector velocity estimation using plane waves and transverse oscillation," in *Proc. IEEE Ultrason. Symp.*, Oct. 2015, pp. 1–4.
- [39] M. I. Haller and B. T. Khuri-Yakub, "A surface micromachined electrostatic ultrasonic air transducer," *IEEE Trans. Ultrason., Ferroelectr., Freq. Control*, vol. 43, no. 1, pp. 1–6, Jan. 1996.
- [40] H. Hasegawa and C. L. de Korte, "Impact of element pitch on synthetic aperture ultrasound imaging," *J. Med. Ultrason.*, vol. 43, no. 3, pp. 317–325, 2016.
- [41] C. R. Cooley and B. S. Robinson, "Synthetic focus imaging using partial datasets," in *Proc. IEEE Ultrason. Symp.*, Oct./Nov. 1994, pp. 1539–1542.
- [42] A. Ponnle, H. Hasegawa, and H. Kanai, "Suppression of grating lobe artifacts in ultrasound images formed from diverging transmitting beams by modulation of receiving beams," *Ultrasound Med. Biol.*, vol. 39, no. 4, pp. 681–691, 2013.



Jonas Jensen was born in 1988. He received the M.Sc. degree in biomedical engineering from the Technical University of Denmark, Kongens Lyngby, Denmark, and the University of Copenhagen, Copenhagen, Denmark, in 2014. He is currently pursuing the Ph.D. degree in biomedical engineering with the Center for Fast Ultrasound Imaging, Technical University of Denmark. The topic of his Ph.D. research includes fast plane-wave methods for anatomical and flow imaging.



Matthias Bo Stuart received the M.Sc. and Ph.D. degrees in computer engineering from the Technical University of Denmark, Lyngby, Denmark in 2006 and 2010, respectively.

He is currently a postdoc with the Center for Fast Ultrasound Imaging with the Department of Electrical Engineering, Technical University of Denmark. His research interests include synthetic aperture methods for both anatomical and flow imaging in both 2-D and 3-D, ultrasound systems, and real-time implementations of ultrasound processing

algorithms.



Jørgen Arendt Jensen (M'93–SM'02–F'12) received the Master of Science degree in electrical engineering in 1985 and the Ph.D. degree in 1989, both from the Technical University of Denmark. He received the Dr.Techn. degree from the university in 1996.

Since 1993, he has been Full Professor of Biomedical Signal Processing with the Department of Electrical Engineering, Technical University of Denmark and head of the Center for Fast Ultrasound Imaging since its inauguration in 1998. He has published more than 450 journal and conference papers on signal processing and medical ultrasound and the book *Estimation of Blood Velocities Using Ultrasound* (Cambridge Univ. Press), 1996. He is also the developer and maintainer of the Field II simulation program. He has been a visiting scientist at Duke University, Stanford University, and the University of Illinois at Urbana-Champaign. He was head of the Biomedical Engineering group from 2007 to 2010. In 2003, he was one of the founders of the biomedical engineering program in Medicine and Technology, which is a joint degree program between the Technical University of Denmark and the Faculty of Health and Medical Sciences at the University of Copenhagen. The degree is one of the most sought-after engineering degrees in Denmark. He was chairman of the study board from 2003 to 2010 and Adjunct Professor with the University of Copenhagen from 2005 to 2010. He has given a number of short courses on simulation, synthetic aperture imaging, and flow estimation at international scientific conferences and teaches biomedical signal processing and medical imaging at the Technical University of Denmark. His research is centered around simulation of ultrasound imaging, synthetic aperture imaging, vector blood flow estimation, and construction of ultrasound research systems.

Dr. Jensen has given more than 60 invited talks at international meetings and received several awards for his research.

**Increased Frame Rate for
Plane Wave Imaging Without Loss of Image Quality**

Jonas Jensen, Matthias Bo Stuart, and Jørgen Arendt Jensen

Proceedings of IEEE International Ultrasonics Symposium, p. 1-4,

Accepted for poster presentation in Taipei, Taiwan, 2015.

Increased Frame Rate for Plane Wave Imaging Without Loss of Image Quality

Jonas Jensen, Matthias Bo Stuart and Jørgen Arendt Jensen

Center for Fast Ultrasound Imaging, Dept. of Elec. Eng. Bldg. 349,
Technical University of Denmark, DK-2800 Lyngby, Denmark

Abstract—Clinical applications of plane wave imaging necessitate the creation of high-quality images with the highest possible frame rate for improved blood flow tracking and anatomical imaging. However, linear array transducers create grating lobe artefacts, which degrade the image quality especially in the near field for λ -pitch transducers. Artefacts can only partly be suppressed by increasing the number of emissions, and this paper demonstrates how the frame rate can be increased without loss of image quality by using $\lambda/2$ -pitch transducers. The number of emissions and steering angles are optimized in a simulation study to get the best images with as high a frame rate as possible. The optimal setup for a simulated 4.1 MHz λ -pitch transducer is 73 emissions and a maximum steering of 22° . The achieved FWHM is 1.3λ and the cystic resolution is -25 dB for a scatter at 9 mm. Only 37 emissions are necessary within the same angle range when using a $\lambda/2$ -pitch transducer, and the cystic resolution is reduced to -56 dB. Measurements are performed with the experimental SARUS scanner connected to a λ -pitch and $\lambda/2$ -pitch transducer. A wire phantom and a tissue mimicking phantom containing anechoic cysts are scanned and show the performance using the optimized sequences for the transducers. Measurements confirm results from simulations, and the λ -pitch transducer show artefacts at undesirable strengths of -25 dB for a low number of emissions.

I. INTRODUCTION

Medical ultrasound synthetic aperture imaging (SA) solves the limitations in conventional line-by-line imaging, which has a reduced frame rate and only optimal focusing at one depth. SA has been used with spherical waves [1], [2] and plane waves (PW) [3], [4]. By using emissions with wide areas of insonification, a low-resolution (LR) image is created for each emission, however, each LR image has low contrast. To regain contrast, LR images are combined to high-resolution (HR) images at the cost of a reduced frame rate. For anatomical imaging [5], [6] and flow estimation [7]–[9], it is important to use as few emissions as possible to keep the frame rate high and still obtain high-quality images.

The spatial sampling of a transducer aperture into array elements with λ -pitch results in aliasing of spatial frequencies. An unfocused emission from a transducer with a pitch equal to the pulse wavelength, λ , generates grating lobes in the emitted pressure field as illustrated in Fig. 1. A steered plane wave at 10° is simulated, and a grating lobe behind the wave front has amplitudes around -25 dB, which introduce artefacts in a beamformed image. Grating lobe artefacts can be suppressed by increasing the number of emissions, however, a $\lambda/2$ -pitch transducer avoids grating lobes and can therefore

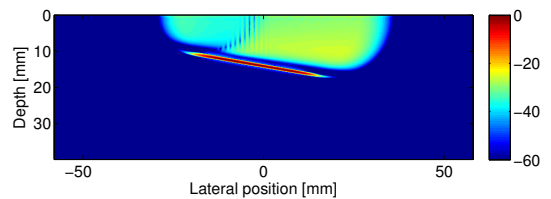


Fig. 1. Field II simulation of emitted field from a λ -pitch transducer, when a plane wave is emitted at 10° .

potentially increase the frame rate without compromising the image quality.

Small parts SA/PW imaging in related work [5]–[9] have so far been conducted with commercially available λ -pitch transducers, which are actually intended for line-by-line imaging with no steering. The pitch size is a compromise between having a high center frequency and a wide aperture to get a large field of view for small parts imaging, and the limitation of 128–192 channels in commercial scanners. Therefore, a transducer with the same aperture size and a pitch around $\lambda/2$ can only be obtained by using more channels, a lower center frequency, or not sampling all elements.

This paper investigates the image quality of PW images using a $\lambda/2$ -pitch transducer and compares it to a conventional λ -pitch transducer. The relationship between image quality and frame rate is investigated for both transducers, and it is shown that a higher frame rate can be obtained by using a $\lambda/2$ -pitch transducer compared to a λ -pitch transducer without loss of image quality. For a fair comparison between the transducers, a method for selecting the number of PW emissions and maximum steering angle based on the optimal image quality is presented. The method is presented with a simulation study in Section II. In Section III, methods for implementing the approach on the experimental scanner SARUS are described. The results of phantom measurements are presented in Section IV.

II. OPTIMIZATION PROCEDURE

A procedure for optimizing the image quality in terms of detail resolution and contrast is conducted for a λ -pitch and $\lambda/2$ -pitch transducer. The detail resolution is quantified as the full width at half maximum (FWHM), while the contrast is

TABLE I
PARAMETERS USED FOR SIMULATION AND MEASUREMENTS.

Parameter	λ -pitch	$\lambda/2$ -pitch
Number of elements	96	192
Center frequency f_0	4.1 MHz	4.1 MHz
Cycles in emitted pulse	1	1
Wavelength λ	0.376 mm	0.376 mm
Element pitch	0.4 mm	0.2 mm
Element height	6 mm	6 mm
Elevation focus	38 mm	38 mm
Transmit apodization	Tukey (weight 0.5)	Tukey (weight 0.5)
Receive apodization	Hamming	Hamming
Receive F-number	1	1

accessed through the cystic resolution (CTR), which quantifies the side lobe energy of the point-spread-function (PSF) outside a 4λ radius of the main lobe. The independent variables for the optimization procedure are the maximum steering angle, α_{max} , and the number of PWs, N , while the dependent variables are FWHM and CTR. The procedure is applied on simulated data and uses Pareto efficiency [10]. A Pareto frontier is constructed, which represent solutions, where it is impossible to improve one of the variables (CTR or FWHM) without worsening the other. Thereby, attention can be restricted only to solutions that are Pareto efficient, wherein trade-offs can be made, rather than considering all the solutions.

The actual pitches of the transducers are 1.12λ and 0.56λ , respectively, due to the experimental equipment available for small parts imaging. The $\lambda/2$ -pitch transducer has twice as many elements as the λ -pitch transducer to obtain the same aperture width. Parameters are listed in Table I. Five point targets are simulated at axial distances of 9, 20, 34, 44, and 60 mm from the transducer surface (corresponding to a scanned wire phantom). Simulations are performed using the Field II program [11], [12]. A Tukey apodization on the active transmit aperture is applied to reduce artefacts from edge waves. Plane wave emissions with steering angles from -40° to $+40^\circ$ and with 0.25° separation between each plane wave are simulated, and beamformation is performed using the BFT3 toolbox [13]. The beamformed low-resolution images are subsequently combined to high-resolution images with all combinations of α_{max} and N .

A scatter plot of lateral FWHM and CTR for all the HR images of a scatter at 9 mm is shown in Fig. 2 for the λ -pitch transducer. Axial FWHM are not included, since they are approximately λ in all cases. Solutions that are Pareto optimal are shown as black and the Pareto frontier as a black curve in Fig. 2. Any of the solutions on the Pareto frontier can be selected and used as a Pareto efficient setup for the given depth.

An interesting solution is at the knee point of the frontier, since it represents a trade-off between FWHM and CTR. However, since a Pareto frontier is generated for each of the five simulated point targets, attention should be drawn to all Pareto efficient solutions for the points. The maximum steering angles and number of PWs corresponding to the

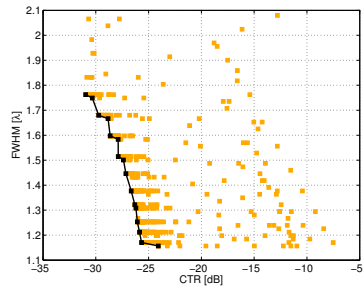


Fig. 2. Scatter plot of FWHM-CTR pairs from the simulated HR images at 9 mm for the λ -pitch transducer. Pareto optimal solutions are shown with black squares and the Pareto frontier as the black curve.

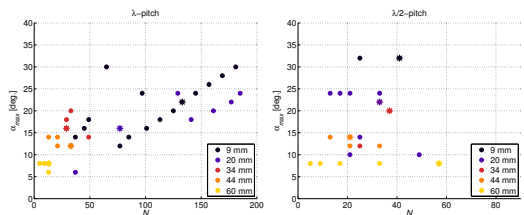


Fig. 3. Maximum steering angles α_{max} and number of emissions N corresponding to Pareto efficient solutions. Shown for each depth and for the λ -pitch (left) and $\lambda/2$ -pitch transducer (right). Knee point solution from frontiers are marked with asterisks.

Pareto efficient solutions are shown in Fig. 3. The figures give an overview of the Pareto efficient solutions in addition to the knee point solutions from the frontier (marked with asterisks).

Deciding on a single combination of max steering angle and number of PWs for all depths is challenging. Here, a setup of 73 PWs and $\alpha_{max} = 22^\circ$ is suggested for the λ -pitch transducer as a compromise between frame rate and a reduced image quality at 9 and 20 mm. It gives a FWHM = 1.3λ and CTR = -25 dB at 9 mm. For the $\lambda/2$ -pitch transducer, a setup of 37 PWs and $\alpha_{max} = 22^\circ$ is chosen and gives FWHM = 1.3λ and CTR = -56 dB. Furthermore, the simulations show that both transducers can obtain similar image quality with CTR < -40 dB for depths higher than 25 mm and using the same setups, while the transducers have a difference in CTR of 15-25 dB down to 25 mm. This is investigated further in measurements.

III. EXPERIMENTAL METHODS

A B-mode imaging sequence was implemented on the experimental scanner SARUS [14] using the parameters listed in Table I. An interleaved sequence with emissions for a $\lambda/2$ -pitch and λ -pitch transducer was used with a pulse repetition frequency of 5 kHz. A linear array transducer was employed, and with its 192 elements and 0.56λ pitch it has identical parameters to the $\lambda/2$ -pitch transducer in Table I. By exciting the first and second element simultaneously, the third and fourth element simultaneously and so forth, a λ pitch trans-

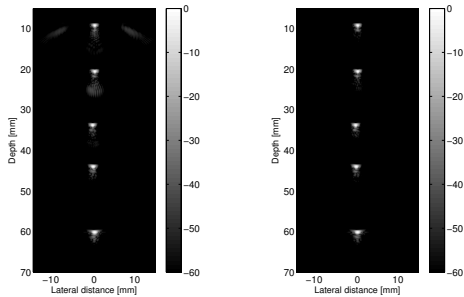


Fig. 4. B-mode image of wire phantom. Using the λ -pitch (left) and $\lambda/2$ -pitch transducer (right), and 37 PWs with $\alpha_{max} = 22^\circ$.

ducer with 96 elements is employed and emulating the λ -pitch transducer in Table I. Data were sampled and stored for all transducer elements and processed offline using the BFT3 toolbox [13]. For the λ -pitch transducer, data from element one and two, three and four, etc. were averaged. Two phantoms were scanned: a water tank phantom containing five wires, and a multi-tissue contrast phantom containing an anechoic cyst at 17 mm (Model 040GSE, CIRS Inc., Virginia, USA) with tissue attenuation of 0.5 dB/(cm·MHz).

IV. EXPERIMENTAL RESULTS

A scan of the wire phantom is shown in Fig. 4 for the λ -pitch and $\lambda/2$ -pitch transducer. The optimized setup for the $\lambda/2$ -pitch transducer is used ($N = 37$ and $\alpha_{max} = 22^\circ$). For the λ -pitch transducer, off-axis energy lobes and artefacts around the wires at 9 and 20 mm degrade the image quality compared to using the $\lambda/2$ -pitch transducer.

The bottom image in Fig. 5 shows the PSF at 9 mm when using the optimized setup for the $\lambda/2$ -pitch transducer, while the number of emissions have been varied for the λ -pitch transducer (three top images). CTR is quantified as a function of N for the PSF at 9 mm in Fig. 6, where $\alpha_{max} = 22^\circ$. While the measurements are in accordance with the simulations for the λ -pitch transducer, there is 15 dB difference for the $\lambda/2$ -pitch transducer. The asymptotic trend of the measured CTR curve indicates that this is because a lower limit has been reached for the used imaging system. Note also, that the λ -pitch transducer never attains the same minimum CTR level as the $\lambda/2$ -pitch transducer even for a high number of emissions.

In Fig. 7, measurements of the cyst phantom are shown. A similar degraded image quality as in Fig. 5 is observed for the λ -pitch transducer compared to the $\lambda/2$ -pitch transducer as a function of N . The Contrast-to-Noise Ratio (CNR),

$$CNR = \frac{\mu_s - \mu_c}{\sqrt{\sigma_s^2 + \sigma_c^2}}, \quad (1)$$

was calculated for the cyst. μ_s and μ_c are the mean intensities of the cyst region and speckle region, while σ_s^2 and σ_c^2 are the corresponding variances. CNR is shown as a function of N in Fig. 7. Furthermore, using only 5 emissions as in blood

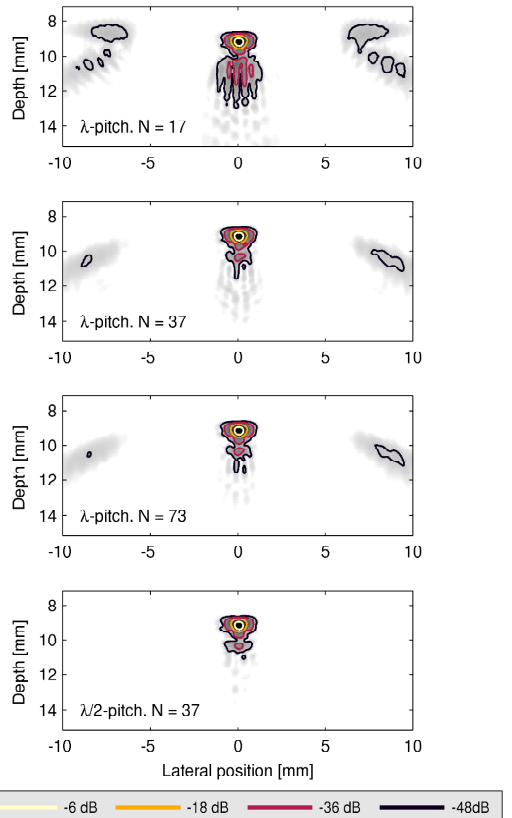


Fig. 5. Measured PSFs at 9 mm depth. The three top figures are for the λ -pitch transducer and the bottom figure is for the $\lambda/2$ -pitch transducer. The maximum steering angle is 22° , and the number of emissions, N , is 17, 37, 73, and 37 for the four figures, respectively. The dynamic range is 60 dB.

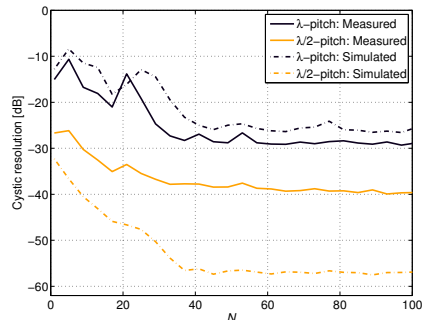


Fig. 6. Cystic resolution as a function of the number of emissions N for a $\alpha_{max} = 22^\circ$. For a PSF at 9 mm. Cystic resolution is shown for a λ and $\lambda/2$ -pitch transducer and for simulated and measured data.

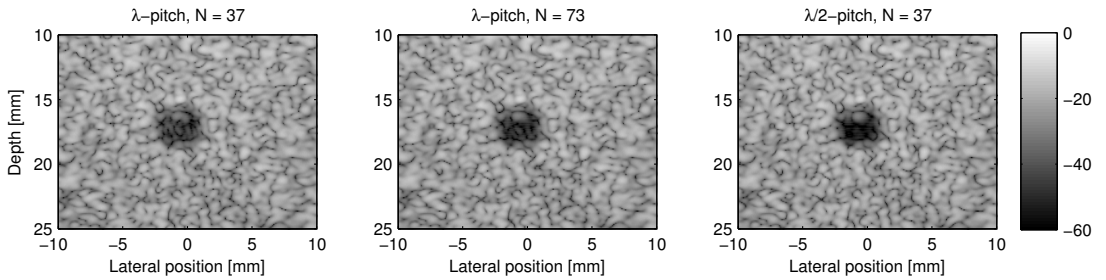


Fig. 7. PW imaging of an anechoic cyst embedded in a tissue mimicking phantom. The left and middle images are for the λ -pitch transducer and the right image is for the $\lambda/2$ -pitch transducer. The number of emissions, N , is 17, 73, and 37 for the three figures, respectively. The maximum steering angle is 22° .

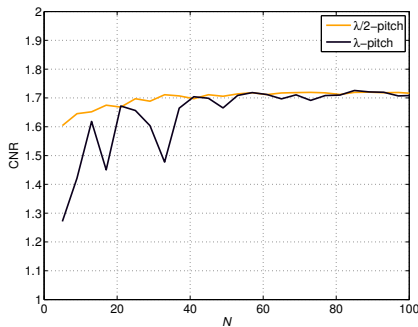


Fig. 8. The contrast-to-noise ratio (CNR) as a function of number of emissions N for the cyst at 17 mm. CNR is shown for the $\lambda/2$ and λ -pitch transducer.

flow estimation, peak intensities are -25 dB inside the cyst, which is undesirable and would give false flow velocities if the vessel wall is moving.

V. CONCLUSION

Image quality of PW images was investigated using a $\lambda/2$ -pitch transducer and compared to a λ -pitch transducer. The number of PW emissions and steering angles were selected based on a proposed procedure for optimizing the image quality. For small parts imaging, it was demonstrated that the number of emissions could be decreased by almost half, from 73 to 37, by using a $\lambda/2$ -pitch transducer rather than a λ -pitch transducer. The image quality was degraded to a depth of 25 mm due to grating lobes from a λ -pitch transducer, and it is therefore recommended always to use a $\lambda/2$ -pitch transducer to avoid artefacts in SA/PW imaging and to increase the frame rate. Potentially, it can have an impact on the frame rate in anatomical imaging and flow estimation systems, and thus, increase the limit of maximum detectable velocities.

ACKNOWLEDGMENTS

This work was supported by grant 82-2012-4 from the Danish National Advanced Technology Foundation and by BK Ultrasound.

REFERENCES

- [1] M. Karaman, P. C. Li, and M. O'Donnell, "Synthetic aperture imaging for small scale systems," *IEEE Trans. Ultrason., Ferroelec., Freq. Contr.*, vol. 42, pp. 429–442, 1995.
- [2] J. A. Jensen, S. Nikolov, K. L. Gammelmark, and M. H. Pedersen, "Synthetic aperture ultrasound imaging," *Ultrasonics*, vol. 44, pp. e5–e15, 2006.
- [3] M. Tanter, J. Bercoff, L. Sandrin, and M. Fink, "Ultrafast compound imaging for 2-D motion vector estimation: application to transient elastography," *IEEE Trans. Ultrason., Ferroelec., Freq. Contr.*, vol. 49, pp. 1363–1374, 2002.
- [4] J. Y. Lu, "2D and 3D high frame rate imaging with limited diffraction beams," *IEEE Trans. Ultrason., Ferroelec., Freq. Contr.*, vol. 44, pp. 839–855, 1997.
- [5] K. L. Gammelmark and J. A. Jensen, "Multielement synthetic transmit aperture imaging using temporal encoding," *IEEE Trans. Med. Imag.*, vol. 22, no. 4, pp. 552–563, 2003.
- [6] G. Montaldo, M. Tanter, J. Bercoff, N. Benech, and M. Fink, "Coherent plane-wave compounding for very high frame rate ultrasonography and transient elastography," *IEEE Trans. Ultrason., Ferroelec., Freq. Contr.*, vol. 56, no. 3, pp. 489–506, March 2009.
- [7] S. I. Nikolov and J. A. Jensen, "In-vivo Synthetic Aperture Flow Imaging in Medical Ultrasound," *IEEE Trans. Ultrason., Ferroelec., Freq. Contr.*, vol. 50, no. 7, pp. 848–856, 2003.
- [8] J. Udesen, F. Gran, K. L. Hansen, J. A. Jensen, C. Thomsen, and M. B. Nielsen, "High frame-rate blood vector velocity imaging using plane waves: Simulations and preliminary experiments," *IEEE Trans. Ultrason., Ferroelec., Freq. Contr.*, vol. 55, no. 8, pp. 1729–1743, 2008.
- [9] J. Bercoff, G. Montaldo, T. Loupas, D. Saverly, F. Meziere, M. Fink, and M. Tanter, "Ultrafast compound Doppler imaging: Providing full blood flow characterization," *IEEE Trans. Ultrason., Ferroelec., Freq. Contr.*, vol. 58, no. 1, pp. 134–147, January 2011.
- [10] K. Deb, "Multi-objective optimization," in *Search methodologies*. Springer, 2005.
- [11] J. A. Jensen and N. B. Svendsen, "Calculation of pressure fields from arbitrarily shaped, apodized, and excited ultrasound transducers," *IEEE Trans. Ultrason., Ferroelec., Freq. Contr.*, vol. 39, pp. 262–267, 1992.
- [12] J. A. Jensen, "Field: A program for simulating ultrasound systems," *Med. Biol. Eng. Comp.*, vol. 10th Nordic-Baltic Conference on Biomedical Imaging, Vol. 4, Supplement 1, Part 1, pp. 351–353, 1996.
- [13] J. M. Hansen, M. C. Hemmsen, and J. A. Jensen, "An object-oriented multi-threaded software beamformation toolbox," in *Proc. SPIE Med. Imag.*, vol. 7968, March 2011, pp. 79680Y 1–9. [Online]. Available: <http://dx.doi.org/10.1117/12.878178>
- [14] J. A. Jensen, H. Holten-Lund, R. T. Nilsson, M. Hansen, U. D. Larsen, R. P. Domsten, B. G. Tomov, M. B. Stuart, S. I. Nikolov, M. J. Pihl, Y. Du, J. H. Rasmussen, and M. F. Rasmussen, "SARUS: A synthetic aperture real-time ultrasound system," *IEEE Trans. Ultrason., Ferroelec., Freq. Contr.*, vol. 60, no. 9, pp. 1838–1852, 2013.

Fast Plane Wave 2-D Vector Flow Imaging Using Transverse Oscillation and Directional Beamforming

Jonas Jensen, Carlos Armando Villagómez-Hoyos, Matthias Bo Stuart,
Caroline Ewertsen, Michael Bachmann Nielsen, and Jørgen Arendt Jensen

Accepted, IEEE Trans. Ultrason., Ferroelec., Freq. Contr., April 6, 2017

Fast Plane Wave 2-D Vector Flow Imaging Using Transverse Oscillation and Directional Beamforming

Jonas Jensen¹, Carlos Armando Villagómez Hoyos¹, Matthias Bo Stuart¹, Caroline Ewertsen²,
Michael Bachmann Nielsen², and Jørgen Arendt Jensen¹

¹Center for Fast Ultrasound Imaging, Department of Electrical Engineering,
Technical University of Denmark, DK-2800 Lyngby, Denmark

²Department of Radiology, Copenhagen University Hospital, DK-2100 Copenhagen, Denmark

Abstract—Several techniques can estimate the 2-D velocity vector in ultrasound. Directional beamforming (DB) estimates blood flow velocities with a higher precision and accuracy than transverse oscillation (TO), but at the cost of a high beamforming load when estimating the flow angle. In this paper, it is proposed to use TO to estimate an initial flow angle, which is then refined in a DB step. Velocity magnitude is estimated along the flow direction using cross-correlation. It is shown that the suggested TO-DB method can improve the performance of velocity estimates compared to TO, and with a beamforming load, which is 4.6 times larger than for TO and seven times smaller than for conventional DB. Steered plane wave transmissions are employed for high frame rate imaging, and parabolic flow with a peak velocity of 0.5 m/s is simulated in straight vessels at beam-to-flow angles from 45° to 90°. The TO-DB method estimates the angle with a bias and standard deviation (SD) less than 2°, and the SD of the velocity magnitude is less than 2%. When using only TO, the SD of the angle ranges from 2° to 17° and for the velocity magnitude up to 7%. Bias of the velocity magnitude is within 2% for TO and slightly larger but within 4% for TO-DB. The same trends are observed in measurements although with a slightly larger bias. Simulations of realistic flow in a carotid bifurcation model provide visualization of complex flow, and the spread of velocity magnitude estimates is 7.1 cm/s for TO-DB, while it is 11.8 cm/s using only TO. However, velocities for TO-DB are underestimated at peak systole as indicated by a regression value of 0.97 for TO and 0.85 for TO-DB. An *in vivo* scanning of the carotid bifurcation is used for vector velocity estimations using TO and TO-DB. The SD of the velocity profile over a cardiac cycle is 4.2% for TO and 3.2% for TO-DB.

I. INTRODUCTION

Ultrasound blood flow estimation is of diagnostic value in investigating hemodynamics in the human cardiovascular system. Conventional color flow mapping uses focused emissions in line-by-line imaging, where each line is acquired sequentially from received echoes of several consecutive pulses. It limits the frame rate significantly, when a large color box and large imaging depth are desired, especially when using duplex imaging. The frame rate can drop to 10-15 Hz, and it is impossible to identify rapid temporal changes in the blood flow. Full flow dynamics of both fast and slow flow are also lost, because of the limited observation time along each focusing direction.

Alternative imaging methods such as synthetic aperture imaging (SA) using either spherical or plane waves have been proposed to increase the frame rate and improve image

quality [1], [2]. An image of the entire insonified region is created for each emission resulting in a low-resolution image (LRI). By using a few broad insonifications, the low-resolution images can be summed to form a high-resolution image (HRI). The methods require parallel acquisition systems, but enable continuous data in the entire image.

Conventional ultrasound systems are limited to estimation of axial flow velocities only along the ultrasound beam. Several methods have been proposed to estimate the 2-D velocity vector without the need for angle correction, e.g., speckle tracking [3], multibeam methods [4], transverse oscillation (TO) [5]–[7], directional beamforming (DB) [8] and color Doppler-derived vector flow mapping [9], [10]. The 2-D vector flow techniques enable estimation of the true blood velocity in complex vessel geometries and for complex flow phenomena, where the flow angle is not constant. The techniques have also been combined with SA [11], [12] and later with plane waves [2], [13]–[15] for high-frame-rate imaging. More recently, plane wave imaging has been combined with the multibeam method [16]–[19] and transverse oscillation [20].

The TO method estimates the velocity vector by introducing a lateral oscillation in the ultrasound field. Only two lines are beamformed for each estimation point, and the estimators are computationally inexpensive [21]. The precision of the velocity estimates is around 5-10 % with decreased performance for smaller beam-to-flow angles [22]. For the DB approach, lines are focused along the direction of the flow. The velocity magnitude can be estimated with high accuracy and precision using a cross-correlation estimator, due to the high signal correlation along the directional lines. It has also been shown that the standard deviation of the velocity estimates can be reduced by a factor of two, when using DB rather than TO [22]. However, the direction of the blood flow needs to be known in advance for DB. Automatic approaches for angle estimation have been proposed and use either the normalized correlation function (NCF) [23], or velocities estimated on the LRIs to numerically triangulate the flow angle [24]. The number of calculations for these conventional angle estimators is, however, very high because signals have to be beamformed in a 360° polar grid and cross-correlated at every angle and for each estimation point. Lines are usually beamformed at every 5° covering a total of 180° [23], which gives 36 directional lines for every estimation point in each frame.

There is, thus, a tradeoff between performance and beamforming load for the TO and DB methods. In this paper, it is proposed to combine the methods by using TO to automatically estimate an initial flow angle, which is then refined by a NCF DB step. The velocity magnitude is estimated along the refined flow direction as in DB. The method is presented as TO-DB. The objectives are to obtain velocity estimates with an improved performance compared to TO and to have a beamforming load, which is between TO and conventional NCF DB. The concept and first measurements were presented in preliminary versions of the method as published in conference proceedings [25], [26]. This paper expands the theory, and a parameter study of simulated parabolic flow in straight vessel phantoms is performed to reveal the ideal performance of the estimator. Realistic flow derived from computational fluid dynamics (CFD) is simulated in a carotid bifurcation model and included to study the performance of the method for complex flow patterns, which are similar to those obtained *in vivo*. Furthermore, two different echo-canceling filters are applied on an *in vivo* data set to investigate the influence of selecting an appropriate echo-canceling filter.

In the next section, the method for plane wave flow imaging is explained. It is validated using simulations and flow rig measurements, and the methods are described in Section III. The results are presented in Section IV, and the paper is concluded with an example of an *in vivo* scan of the carotid bifurcation of a healthy volunteer.

II. METHOD FOR PLANE WAVE FLOW IMAGING

This section presents the proposed method for plane wave flow imaging. The principle of plane wave emissions for fast imaging is explained, and the method for vector flow estimation is presented: first, TO estimators are used to find an initial flow angle, and then three directional lines are beamformed around the TO angle to improve the angle estimate. Velocity magnitude is estimated along a fourth line beamformed in the refined flow direction using a cross-correlation estimator. An illustration of the principle is shown in Fig. 1, where three directional lines are beamformed around the initial TO angle estimate.

A. Plane Wave Imaging

High-frame-rate imaging can be obtained by emitting a few plane waves at different steering angles from a linear array transducer. Using the principle of SA imaging [11], a LRI is created for each emission, and a number of LRIs are combined to form an HRI. An HRI has an improved image quality and sensitivity compared to individual LRIs [1], [27], and this principle is used for both flow and B-mode imaging in this paper. Similar to how LRI and HRI can be constructed, low-resolution lines (LRL) and high-resolution lines (HRL) can be beamformed in any desired direction within the insonified region.

B. Transverse Oscillation

A transverse oscillation can be introduced in the pulse-echo field in addition to the conventional axial oscillation, so that

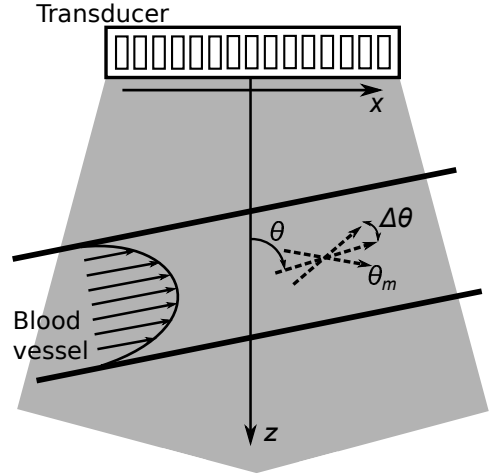


Fig. 1. Plane wave emissions from a linear array transducer are used to insonify flow in a straight vessel. Directional lines are beamformed at angles θ_m around the initial TO angle estimate θ at a single velocity estimation point.

the received signals become sensitive to both an axial and lateral motion in the field. The TO field is usually created in the receive beamforming by changing the apodization function to contain two separate peaks. A lateral oscillation can also be generated in the Fourier domain, known as k -space, to provide better control over the lateral oscillation wavelength. The method was introduced in [28], [29] and is performed in the Fourier domain by filtering the beamformed image in the lateral dimension and only select k -space components around a desired lateral oscillation frequency. The original approach applied a 2-D phase-based block matching estimator for tissue motion estimation, while a fourth order estimator will be used for blood flow estimation in this paper.

The Fourier filtration process is illustrated in Fig. 2. Beamformed data for an HRI has a k -space as illustrated in Fig. 2 (top). An oscillation in the axial direction is centered at the pulse center frequency, while there is no oscillation laterally. A filter $G(f_z, f_x)$ consisting of Gaussian windows centered around a desired TO frequency f_{0x} ,

$$G(f_z, f_x) = \exp(-2(\pi\sigma_x(f_x - f_{0x}))^2) + \exp(-2(\pi\sigma_x(f_x + f_{0x}))^2), \quad (1)$$

where σ_x is the width of the Gaussian window and f_x is the lateral oscillation frequency, is illustrated in Fig. 2 (middle). A multiplication of the filter and the Fourier transformed image gives the TO image in Fig. 2 (bottom). The image has been filtered in the lateral dimension, while the axial dimension is untouched. Any values of the parameters f_{0x} and σ_x can in principle be chosen, but it should be ensured that only k -space components containing energy from flow and not only noise are chosen. By having an effective $F\#$ that is relatively small, energy is retained for larger f_x .

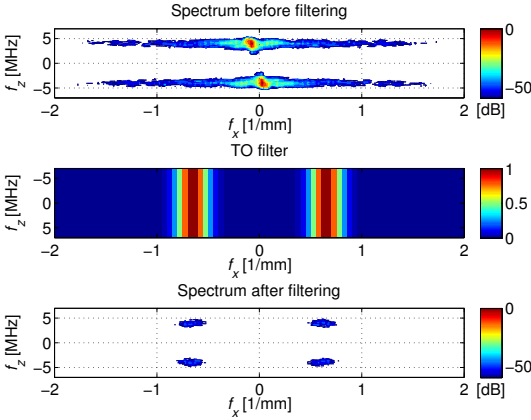


Fig. 2. The 2-D Fourier spectrum of a beamformed RF image is shown in the top figure. The spectrum of the TO filter $G(f_z, f_x)$ is shown in the middle, and the spectrum of beamformed RF image after applying the TO filter is shown in the lower figure. The resulting RF image contains transverse oscillations with a mean lateral frequency according to the desired oscillation frequency of the TO filter.

The directional information of the flow is preserved by keeping only one quadrant of the Fourier spectrum. This avoids applying the Hilbert transform on the TO image or having a spatial quadrature between two beamformed signals [21]. A standard fourth order autocorrelation estimator for the transverse velocity component v_x is employed as proposed in [30]. For the axial velocity component v_z , a cross-correlation estimator is employed [31].

The flow angle is found at each estimation point from:

$$\theta = \arctan(v_x, v_z) \quad (2)$$

using the estimated v_x and v_z .

C. Directional Beamforming

The initial angle estimate from (2) is used to construct a directional line, where points are focused at

$$\vec{r}_p(k) = (\Delta r \cdot k \cdot \sin \theta + x_{st}, \Delta r \cdot k \cdot \cos \theta + z_{st}), \quad (3)$$

where Δr is the spatial sampling interval, k is the sample index, and (x_{st}, z_{st}) is the velocity estimation point. Beamforming for the points $\vec{r}_p(k)$ gives a directionally focused signal $y_d(k)$. The pulse repetition period is T_{prf} and the number of LRIs per HRI is N_t , thus, cross-correlating signals from two HRIs gives

$$\begin{aligned} R_{12}(l) &= \frac{1}{N_k + 1} \sum_{k=-N_k/2}^{N_k/2} y_d^{(n)}(k) y_d^{(n+N_t)}(k+l) \\ &= \frac{1}{N_k + 1} \sum_{k=-N_k/2}^{N_k/2} y_d^{(n)}(k) y_d^{(n)}(k+l-k_s) \\ &= R_{11}(l-k_s) \end{aligned}$$

where $y_d^{(n)}(k)$ is the directional signal focused after emission n , N_k is the number of samples in $y_d(k)$, and $R_{11}(l-k_s)$ is

the shifted autocorrelation of $y_d^{(n)}(k)$. A global maximum is attained at $l = k_s$.

Lines can also be beamformed at other angles θ_m , and beamforming three directional signals at $\theta_m \in \{\theta - \Delta\theta, \theta, \theta + \Delta\theta\}$ yield correlation functions $R_{12}(l, \theta_m)$. They are used to calculate the normalized cross-correlation estimate

$$R_{12n}(\theta_m) = \left(\frac{\max(R_{12}(l, \theta_m))}{P_{12}(\theta_m)} \right), \quad (4)$$

which gives the maximum normalized cross-correlation as a function of the angle, and

$$P_{12}(\theta_m) = \sqrt{\sum_k y_d^{(n)}(k, \theta_m)^2 \cdot \sum_k y_d^{(n+N_t)}(k, \theta_m)^2} \quad (5)$$

represents the power of the signals. Using three angles for directional beamforming, $R_{12n}(\theta_m)$ has three values. The angle estimate, θ_d , is found as the angle yielding the largest correlation

$$\theta_d = \arg \max_{\theta_m} \{R_{12n}(\theta_m)\}. \quad (6)$$

If $R_{12}(\theta_m)$ has its peak value at the center angle, the accuracy of the angle estimate can be improved using a parabolic interpolation [32]

$$\hat{\theta} = \theta_d - \frac{R_{12n}(\theta + \Delta\theta) - R_{12n}(\theta - \Delta\theta)}{2(R_{12n}(\theta + \Delta\theta) - 2R_{12n}(\theta) + R_{12n}(\theta - \Delta\theta))} \Delta\theta, \quad (7)$$

where $\Delta\theta$ is the angle span between the three directional lines. Three angle estimates - one for each line - are sufficient to perform a parabolic interpolation, where the correlation values are weights in the interpolation. If the peak value of $R_{12}(\theta_m)$ is not at the center angle, the corresponding angle θ_m is chosen. $\Delta\theta$ can be selected as a fixed angle span or depend on the estimated TO angle as presented in this paper and explained in Section III.

The angle estimate $\hat{\theta}$ from (7) is then used to beamform a fourth directional line at this angle. The velocity magnitude can be found from the lag of the maximum cross-correlation $R_{12}(l, \hat{\theta})$

$$l_{max} = \arg \max_l R_{12}(l, \hat{\theta}), \quad (8)$$

which corresponds to the velocity magnitude

$$|v| = \frac{l_{max} \Delta r}{T_{prf} N_t}. \quad (9)$$

The accuracy of the velocity estimates can be enhanced by making an interpolation around the maximum lag l_{max} using an equation similar to (7).

D. Beamforming Load

The beamforming load for the TO, TO-DB and DB methods are very different as will be shown here. Considering a single velocity estimation point, the TO method requires two beamformed lines: one axial containing N_z samples and one lateral containing N_x samples, in total

$$N_{TO} = N_z + N_x. \quad (10)$$

For TO-DB, four directional lines are beamformed additionally, each containing N_x samples

$$N_{TO-DB} = N_z + 5 \cdot N_x. \quad (11)$$

For a conventional NCF DB estimator the number of directional lines are usually 36 [23]:

$$N_{DB} = 36 \cdot N_x. \quad (12)$$

Typical values are $N_z = 30$ and $N_x = 250$ for a line length of 1.5λ axially and 12.5λ laterally/directionally as will be used in this paper. The ratio between the TO-DB and TO method is

$$\frac{N_{TO-DB}}{N_{TO}} = \frac{N_z + 5 \cdot N_x}{N_z + N_x} = \frac{30 + 5 \cdot 250}{30 + 250} = 4.6 \quad (13)$$

and between the DB and TO-DB method

$$\frac{N_{DB}}{N_{TO-DB}} = \frac{36 \cdot N_x}{N_z + 5 \cdot N_x} = \frac{36 \cdot 250}{30 + 5 \cdot 250} = 7 \quad (14)$$

Thus, the beamforming load for TO-DB is 4.6 times larger than for TO, but seven times smaller than for conventional NCF DB.

III. METHODS FOR SIMULATIONS AND EXPERIMENTS

This section describes the simulation method and the implementation on the experimental scanner SARUS [33] for flow rig measurements and *in vivo* scanning.

A 192-element 0.6λ -pitch transducer is employed, and a duplex sequence is constructed to interweave both flow and B-mode emissions. Three steered flow emissions are emitted at a pulse repetition frequency f_{prf} , and then a B-mode emission is transmitted. It results in an effective pulse repetition frequency, $f_{prf,eff} = f_{prf}/4$, for flow estimation. To construct a full B-mode image, 21 emissions are used, which are selected based on the optimization in [34]. Transducer and acquisition parameters are listed in Table I. A short excitation pulse (1.5-cycle sinusoid) is used for the flow emissions, since the precision of the cross-correlation estimator used for DB is proportional to the bandwidth of the system [32]. Conversely, the precision of the TO phase-shift estimator is inversely proportional to the system bandwidth. This requirement is met by convolving the beamformed signals used for TO estimation with a 4-cycle sinusoid at wavelength λ to achieve narrow-band signals. Similar signals could have been received, if the excitation pulse had a pulse length of 5-6 cycles, which is often used for a phase-shift estimator.

Delay-and-sum beamforming are performed using the Beamformation Toolbox III [35] and processing parameters are listed in Table II. Dynamic receive apodization with an $F\#$ of 0.8 is applied, which is within the angular response of the transducer elements [34]. At each velocity estimation point, an axial and lateral line are used to estimate v_z and v_x with the TO method. For the TO-DB angle refinement, three directional lines are beamformed at each estimation point: one at the TO angle θ and at $\pm\Delta\theta$. The selected angle span $\Delta\theta$ depends on the estimated TO angle:

$$\begin{aligned} \Delta\theta &= 2^\circ \text{ for } |\theta| \geq 80^\circ, \\ \Delta\theta &= 5^\circ \text{ for } 50^\circ \leq |\theta| < 80^\circ, \\ \Delta\theta &= 10^\circ \text{ for } |\theta| < 50^\circ. \end{aligned} \quad (15)$$

TABLE I
TRANSDUCER AND ACQUISITION PARAMETERS.

Parameter	Value
Number of elements	192
Transducer center frequency f_0	4.1 MHz
Element pitch	0.2 mm (0.6 λ)
Element height	6 mm
Elevation focus	38 mm
Cycles in emitted pulse	1.5 (flow) and 1 (B-mode)
Transmit apodization	Tukey (weight 0.5)
Pulse repetition frequency f_{prf}	10 kHz
Max steering angle	15° (flow) and 20° (B-mode)
Number of plane waves	3 (flow) and 21 (B-mode)

TABLE II
PROCESSING PARAMETERS.

Parameter	TO	TO-DB
Receive apodization	Tukey (weight 0.5)	Tukey (weight 0.5)
Receive F-number	0.8	0.8
Sampling interval dr	$\lambda/20$	$\lambda/20$
Desired lateral wavelength	1.53 mm	-
TO window size	1.5 mm	-
Number of HRI/estimate	32	32
Line length	-	12.5 λ

The selection of $\Delta\theta$ is based on the standard deviation (SD) of the TO angle estimate θ . As it covers 68 % of the estimates around θ , it is 68 % confident that the flow angle is within $\Delta\theta$, when considering a normal distribution. This is further explained in Section IV-A1.

Each velocity estimate is obtained by correlating 32 HRIs. For constant flow, 10 non-consecutive estimates are used to calculate the mean and SD of the velocity estimates at each estimation point.

Echo-canceling of beamformed data is performed with a Hoeks filter [36] for simulated and measured flow in a flow rig. For *in vivo* data, an energy-based filter with manual threshold is used [37], [38]. The energy-based cut-off filter is used instead of a conventional frequency cut-off filter to better separate the blood signal from the tissue signal of the moving vessel wall. This is important for transverse flow estimation, because the velocity spectra of blood and tissue will overlap more as shown in Fig. 3. The energy-based filter uses energy or amplitude characteristics of blood and tissue, and tissue components are attenuated by limiting the amplitude of the tissue velocity spectrum to a cut-off threshold A_c . Thus, energy of the narrow-band tissue signal, $\int G'(\omega_t)d\omega$, is overpowered by the energy of a more broad-band blood signal $\int G(\omega_b)d\omega$. Here, the threshold A_c is manually determined after calculating the energy-levels of tissue and blood, and the value depends on the particular scan.

A. Simulations

Simulations of channel RF data are performed using the Field IIpro program [39]–[41]. Constant parabolic flow is simulated inside a straight rigid-wall vessel with a radius of 6 mm and centered at a depth of 20 mm. The vessel is rotated to the angle θ , and the peak velocity of the flow

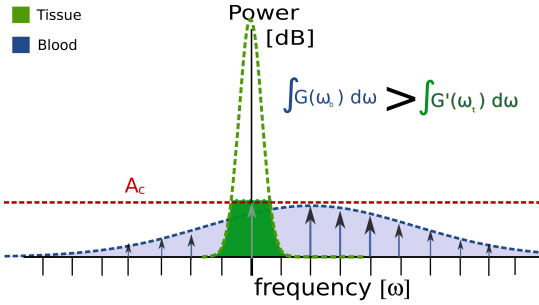


Fig. 3. Velocity spectra for the tissue signal (green curve) and blood signal (blue curve). The energy-based echo-canceling filter limits the velocity spectrum of tissue to an amplitude cut-off A_c . The energy of tissue signal (green area) is overpowered by the energy of the blood signal (blue area).

is 0.5 m/s. Approximately 10 point scatterers are simulated per resolution cell randomly distributed and with amplitudes generated from a Gaussian distribution. The influence of noise on the performance of the TO estimator is also investigated in a separate simulation study for a beam-to-flow angle of 90° . White noise is added to the received element RF signals before beamforming to obtain signal-to-noise ratios (SNR) corresponding to specified levels for the HRI. No vessel wall is simulated and echo-canceling is disabled for the SNR investigation.

A carotid bifurcation model is also employed for investigation of more complex flow conditions in a realistic vascular geometry. A computational fluid dynamics (CFD) dataset provided by Swillens et al. [42] contains a bifurcation geometry from a CT scan of a healthy volunteer. An eccentric plaque is artificially inserted in the internal branch. Flow is simulated with the CFD-package Fluent for a cardiac cycle of 1 second in steps of 5 ms. An inlet velocity profile is applied at the common carotid artery, which was obtained from a spectral velocity measurement on the volunteer. Furthermore, rigid walls are assumed with no modeling of tissue movement. Swillens et al. also provide a framework (BioMMeda.ugent.be), where the CFD velocities are used for propagating scatterers and coupled to Field II for ultrasound simulations. Spatial and temporal interpolation are handled by the framework for updating the scatterer positions according to the ultrasound simulation.

B. Flow Rig Measurements

The approach is implemented on the experimental scanner SARUS [33] for acquisition of channel RF data. The setup is the same as for simulations, and a transducer with parameters as listed in Table I is employed. A flow rig system is used, where the radius of the tube is 6 mm. Constant parabolic flow is circulated by a Cole-Parmer centrifugal pump (Vernon Hills, IL, USA), and volume flow is measured by a magnetic flow meter for reference (MAG1100, Danfoss, Nordborg, Denmark). The f_{prf} is reduced to 2 kHz to avoid reverberations in the water tank, and the volume flow in the flow rig system is adjusted to match the peak velocity-to- f_{prf} ratio in the simulations. The match of parameters used in flow rig scans

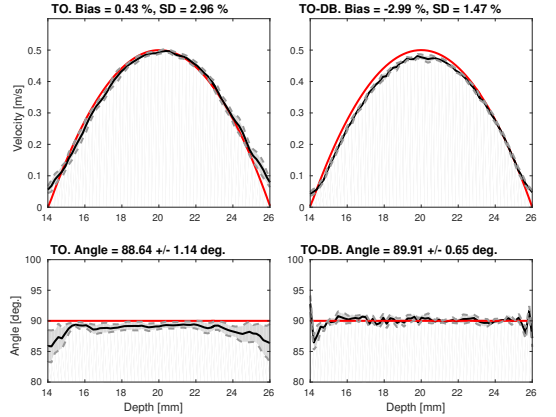


Fig. 4. Simulated velocity profiles for a straight vessel phantom at a 90° beam-to-flow-angle. Velocity magnitude (top) and angles (bottom) for TO (left) and TO-DB (right). Mean estimates are shown in black with ± 1 SD and true profiles are in red.

and straight vessel simulations allows for direct comparison between simulations and measurements.

C. In Vivo Measurement

An *in vivo* scan is conducted after approval by the local research ethics committee (Protocol No. H-1-2014-fsp-072). A 27-year old healthy male is scanned after informed consent by an experienced radiologist. The right carotid bifurcation is scanned in a longitudinal view. The scan sequence is the same as for simulation and flow rig measurements, and the f_{prf} is 10 kHz. Data are acquired for 10 s. Discrimination between tissue and blood is based on intensity values in the B-mode images, where intensities below a threshold are considered to be blood.

Intensity and temperature measurements are performed prior to the *in vivo* scan to assure compliance with FDA regulations [43]. Mechanical index (MI) and derated spatial-peak temporal average intensity ($I_{spta.3}$) are measured using the Acoustic Intensity Measurement System AIMS III (Onda Corp., Sunnyvale, CA, USA) and an Onda HGL-0400 hydrophone. The approach described in [44] is used, and results for the sequence are $MI = 1.25$ and $I_{spta.3} = 267 \text{ mW/cm}^2$. This is within FDA limits, which are $MI = 1.9$ and $I_{spta.3} = 720 \text{ mW/cm}^2$. Transducer surface temperature rise is measured to 18.6°C in still air and 6.3°C when attached to a phantom. The values are below the FDA limits of 27°C and 10°C , respectively.

IV. RESULTS

A. Simulations

1) *Straight vessel phantom*: Results for simulated straight vessel phantoms are shown in Fig. 4 and 5 for beam-to-flow angles of 90° and 60° , respectively. The mean velocity magnitude and angles for the center line are shown in black with ± 1 SD, and the true velocities and angles are shown in red. Results from the TO estimation are shown in the left

figures, while results for the TO-DB are shown in the right figures. Using TO, the flow angle is accurate especially in the central part of the vessel, and with a larger bias near the vessel walls. Applying TO-DB based on the TO estimates improves the precision of the angle estimates while maintaining a high accuracy. Accuracy and precision of velocity estimates are quantified with mean bias and mean SD relative to the true peak velocity. The velocities are estimated accurately with a bias less than 3% for both TO and TO-DB, and there is a reduction in SD from 5.7% to 1.1% for the 60° beam-to-flow angle when using TO-DB rather than only TO. Relative bias and SD are summarized in Fig. 6 for beam-to-flow angles from 30° to 90°. TO-DB maintains a low SD less than 2° for angles and 2% for velocities at all beam-to-flow angles, while the SD of the TO angle estimate increases significantly, when the beam-to-flow angle is below 60°. There is a small reduction in angle bias using TO-DB rather than only TO, and both TO and TO-DB estimate velocities with a bias less than 4% for all investigated angles. Even though the angles are detected correctly for beam-to-flow angles larger than 60°, there are slightly larger biases on the velocity magnitude estimates for TO-DB than TO. Especially beam-to-flow angles close to 90° are challenging for TO-DB, because the directional (transverse) signals contain mainly low frequencies, and this makes it difficult to accurately detect the lag between the signals.

The variation in SD for TO angles as a function of beam-to-flow angle is also the reason for the choice of different $\Delta\theta$ -steps for DB. There is a larger uncertainty in TO angle estimates at smaller beam-to-flow-angles compared to beam-to-flow angles close to 90°. Thus, a larger $\Delta\theta$ is needed to cover 68 % of the estimates for imprecise TO angles. For beam-to-flow angles less than 45°, the SD of the TO angles are 12° - 17°, however, $\Delta\theta$ for DB is set to 10° in (15). The simulations have also been tested for $\Delta\theta = 17^\circ$ at a 30° beam-to-flow angle, but showed no significant improvement in performance compared to $\Delta\theta = 10^\circ$.

Lateral TO velocity estimates, v_x , are obtained after TO filtering prior to applying the phase-shift TO estimator. The filtering removes energy, and the performance of the estimator is therefore investigated for a variation in SNR, see Fig. 7. The performance of the time-shift estimator used for the axial velocity component v_z is also shown in the figure. A loss in SNR degrades the velocity estimates, and the SD of v_x increases significantly when the SNR is below 0 dB, and below 5 dB for v_z . The bias is maintained below 5% for v_z and v_x at 0 dB SNR.

2) *CFD simulations*: Vector flow images at time instances during peak systole and systolic deceleration are shown in Fig. 8 and 9. The reference CFD frames are shown to the left, where velocity vectors are overlaid on a color wheel map, which depends on both velocity magnitude and angle. The ultrasound simulated estimates after TO and TO-DB processing are shown in the middle and to the right, respectively. There is a good agreement between the reference CFD images and estimated VFI frames as provided by visual inspection of the images. At peak systole in Fig. 8 there are, however, wrong estimations close to the vessel walls, where velocities are low,

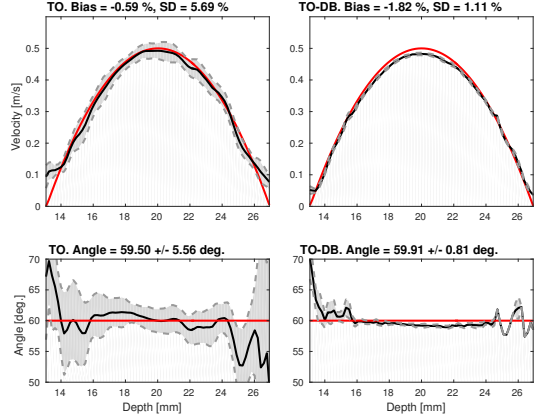


Fig. 5. Simulated velocity profiles for a straight vessel phantom at a 60° beam-to-flow-angle. Velocity magnitude (top) and angles (bottom) for TO (left) and TO-DB (right). Mean estimates are shown in black with ± 1 SD and true profiles are in red.

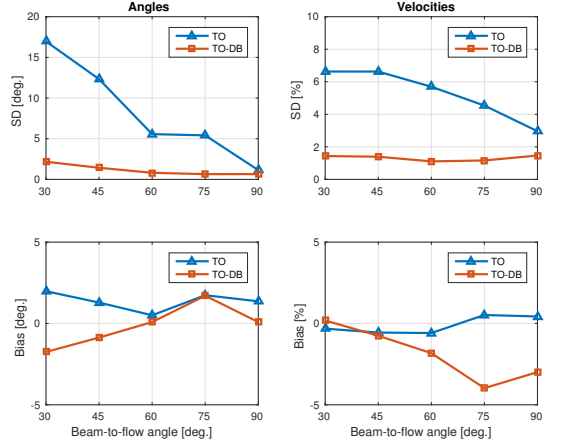


Fig. 6. Results for simulated vessel phantoms with beam-to-flow angles from 30° to 90°. SD (top) and bias (bottom) for estimation of angles (left) and velocities (right). Red graphs show results for TO and blue graphs show results for TO-DB.

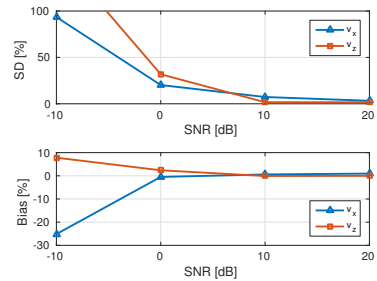


Fig. 7. Variation in SD (top) and bias (bottom) as a function of SNR. Blue graphs are for lateral velocity estimates v_x , and red graphs are for axial velocity estimates v_z .

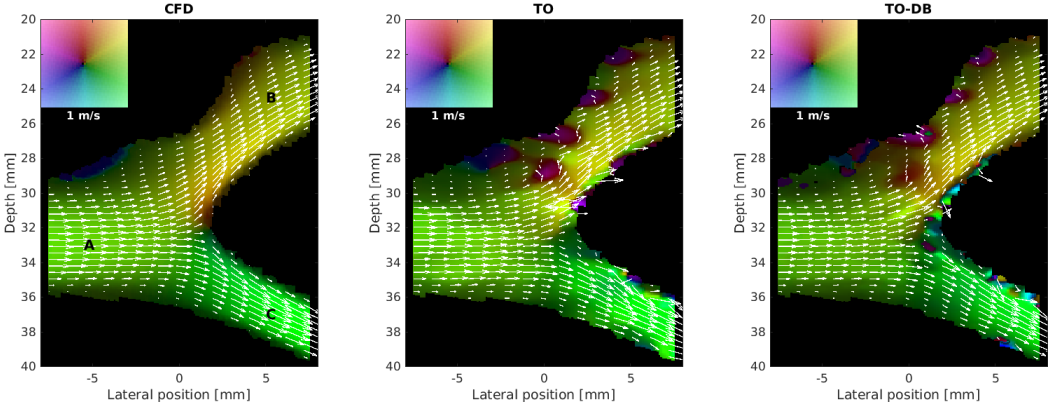


Fig. 8. Results from simulation of flow in a carotid bifurcation model. Frames are shown at peak systole from the reference CFD model (left), estimated velocities using TO (middle), and estimated velocities using TO-DB (right). A, B and C indicate the common, internal, and external carotid artery, respectively

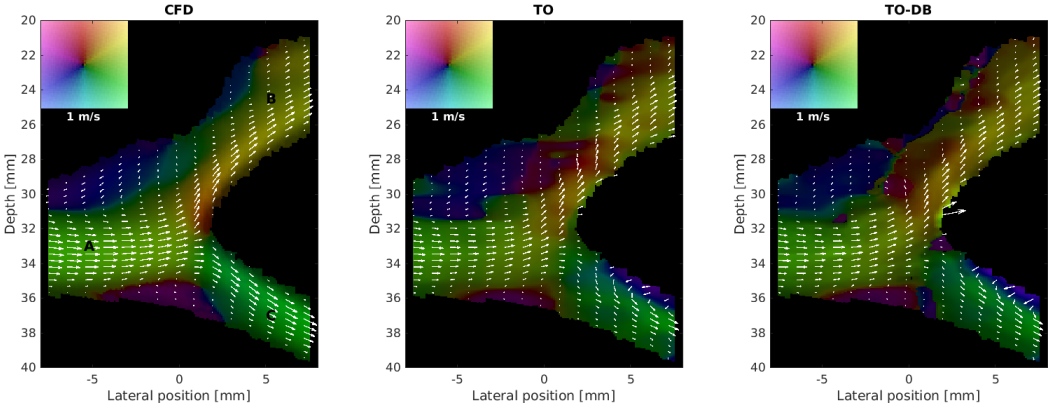


Fig. 9. Results from simulation of flow in a carotid bifurcation model. Frames are shown at systolic deceleration from the reference CFD model (left), estimated velocities using TO (middle), and estimated velocities using TO-DB (right). A, B and C indicate the common, internal, and external carotid artery, respectively

and also areas with wrong angle estimates in the internal carotid artery. Fig. 9 presents complex flow patterns, and the two vortices are clearly visualized and defined using TO-DB. Wrong TO angle estimates with low velocities in the area around (5, 23) mm in the internal carotid artery are corrected with the TO-DB step.

Scatter plots of estimated versus reference velocities and angles are shown in Fig. 10 and 11 to provide a quantitative comparison. Estimated velocities and angles at all spatial points for the frame at peak systole are used for the scatter plots with TO estimates to the left and TO-DB to the right. The colors encode either estimated angle or velocity magnitude, and the straight red lines are the reference values. For velocity magnitude, there is an underestimation of velocities when using TO-DB, represented by a linear regression slope of 0.85 for TO-DB compared to 0.97 for TO. The spread of estimates along the regression line is quantified as the interquartile range, which is 11.8 cm/s for TO and 7.1 cm/s for TO-DB. For the angle scatter plots in Fig. 11, the linear regression slope is 1.01

for both TO and TO-DB, while the angle spread is highest for TO: 6.7° for TO and 4.7° for TO-DB.

It is also seen in Fig. 11 that wrongly estimated angles in the internal carotid artery in Fig. 8 are present as 300° angle estimates for true 60° angles. True angles at 120° (in the external carotid) are also wrongly estimated as random angles. Furthermore, backflow near the upper wall in the common carotid artery (true 240° angles) are estimated as angles ranging from 100° to 200° . The angle errors are further investigated by plotting the distribution of angle errors as a function of velocity as shown in Fig. 12 for TO-DB estimates. It shows that the largest angle errors are found for true velocities less than 0.3 m/s, which are found close to the vessel walls. The angle error is smaller for high velocities.

B. Flow Rig Measurements

Results from flow rig measurements are shown in Fig. 13 for a 90° beam-to-flow angle and in Fig. 14 for a 60°

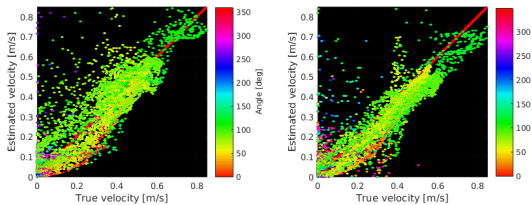


Fig. 10. Scatter plots of true (CFD) velocities versus ultrasound estimations of velocity magnitudes at peak systole. Estimates from TO (left) and TO-DB (right) color encoded with estimated angle.

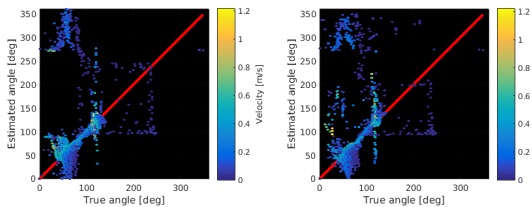


Fig. 11. Scatter plots of true (CFD) angles versus ultrasound estimations of angles at peak systole. Estimates from TO (left) and TO-DB (right) color encoded with estimated velocity.

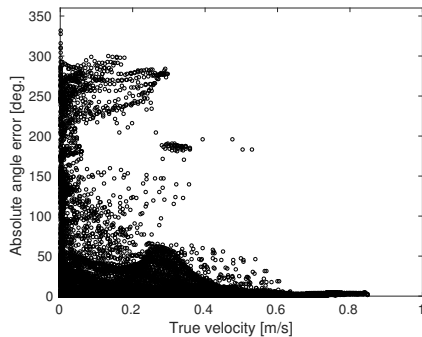


Fig. 12. Scatter plot of the angle error versus velocity magnitude for TO-DB estimation.

beam-to-flow angle. The same trends from the straight vessel simulations are present: a reduction in SD of velocity and angle estimates when using TO-DB rather than only TO, and bias at the same or slightly increased level for TO-DB compared to TO. The wrong estimations close to the vessel walls are due to the echo-canceling filter, which removes all energy from blood and tissue. To avoid the boundary effects, bias and SD are calculated within 90% of the vessel radius. The SD of the velocity magnitude estimates is above 7% when using TO in the two measurements, but is reduced to less than 2% using TO-DB. The 60° beam-to-flow angle is estimated to a mean angle ± 1 SD of $58.9^\circ \pm 5.6^\circ$ using TO and $59.4^\circ \pm 0.9^\circ$ using TO-DB. The experimental results are overall in good agreement with simulation results, only with a small increase in bias and SD for experiments compared to simulations.

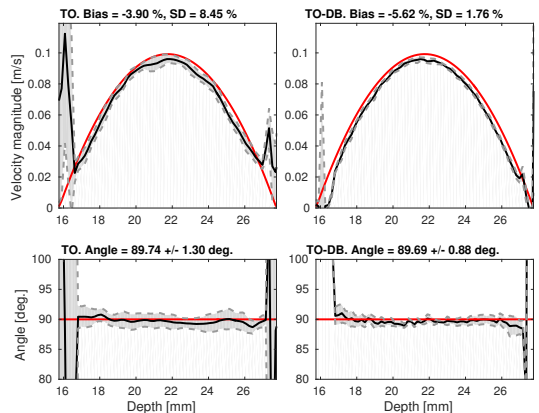


Fig. 13. Measured velocity profiles for a straight vessel phantom at a 90° beam-to-flow-angle. Velocity magnitude (top) and angles (bottom) for TO (left) and DB (right). Mean estimates are shown in black with ± 1 SD and true profiles are in red.

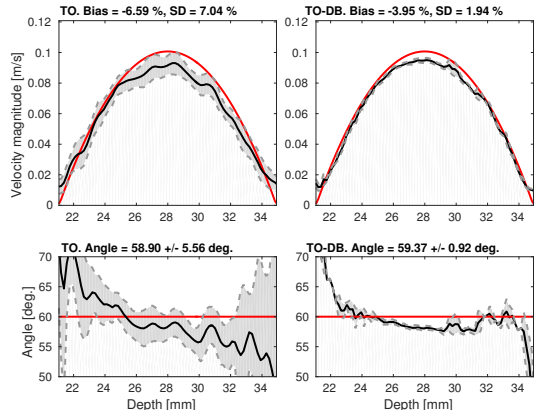


Fig. 14. Measured velocity profiles for a straight vessel phantom at a 60° beam-to-flow-angle. Velocity magnitude (top) and angles (bottom) for TO (left) and DB (right). Mean estimates are shown in black with ± 1 SD and true profiles are in red.

C. In Vivo Measurement

Frames from the *in vivo* scan at peak systole and late systole are shown in Fig. 15, which are processed using TO (left images) and TO-DB (right images). The carotid bifurcation was scanned with a longitudinal view, and the internal carotid is the shallow vessel, while the external carotid is the deep vessel. The direction of flow is indicated by arrows, and reveal a vortex at peak systole in the internal carotid artery. Both TO and TO-DB visualize the vortex, and the TO-DB method estimates a more streamlined flow with less angle spread at the inlet of the internal carotid. TO and TO-DB estimate similar angles and velocities during late systole, however, back-flow close to the vessel walls as estimated using TO is not detected using TO-DB. Low velocities close to vessel walls are challenging to estimate, and since the TO flow angle might

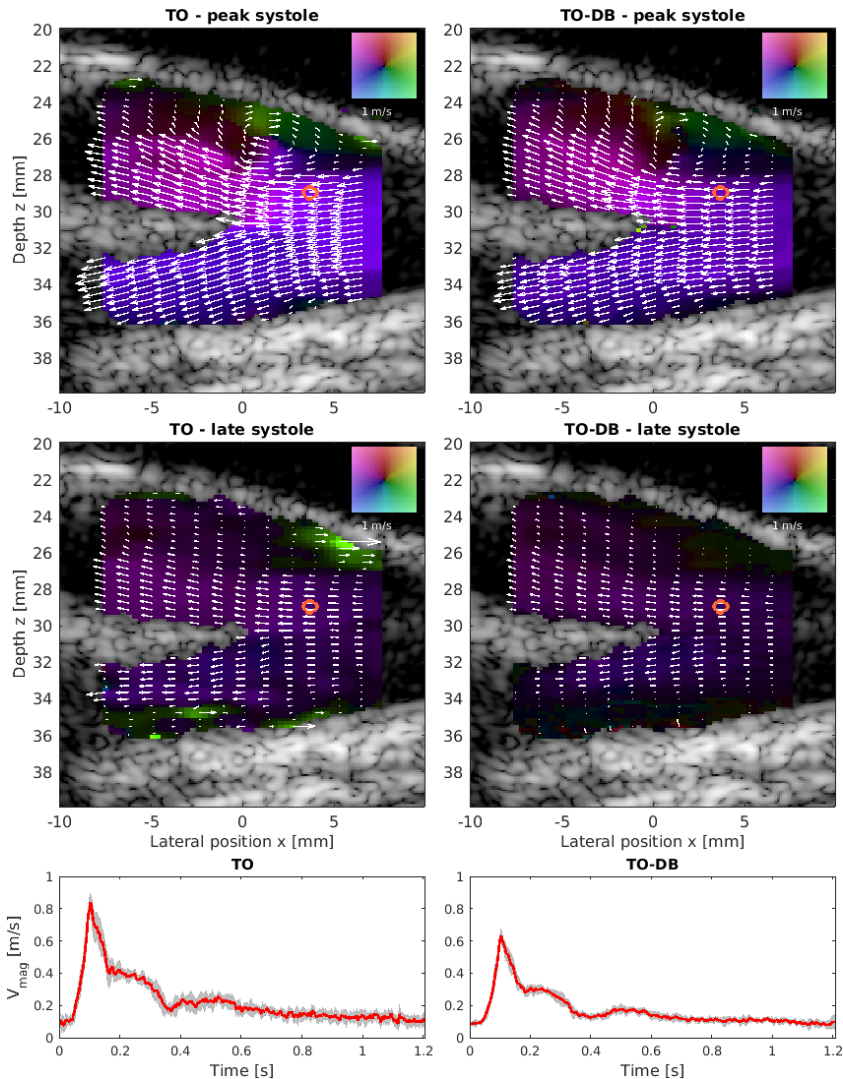


Fig. 15. *In vivo* scan of the carotid bifurcation on a 27 year old healthy volunteer. VFI for frames at peak systole (top) and late systole (middle), and estimates using TO are in the left images while estimates using DB are in the right images. The bottom figures show velocity magnitude at a single estimation point (orange circle on VFI) after alignment to the cardiac cycle. The mean \pm one SD is shown for TO (left) and TO-DB (right).

be estimated wrongly here, the estimated velocity magnitude using TO-DB will be close to zero.

Seven distinct cardiac cycles are detected during the scan acquisition, and the velocity magnitude profiles are divided and aligned to the cardiac cycle. This is shown for the velocity magnitude at the indicated orange circle in Fig. 15 (bottom) for TO (left) and TO-DB (right). The red curves are the mean estimates and the gray area is \pm one SD. The mean SD of the velocity magnitude for TO is calculated to 4.2% and 3.2% for TO-DB. The mean peak velocity is 0.84 m/s for TO and 0.64 m/s for TO-DB. A video sequence from the full acquisition

is available as a multimedia attachment, where velocities are estimated at a frame rate of 300 frames/s. This frame rate is fast enough to capture the formation of the vortex present during peak systole, but the frame rate for velocity estimation could be increased to its maximum of 2000 frames/s using the acquired data. The corresponding B-mode imaging has a frame rate of 119 Hz.

Fig. 16 shows a VFI frame at peak systole taken from the same time instance as in Fig. 15 (top). TO is used for velocity estimation, but a Hoeks filter is applied for echo-canceling. The vortex is poorly estimated and flow in the external carotid

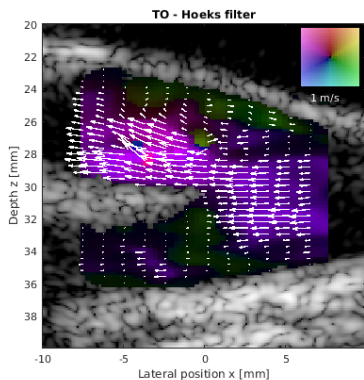


Fig. 16. VFI frame at peak systole using TO for velocity estimation. A Hoeks filter is used for echo-canceling.

artery is lost. Large vessel wall movements and flow in the transverse direction to the ultrasound beam compromise echo-canceling using the Hoeks filter. Low velocities from vessel wall clutter passes the echo-canceling filter and overpowers the blood signal. The example shows that using the energy-based echo-canceling filter is superior to the traditional Hoeks filter in this case.

V. DISCUSSION

The TO-DB method estimates flow angle and velocity magnitude accurately for constant flow in a vessel at all investigated beam-to-flow angles as shown in Fig. 6. The method features a constant low SD less than 2% for velocities and 2° for angles. This is also an improvement compared to TO, which has a SD larger than 6% on the velocity magnitude for small beam-to-flow angles. The bias is within 2% for TO, which is also the case for TO-DB except at 75° and 90° , where bias is closer to 4%. This is still within acceptable levels. An alternative is to compensate for the velocity bias at beam-to-flow angles close to 90° , due to the low bias on the angles and the low SD of both velocity magnitudes and angles. There is also some over and underestimation of the flow angle near the vessel walls (Fig. 5 and 14), which may be due to the echo-canceller, which removes nearly all energy from blood here. The simulation of flow in a bifurcation model provided good estimation of velocities and angles during systolic deceleration, when using TO-DB. Velocities were underestimated during systole (regression coefficient of 0.85 for TO-DB and 0.97 for TO), but with less spread of the estimates for TO-DB. The problem of underestimated velocities around 90° may be solved by increasing the high frequency content in the directional signals, which helps to detect more accurately the lag between signals. It can be achieved by using a lower receive $F\#$ and/or larger steering of the emitted plane waves. The low frequency signals are mainly an issue for broad band estimators like TO-DB, while TO uses a narrow band estimator and mainly considers the phase-shift around a desired lateral oscillation frequency. TO and DB use

fundamentally different estimators: TO estimates the velocity vector by two independent axial and lateral estimators, while DB estimates velocity magnitude from a given flow angle. Any small angle error results in underestimated velocities for DB due to the cosine factor.

The initial estimation of angle and velocity using TO can potentially be employed as prior information for TO-DB to choose line length, correlation time, and angle span $\Delta\theta$. Fig. 12 showed that the smallest angle errors were obtained for high velocities, while the angle error increased for low velocities. Estimated velocities scale with f_{prf} , and the angle errors can possibly be reduced for low velocities by reducing f_{prf} . Since continuous data is available, a lower effective f_{prf} can be synthesized artificially during periods with slow flow by skipping HRIs used for velocity estimation, while maintaining the system f_{prf} .

A weakness of the proposed method is its dependence on the TO angle estimate. If the TO angle is estimated with an error more than $\pm\Delta\theta$, then the TO-DB angle estimate will also be biased. The improvement on the angle estimate using TO-DB can only be within the investigated angle span $\pm\Delta\theta$. When the TO-DB angles are detected and the SD of the angle estimates are calculated, it is expected that the SD of the angle estimate will be lower than the angle span, because it limits the search span for angles. Yet, it is not guaranteed that the SD of the velocity magnitude estimate is reduced compared to TO, and that it is detected accurately. This is, however, what is achieved using the method as shown in Fig. 6. It should be noted that other angle spans (15) may be used, or additional lines within the three lines can be beamformed to reduce the angle span, e.g. for small beam-to-flow angles, where the SD of the TO estimates is larger than 10° . It might also reduce the risk of detecting false angles, which would otherwise draw the TO-DB angle away from a correct TO angle. Another proposal could be to use only the TO angle and directionally beamform a line in this direction to estimate velocity magnitude using cross-correlation.

Given a beamforming load for the TO-DB method, which is 4.6 times larger than for TO and seven times smaller than for NCF DB, the method places itself between TO and NCF DB. An exact comparison depends on the implementation details, since optimization can be performed and some beamformed points can be used for several velocity estimation points.

Phase-based velocity estimators for axial and lateral velocity estimation using TO can suffer from aliasing, which limits the maximum detectable velocity. This is especially an issue in SA systems, where the summation of a number of LRIs reduces the effective f_{prf} . However, the lateral wavelength λ_x can be chosen relatively independent. A small value of λ_x can increase the precision for low velocities, while a larger λ_x avoids aliasing for large velocities. If, e.g. $\lambda_x = 0.2$ cm, the maximum v_x is:

$$v_{x,max} = \frac{\lambda_x}{4} f_{prf,eff} = \frac{0.2 \text{ cm}}{4} \cdot 2 \text{ kHz} = 1 \text{ m/s}. \quad (16)$$

This is sufficient for peak velocities during systole and is about four times larger than the maximum detectable v_z ($v_{z,max} = 0.23$ m/s). In this paper, the axial velocity was estimated using

a cross-correlation estimator to circumvent aliasing problems, which may occur for vessels with a beam-to-flow angle less than 75° . The precision of the cross-correlation estimator can, however, decrease for large beam-to-flow angles [32].

The carotid bifurcation scanning on a volunteer demonstrated the feasibility of the method *in vivo*, where tissue movement, absorption, and complex flow patterns complicate vector flow estimation. Peak velocities were estimated lower for TO-DB compared to TO, which was also the case in the simulated bifurcation model. The flow angle is close to 90° at the estimation point, where small angle errors may give an underestimated velocity magnitude. The transmission of a few plane waves per frame (HRI) is a compromise between capturing fast transient flow events, and having HRI with sufficient image quality in terms of contrast and resolution for detailed flow estimation. Plane wave and SA methods also have the advantages of continuous data everywhere in the image, which may improve slow flow estimation [27] and the use of more advanced echo-canceling filters [45].

One must be careful with comparison to other vector flow imaging methods, since different setups can be used and each method has its own strengths and limitations. Reduced performance for the lateral velocity estimate at low beam-to-flow angles were found for phase-based TO [20] and speckle tracking [13], and this trend was confirmed for the TO estimates here. The reduced performance was solved by applying the TO-DB step. On the contrary, cross-beam Doppler methods are susceptible to velocity errors at large beam-to-flow angles [17].

VI. CONCLUSION

A method for 2-D vector flow imaging where the flow angle is found using a combination of TO and DB was presented. The beamforming load of the TO-DB method is 4.6 times larger than for TO and seven times smaller than for conventional DB. In straight vessel simulations and flow rig measurements, the method estimates flow angle accurately and with a bias and SD less than 2° . The SD of the velocity magnitude estimates is less than 2%, which is 2-3 times less than for the TO method. Simulations of realistic flow in a carotid bifurcation model provided good visualization of complex flow during systolic deceleration when using TO-DB. However, an underestimation of velocities was obtained at peak systole. The method was employed with plane waves in transmit, and this acquisition scheme achieves a very high frame rate of 2000 fps for flow estimation. Such high frame rates can capture fast transient flow events, and it was demonstrated in the carotid bifurcation *in vivo*.

ACKNOWLEDGMENTS

This work was supported by grant 82-2012-4 from the Danish National Advanced Technology Foundation and by BK Ultrasound Aps.

REFERENCES

- [1] J. A. Jensen, S. Nikolov, K. L. Gammelmark, and M. H. Pedersen, "Synthetic aperture ultrasound imaging," *Ultrasonics*, vol. 44, pp. e5–e15, 2006.
- [2] M. Tanter, J. Bercoff, L. Sandrin, and M. Fink, "Ultrafast compound imaging for 2-D motion vector estimation: application to transient elastography," *IEEE Trans. Ultrason., Ferroelec., Freq. Contr.*, vol. 49, pp. 1363–1374, 2002.
- [3] G. E. Trahey, J. W. Allison, and O. T. von Ramm, "Angle independent ultrasonic detection of blood flow," *IEEE Trans. Biomed. Eng.*, vol. BME-34, no. 12, pp. 965–967, 1987.
- [4] B. Dunmire, K. W. Beach, K.-H. Labs, M. Plett, and D. E. Strandness, "Cross-beam vector Doppler ultrasound for angle independent velocity measurements," *Ultrasound Med. Biol.*, vol. 26, pp. 1213–1235, 2000.
- [5] J. A. Jensen and P. Munk, "A new method for estimation of velocity vectors," *IEEE Trans. Ultrason., Ferroelec., Freq. Contr.*, vol. 45, no. 3, pp. 837–851, 1998.
- [6] M. E. Anderson, "Multi-dimensional velocity estimation with ultrasound using spatial quadrature," *IEEE Trans. Ultrason., Ferroelec., Freq. Contr.*, vol. 45, pp. 852–861, 1998.
- [7] H. Liebgott, J. Wilhelm, J. A. Jensen, D. Vray, and P. Delachartre, "PSF dedicated to estimation of displacement vectors for tissue elasticity imaging with ultrasound," *IEEE Trans. Ultrason., Ferroelec., Freq. Contr.*, vol. 54, no. 4, pp. 746–756, 2007.
- [8] J. A. Jensen, "Directional velocity estimation using focusing along the flow direction: I: Theory and simulation," *IEEE Trans. Ultrason., Ferroelec., Freq. Contr.*, vol. 50, pp. 857–872, 2003.
- [9] S. Ohtsuki and M. Tanaka, "The flow velocity distribution from the doppler information on a plane in three-dimensional flow," *J. of Visualization*, vol. 9, no. 1, pp. 69–82, 2006.
- [10] D. García, J. C. del Alamo, D. Tanne, R. Yotti, C. Cortina, E. Bertrand, J. C. Antoranz, E. Perez-David, R. Rieu, F. Fernandez-Aviles, and J. Bermejo, "Two-dimensional intravascular flow mapping by digital processing conventional color-doppler echocardiography images," *IEEE Trans. Med. Imag.*, vol. 29, no. 10, pp. 1701–1713, 2010.
- [11] S. I. Nikolov and J. A. Jensen, "Velocity estimation using synthetic aperture imaging," in *Proc. IEEE Ultrason. Symp.*, 2001, pp. 1409–1412.
- [12] —, "In-vivo synthetic aperture flow imaging in medical ultrasound," *IEEE Trans. Ultrason., Ferroelec., Freq. Contr.*, vol. 50, no. 7, pp. 848–856, 2003.
- [13] J. Udesen, F. Gran, K. L. Hansen, J. A. Jensen, C. Thomsen, and M. B. Nielsen, "High frame-rate blood vector velocity imaging using plane waves: simulations and preliminary experiments," *IEEE Trans. Ultrason., Ferroelec., Freq. Contr.*, vol. 55, no. 8, pp. 1729–1743, 2008.
- [14] K. L. Hansen, J. Udesen, F. Gran, J. A. Jensen, and M. B. Nielsen, "In-vivo examples of flow patterns with the fast vector velocity ultrasound method," *Ultraschall in Med.*, vol. 30, pp. 471–476, 2009.
- [15] J. Bercoff, G. Montaldo, T. Loupas, D. Savery, F. Meziere, M. Fink, and M. Tanter, "Ultrafast compound Doppler imaging: providing full blood flow characterization," *IEEE Trans. Ultrason., Ferroelec., Freq. Contr.*, vol. 58, no. 1, pp. 134–147, January 2011.
- [16] I. K. Ekroll, A. Swillens, P. Segers, T. Dahl, H. Torp, and L. Lovstakken, "Simultaneous quantification of flow and tissue velocities based on multi-angle plane wave imaging," *IEEE Trans. Ultrason., Ferroelec., Freq. Contr.*, vol. 60, no. 4, pp. 727–738, 2013.
- [17] S. Fadnes, I. K. Ekroll, S. A. Nytnes, H. Torp, and L. Løvstakken, "Robust angle-independent blood velocity estimation based on dual-angle plane wave imaging," *IEEE Trans. Ultrason., Ferroelec., Freq. Contr.*, vol. 62, no. 10, pp. 1757–1767, October 2015.
- [18] B. Y. Yiu, S. S. Lai, and A. C. Yu, "Vector projectile imaging: time-resolved dynamic visualization of complex flow patterns," *Ultrasound Med. Biol.*, vol. 40, no. 9, pp. 2295–2309, sept 2014.
- [19] S. Ricci, L. Bassi, and P. Tortoli, "Real-time vector velocity assessment through multigate Doppler and plane waves," *IEEE Trans. Ultrason., Ferroelec., Freq. Contr.*, vol. 61, no. 2, pp. 314–324, 2014.
- [20] M. Lenge, A. Ramalli, P. Tortoli, C. Cachard, and H. Liebgott, "Plane-wave transverse oscillation for high-frame-rate 2-D vector flow imaging," *IEEE Trans. Ultrason., Ferroelec., Freq. Contr.*, vol. 62, no. 12, pp. 2126–2137, December 2015.
- [21] J. A. Jensen, "Directional transverse oscillation vector flow estimation," *IEEE Trans. Ultrason., Ferroelec., Freq. Contr.*, vol. 63, p. Submitted, 2016.
- [22] —, "Comparison of vector velocity imaging using directional beamforming and transverse oscillation for a convex array transducer," in *Proc. SPIE Med. Imag.*, vol. 9040, 2014, pp. 904012–1–8.
- [23] J. A. Jensen and N. Odershed, "Estimation of velocity vectors in synthetic aperture ultrasound imaging," *IEEE Trans. Med. Imag.*, vol. 25, pp. 1637–1644, 2006.
- [24] C. A. Villagomez-Hoyos, M. B. Stuart, K. L. Hansen, M. B. Nielsen, and J. A. Jensen, "Accurate angle estimator for high frame rate 2-D

- vector flow imaging," *IEEE Trans. Ultrason., Ferroelec., Freq. Contr.*, vol. 63, no. 6, pp. 842–853, 2016.
- [25] J. Jensen, M. B. Stuart, and J. A. Jensen, "High frame rate vector velocity estimation using plane waves and transverse oscillation," in *Proc. IEEE Ultrason. Symp.*, 2015, pp. 1–4.
- [26] J. Jensen, C. A. Villagomez-Hoyos, M. B. Stuart, C. Ewertsen, M. B. Nielsen, and J. A. Jensen, "In vivo high frame rate vector flow imaging using plane waves and directional beamforming," in *Proc. IEEE Ultrason. Symp.*, 2016, pp. 1–4.
- [27] E. Mace, G. Montaldo, I. Cohen, M. Baulac, M. Fink, and M. Tanter, "Functional ultrasound imaging of the brain," *Nature methods*, vol. 8, no. 8, pp. 662–664, 2011.
- [28] F. Varray and H. Liebgott, "An alternative method to classical beamforming for transverse oscillation images: Application to elastography," *IEEE 10th Int. Symp. Biomedical Imaging*, pp. 716–719, 2013.
- [29] S. Salles, A. J. Y. Chee, D. Garcia, A. C. H. Yu, D. Vray, and H. Liebgott, "2-D arterial wall motion imaging using ultrafast ultrasound and transverse oscillations," *IEEE Trans. Ultrason., Ferroelec., Freq. Contr.*, vol. 62, no. 6, pp. 1047–1058, 2015.
- [30] J. A. Jensen, "A new estimator for vector velocity estimation," *IEEE Trans. Ultrason., Ferroelec., Freq. Contr.*, vol. 48, no. 4, pp. 886–894, 2001.
- [31] O. Bonnefous and P. Pesqué, "Time domain formulation of pulse-Doppler ultrasound and blood velocity estimation by cross correlation," *Ultrason. Imaging*, vol. 8, pp. 73–85, 1986.
- [32] S. G. Foster, P. M. Embree, and W. D. O'Brien, "Flow velocity profile via time-domain correlation: Error analysis and computer simulation," *IEEE Trans. Ultrason., Ferroelec., Freq. Contr.*, vol. 37, pp. 164–175, 1990.
- [33] J. A. Jensen, H. Holten-Lund, R. T. Nilsson, M. Hansen, U. D. Larsen, R. P. Domsten, B. G. Tomov, M. B. Stuart, S. I. Nikolov, M. J. Pihl, Y. Du, J. H. Rasmussen, and M. F. Rasmussen, "SARUS: A synthetic aperture real-time ultrasound system," *IEEE Trans. Ultrason., Ferroelec., Freq. Contr.*, vol. 60, no. 9, pp. 1838–1852, 2013.
- [34] J. Jensen, M. B. Stuart, and J. A. Jensen, "Optimized plane wave imaging for fast and high-quality ultrasound imaging," *IEEE Trans. Ultrason., Ferroelec., Freq. Contr.*, vol. 63, no. 11, pp. 1922–1934, 2016.
- [35] J. M. Hansen, M. C. Hemmsen, and J. A. Jensen, "An object-oriented multi-threaded software beamformation toolbox," in *Proc. SPIE Med. Imag.*, vol. 7968, March 2011, pp. 79 680Y–1–79 680Y–9.
- [36] A. P. G. Hoeks, M. Hennerici, and R. S. Reneman, "Spectral composition of Doppler signals," *Ultrasound Med. Biol.*, vol. 17, pp. 751–760, 1991.
- [37] C. A. Villagomez-Hoyos, "Synthetic aperture vector flow imaging," Ph.D. dissertation, Technical University of Denmark, 2016. [Online]. Available: <http://findit.dtu.dk/en/catalog/2347162876>
- [38] C. A. Villagomez-Hoyos, M. B. Stuart, T. Bechsgaard, M. B. Nielsen, and J. A. Jensen, "High frame rate synthetic aperture vector flow imaging for transthoracic echocardiography," in *Proc. SPIE Med. Imag.*, 2016.
- [39] J. A. Jensen and N. B. Svendsen, "Calculation of pressure fields from arbitrarily shaped, apodized, and excited ultrasound transducers," *IEEE Trans. Ultrason., Ferroelec., Freq. Contr.*, vol. 39, pp. 262–267, 1992.
- [40] J. A. Jensen, "Field: A program for simulating ultrasound systems," *Med. Biol. Eng. Comp.*, vol. 10th Nordic-Baltic Conference on Biomedical Imaging, Vol. 4, Supplement 1, Part 1, pp. 351–353, 1996.
- [41] —, "A multi-threaded version of Field II," in *Proc. IEEE Ultrason. Symp.* IEEE, 2014, pp. 2229–2232.
- [42] A. Swillens, L. Løvstakken, J. Kips, H. Torp, and P. Segers, "Ultrasound simulation of complex flow velocity fields based on computational fluid dynamics," *IEEE Trans. Ultrason., Ferroelec., Freq. Contr.*, vol. 56, no. 3, pp. 546–556, 2009.
- [43] FDA, "Information for manufacturers seeking marketing clearance of diagnostic ultrasound systems and transducers," Center for Devices and Radiological Health, United States Food and Drug Administration, Tech. Rep., 2008.
- [44] J. A. Jensen, M. F. Rasmussen, M. J. Pihl, S. Holbek, C. A. Villagomez-Hoyos, D. P. Bradway, M. B. Stuart, and B. G. Tomov, "Safety assessment of advanced imaging sequences. I: Measurements," *IEEE Trans. Ultrason., Ferroelec., Freq. Contr.*, vol. 63, no. 1, pp. 110–119, 2016.
- [45] C. Demene, T. Defieux, M. Pernot, B.-F. Osmanski, V. Biran, J.-L. Gennisson, L.-A. Sieu, A. Bergel, S. Franqui, J.-M. Correas, I. Cohen, O. Baud, and M. Tanter, "Spatiotemporal clutter filtering of ultrafast ultrasound data highly increases Doppler and fUltrasound sensitivity," *IEEE Trans. Med. Imag.*, vol. 34, no. 11, pp. 2271–2285, 2015.

High Frame Rate Vector Velocity Estimation using Plane Waves and Transverse Oscillation

Jonas Jensen, Matthias Bo Stuart, and Jørgen Arendt Jensen

Proceedings of IEEE International Ultrasonics Symposium, p. 1-4,

Accepted for poster presentation in Taipei, Taiwan, 2015.

High Frame Rate Vector Velocity Estimation using Plane Waves and Transverse Oscillation

Jonas Jensen, Matthias Bo Stuart and Jørgen Arendt Jensen

Center for Fast Ultrasound Imaging, Dept. of Elec. Eng. Bldg. 349,
Technical University of Denmark, DK-2800 Lyngby, Denmark

Abstract—This paper presents a method for estimating 2-D vector velocities using plane waves and transverse oscillation. The approach uses emission of a low number of steered plane waves, which result in a high frame rate and continuous acquisition of data for the whole image. A transverse oscillating field is obtained by filtering the beamformed RF images in the Fourier domain using a Gaussian filter centered at a desired oscillation frequency. Performance of the method is quantified through measurements with the experimental scanner SARUS and the BK 2L8 linear array transducer. Constant parabolic flow in a flow rig phantom is scanned at beam-to-flow angles of 90, 75, and 60°. The relative bias is between -1.4 % and -5.8 % and the relative std. between 5 % and 8.2 % for the lateral velocity component at the measured beam-to-flow angles. The estimated flow angle is $73.4^\circ \pm 3.6^\circ$ for the measurement at 75°. Measurement of pulsatile flow through a constricted vessel demonstrate the application of the method in a realistic flow environment with large spatial and temporal flow gradients.

I. INTRODUCTION

Ultrasound blood flow estimation is of diagnostic value for investigating hemodynamic problems in the human cardiovascular system. Conventional ultrasound imaging systems are limited to only estimate the axial flow velocities along the ultrasound beam and suffer from a very low frame rate. Several methods have been proposed to estimate the full 2-D velocity vector without the need for angle correction, e.g., speckle tracking [1], directional beamforming [2], multibeam methods [3], and transverse oscillation (TO) [4]. The TO method has been FDA approved for clinical use and employs focused beams in line-by-line imaging, however, it is limited by a frame rate, which can be too low for capturing complex flow phenomena and full flow dynamics.

Alternative imaging methods such as synthetic aperture imaging (SA) using either spherical or plane waves (PW) have been proposed to increase the frame rate and improve image quality. An image of the entire insonified region is created for each emission resulting in a low-resolution image. By using a few broad insonifications, the low-resolution images can be summed to form a high-resolution (HR) image. SA has been used for flow estimation [5], and plane waves for 2-D motion estimation [6] and blood flow imaging using speckle tracking [7]. While especially the latter method is computationally demanding, the TO approach is relatively inexpensive in terms of number of calculations.

The objective of this paper is to show the feasibility of TO implemented in a fast imaging sequence using multiple plane

waves to obtain flow estimates for a large field of view. The proposed method uses steered plane wave emissions, which are combined to HR images. The TO fields are generated in the Fourier domain, and computational inexpensive autocorrelation estimators are used for blood vector velocity estimation. A similar approach was proposed in [8], [9], but used only a single plane wave and applied a phase-based block matching method for tissue motion estimation.

II. METHODS

This section describes the method for vector velocity estimation, which is based on the TO approach [4]. A lateral oscillation in the pulse-echo field is introduced along with the conventional axial oscillation, so that the received signals become sensitive to both an axial and lateral motion in the field. The TO field is usually created in the receive beamforming by changing the apodization function to contain two separated peaks. However, a lateral oscillation can also be generated in the Fourier domain, known as k -space, to provide better control over the lateral oscillation wavelength. This is accomplished by using a filter in the Fourier domain, which filters the beamformed image in the lateral dimension to only select k -space components around a desired lateral oscillation frequency.

The process is illustrated in Fig. 1. Beamformed data for a HR image has a k -space as illustrated in Fig. 1 (top). An oscillation in the axial direction is centered at the pulse center frequency, while there is no oscillation laterally. A filter $G(f_z, f_x)$ consisting of Gaussian windows centered around a desired TO frequency f_{0x} ,

$$G(f_z, f_x) = \exp(-2(\pi\sigma_x(f_x - f_{0x}))^2) + \exp(-2(\pi\sigma_x(f_x + f_{0x}))^2), \quad (1)$$

where σ_x is the width of the Gaussian window and f_x is the lateral oscillation frequency, is illustrated in Fig. 1 (middle). A multiplication of the filter and the Fourier transformed image gives the TO image in Fig. 1 (bottom). The image has been filtered in the lateral dimension, while the axial dimension is untouched. Any values of the parameters f_{0x} and σ_x can in principle be chosen, but it should be ensured only to choose k -space components containing energy from flow and not only noise. By having an effective $F\#$ that is relatively small, energy is retained for larger f_x .

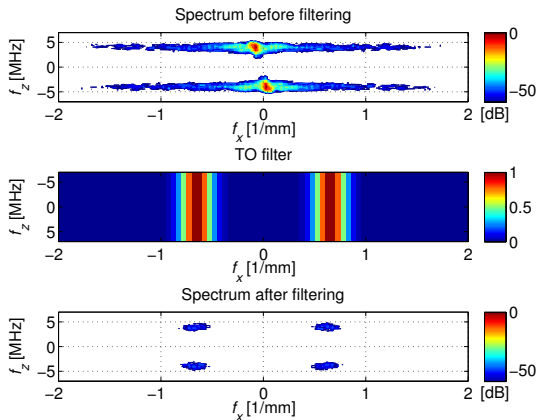


Fig. 1. The 2-D Fourier spectrum of a beamformed RF image is shown in the top figure. The spectrum of the TO filter $G(f_z, f_x)$ is shown in the middle, and the spectrum of beamformed RF image after applying the TO filter is shown in the bottom figure. The resulting RF image contains transverse oscillations with a mean lateral frequency according to the desired oscillation frequency of the TO filter.

The directional information of the flow is preserved by applying the Hilbert transform on the TO image (spatial domain) for each of the lines in the lateral direction. This avoids having a spatial quadrature between two beamformed signals.

The actual mean lateral oscillation frequency \bar{f}_x at a given depth can be estimated from the TO image and used directly in the velocity estimator:

$$\bar{f}_x = \frac{\int_{-f_{sz}/2}^{+f_{sz}/2} \int_{-f_{sx}/2}^{+f_{sx}/2} f_x |H(f_z, f_x)|^2 df_z df_x}{\int_{-f_{sz}/2}^{+f_{sz}/2} \int_{-f_{sx}/2}^{+f_{sx}/2} |H(f_z, f_x)|^2 df_z df_x}, \quad (2)$$

where f_{sz} and f_{sx} are axial and lateral sampling frequencies, respectively, and $H(f_z, f_x)$ is the Fourier transform of the TO image. Echo canceling is performed by subtracting the mean value across all the emissions from the RF signals. A standard fourth order autocorrelation estimator for the transverse velocity component is employed as proposed in [10] and with the estimated mean \bar{f}_x .

III. EXPERIMENTAL SETUP

A BK Ultrasound 2L8 linear array transducer with a center frequency of 4.1 MHz and 0.55 λ pitch is connected to the experimental SARUS scanner [11]. A duplex imaging sequence is implemented, one for B-mode and one for flow. For the B-mode sequence, 33 plane wave emissions equally spaced from -22° to 22° are used. For the flow sequence, plane waves are emitted at three angles (-15° , 0° , and 15°) and a Tukey window is used in transmit to reduce the artifacts from edge waves. The system pulse repetition frequency f_{prf} is 7.5 kHz giving an effective $f_{prf,eff} = f_{prf} / (3 + 1) = 1875$ Hz. Parabolic constant flow in a 6 mm radius tube in a flow rig system is scanned and the volume flow is measured by a magnetic flow meter

TABLE I
VARIED PARAMETERS

Variable parameter	Value
Beam-to-flow angle	60, 75 , 90 [$^\circ$]
Number of emitted PWs	1, 3 , 5, 9
f_{0x}	1, 1.25, 1.53 , 2, 4 [mm]
σ_x	0.5, 1, 1.5 , 2 [mm]
Number of HR images	5, 10, 22, 45 , 90

Default conditions are shown in bold.

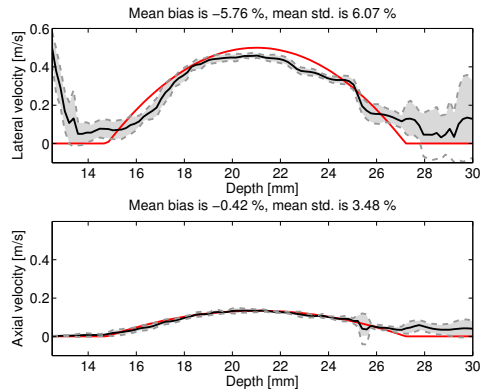


Fig. 2. Measured velocity profiles at a 75° beam-to-flow angle. Lateral (top) and axial (bottom) velocity estimates with the true velocity profiles in red.

for reference (MAG 3000, Danfoss, Nordborg, Denmark). The vessel is at a depth of 22 mm, and flow with a peak velocity of 0.5 m/s is measured at beam-to-flow angles of 90, 75, and 60° . Table I lists the parameters that are varied in the study, and the parameters indicated with bold are for the default setup.

Pulsating flow was also scanned using an in-house fabricated flow phantom comprised of a straight tube with a concentric constriction of 36%. The tube was surrounded by a tissue-mimicking material consisting of 15% polyvinyl alcohol cryogel, 1% silicon dioxide, 0.3% potassium sorbate, and 83.7% distilled water [12]. A blood-mimicking fluid was circulated through the tube in a closed loop circuit, and flow was generated by a CompuFlow 1000 system (Shelley Automation, Toronto, Canada).

Data were processed off-line, and delay-and-sum beamforming was performed using a dynamic apodization in receive with an $F\# = 1$.

IV. RESULTS

A. Constant flow

Velocity profiles for a measurement at a 75° beam-to-flow angle using the default setup are shown in Fig. 2, where the top figure shows mean and standard deviation (std.) of the profile for the lateral velocity component. The relative bias for the lateral component is -5.8% . Selections of 45 HR images are used for each velocity estimate and with an overlap of 75% between each selection, the frame rate is 167 Hz.

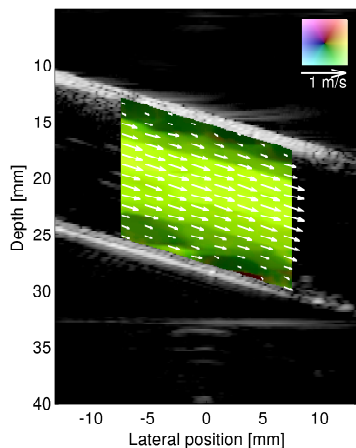


Fig. 3. Vector flow image of a measurement on the flow rig at a beam-to-flow angle of 75° . The flow is constant and parabolic with a peak velocity of 0.5 m/s.

A vector flow image for the measurement at 75° is shown in Fig. 3, where the arrows indicate direction and magnitude of the flow. The beam-to-flow angle was estimated from the velocity data to be $73.4^\circ \pm 3.6^\circ$ at the center line.

Fig. 4 shows the performance of the lateral velocity component when four parameters have been varied. The relative bias is shown with a solid line, while the relative std. is a dashed line. Measurements at beam-to-flow angles of 60° , 75° , and 90° are shown in Fig. 4(a), and the relative std. is lowest at 90° (5.6%), while it increases for smaller beam-to-flow angles.

The performance of the method, when changing the number of emitted plane waves are shown in Fig. 4(b). The experiment was performed at 75° beam-to-flow angle, with a flow sequence of 9 PWs emitted from -15° to 15° , and the peak velocity of the flow reduced to 0.25 m/s to avoid aliasing. The number of PWs used for each HR image was then varied in the post-processing. The relative std. is constant and around 5% as a function of the number of emitted PWs, while the bias is smallest for 1 and for 9 PWs. The motivation for using steered PWs is that a larger aperture is synthesized, i.e., the lateral resolution is improved and more energy is collected for larger f_x . A larger number of emitted PWs reduces $f_{prf,eff}$ and the maximum detectable velocity, but should decrease the std., theoretically. It was, however, not the case with the current setup.

The result of varying parameters for the TO filter, i.e., the desired lateral oscillation frequency f_{0x} and width of the Gaussian window σ_x is shown in Fig. 4(c) and (d), respectively. It is calculated for the default measurement setup at 75° . While the bias and std. are almost constant for a changing σ_x , they are more influenced by f_{0x} . The std. increases from 5% to 12.5%, when reducing $1/f_{0x}$ from 1.53 mm to 1 mm. It indicates that

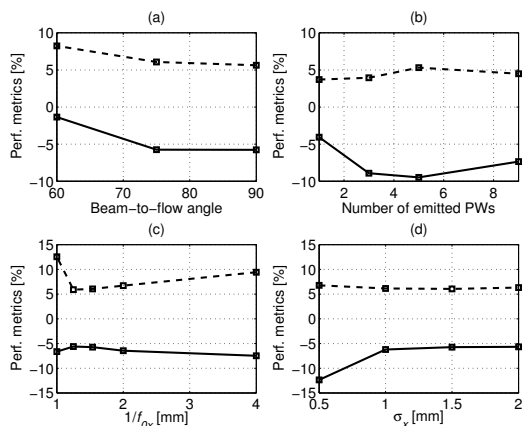


Fig. 4. Performance metrics for the lateral velocity component as a function of various parameter settings: Relative mean bias (solid line) and relative mean std. (dashed line).

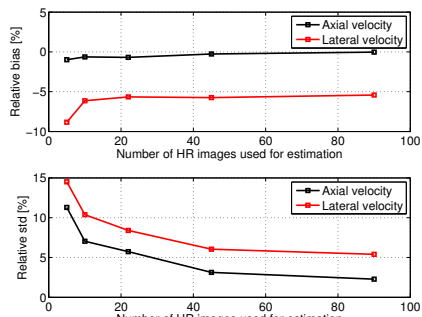


Fig. 5. Relative bias (top) and std (bottom) for a variation in the number of HR images used for velocity estimation. The beam-to-flow angle is 75° .

more energy is picked up from noise by the TO filter at $1/f_{0x} = 1$ mm. The smallest bias and std. are obtained by setting $1/f_{0x} = 1.53$ m and $\sigma_x = 1.5$ mm.

The relative bias and std. as a function of the number of HR images used for velocity estimation are shown in Fig. 5 for the axial and lateral velocity components. The beam-to-flow angle is 75° and the bias is -5% and std. reaches 5% for the lateral component, when using 90 HR images, while the axial velocity is unbiased. The std. follows the expected $1/\sqrt{N}$ trend, where N is the number of HR images.

B. Pulsatile flow

A carotid flow profile is generated by the pump with a peak volume flow set to 3 mL/s and a cardiac period of 0.84 sec. Three seconds of data were acquired and processed with the TO method. A vector flow image from peak systole is shown in Fig. 6 and from diastole in Fig. 7. The lateral velocity estimate v_x in the center of the constricted tube is shown as a function of time in the bottom figures. Back-flow occur after

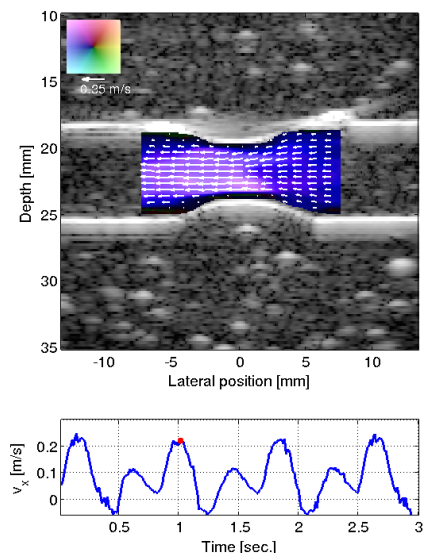


Fig. 6. Measurement of constricted vessel with pulsatile flow. The top figure shows the vector flow image at peak systole, and the bottom figure is the lateral velocity profile estimated in the center of the constriction.

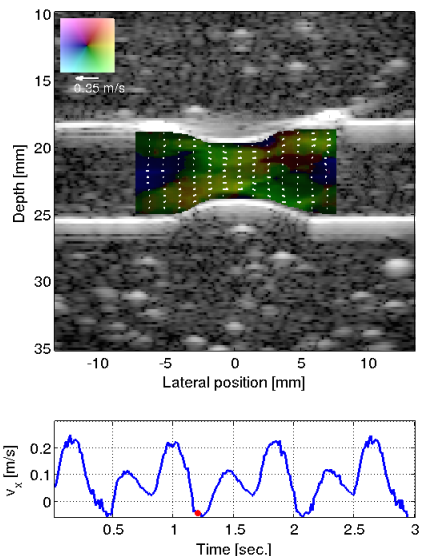


Fig. 7. Measurement of constricted vessel with pulsatile flow. The top figure shows the vector flow image at diastole, and the bottom figure is the lateral velocity profile estimated in the center of the constriction.

the systole, which can be due to the vessel compliance. By dividing the profile of v_x into three segments of length of a cardiac period, the mean std. of the profile is calculated to be 4.9 % relative to the peak velocity.

V. DISCUSSION AND CONCLUSION

A high-frame rate method for estimating 2-D vector velocities using plane waves and transverse oscillation were presented. Three steered plane waves were emitted and the beamformed images were summed and used for flow estimation. A transverse oscillating field was obtained by filtering the beamformed RF images in the Fourier domain. The method provides large flexibility, since beamforming is performed once, and TO is generated subsequently at a desired wavelength and window width, which adaptively can be changed depending on the type of flow. The bias and std. were measured to be -5.8 % and 5.6 %, respectively, for fully transverse flow. The frame rate of the method was 167 Hz and can be changed depending on the number of HR images and overlap of selections used for estimation.

ACKNOWLEDGEMENT

This work was supported by grant 82-2012-4 from the Danish National Advanced Technology Foundation and by BK Ultrasound.

REFERENCES

- [1] G. E. Trahey, J. W. Allison, and O. T. von Ramm, "Angle independent ultrasonic detection of blood flow," *IEEE Trans. Biomed. Eng.*, vol. BME-34, pp. 965–967, 1987.
- [2] J. A. Jensen, "Directional velocity estimation using focusing along the flow direction: I: Theory and simulation," *IEEE Trans. Ultrason., Ferroelec., Freq. Contr.*, vol. 50, pp. 857–872, 2003.
- [3] B. Dunmire, K. W. Beach, K.-H. Labs, M. Plett, and D. E. Strandness, "Cross-beam vector Doppler ultrasound for angle independent velocity measurements," *Ultrasound Med. Biol.*, vol. 26, pp. 1213–1235, 2000.
- [4] J. A. Jensen and P. Munk, "A new method for estimation of velocity vectors," *IEEE Trans. Ultrason., Ferroelec., Freq. Contr.*, vol. 45, pp. 837–851, 1998.
- [5] S. I. Nikolov and J. A. Jensen, "In-vivo Synthetic Aperture Flow Imaging in Medical Ultrasound," *IEEE Trans. Ultrason., Ferroelec., Freq. Contr.*, vol. 50, no. 7, pp. 848–856, 2003.
- [6] M. Tanter, J. Bercoff, L. Sandrin, and M. Fink, "Ultrafast compound imaging for 2-D motion vector estimation: application to transient elastography," *IEEE Trans. Ultrason., Ferroelec., Freq. Contr.*, vol. 49, pp. 1363–1374, 2002.
- [7] J. Udesen, F. Gran, K. L. Hansen, J. A. Jensen, C. Thomsen, and M. B. Nielsen, "High frame-rate blood vector velocity imaging using plane waves: Simulations and preliminary experiments," *IEEE Trans. Ultrason., Ferroelec., Freq. Contr.*, vol. 55, no. 8, pp. 1729–1743, 2008.
- [8] S. Salles, A. J. Y. Chee, D. Garcia, A. C. H. Yu, D. Vray, and H. Liebgott, "2-D arterial wall motion imaging using ultrafast ultrasound and transverse oscillations," *IEEE Trans. Ultrason., Ferroelec., Freq. Contr.*, vol. 62, no. 6, pp. 1047–1058, 2015.
- [9] F. Varray and H. Liebgott, "An alternative method to classical beamforming for transverse oscillation images: Application to elastography," *IEEE 10th Int. Symp. Biomedical Imaging*, pp. 716–719, 2013.
- [10] J. A. Jensen, "A new estimator for vector velocity estimation," *IEEE Trans. Ultrason., Ferroelec., Freq. Contr.*, vol. 48, no. 4, pp. 886–894, 2001.
- [11] J. A. Jensen, H. Holten-Lund, R. T. Nilsson, M. Hansen, U. D. Larsen, R. P. Domsten, B. G. Tomov, M. B. Stuart, S. I. Nikolov, M. J. Pihl, Y. Du, J. H. Rasmussen, and M. F. Rasmussen, "SARUS: A synthetic aperture real-time ultrasound system," *IEEE Trans. Ultrason., Ferroelec., Freq. Contr.*, vol. 60, no. 9, pp. 1838–1852, 2013.
- [12] S. S. Lai, B. Y. S. Yiu, A. K. Poon, and A. C. Yu, "Design of anthropomorphic flow phantoms based on rapid prototyping of compliant vessel geometries," *Ultrasound Med. Biol.*, vol. 39, no. 9, pp. 1654–1664, 2013.

***In Vivo* High Frame Rate Vector Flow Imaging
Using Plane Waves and Directional Beamforming**

Jonas Jensen, Carlos Armando Villagómez-Hoyos, Matthias Bo Stuart,
Caroline Ewertsen, Michael Bachmann Nielsen, and Jørgen Arendt Jensen

Proceedings of IEEE International Ultrasonics Symposium, p. 1-4,

Accepted for oral presentation in Tours, France, 2016.

In Vivo High Frame Rate Vector Flow Imaging Using Plane Waves and Directional Beamforming

Jonas Jensen¹, Carlos Armando Villagómez Hoyos¹, Matthias Bo Stuart¹, Caroline Ewertsen², Michael Bachmann Nielsen², and Jørgen Arendt Jensen¹

¹Center for Fast Ultrasound Imaging, Department of Electrical Engineering, Technical University of Denmark, DK-2800 Lyngby, Denmark

²Department of Radiology, Copenhagen University Hospital, DK-2100 Copenhagen, Denmark

Abstract—Directional beamforming (DB) estimates blood flow velocities accurately when the flow angle is known. However, for automatically finding the flow angle a computationally expensive approach is used. This work presents a method for estimating the flow angle using a combination of inexpensive transverse oscillation (TO) estimators and only 3 directional beamformed lines. The suggested DB vector flow estimator is employed with steered plane wave transmissions for high frame rate imaging. Two distinct plane wave sequences are used: a short sequence (3 angles) for fast flow and an interleaved long sequence (21 angles) for both slow flow and B-mode. Parabolic flow with a peak velocity of 0.5 m/s is measured at beam-to-flow angles of 60° and 90°. The DB method estimates the angle with a bias and standard deviation (STD) less than 2°, and the STD of the velocity magnitude is 2.5 %. This is 7 - 8.5 % when using TO. The long sequence has a higher flow sensitivity, and when used for estimation of slow flow with a peak velocity of 0.04 m/s, the SD is 2.5 % and bias is 0.1 %. This is a factor of 4 better than if the short sequence is used. The carotid bifurcation was scanned on a healthy volunteer, and the short sequence was used with TO and DB to estimate velocity vectors. The STD of the velocity profile over a cardiac cycle was 6.1 % for TO and 4.9 % for DB.

I. INTRODUCTION

Ultrasound blood flow estimation is of diagnostic value in investigating hemodynamics in the human cardiovascular system. Conventional color flow mapping uses focused emissions in line-by-line imaging, where each line is acquired sequentially from received echoes of several consecutive pulses. It limits the frame rate significantly, and full flow dynamics of both fast and slow flow are lost, because of the limited observation time along each focusing direction.

Plane wave imaging is a synthetic aperture technique, which can increase the frame rate and improve image quality [1]. An image of the entire insonified region is created for each emission resulting in a low-resolution image (LRI). By using a few emissions, the low-resolution images can be summed to form a high-resolution image (HRI).

Vector flow imaging methods reveal the 2-D velocity vector without the need for angle correcting conventional 1-D estimates. Transverse Oscillation (TO) [2] and directional beamforming (DB) [3] are two methods capable of estimating 2-D velocity vectors. The DB approach uses focusing along a line following the direction of the flow. The velocity magnitude is estimated accurately using a cross-correlation estimator, and it has also been shown that the standard deviation of the

velocity estimates can be reduced by a factor 2, when using DB rather than TO [4]. However, the direction of the blood flow needs to be known in advance for DB [5]. Automatic approaches for angle estimation have been proposed [6], [7]. The number of calculations for these angle estimators are, however, very high, because signals have to be beamformed in a polar grid and cross-correlated at every angle and for each estimation point. If lines are beamformed at every 5°, the number of directional lines is 37. Therefore, it is of interest to investigate angle estimators, which reduce the number of calculations.

This paper presents a method for DB, where the flow angle is found automatically using a combination of inexpensive TO estimators and DB. Only 3 lines are beamformed for each estimation point in addition to 2 lines for TO, thus, at least a sevenfold reduction in beamforming load is achieved compared to the current angle estimators. The method is a two-step procedure, where the initial TO estimate is followed by a DB estimate. The estimates obtained by TO and DB can, thus, be compared. Plane waves are used for high-frame rate imaging, and it is shown that both fast and slow flow can be estimated accurately, when interleaving a short and a long emission sequence.

II. METHOD FOR PLANE WAVE FLOW IMAGING

The proposed method for vector flow imaging uses steered plane waves in transmit and a two-step procedure for velocity estimation: First, TO estimators are used to find an initial flow angle, and then 3 directional lines are beamformed around the TO angle to improve the angle estimate. The velocity magnitude is estimated along the flow direction using cross-correlation estimators. An illustration of the principle is shown in Fig. 1, where 3 directional lines are beamformed around the initial TO angle estimate.

A. Transverse Oscillation

A transverse oscillation in the pulse-echo field can be created in the receive beamforming by using a two-peak apodization function, or in the Fourier domain by filtering the beamformed image in the lateral dimension. The latter approach is used here, where a Gaussian filter is applied on the Fourier transformed HRIs to only select Fourier components around a desired lateral oscillation frequency [8], [9].

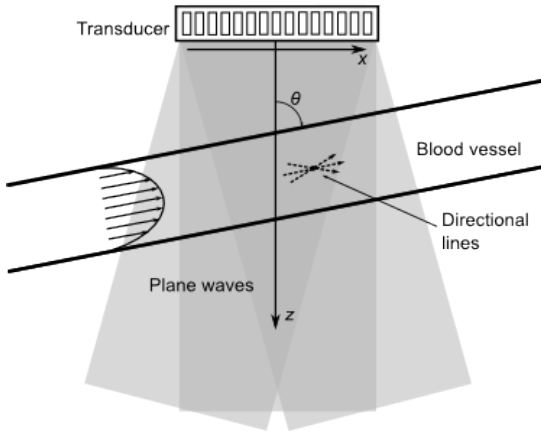


Fig. 1. Plane wave emissions from a linear array transducer are used to insonify flow in a straight vessel, which has a beam-to-flow angle θ . Directional lines are beamformed around the initial TO angle estimate.

The directional information of the flow is preserved by applying the Hilbert transform on the TO image for each of the lines in the lateral direction. This avoids having a spatial quadrature between two beamformed signals [10]. The actual mean lateral oscillation frequency at a given depth is estimated directly from the data and used for the transverse velocity component v_x . For the axial velocity component v_z , a cross-correlation estimator is employed.

The flow angle is found at each estimation point from:

$$\theta = \arctan(v_x, v_z) \quad (1)$$

using the estimated v_x and v_z .

B. Directional Beamforming

The initial angle estimate from (1) is used to directionally beamform a signal $y_d(k)$ at an estimation point and at an angle θ . Correlating signals from two HRI acquired $T_{prf,eff}$ seconds apart gives

$$R_{12}(l) = \frac{1}{N_k + 1} \sum_{k=-N_k/2}^{N_k/2} y_d^{(t)}(k) y_d^{(t+T_{prf,eff})}(k+l), \quad (2)$$

where $y_d^{(t)}(k)$ is the directional signal focused at time t .

Beamforming signals at other angles $\theta_m = \theta \pm \Delta\theta$ yield correlation functions $R_{12}(l, \theta_m)$. They are used to calculate the normalized cross-correlation estimate

$$R_{12n}(\theta_m) = \left(\frac{\max(R_{12}(l, \theta_m))}{R_{11}(0, \theta_m)} \right), \quad (3)$$

which gives the maximum normalized cross-correlation for three angles. $R_{11}(0, \theta_m)$ is the power of the signal. The angle estimate, $\hat{\theta}$, is found as the angle yielding the largest correlation in (3). The estimate is also improved by interpolation.

TABLE I
PROCESSING PARAMETERS.

Parameter	TO	DB
Receive apodization	Tukey	Tukey
Receive F-number	0.8	0.8
Sampling interval Δr	$\lambda/20$	$\lambda/20$
Desired lateral wavelength	1.53 mm	-
TO window size	1.5 mm	-
Number of HRI/estimate	32	32
Line length	-	12.5 λ

The angle estimate $\hat{\theta}$ is used to directional beamform a line for this angle. The velocity magnitude is found from the lag l_{max} , where $R_{12}(l, \hat{\theta})$ is maximum, and convert it to velocity

$$|v| = \frac{l_{max} \Delta r}{T_{prf,eff}}. \quad (4)$$

III. METHODS FOR EXPERIMENTS

A short plane wave sequence ($-15^\circ, 0^\circ, 15^\circ$) is used for fast flow estimation, and a long sequence (21 angles, max steering 20°) is used for both B-mode imaging and slow flow estimation. The sequences are interleaved in a 3+1 procedure, i.e., one emission from the long sequence is transmitted after the short sequence. The pulse repetition frequency f_{prf} is 10 kHz, thus, the effective $f_{prf,eff}$ for the short sequence is $f_{prf}/4$ and $f_{prf}/84$ for the long sequence. A 1.5-cycle excitation pulse is used in both sequences, since the precision of the cross-correlation estimator used for DB is proportional to the bandwidth of the system. To achieve narrow-band signals suitable for TO estimation, beamformed signals are convolved with a 4-cycle sinusoid.

Processing parameters are listed in Table I. Three directional lines are beamformed at each estimation point for DB: one at the TO angle θ and at $\pm\Delta\theta$. For constant flow, $\Delta\theta = 1$ standard deviation (STD) of the TO angle estimate, which is calculated from 10 non-consecutive estimates at each estimation point. Due to pulsation of flow for the *in vivo* scan, lines are beamformed at a fixed $\Delta\theta = 2.5^\circ$ around the TO angle in this case.

A. Measurement Setup

The approach is implemented on the experimental scanner SARUS [11] for acquisition of channel RF data. A 192-element 4.1 MHz transducer is employed (pitch 0.6λ). A flow rig phantom with a tube radius of 6 mm and placed at a depth of 20 mm is scanned, and the beam-to-flow angle θ is 60° and 90° . Constant parabolic flow is circulated and volume flow is measured by a magnetic flow meter for reference (MAG 3000, Danfoss, Nordborg, Denmark). The f_{prf} is reduced to 2 kHz and the peak velocity is 0.1 m/s to avoid turbulence (corresponds to fast velocity flow of 0.5 m/s at 10 kHz f_{prf}). Slow velocity flow is also measured on a flow phantom with a 3.5 mm tube radius and 90° beam-to-flow angle. In this case the peak velocity is 0.04 m/s and $f_{prf} = 10$ kHz. Echo-cancelling is performed on beamformed data with a Hoeks filter [12].

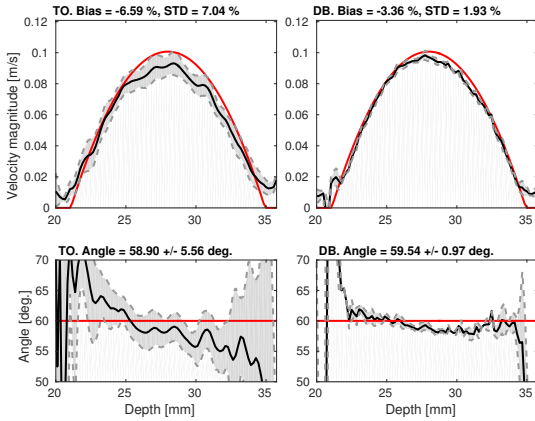


Fig. 2. Measurement on a straight vessel phantom at 60° beam-to-flow-angle. Velocity magnitude (top) and angles (bottom) for TO (left) and DB (right). Mean estimates are shown in black with ± 1 STD and true profiles in red.

The right carotid bifurcation on a 27-year old healthy male is scanned with a longitudinal view by an experienced radiologist. The scan sequence is the same as for simulation and phantom measurements, and f_{prf} is 10 kHz. Data are acquired for 4.5 s. Echo-canceling is performed with a Hoeks filter for diastolic flow and an energy-based filter with manual threshold for systolic flow [13].

IV. RESULTS

A. Phantom Measurements

Fig. 2 shows results from a flow rig measurement, where the beam-to-flow angle is 60° and f_{prf} is 2 kHz. The short sequence is used for flow estimation. The mean velocity magnitude and angles are shown in black with ± 1 STD, and the true velocities and angles are shown in red. Results from TO are shown in the left figures, while results for DB are shown in the right figures. The initial TO estimate gives a mean flow angle of $58.9 \pm 5.6^\circ$, which is improved in the DB step to $59.5 \pm 1^\circ$. The resulting velocity magnitude estimate is accurate with a mean bias of -3.4%, and the STD of the velocity reduces from 7% (TO) to 1.9% (DB). For the 90° beam-to-flow angle measurement, the angle is estimated to $89.7 \pm 1.3^\circ$ using TO and $89.8 \pm 0.5^\circ$ using DB. The STD of the velocity magnitude is 8.5% for TO and 2.5% for DB, while bias changes slightly from -3.9% for TO to -5.4% for DB.

Results from the slow velocity flow measurement are shown in Fig. 3. The short sequence is used with the DB method for the result in the bottom figure, where the bias and STD are -6% and 10%, respectively. The performance can be improved by using the long sequence for flow estimation as shown in the top figure. The STD is reduced by a factor 4. The long sequence has a higher sensitivity than the short sequence, because 21 rather than 3 LRI are combined, thus, reducing side-lobe levels and improving contrast. Estimates are correlated at every

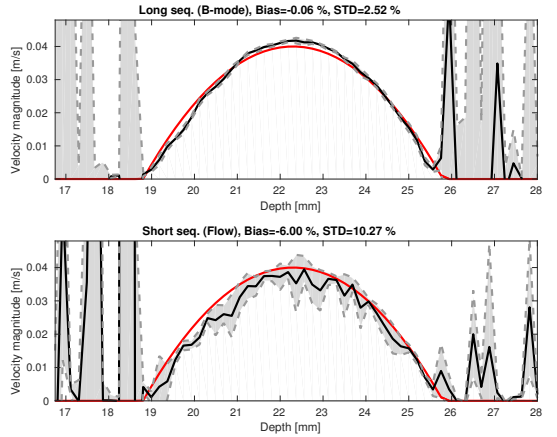


Fig. 3. Estimation of slow velocity flow using the long sequence (top) and short sequence (bottom). The beam-to-flow angle is 90° .

8.4 ms, which reduces $v_{x,max}$ to 5.9 cm/s. Note that echo-canceling has been performed for the same time period (0.18 s) for the two sequences. It is possible to use the slow flow sequence also for B-mode imaging, if a separate B-mode sequence cannot be included in the emission sequence. In that case, a compromise needs to be made for the receive gain.

B. In Vivo Measurement

A frame from the *in vivo* measurement of peak systole is shown in Fig. 4, which is processed using TO (left image) and DB (right image). The short sequence is used for flow estimation and the long for B-mode images. The direction of flow is indicated by arrows and follows the vessel anatomy. The DB method estimates larger velocities at the inlet of the external carotid artery, while low or no velocity is estimated in the top left corner of the flow image. This can be due to echo-canceling effects and/or angle estimation problems. The velocity magnitude at the indicated green point is shown as a function of time in Fig. 4 (bottom). After alignment of the profiles to the cardiac cycle, the STD for TO is calculated to 6.1% and 4.9% for DB.

V. DISCUSSION AND CONCLUSION

A method for 2-D vector flow imaging, where the flow angle is found using a combination of TO and DB was presented. Compared to conventional DB methods, at least a sevenfold reduction in beamforming load is achieved for angle estimation. Rather than beamforming lines in a polar grid at all angles, the presented method uses an initial TO angle estimate to limit the angle search range and beamforms only 3 lines around the TO angle. It was demonstrated in phantom measurements that the method estimates flow angle accurately and with a bias and STD less than 2° . The STD of the velocity magnitude estimates was less than 2.5%, which was an order of 2-3 times less than for the TO method. The

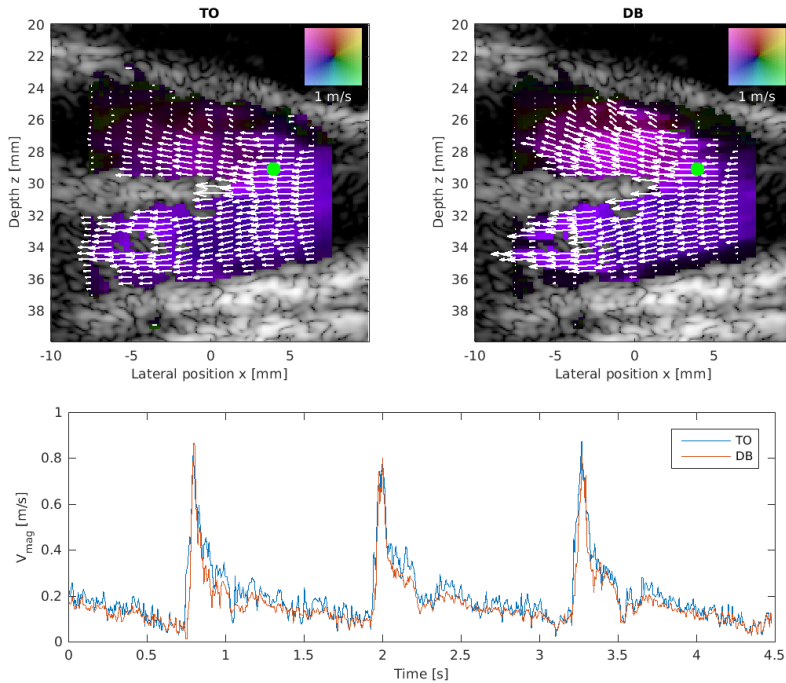


Fig. 4. Vector flow imaging of the carotid bifurcation. Flow in the systole is shown using TO in the left imaging and DB in the right image. The bottom figure shows velocity magnitude at a single estimation point (green point on VFI) as a function of time for the two methods.

method was employed with plane waves in transmit, and this acquisition scheme achieves a very high frame rate of 2000 fps for fast flow estimation. An interleaved long sequence was used for B-mode imaging and also used to improve slow flow estimation in a phantom. Potentially, this may improve slow and fast flow estimation, as it will be possible to use data simultaneously from the two sequences for flow estimation. It can also be an advantage for visualization of flow in both large and small vessels.

ACKNOWLEDGMENTS

This work was supported by grant 82-2012-4 from the Danish National Advanced Technology Foundation and by BK Ultrasound Aps.

REFERENCES

- [1] M. Tanter, J. Bercoff, L. Sandrin, and M. Fink, "Ultrafast compound imaging for 2-D motion vector estimation: application to transient elastography," *IEEE Trans. Ultrason., Ferroelec., Freq. Contr.*, vol. 49, pp. 1363–1374, 2002.
- [2] J. A. Jensen and P. Munk, "A new method for estimation of velocity vectors," *IEEE Trans. Ultrason., Ferroelec., Freq. Contr.*, vol. 45, pp. 837–851, 1998.
- [3] J. A. Jensen, "Directional velocity estimation using focusing along the flow direction: I: Theory and simulation," *IEEE Trans. Ultrason., Ferroelec., Freq. Contr.*, vol. 50, pp. 857–872, 2003.
- [4] —, "Comparison of vector velocity imaging using directional beamforming and transverse oscillation for a convex array transducer," in *Proc. SPIE Med. Imag.*, vol. 9040, 2014, pp. 904012–1–8.
- [5] J. Udesen, F. Gran, and J. A. Jensen, "Fast Color Flow Mode Imaging Using Plane Wave Excitation and Temporal Encoding," in *Proc. SPIE Med. Imag.*, vol. 5750, Feb. 2005, pp. 427–436.
- [6] J. A. Jensen and N. Oddershede, "Estimation of velocity vectors in synthetic aperture ultrasound imaging," *IEEE Trans. Med. Imag.*, vol. 25, pp. 1637–1644, 2006.
- [7] C. A. Villagomez-Hoyos, M. B. Stuart, K. L. Hansen, M. B. Nielsen, and J. A. Jensen, "Accurate angle estimator for high frame rate 2-D vector flow imaging," *IEEE Trans. Ultrason., Ferroelec., Freq. Contr.*, p. Accepted, 2016.
- [8] S. Salles, A. J. Y. Chee, D. Garcia, A. C. H. Yu, D. Vray, and H. Liebgott, "2-D arterial wall motion imaging using ultrafast ultrasound and transverse oscillations," *IEEE Trans. Ultrason., Ferroelec., Freq. Contr.*, vol. 62, no. 6, pp. 1047–1058, 2015.
- [9] J. Jensen, M. B. Stuart, and J. A. Jensen, "High frame rate vector velocity estimation using plane waves and transverse oscillation," in *Proc. IEEE Ultrason. Symp.*, 2015, pp. 1–4.
- [10] J. A. Jensen, "Improved vector velocity estimation using directional transverse oscillation," in *Proc. IEEE Ultrason. Symp.* IEEE, 2015, pp. 1–4.
- [11] J. A. Jensen, H. Holten-Lund, R. T. Nilsson, M. Hansen, U. D. Larsen, R. P. Domsten, B. G. Tomov, M. B. Stuart, S. I. Nikolov, M. J. Pihl, Y. Du, J. H. Rasmussen, and M. F. Rasmussen, "SARUS: A synthetic aperture real-time ultrasound system," *IEEE Trans. Ultrason., Ferroelec., Freq. Contr.*, vol. 60, no. 9, pp. 1838–1852, 2013.
- [12] A. P. G. Hoeks, M. Hennerici, and R. S. Reneman, "Spectral composition of Doppler signals," *Ultrasound Med. Biol.*, vol. 17, pp. 751–760, 1991.
- [13] C. A. Villagomez-Hoyos, "Synthetic aperture vector flow imaging," Ph.D. dissertation, Technical University of Denmark, 2016.

Accuracy and precision of plane wave vector flow imaging for laminar and complex *in vivo* flow

Jonas Jensen, Carlos Armando Villagómez-Hoyos, Jacob Bjerring Olesen,
Borislav Tomov, Ramin Moshavegh, Simon Holbek, Marie Sand Traberg,
Matthias Bo Stuart, Caroline Ewertsen, Kristoffer Lindskov Hansen,
Carsten Thomsen, Michael Bachmann Nielsen, and Jørgen Arendt Jensen

Submitted to Ultrasound in Medicine and Biology, April 2017

Accuracy and precision of plane wave vector flow imaging for laminar and complex *in vivo* flow

Jonas Jensen^{a,*}, Carlos Armando Villagómez Hoyos^a, Jacob Bjerring Olesen^a, Borislav Tomov^a, Ramin Moshavegh^a, Simon Holbek^a, Marie Sand Traberg^a, Matthias Bo Stuart^a, Caroline Ewertsen^b, Kristoffer Lindskov Hansen^b, Carsten Thomsen^b, Michael Bachmann Nielsen^b, Jørgen Arendt Jensen^a

^aCenter for Fast Ultrasound Imaging, Dept. of Elec. Eng., Bldg. 349,
Technical University of Denmark, DK-2800 Lyngby, Denmark

^bDepartment of Radiology, Copenhagen University Hospital, DK-2100 Copenhagen, Denmark

Abstract

The objective of this paper is to investigate the accuracy and precision of a plane wave 2-D vector flow imaging (VFI) method under laminar and complex blood flow conditions *in vivo*. The approach was to study (1) accuracy for complex flow by comparing VFI estimates obtained from an anthropomorphic flow phantom to computational fluid dynamics (CFD) simulated velocities; (2) accuracy for laminar flow *in vivo* by comparing peak systolic velocities from VFI with magnetic resonance angiography (MRA); (3) precision of VFI estimation *in vivo* at several evaluation points in the vessels. The carotid arteries at the bifurcation in ten healthy volunteers were scanned using the fast plane wave ultrasound sequence, and the same volunteers were also scanned using MRA. The acquired MRA geometry from one of the volunteers was used to fabricate an anthropomorphic flow phantom, which was also scanned using the fast plane wave sequence. The same geometry was used in a CFD simulation to calculate the velocity field. Results showed that similar flow patterns and vortices were estimated with CFD and VFI in the phantom of the carotid bifurcation. Mean differences for velocity magnitudes were within 10 %. A mean difference of -20 % was obtained in the external branch. For the ten volunteers, the mean difference between VFI and MRA was -0.17 m/s for peak systolic velocities of laminar flow *in vivo*. The precision *in vivo* was calculated as the mean standard deviation (SD) of estimates aligned to the heart cycle and was highest in the center of the common carotid artery (SD 4.4 % for velocity magnitudes, 4.1° for angles) and lowest in the external branch and for vortices (SD 16 % for velocity magnitudes, > 50° for angles). The results indicate that plane wave VFI measures flow precisely, and that estimates are in good agreement with a CFD simulation and MRA.

Introduction

Atherosclerosis is a precursor for many cardiovascular diseases, which are the leading cause of death worldwide (Naghavi et al., 2003). Blood clots originating from the carotid arteries are especially important, as they may be responsible for stroke (Bamford et al., 1991). Monitoring the health of blood vessels is therefore of particular interest. Magnetic resonance angiography (MRA) and ultrasound (US) are non-invasive techniques for imaging

flow in blood vessels. MRA is a time-consuming and expensive technique with millimeter resolution and poor temporal resolution, where hundreds of heart cycles are combined over several minutes. US imaging is a relatively inexpensive technique, which is used in daily clinical practice and provides blood flow velocities in real-time with sub-millimeter resolution. B-mode and color flow imaging are used for orientation and flow visualization, while quantitative parameters are calculated from the spectrogram.

Although peak systolic velocities (PSV), end diastolic velocities, resistive index, and volume flow are typical and widely used quantitative measures for characterizing the flow, there are several limi-

*Corresponding Author: Jonas Jensen, Technical University of Denmark, Ørstedes Plads, Building 349, DK-2800 Lyngby, Denmark; Email, jonjens@elektro.dtu.dk; Phone, +45 45253903

tations. The velocity estimate is only found along the US beam, i.e. in the axial direction, and has to be corrected for the beam-to-flow angle. This is often performed manually by the examiner, is largely inter/intra-operator dependent, and the estimates are prone to large errors (Corriveau and Johnston, 2004; Stewart, 2001). The correction only works when laminar flow is parallel to the vessel (Kruskal et al., 2004). However, pulsating flow changes the flow pattern during the cardiac cycle, resulting in a variation in the flow angle. Furthermore, most vessels are curved and have branches, creating non-laminar and very complex blood flow patterns. Thus, there is no single flow angle as it varies depending on spatial location and time in the cardiac cycle. Spectral Doppler is also limited by the range gate providing velocities from a single location in the vessel. Placing the gate is operator dependent (Lui et al., 2005) and information about flow in the entire image is lost.

The development within 2-D vector flow imaging (VFI) has provided velocity estimation methods without the need for angle correction. Cross-beam methods (Dunmire et al., 2000), speckle tracking (Trahey et al., 1987), transverse oscillation (TO) (Jensen and Munk, 1998; Anderson, 1998), directional beamforming (DB) (Jensen, 2003), and spectral-based methods (Newhouse et al., 1987; Tortoli et al., 2006) have been suggested for finding the 2-D velocity vector. The combination of VFI and high-frame-rate techniques such as synthetic aperture (Nikolov and Jensen, 2001, 2003; Jensen et al., 2006) and plane wave imaging (Udesen et al., 2008; Bercoff et al., 2011; Ekroll et al., 2013; Yiu et al., 2014; Tanter and Fink, 2014; Lenge et al., 2015) have further improved performance of the methods. The advantages are that quantitative velocity estimates can be obtained everywhere in the image at hundreds to thousands of frames/s, and no angle correction is needed. VFI provides a more complete picture of flow patterns, which are often transient and complex (Hansen et al., 2009a, 2016). Data are available continuously for plane wave and SA imaging, which improve the precision of the estimates because averaging can be performed over a number of emissions without sacrificing frame rate (Nikolov and Jensen, 2003).

Any VFI method must give precise and accurate velocity estimates for both laminar and complex flow when measured *in vivo*. This is especially important for quantitative measurements derived from any spatial estimation point in the image. The

accuracy of VFI methods has previously been investigated under laminar flow conditions by comparing PSV and volume flow estimates with independent methods such as spectral Doppler and MRA (Hansen et al., 2009b; Pedersen et al., 2012; Ekroll et al., 2014; Tortoli et al., 2015; Hansen et al., 2015). However, two challenges arise for further investigation of accuracy and precision: (1) compared to VFI methods, neither spectral Doppler nor MRA has sufficient high spatial and temporal resolution to accurately capture complex flow patterns *in vivo*; and (2) to evaluate the precision of a method in terms of repeatability of estimates, it requires data acquisition of at least two to three heart beats, but this generates more transducer element data than most scanners can store, when using high-frame-rate imaging.

In relation to (1), an approach to investigate complex flow is to perform a realistic phantom study. Novel fabrication processes for flow phantoms use anthropomorphic geometries, whereby complex flow patterns in a realistic vessel geometry and environment may be measured using US (Lai et al., 2013). The same vessel geometry and boundary conditions may be used for computational fluid dynamics (CFD) simulations of the velocity field. CFD modelling is employed as an independent method and has been extensively used to study the flow fields existing in carotid arteries by comparing CFD to MRA (Cebal et al., 2002) and particle image velocimetry (Steinman et al., 2000). The CFD simulated velocities can be compared to the measured VFI estimates from the phantom and allows for a cross-validation of the methods. In relation to (2), the experimental scanner SARUS has the possibility to store data up to 96 Gb, i.e. 10 s scans can be performed and all element data stored (Jensen et al., 2013). Thereby, the precision of flow estimation methods can be evaluated from several heart beats.

The method for VFI in this paper is based on plane wave imaging and a combination of TO and DB (Jensen et al., 2017). It has previously been validated in simulations under ideal conditions. Straight vessel phantom measurements and a single *in vivo* scan have also been presented. The objective of this paper is to investigate the accuracy and precision of the method *in vivo* under laminar and complex flow conditions in ten healthy volunteers.

The approach taken here is to evaluate

- the accuracy of the method under complex

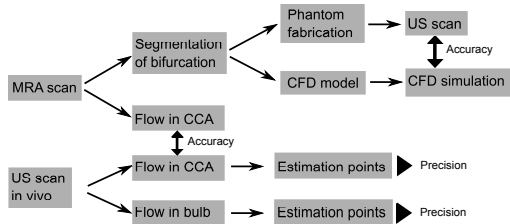


Figure 1: Schematic illustration of the approach for investigating accuracy and precision of the plane wave VFI method.

flow conditions by comparing VFI estimates obtained from an anthropomorphic phantom measurement to a CFD simulated velocity field derived from the same geometry,

- the accuracy of the method *in vivo* under laminar flow conditions by comparing VFI estimates with spectral Doppler and MRA, and
- the precision of the method *in vivo* by calculating the repeatability of the VFI estimates at several estimation points in the vessels.

The approach is illustrated in Fig. 1. The vessel of interest is the carotid artery encompassing the bifurcation in healthy volunteers. Flow in the common carotid artery (CCA) is expected to be laminar, while complex flow patterns occur in the carotid bulb. These parts of the carotid artery are used to study the VFI method.

Experimental methods

Ten healthy volunteers with no history of cardiac, vascular, or neurologic disease were recruited (8 males and 2 females; mean BMI: 24 kg m^{-2} ; mean age: 32 years, range 25-52 years). The volunteers participated after informed consent, and the study was approved by the National Committee on Biomedical Research Ethics (Protocol No. H-1-2014-fsp-072). Data acquisition for each volunteer spanned one day. The *in vivo* VFI scan was conducted during a session in the morning, and the MRA scan was performed in the evening. One radiologist, either CE or KLH, performed the US VFI scan, while both acquired the MRA scan. All measurements were performed with the volunteer in a supine position. The volunteers rested in this position for at least 10 minutes before each scan.

Table 1: Transducer and acquisition parameters.

Parameter	Value
Number of elements	192
Transducer center frequency f_0	4.1 MHz
Cycles in emitted pulse	1.5 (flow); 1 (B-mode)
Transmit apodization	Tukey (weight 0.5)
Pulse repetition frequency f_{prf}	10 kHz
Max steering angle	15° (flow); 20° (B-mode)
Number of plane waves	3 (flow); 21 (B-mode)
Receive apodization	Tukey (weight 0.5)
Desired TO wavelength	2 mm
Number of HRI/estimate	32

In vivo VFI scans and processing

Prior to the plane wave VFI scans, a scan of the right CCA in long axis view was performed 2-3 cm upstream of the bifurcation using a linear array transducer (BK 8L2, BK Ultrasound, Herlev, Denmark) with a commercial scanner (BK3000, BK Ultrasound, Herlev, Denmark). A spectral Doppler measurement was made, and a 15 s cine loop with the spectrogram was recorded. The plane wave VFI scans were then performed using the same transducer type, which was connected to the experimental US scanner SARUS (Jensen et al., 2013). A duplex sequence consisting of both flow and B-mode emissions was employed (Jensen et al., 2017). Transducer and processing parameters are listed in Table 1. Each of the two scans listed below was recorded separately:

- a longitudinal scan at the right CCA 2-3 cm upstream of the bifurcation, and
- a longitudinal scan at the carotid bulb with the most optimal view of the bifurcation.

Transducer element RF data were acquired for a total of 10 s for each scan and were stored for further processing.

Beamforming was performed off-line, and an energy-based filter with manual threshold was used for echo-canceling of beamformed data (Villagomez-Hoyos et al., 2016a). The threshold was determined by using data from one of the volunteers as a training set, and the same threshold was then applied to all scans of volunteers.

A two-step procedure was employed for vector velocity estimation: First, the TO method was used to find an initial flow angle θ calculated from the axial, v_z , and lateral, v_x , velocity components. The transverse oscillation was created by applying a Gaussian filter on the beamformed images in the

Fourier domain (Salles et al., 2015). Second, three directional lines were beamformed around the TO angle θ at each estimation point in the image to find a refined angle estimate $\hat{\theta}$ (Oddershede and Jensen, 2007). The refined angle was calculated from the angle yielding the largest normalized cross-correlation estimate based on the three directional lines. The velocity magnitude was estimated along the flow direction $\hat{\theta}$ using a cross-correlation estimator. For further details on the vector velocity method, the reader is referred to (Jensen et al., 2017).

Intensity and temperature measurements were performed prior to the *in vivo* scans to assure compliance with FDA regulations. Mechanical index (*MI*) and derated spatial-peak temporal average intensity ($I_{spta.3}$) were measured using the Acoustic Intensity Measurement System AIMS III (Onda Corp., Sunnyvale, CA, USA) and an Onda HGL-0400 hydrophone. Results for the sequence were $MI = 1.25$ and $I_{spta.3} = 267 \text{ mW/cm}^2$. This is within FDA limits, which are $MI = 1.9$ and $I_{spta.3} = 720 \text{ mW/cm}^2$. Transducer surface temperature rise was measured to 18.6°C in still air and 6.3°C when attached to a phantom. The values were below the FDA limits of 27°C and 10°C , respectively.

MRA scans and processing

A 1.5 T whole body scanner (Magnetom Avanto, Siemens, Erlangen, Germany) was used in combination with a head and a neck matrix coil. A time-of-flight sequence was performed as a localizer for the carotid artery. A cross-sectional plane of the CCA was selected 2-3 cm upstream of the bifurcation by consulting the anatomical image. Through-plane velocities were estimated within the plane by using a retrospective ECG gated phase contrast sequence. The sequence had a repetition time of 42 ms, echo time 3 ms, flip angle 20° , pixel resolution of $1.1 \times 1.1 \text{ mm}$, and slice thickness 5 mm. Estimates were retrieved from 210 heartbeats, and the total number of phases per heart beat was 50. The phase contrast sequence was repeated three times to obtain three independent estimates of velocities within the same plane. Anatomical images were also acquired for a volume covering the common carotid artery and carotid bulb. The acquisition was made in parallel to the applied flow sequence, and the resolution was the same as for the flow data.

The stored MRA DICOM files contained anatomical and through-plane velocity estimates in 50

frames during a cardiac cycle. Each velocity data set was processed offline in Matlab (MathWorks Inc., Natick, MA) by adding the 50 frames to create a combined anatomical intensity map. Thereby, noise was suppressed and vessel regions enhanced. Vessel regions were segmented by creating a binary image based on the intensity map and applying a manually selected threshold. The threshold was adjusted for each data set and each volunteer. Potential vessels were detected by applying morphological operations on the binary image (Holbek et al., 2017). A vessel region containing the right CCA was selected manually, and flow estimates within this region were detected and stored for further analysis of MRA flow.

A 3-D geometry representing the carotid artery of one of the volunteers was used for producing a CFD model and a flow phantom with similar geometry as the scanned vessel. This was achieved by concatenating the collected MRA images in ScanIP (Simpleware ldt. Exeter, United Kingdom) and marking the vessel region by creating a binary mask from applying a threshold onto the anatomical intensity images. The segmented flow volume was imported into SolidWorks (Education edition, Dassault Systèmes SolidWorks Corp., Vélizy, France), where smoothing of the geometry was performed prior to flow phantom fabrication and CFD simulation.

Flow phantom fabrication and scan

An anthropomorphic flow phantom matching the flow domain of the original scanned vessel was fabricated using stereolithography, a technique described by Lai et al. (2013). A Leapfrog Creatr HS XL printer (Leapfrog BV, Alphen aan den Rijn, The Netherlands) with a depth-width resolution of $17 \mu\text{m}$ and a resolution in height of $20 \mu\text{m}$ was used to print the drafted vessel. The 3-D printed geometry constituted a temporary core in the wall-less phantom. The core was fixated in a container and cast in polyvinyl alcohol (PVA) cryogel to obtain a surrounding medium, which mimicked the properties of human tissue. The PVA cryogel contained 15 % PVA, 1 % silicon dioxide, 0.3 % potassium sorbate, and 83.7 % distilled water. The elastic properties of the cast material was controlled by varying the number of freeze-thaw cycles. Three freeze-thaw cycles were used, where each half-cycle lasted 24 hours, the freeze settings were $-20^\circ\text{C} \pm 0.5^\circ\text{C}$, and the thaw settings were $4^\circ\text{C} \pm 0.5^\circ\text{C}$.

The core was removed manually after the completion of three cycles (total duration of 144 hours). The resulting phantom was core-less with a fluid domain identical to the original scanned vessel.

The anthropomorphic phantom was connected to a closed loop flow system (CompuFlow 1000, Shelley Medical Imaging Technologies, Toronto, Canada) that circulated a blood-mimicking fluid (BMF-US, Shelley Medical Imaging Technologies, Toronto, Canada) with a viscosity of $4.1 \cdot 10^{-3}$ Pa·s and a density of 1030 kg/m³. The CompuFlow system was set to generate a standard carotid artery waveform to mimic the flow in this artery. The peak volume flow was 15 mL/s and the cardiac period was 0.84 s, which were within representative physiological ranges. The US transducer (8L2, BK Ultrasound, Herlev, Denmark) was placed on the phantom and the scan plane was longitudinal to the bifurcation. Data of 10 s recordings were acquired with the SARUS scanner using the same sequence and same parameters as for the *in vivo* scans.

CFD model

The drafted vessel geometry was imported into Comsol Multiphysics (v5.2a, Comsol AB, Stockholm, Sweden). Here, fields of flow were simulated based on parameters set to match those of the experimental set-up. A direct PARDISO solver (www.pardiso-project.org) was applied. A time-varying waveform for the volume flow was imposed on the whole inlet plane under the assumption of fully developed parabolic flow. The waveform was obtained from the plane wave VFI phantom measurement at a velocity estimation point in the CCA. An outlet pressure of 0 Pa was set for the two exit branches representing the internal carotid artery (ICA) and external carotid artery (ECA), while a no-slip condition was set at the walls of the flow domain. The properties of the emulated fluid matched those of the experimental used blood-mimicking fluid, i.e. a viscosity of $4.1 \cdot 10^{-3}$ Pa·s and a density of 1030 kg/m³. The simulated velocity fields were exported to Matlab, where the comparison between the CFD simulated flow fields and the flow fields measured with plane wave VFI was made.

Methods for evaluation

Comparison between phantom VFI and CFD simulation

The comparison between the flow field of the CFD simulation and phantom VFI measurement re-

quired that the geometries were aligned. The VFI measurement provided velocities in a plane of the 3-D geometrical phantom, and the CFD model provided velocities in the full 3-D volume of the phantom. The vessel was manually segmented on a B-mode image from the VFI to provide a geometry of the vessel in the scanned plane. The CFD geometry was then rotated and translated to the coordinate system of the VFI plane to align the two geometries. This was performed manually by visual inspection of the geometries. The applied translation and rotation was saved in a transformation matrix.

The transformation matrix was also used to convert the CFD velocities into velocity components in the coordinate system corresponding to the VFI. CFD velocities were interpolated to the same locations as in the VFI, and an inter-frame linear interpolation was used to process the same time instances.

Comparison between VFI, MRA and spectral Doppler

The peak systolic velocity (PSV) in scans of laminar flow in the CCA of each volunteer was compared for plane wave VFI, spectral Doppler, and MRA. For the plane wave VFI of the CCA, PSVs were estimated at every velocity estimation point within the segmented vessel and for each cardiac cycle. The estimation point with the maximum PSV was detected, and the mean and standard deviation (SD) of the PSVs during the 10 s scan sequence were calculated. For the spectral Doppler scans, the PSV in each cardiac cycle was read from the 15 s cine loop for each volunteer. For the MRA scans, mean velocities were provided throughout a cardiac cycle, due to the combination of several cardiac cycles with ECG gating. The PSV was found for each of the three MRA datasets for each volunteer and averaged. The PSV for plane wave VFI was compared to MRA and spectral Doppler using Bland-Altman plots and linear regression.

Precision of VFI in vivo

The VFI and B-mode datasets from the *in vivo* scans were imported into an in-house developed Matlab-based visualization tool. Vector velocities were overlaid B-mode images, and a colorwheel map represented velocity magnitude and direction of the blood flow. A video of the full 10 s acquisition was played and could be stopped at any frame.

A medical doctor (KLH) with 10 years of experience in VFI evaluated each of the 2x10 scans by

selecting evaluation points according to a defined procedure for:

- longitudinal scans of the CCA: one point in the center of the vessel and one point near the upper vessel wall
- longitudinal scans at the carotid bulb: a point in the center of a part of the CCA, near the upper vessel wall of the CCA, in the ECA, in the ICA, and the vortex in the carotid bulb.

If any of the vessels or a vortex were not visible on the scans, an evaluation point was not selected.

For each selected evaluation point, the program automatically calculated the mean cardiac cycle based on the velocity estimates by using the auto-correlation function. A 10 s scan sequence typically consisted of 8-11 cardiac cycles. The velocity magnitude and angle estimates were coherently aligned according to the cardiac period. 90 % of the cardiac period was used for the alignment to account for small deviations in heart rate throughout the 10 s scan period. The standard deviation $\sigma(t)$ at time t in the cardiac cycle was calculated among the aligned velocity magnitude and angle estimates. The mean SD for each point was then

$$SD = \sqrt{\frac{1}{N_f} \sum_{t=1}^{N_f} \sigma(t)^2} \quad (1)$$

where N_f is the number of frames encompassing a cardiac cycle. For the mean SD of velocity magnitude estimates, (1) was calculated relative to the peak velocity magnitude v_0 . The mean SD among the ten volunteers was also calculated for each of the evaluation points.

Results

Comparison between phantom VFI and CFD simulation

The VFI scan plane (segmented vessel) aligned with the CFD geometry is shown in Fig. 2. The width of the scan plane in the elevation direction was set according to the FWHM calculated at the elevation focus of the probe. The segmented vessel from the VFI fitted generally well within the 3-D mesh of the CFD simulation. There was, however, about 0.5 to 1 mm misalignment in the ECA and at the outlet of the ICA. A qualitative comparison between velocity fields obtained from plane wave

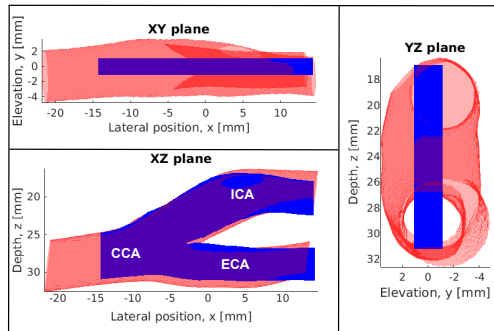


Figure 2: Alignment of the CFD vessel geometry (red) to the VFI scan plane (blue) in the phantom scan. The elevation extend of the US beam is indicated by the width of the blue rectangle in the XY and YZ plane.

VFI and the CFD simulation is presented below, while a quantitative comparison follows hereafter.

Frames from two phases of the cardiac cycle are shown in Fig. 3 and 4: during peak systole (0.16 s) and systolic deceleration (0.32 s). Estimates are shown for the CFD simulation and for the first cardiac cycle in the VFI scan. During peak systole, the VFI velocity fields in the CCA and ECA had similar patterns with the CFD simulation. The velocity magnitudes were at the same levels, and the arrows pointed in the same direction. For the ICA, there were differences in the velocity fields of the VFI estimates and the CFD. The vortex in the ICA was moved further up and extended a larger area in the VFI measurement and was merely an area of very low velocities rather than a well-defined vortex. It also affected the blood flow pattern downstream. During systolic deceleration (Fig. 4), both the CFD and VFI showed a large vortex, which extended from the CCA into the ICA. There were small differences in the extend of the vortex for CFD and VFI, but similar flow patterns were provided. A jet of streamlined forward flow was found close to the inner vessel wall of the ICA in the CFD and VFI. A smaller vortex in the ECA was also visible in both CFD and VFI, and the location of the vortex was within 1-2 mm in the VFI compared to the CFD. Furthermore, flow in the ECA had a lower speed in the VFI compared to the CFD.

A quantitative comparison between the CFD and VFI velocity magnitude estimates is given in Fig. 5. Velocity profiles were sampled at locations in the CCA, ICA, and ECA (at lateral positions $x = \pm 5$

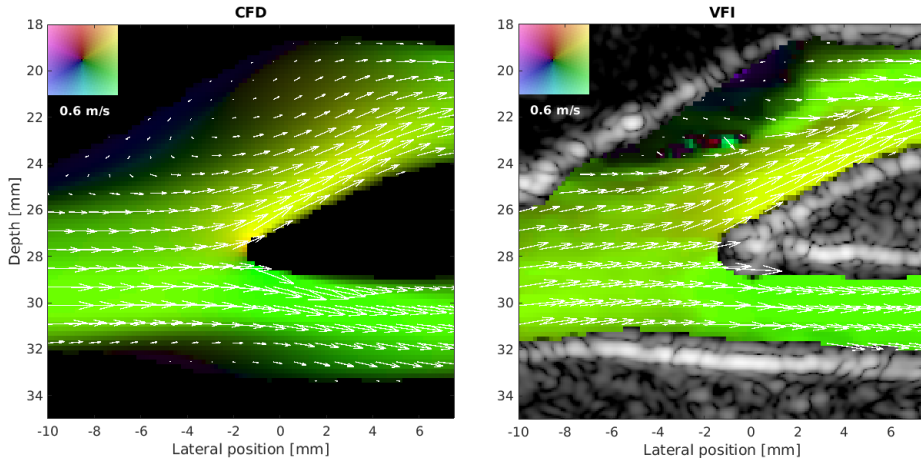


Figure 3: Velocity estimates from CFD simulation (left image) and VFI scan of phantom (right image). The frame is from the systolic phase ($t = 0.16$ s).

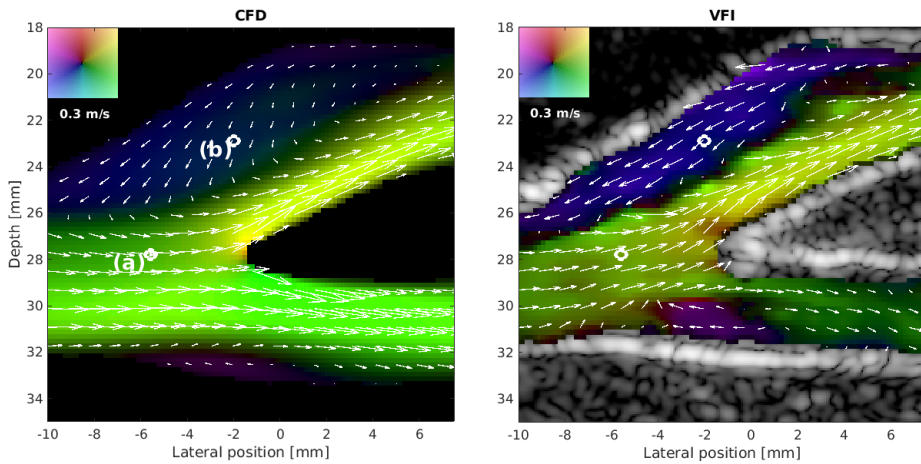


Figure 4: Velocity estimates from CFD simulation (left image) and VFI scan of phantom (right image). The frame is within the systolic deceleration ($t = 0.32$ s). The white circles are estimation points (a) and (b) for the plots in Fig. 6.

mm), and at three time instances during the pump cycle. The mean difference between CFD and VFI was calculated in each vessel and relative to the peak velocity of 0.55 m/s. The mean difference was between -2 % and 6.8 % at the three time instances in the CCA, while it was between 2 % and 11.3 % in the ICA. The largest difference of 11.3 % in the ICA was at peak systole, which might be due to the different vortices found for CFD and VFI as shown

in Fig. 3. In the ECA, the mean differences were between 3.5 % and -20 %; the largest difference was at systolic deceleration ($t = 0.32$ s).

The temporal evolution of the flow patterns was evident in a video sequence from the full acquisition (Movie 1). It revealed that a vortex quickly built up and disappeared in the ICA during systole for the VFI scan, before a larger vortex then appeared at the same location and was fully developed during

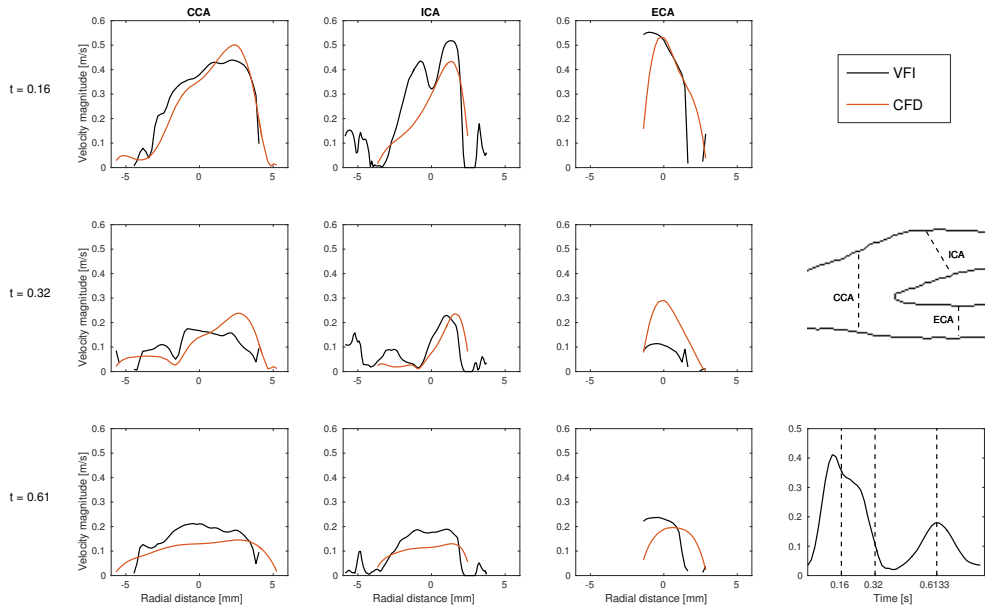


Figure 5: Comparison of velocity magnitude profiles at selected locations in the CCA (left column), ICA (middle column), and ECA (right column). Sampling were performed at $t = 0.16$ s (top row), $t = 0.32$ s (middle row), and $t = 0.61$ s (bottom row). Red profiles indicate CFD estimates and black VFI estimates.

systolic deceleration. For the CFD simulation, a single vortex in the ICA built up during late systole and was fully developed in systolic deceleration.

The temporal changes in the flow field were also observed at individual velocity estimation points. Fig. 6 shows the velocity magnitude and angles as a function of time, and the estimates were aligned to the pump cycle. Results for two estimation points are shown: for (a) the CCA and (b) the vortex in the ICA, and the locations of the points are indicated by the white circles in Fig. 4. In the CCA, flow was mainly laminar, and the shape of the velocity magnitude profile for VFI matched the one from CFD. The mean difference between CFD and VFI was 6.6 % and the mean SD was 5 %. For the ICA, the evolution of vortices during two time instances in Movie 1 was also confirmed: the angle changed from 65° to around 200° at 0.13 s and at 0.3 s in the VFI measurements, while a single vortex built up after 0.15 s in the CFD simulation. It was suspected that the vessel wall movement in the phantom might be a reason for the different flow patterns between the VFI and CFD simulation during systole. The vessel wall movement was

therefore quantified by estimating tissue velocities from the flow data and disabling the echo-canceling filter. The largest tissue velocities for a point on the proximal vessel wall were ± 2 mm/s, which were attained at 0.1 s and 0.2 s during systole. A few milliseconds later, vortices appeared in the ICA in the phantom measurement.

Comparison between VFI, MRA and spectral Doppler

The PSVs for plane wave VFI were compared to MRA and spectral Doppler for the volunteers in Fig. 7, which shows a Bland-Altman plot for plane wave VFI vs. MRA and plane wave VFI vs. spectral Doppler. The mean difference between plane wave VFI and MRA was -0.17 m/s, and the mean difference between plane wave VFI and spectral Doppler was 0.07 m/s. The highest PSV was 1.2 m/s. Linear regression between plane wave VFI and MRA provided a correlation coefficient of 0.78, and between plane wave VFI and spectral Doppler 0.70. MRA consistently estimated PSV lower compared to plane wave VFI, while spectral Doppler estimated higher PSVs than plane wave VFI for all

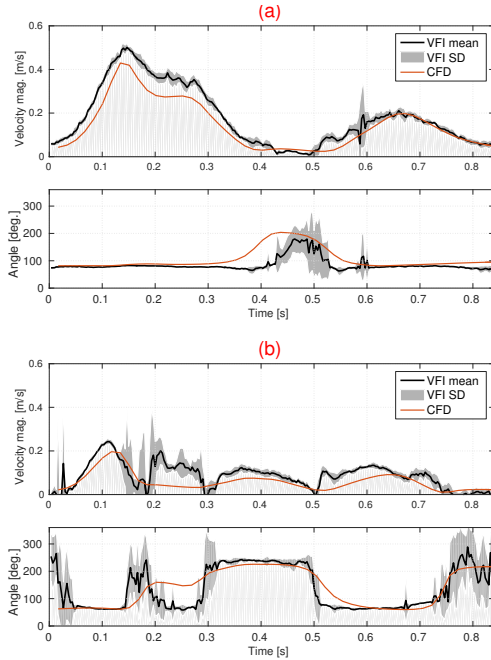


Figure 6: Velocity magnitude and angle estimates as a function of time during the cardiac cycle. The two top images show estimates for estimation point (a) in the CCA and the bottom images show estimates from point (b) in the ICA. The estimation points are also marked by white circles in Fig. 4. Black graphs are the mean VFI estimates, gray area is the SD of VFI estimates, and red graphs are CFD estimates.

volunteers except for two volunteers. It can also be noted that the differences between the methods were more pronounced for high PSVs compared to low PSVs.

Precision of VFI *in vivo*

Fig. 8 shows an example of velocity profiles and angles aligned according to the cardiac cycle. The data were from an evaluation point close to the vessel wall of the CCA. Initially, the SD of angles and velocities were calculated as a mean throughout the whole cardiac cycle automatically by the visualization program using (1). However, the angle naturally fluctuated randomly when very low velocities were present, which is shown in Fig. 8. The angles were much more stable when higher-velocity flow was present. Data for the angles were therefore also analysed for each volunteer by calculating

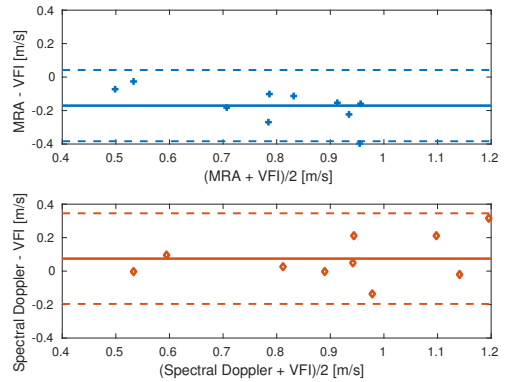


Figure 7: Bland-Altman plot of PSVs for plane wave VFI compared to MRA (top) and spectral Doppler (bottom). The solid lines are the mean differences and the dashed lines are the mean \pm 2 SD.

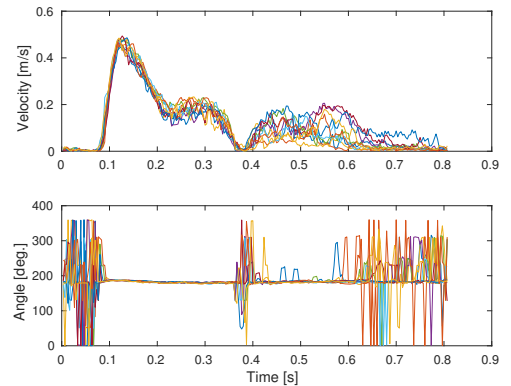


Figure 8: Velocities (top) and angles (bottom) for volunteer 6 with the evaluation point close to the vessel wall. Estimates are aligned to the cardiac cycle, and each coloured curve is for a cardiac cycle.

the SD of the angles, when the velocity magnitude was above 10 % of the maximum velocity at the evaluation point.

The mean SD of velocity magnitude estimates and angles are shown for each volunteer in Fig. 9 for evaluations of CCA scans. Results are shown for evaluation points in the center of the CCA and near the upper vessel wall, and the dashed horizontal lines are the mean SDs among the volunteers. The results for angles were calculated as a mean throughout the whole cardiac cycle (dark blue bars) and as a mean through frames where low-velocity

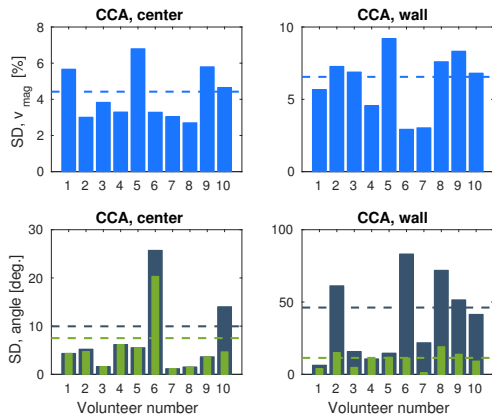


Figure 9: Mean SD of velocity magnitude (top) and angles (bottom) for each of the volunteers. Evaluation points were selected in the center of the CCA (left) and close to the upper vessel wall (right) for scans of the CCA. The green bars are when excluding low velocity flow. Dashed line is the mean SD among volunteers. Note the different scaling on the vertical axes.

flow was excluded (green bars). A high precision of the velocity magnitude was obtained in the center (mean SD was 4.4 %) and a slightly lower precision was obtained near the vessel wall (mean SD was 6.6 %). The angle estimates in the center of the CCA attained a precision of 10° , when using estimates throughout the cardiac cycle (dark blue bars in Fig. 9). The mean SD reduced to 7.5° , when excluding frames with low velocity flow (green bars in Fig. 9). Considering volunteer 6 as an outlier, the mean SD was 4.1° for the remaining volunteers. Near the vessel wall, the mean SD among the volunteers was increased to 46° , when using estimates throughout the cardiac cycle. The mean SD reduced to 11.4° , when excluding low velocity flow.

For evaluation points in the CCA of the scans of the carotid bulb, the mean SD of the velocity magnitudes was slightly higher than for the CCA scans, e.g. the mean SD in the CCA center was 8.1 % for the bulb scans. The SDs of the angle estimates were about the same levels as for the CCA scans.

Results for evaluation points in the ICA, ECA and vortices for the scans of the carotid bulb are shown in Fig. 10. Velocity magnitude and angles were estimated with a higher precision in the ICA than the ECA: mean SD of the velocity magnitude

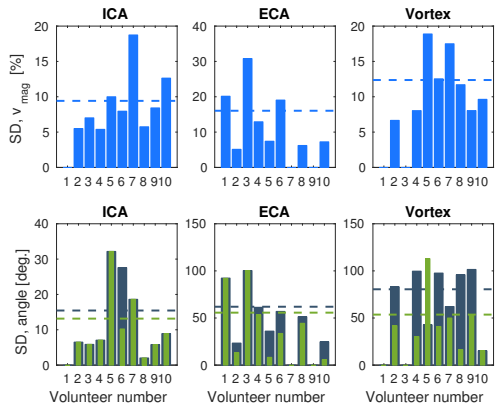


Figure 10: Mean SD of velocity magnitude (top) and angles (bottom) for each of the volunteers. Evaluation points were selected in the ICA (left), ECA (middle), and vortex (right) for scans of the carotid bulb. The green bars are when excluding low velocity flow. Dashed line is the mean SD among volunteers. Note the different scaling on the vertical axes.

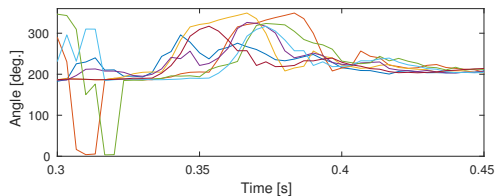


Figure 11: Angles for an evaluation point in a vortex, which was present from 0.33 s to 0.4 s. Estimates were aligned to the cardiac cycle, and each coloured curve is for a cardiac cycle.

was 9.4 % in the ICA and 16 % in the ECA. Mean SD of the angles was 15.4° in the ICA and 62° in the ECA, when using estimates throughout the cardiac cycle. Small reductions in SD to 13.2° and 55° for the ICA and ECA, respectively, were obtained when excluding frames with low velocity flow. For the vortices, the velocity magnitude was estimated with a precision of 12.4 %, while large fluctuations in the angles were obtained throughout the cardiac cycle (mean SD was 80°). When calculating the precision during the short time span, where the vortices were present, the mean SD reduced to 54° as shown with the green bars in Fig. 10. The precision for vortices was mainly affected by small variations in the time of development and disappearance of vortices. Fig. 11 shows an example of the angle variation for a vortex present from 0.33 s to 0.4 s.

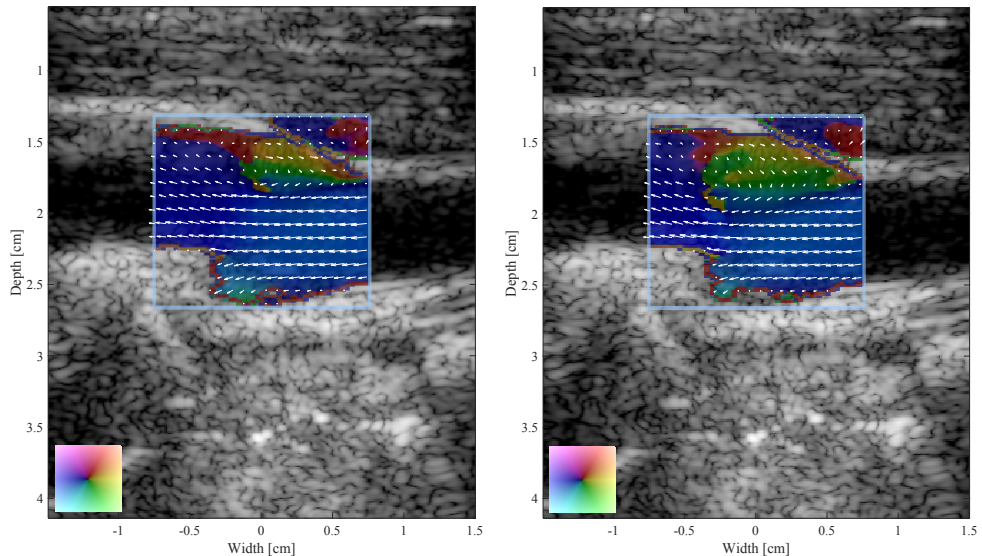


Figure 12: VFI of the carotid bulb for volunteer 8. A large vortex was created at the inlet of the ICA (left image) and it moved downstream (right image). The time between the two frames was 10 ms.

The vortex did not develop at exactly the same time in each cardiac cycle, which lead to large variations in the angle estimates.

In vivo complex flow patterns

The carotid bulb scans on the ten volunteers showed a number of interesting flow patterns, and examples are presented in this section. Vortices were present in eight out of ten volunteers - some vortices were very small and rapidly formed and disappeared, while others filled most of the carotid sinus. Fig. 12 show two frames during systole for volunteer 8 with 10 ms between the frames. The high frame rate of the VFI method captured the formation of a vortex initiated upstream in the carotid bulb and with increasing size as it moved downstream in the ICA. The same pattern was observed for volunteer 5 as shown in Fig. 13. This flow feature has previously been captured by synthetic aperture imaging (Villagomez-Hoyos et al., 2016b) and plane wave imaging (Hansen et al., 2009a).

Fig. 14 shows the carotid bulb for volunteer 3. During the entire cardiac cycle, flow filled the ICA (superficial vessel) from the ECA (deep vessel). It contributed to ensuring that flow was antegrade in the ICA during the entire cardiac cycle, while flow

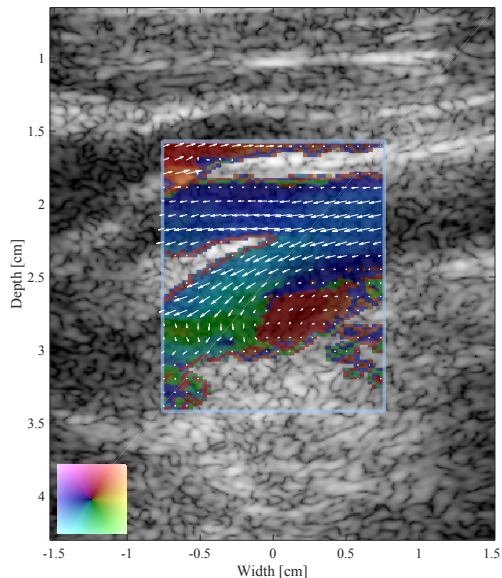


Figure 13: VFI of the carotid bulb for volunteer 5. A large vortex was formed and moved downstream in the ICA.

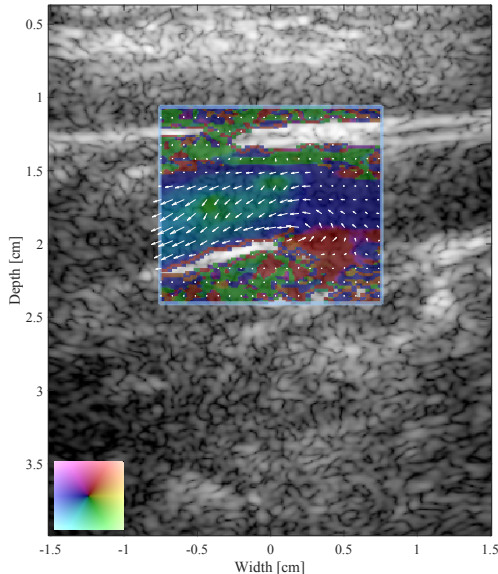


Figure 14: VFI of the carotid bulb for volunteer 3.

was antegrade or very slow in parts of the ECA during most of the cardiac cycle. A similar flow pattern has previously been observed Hansen et al. (2009a), where retrograde blood from the subclavian artery filled the CCA during diastole. However, in this study, it was visualized in detail that flow from the ECA also contributes to antegrade flow to the brain through the ICA during diastole.

Discussion

The VFI phantom measurement and CFD simulation of the velocity field provided a study for comparing the performance of the two independent methods to estimate complex flow fields in an anthropomorphic geometry. The comparison showed that similar velocity magnitudes and shapes of velocity profiles were obtained throughout the bifurcation at the three time instances (Fig. 3-5) with mean differences within 10 %, when calculated across vessels. The largest differences were obtained in the ECA during systolic deceleration (mean difference -20 %) and in the ICA during systole (mean difference 11.3 %). While the flow conditions in the CCA were close to the imposed inlet conditions, the flow conditions were much more complex in the

ECA and ICA, because the flow patterns changed through the bifurcation. Vortices were also present in both measurements and simulations at locations within 1-2 mm, and they appeared at the same time during systolic deceleration or slightly earlier in measurements. This was also shown in Fig. 6 (bottom), where the variation in angle for a vortex showed good agreement between CFD simulation and VFI, except at the onset of the vortex at 0.15 s.

Previous works have used simulated ultrasound images obtained with Field II to compare derived flow estimates with CFD simulated velocities in carotid bifurcation geometries, in the forearm vasculature, and in a neonatal heart model (Swillens et al., 2009; Canneyt et al., 2013; Cauwenberge et al., 2016). Simulations represent ideal situations, whereas measurements do not. Measurements are affected by noise in the ultrasound system and by imperfections of the transducer, phantom and flow pump. The phantom measurement resembled several conditions under an *in vivo* scan, but provided better control over the scan environment.

The alignment between transducer scan plane in the measurement and CFD simulated velocities was not perfect. Especially the ECA appeared more narrow and/or slightly translated vertically, which was apparent from the velocity profiles in Fig. 5. Furthermore, the phantom material had slightly shrunken during the time from initial fabrication to measurement, which may have affected the size of the vessels. A limitation of the CFD simulation was that the vessel walls were assumed rigid. However, the vessel walls of the fabricated phantom moved during systole (axial velocities of ± 2 mm/s), which changed the flow pattern and may explain the differences in vortex development between measurement and CFD simulation. If vessel wall movement should be taken into account in the CFD simulation, fluid-structure interaction simulation models could be included (Swillens et al., 2010). This requires a much more complicated CFD model, which has yet to be developed. The CFD simulation should be considered an independent method to compare VFI with - and not the ground truth, since CFD is based on models and assumptions, which may not be entirely valid for the specific measurement. These include assumptions of the inlet and outlet boundary conditions. The temporal shape of the inlet profile for the simulation was obtained from the measurement, however, the spatial velocity profiles were assumed parabolic

and rotational symmetric, which may not be the case for the measurement.

The investigation of accuracy of PSV for laminar flow in the CCA (Fig. 7) showed a mean difference of -0.17 m/s between plane wave VFI and MRA. Previous studies have reported negative bias, when comparing MRA with spectral Doppler for flow in the carotid bifurcation (Harloff et al., 2013) and across the mitral valve (Karwatowski et al., 1995). The difference may be due to lower spatial and temporal resolutions in MRA than plane wave VFI. Data from VFI were averaged over around 10 cardiac cycles during the 10 s scan sequence, while MRA data were averaged over 210 cardiac cycles, which was effectively a low-pass filtering of the data. The mean difference between plane wave VFI and spectral Doppler was 0.07 m/s. It is known that spectral Doppler has a positive bias due to spectral broadening, which was also reported for plane wave vector Doppler (Tortoli et al., 2015). In addition to spectral broadening, the performance of spectral estimators is affected by several other factors including windowing effects, the observation time, and manual determination of beam-to-flow angle (Newhouse et al., 1980). Furthermore, the Bland-Altman plot in Fig. 7 showed a larger difference in PSV for higher mean PSV than low. This may be due to transit time broadening of the Doppler spectrum, where blood moving at high velocities get observed for a shorter period of time within the US beam, which further broadens the spectrum (Jensen, 1996). The plane wave VFI method was not affected by the same factors as spectral estimators, because received signals from emission to emission were directly correlated to find the time or phase shift between pulses.

Precision of the plane wave VFI method was investigated at several evaluation points in the vessels. The highest precisions were found in the center of the CCA with laminar flow conditions (mean SD was 4.4 % for velocities and 4.1° for angles for nine of the volunteers). The precision was lower close to the vessel walls, but still at acceptable levels (mean SD was 6.6 % for velocities and 11.4° for angles when low velocity flow was excluded). The precision of velocities got progressively lower when estimating flow in the ICA (mean SD 9.4 %) and in the ECA (mean SD 16 %), where flow patterns deviated from laminar flow conditions and the vessels were smaller. The lowest precision for angles was found in the ECA and in vortices, where the mean SD was around 50° . Both locations were af-

ected by low velocities and flow patterns, which were not exactly repeatable from one cardiac cycle to the next one.

Measurement conditions *in vivo* are affected by physiological factors such as breathing, tissue and transducer movement, heart rate variations etc. The very high precision in the CCA was approximately the same as the precision found in the phantom measurements, which indicated that the measurement conditions approached each other.

A number of interesting flow patterns were captured *in vivo* with plane wave VFI, including the development of vortices and supply of flow from the ECA to the CCA. Similar flow patterns have been visualized with other VFI techniques (Hansen et al., 2009a; Ekroll et al., 2014), but color flow imaging and spectral Doppler lack this feature. The VFI phantom measurement of complex flow showed that similar flow patterns were predicted by CFD, which strengthens the validity of plane wave VFI to measure these flow patterns. Furthermore, the population size with ten volunteers in this study gives an indication of the precision of VFI estimates *in vivo*. Previous studies have only included a few volunteers (Jensen et al., 2017; Villagomez-Hoyos et al., 2016b). Larger population studies with healthy volunteers and patients with cardiovascular diseases are needed to further establish the VFI techniques and to reveal how vortices, turbulent flow and other complex flow patterns may provide new information to the clinician. This has been indicated for patients with stenotic aortic valves (Hansen et al., 2016).

Conclusion

The study investigated the precision and accuracy of plane wave VFI for laminar and complex flow among ten volunteers. A comparison between flow measured in a carotid bifurcation phantom using VFI and CFD velocities simulated in the same geometry showed the same laminar and complex flow patterns. Mean differences between CFD and VFI for velocity magnitudes were within 7 % in the common carotid, but a mean difference of -20 % was obtained in the ECA. Among the ten volunteers, the precision *in vivo* was highest in the center of the common carotid artery (standard deviation 4.4 % for velocity magnitudes) and lowest in the ECA and for vortices (standard deviation 16 % for velocity magnitudes). Plane wave VFI showed a number of interesting flow patterns *in vivo*, and

angle-independent and quantitative estimates could be obtained everywhere in the images. The study showed that plane wave VFI can yield quantitative estimates of both laminar and complex flow dynamics, which may give the clinician a new tool for assessing the health of blood vessels.

Acknowledgments

This work was supported by grant 82-2012-4 from the Danish National Advanced Technology Foundation and by BK Ultrasound Aps.

References

- Anderson ME. Multi-dimensional velocity estimation with ultrasound using spatial quadrature. *IEEE Trans. Ultrason., Ferroelec., Freq. Contr.*, 1998;45:852–861.
- Bamford J, Sandercock P, Dennis M, Burn J, Warlow C. Classification and natural history of clinically identifiable subtypes of cerebral infarction. *Lancet*, 1991;337:1521–1526.
- Bercoff J, Montaldo G, Loupas T, Savery D, Meziere F, Fink M, Tanter M. Ultrafast compound Doppler imaging: providing full blood flow characterization. *IEEE Trans. Ultrason., Ferroelec., Freq. Contr.*, 2011;58:134–147.
- Canneyt KV, Swillens A, Løvtakken L, Antiga L, Verdonck P, Segers P. The accuracy of ultrasound volume flow measurements in the complex flow setting of a forearm vascular access. *J. Vasc. Access*, 2013;14:281–290.
- Cauwenberge JV, Lovstakken L, Fadnes S, Rodriguez-Morales A, Vierendeels J, Segers P, Swillens A. Assessing the performance of ultrafast vector flow imaging in the neonatal heart via multiphysics modeling and in vitro experiments. *IEEE Trans. Ultrason., Ferroelec., Freq. Contr.*, 2016;63:1772–1785.
- Cebal J, Yim P, Lohner R, Soto O, Choyke P. Blood flow modeling in carotid arteries with computational fluid dynamics and MR imaging. *Acad. Radiol.*, 2002;9:1286–1299.
- Corriveau M, Johnston K. Interobserver variability of carotid Doppler peak velocity measurements among technologists in an ICAVL-accredited vascular laboratory. *J. Vasc. Surg.*, 2004;39:735–741.
- Dunmire B, Beach KW, Labs. KH, Plett M, Strandness DE. Cross-beam vector Doppler ultrasound for angle independent velocity measurements. *Ultrasound Med. Biol.*, 2000;26:1213–1235.
- Ekroll IK, Dahl T, Torp H, Løvtakken L. Combined vector velocity and spectral doppler imaging for improved imaging of complex blood flow in the carotid arteries. *Ultrasound Med. Biol.*, 2014;40:1629–1640.
- Ekroll IK, Swillens A, Segers P, Dahl T, Torp H, Lovstakken L. Simultaneous quantification of flow and tissue velocities based on multi-angle plane wave imaging. *IEEE Trans. Ultrason., Ferroelec., Freq. Contr.*, 2013;60:727–738.
- Hansen KL, Møller-Sørensen H, Kjaergaard J, Jensen MB, Lund JT, Pedersen MM, Lange T, Jensen JA, Nielsen MB. Intraoperative vector flow imaging using ultrasound of the ascending aorta among 40 patients with normal, stenotic and replaced aortic valves. *Ultrasound Med. Biol.*, 2016;42:2414–2422.
- Hansen KL, Møller-Sørensen H, Kjaergaard J, Jensen MB, Lund JT, Pedersen MM, Olesen JB, Jensen JA, Nielsen MB. Vector flow imaging compared with conventional doppler ultrasound and thermodilution for estimation of blood flow in the ascending aorta. *Ultrasonic Imaging*, 2015;1–16.
- Hansen KL, Udesen J, Gran F, Jensen JA, Nielsen MB. In-vivo examples of flow patterns with the fast vector velocity ultrasound method. *Ultraschall in Med.*, 2009a;30:471–476.
- Hansen KL, Udesen J, Oddershede N, Henze L, Thomsen C, Jensen JA, Nielsen MB. In vivo comparison of three ultrasound vector velocity techniques to MR phase contrast angiography. *Ultrasonics*, 2009b;49:659–667.
- Harloff A, Zech T, Wegent F, Strecker C, Weiller C, Markl M. Comparison of blood flow velocity quantification by 4D flow MR imaging with ultrasound at the carotid bifurcation. *Am. J. Neuroradiol.*, 2013;34:1407–1413.
- Holbek S, Ewertsen C, Bouzari H, Pihl MJ, Hansen KL, Stuart MB, Nielsen MB, Jensen JA. Ultrasonic 3-D vector flow method for quantitative in vivo peak velocity and flow rate estimation. *IEEE Trans. Ultrason., Ferroelec., Freq. Contr.*, 2017;64:544–554.
- Jensen J, Villagomez-Hoyos CA, Stuart MB, Ewertsen C, Nielsen MB, Jensen JA. Fast plane wave 2-d vector flow imaging using transverse oscillation and directional beamforming. *IEEE Trans. Ultrason., Ferroelec., Freq. Contr.*, 2017:Submitted.
- Jensen JA. Estimation of Blood Velocities Using Ultrasound: A Signal Processing Approach. Cambridge University Press, New York, 1996.
- Jensen JA. Directional velocity estimation using focusing along the flow direction: I: Theory and simulation. *IEEE Trans. Ultrason., Ferroelec., Freq. Contr.*, 2003;50:857–872.
- Jensen JA, Holtén-Lund H, Nilsson RT, Hansen M, Larsen UD, Domsten RP, Tomov BG, Stuart MB, Nikolov SI, Pihl MJ, Du Y, Rasmussen JH, Rasmussen MF. SARUS: A synthetic aperture real-time ultrasound system. *IEEE Trans. Ultrason., Ferroelec., Freq. Contr.*, 2013;60:1838–1852.
- Jensen JA, Munk P. A new method for estimation of velocity vectors. *IEEE Trans. Ultrason., Ferroelec., Freq. Contr.*, 1998;45:837–851.
- Jensen JA, Nikolov S, Gammelmark KL, Pedersen MH. Synthetic aperture ultrasound imaging. *Ultrasonics*, 2006;44:e5–e15.
- Karwatowski SP, Brecker SJD, Yang GZ, Firmin DN, Sutton MSJ, Underwood SR. Mitral valve flow measured with cine MR velocity mapping in patients with ischemic heart disease: comparison with Doppler echocardiography. *J. Magn. Reson. Imaging*, 1995;5:89–92.
- Kruskal JB, Newman PA, Sammons LG, Kane RA. Optimizing Doppler and color flow US: Application to hepatic sonography. *Radiographics*, 2004;24:657–675.
- Lai SSM, Yiu BYS, Poon AKK, Yu ACH. Design of anthropomorphic flow phantoms based on rapid prototyping of compliant vessel geometries. *Ultrasound Med. Biol.*, 2013;39:1654–1664.
- Lenge M, Ramalli A, Tortoli P, Cachard C, Liebgott H. Plane-wave transverse oscillation for high-frame-rate 2-D vector flow imaging. *IEEE Trans. Ultrason., Ferroelec., Freq. Contr.*, 2015;62:2126–2137.
- Lui E, Steinman A, Cobbold R, Johnston K. Human factors as a source of error in peak Doppler velocity measurement.

- J. Vasc. Surg., 2005;42:972–979.
- Naghavi M, Libby P, Falk E, Casscells SW, Litovsky S, Rumberger J, Badimon JJ, Stefanadis C, Moreno P, Pasterkamp G, Fayad Z, Stone PH, Zipes DP, Shah PK, Willerson JT. From vulnerable plaque to vulnerable patient: a call for new definitions and risk assessment strategies: Part 1. *Circulation*, 2003;108:1664–1672.
- Newhouse VL, Censor D, Vontz T, Cisneros JA, Goldberg BB. Ultrasound Doppler probing of flows transverse with respect to beam axis. *IEEE Trans. Biomed. Eng.*, 1987;BME-34:779–788.
- Newhouse VL, Furgason ES, Johnson GF, Wolf DA. The dependence of ultrasound Doppler bandwidth on beam geometry. *IEEE Trans. Son. Ultrason.*, 1980;SU-27:50–59.
- Nikolov SI, Jensen JA. Velocity estimation using synthetic aperture imaging. In: *Proc. IEEE Ultrason. Symp.*, 2001. pp. 1409–1412.
- Nikolov SI, Jensen JA. In-vivo synthetic aperture flow imaging in medical ultrasound. *IEEE Trans. Ultrason., Ferroelec., Freq. Contr.*, 2003;50:848–856.
- Oddershede N, Jensen JA. Effects influencing focusing in synthetic aperture vector flow imaging. *IEEE Trans. Ultrason., Ferroelec., Freq. Contr.*, 2007;54:1811–1825.
- Pedersen MM, Pihl MJ, Haugaard P, Hansen JM, Hansen KL, Nielsen MB, Jensen JA. Comparison of real-time in vivo spectral and vector velocity estimation. *Ultrasound Med. Biol.*, 2012;38:145–151.
- Salles S, Chee AJY, Garcia D, Yu ACH, Vray D, Liebgott H. 2-D arterial wall motion imaging using ultrafast ultrasound and transverse oscillations. *IEEE Trans. Ultrason., Ferroelec., Freq. Contr.*, 2015;62:1047–1058.
- Steinman D, Poepping T, Tambasco M, Rankin R, Holdsworth D. Flow patterns at the stenosed carotid bifurcation: Effect of concentric versus eccentric stenosis. *Ann. Biomed. Eng.*, 2000;28:415–423.
- Stewart SFC. Effects of transducer, velocity, doppler angle, and instrument settings on the accuracy of color doppler ultrasound. *Ultrasound Med. Biol.*, 2001;27:551–564.
- Swillens A, Degroote J, Vierendeels J, Løvstakken L, Segers P. A simulation environment for validating ultrasonic blood flow and vessel wall imaging based on fluid-structure interaction simulations: Ultrasonic assessment of arterial distension and wall shear rate. *Medical Physics*, 2010;37:4318–4330.
- Swillens A, Løvstakken L, Kips J, Torp H, Segers P. Ultrasound simulation of complex flow velocity fields based on computational fluid dynamics. *IEEE Trans. Ultrason., Ferroelec., Freq. Contr.*, 2009;56:546–556.
- Tanter M, Fink M. Ultrafast imaging in biomedical ultrasound. *IEEE Trans. Ultrason., Ferroelec., Freq. Contr.*, 2014;61:102–119.
- Tortoli P, Bambi G, Ricci S. Accurate Doppler angle estimation for vector flow measurements. *IEEE Trans. Ultrason., Ferroelec., Freq. Contr.*, 2006;53:1425–1431.
- Tortoli P, Lenge M, Righi D, Ciuti G, Liebgott H, Ricci S. Comparison of carotid artery blood velocity measurements by vector and standard Doppler approaches. *Ultrasound Med. Biol.*, 2015;41:1354–1362.
- Trahey GE, Allison JW, von Ramm OT. Angle independent ultrasonic detection of blood flow. *IEEE Trans. Biomed. Eng.*, 1987;BME-34:965–967.
- Udesen J, Gran F, Hansen KL, Jensen JA, Thomsen C, Nielsen MB. High frame-rate blood vector velocity imaging using plane waves: simulations and preliminary experiments. *IEEE Trans. Ultrason., Ferroelec., Freq. Contr.*, 2008;55:1729–1743.
- Villagomez-Hoyos CA, Stuart MB, Bechsgaard T, Nielsen MB, Jensen JA. High frame rate synthetic aperture vector flow imaging for transthoracic echocardiography. In: *Proc. SPIE Med. Imag.*, 2016a.
- Villagomez-Hoyos CA, Stuart MB, Hansen KL, Nielsen MB, Jensen JA. Accurate angle estimator for high frame rate 2-D vector flow imaging. *IEEE Trans. Ultrason., Ferroelec., Freq. Contr.*, 2016b;63:842–853.
- Yiu BY, Lai SS, Yu AC. Vector projectile imaging: time-resolved dynamic visualization of complex flow patterns. *Ultrasound Med. Biol.*, 2014;40:2295–2309.

Paper VII

Vector velocity volume flow estimation: Sources of error and corrections applied for arteriovenous fistulas

Jonas Jensen, Jacob Bjerring Olesen, Matthias Bo Stuart, Peter Møller Hansen, Michael Bachmann Nielsen, and Jørgen Arendt Jensen

Ultrasonics, vol. 70, p. 136-146, August 2016.



Vector velocity volume flow estimation: Sources of error and corrections applied for arteriovenous fistulas



Jonas Jensen^{a,*}, Jacob Bjerring Olesen^a, Matthias Bo Stuart^a, Peter Møller Hansen^{a,b}, Michael Bachmann Nielsen^b, Jørgen Arendt Jensen^a

^a Center for Fast Ultrasound Imaging, Dept. of Elec. Eng., Bldg. 349, Technical University of Denmark, DK-2800 Lyngby, Denmark

^b Department of Radiology, Copenhagen University Hospital, DK-2100 Copenhagen, Denmark

ARTICLE INFO

Article history:

Received 16 October 2015

Received in revised form 13 April 2016

Accepted 29 April 2016

Available online 30 April 2016

Keywords:

Volume flow

Transverse oscillation

Error sources

Arteriovenous fistula

ABSTRACT

A method for vector velocity volume flow estimation is presented, along with an investigation of its sources of error and correction of actual volume flow measurements. Volume flow errors are quantified theoretically by numerical modeling, through flow phantom measurements, and studied *in vivo*. This paper investigates errors from estimating volumetric flow using a commercial ultrasound scanner and the common assumptions made in the literature. The theoretical model shows, e.g. that volume flow is underestimated by 15%, when the scan plane is off-axis with the vessel center by 28% of the vessel radius. The error sources were also studied *in vivo* under realistic clinical conditions, and the theoretical results were applied for correcting the volume flow errors. Twenty dialysis patients with arteriovenous fistulas were scanned to obtain vector flow maps of fistulas. When fitting an ellipsis to cross-sectional scans of the fistulas, the major axis was on average 10.2 mm, which is 8.6% larger than the minor axis. The ultrasound beam was on average 1.5 mm from the vessel center, corresponding to 28% of the semi-major axis in an average fistula. Estimating volume flow with an elliptical, rather than circular, vessel area and correcting the ultrasound beam for being off-axis, gave a significant ($p = 0.008$) reduction in error from 31.2% to 24.3%. The error is relative to the Ultrasound Dilution Technique, which is considered the gold standard for volume flow estimation for dialysis patients. The study shows the importance of correcting for volume flow errors, which are often made in clinical practice.

© 2016 Elsevier B.V. All rights reserved.

1. Introduction

Quantifying blood flow to organs is desirable for evaluating the pathological state of the vascular system, e.g., in the carotid artery [1] or at arteriovenous fistulas (AVF) [2], where the latter case is the main concern of this paper. An AVF is a surgically created connection of an artery and a vein in the upper extremity of patients undergoing dialysis. It is needed in hemodialysis for high blood flow facilitation and repeated cannulation [3]. Ideally, the AVF matures and results in the required increase in blood volume flow from a preoperative to postoperative state of the fistula [4,5]. However, AVF non-maturation occurs and up to 60% of patients will experience some degree of fistula dysfunction during the first 18 months after its creation [6]. Stenosis and thrombosis are common complications of AVFs, and it is recommended to monitor their function by measuring volume flow [7]. The standard and

referential method for volume flow estimation in an AVF is the Ultrasound Dilution Technique (UDT), which is an indirect method performed during dialysis [8]. A known amount of indicator substance (saline) is injected into the bloodstream, and the change in blood concentration diluted by the indicator is measured. Concentration is monitored by two sensors attached to the dialysis blood lines, which have to be reversed to create a recirculation between the blood lines. Research in alternatives to UDT for non-invasive volume flow estimation in AVFs has focused on medical ultrasound, which provides a direct and real-time quantification of blood velocities and morphology [9,10]. AVFs are irregular and superficial vessels and, therefore, difficult to scan even for experienced medical doctors. This results in different sources of error depending on the method used for volume flow estimation.

The simplest and most widely available method for volume flow estimation using ultrasound is based on the single-point Doppler method. The peak velocity is estimated at one location along the presumed centerline of a vessel, and volume flow is calculated by multiplying the average velocity with a circular cross-sectional area of the vessel. To translate the velocity estimate into the full

* Corresponding author at: Technical University of Denmark, Ørstedes Plads, Building 349, DK-2800 Lyngby, Denmark.

E-mail address: jonjens@elektro.dtu.dk (J. Jensen).

cross-sectional velocity profile, it is assumed that flow is steady and attains either a parabolic or flat velocity profile [11]. Several authors have documented the error associated with this method for volume flow estimation [11–13] and specifically in AVFs [14]. Pulsatile flow behavior is more accurately described by Womersley's model [15], which was applied for volume flow estimation and tested *in vivo* by Leguy et al. [16].

A more accurate method is to estimate velocities at several points along the whole vessel diameter, thereby obtaining the actual in-plane velocity profile, which is then used in the estimator [11]. This eliminates assumptions about the velocity profile, since the actual velocity profile is measured. The method showed a bias of 5% for constant flow, when using conventional Doppler ultrasound for velocity estimation [17]. The multi-point method performed as well as the single point method for laminar flow conditions in an AVF setting, and reduced bias from –50% to –20% under complex flow conditions [18]. However, the multi-point method still relies on several assumptions to estimate volume flow, and it is, furthermore, limited to uni-directional flow as only the velocity component along the ultrasound beam is captured. A major limitation of the method is, therefore, associated with determining the correct beam-to-flow angle, which introduces uncertainties in volume flow estimation. Picot and Embree [19] showed that the estimation of the beam-to-flow angle was the most dominant source of error in volume flow estimation. In a study by Van Canneyt et al. [14], where volume flow in AVFs were estimated using simulations, the angle-dependency problem was also found to be a major source of error and resulted in inaccuracies for complex flow. Furthermore, conventional velocity estimation is challenging in superficial vessels, e.g., in AVFs, where flow is nearly transverse to the ultrasound beam. These issues motivate the introduction of volume flow estimators based on angle-independent velocity estimation methods and investigate the sources of errors to correct for them and obtain more accurate volume flow estimates.

Volume flow estimation based on 2D vector velocities removes the angle dependency. Vector velocity methods extend the conventional 1D velocity estimate to vector estimates. Transverse Oscillation (TO) is one such method capable of estimating the axial and lateral velocity components independent of each other [20]. This makes the TO method attractive for angle independent volume flow estimation. However, velocities are only estimated in one scan plane along the vessel, and assumptions of axisymmetric flow, circular vessels and velocity sampling along a vessel diameter still have to be made. Deviations from these assumptions introduce errors in volume flow estimation and should be taken into account to improve the accuracy of volume flow estimates. Picot and Embree [19] already investigated some of these errors and applied the results to 1D velocity estimates with a fixed angle. This paper investigates 2D vector velocity volume flow, which is capable of automatically handling a spatial and temporal variation in beam-to-flow angle over the cardiac cycle.

The ideal method for volume flow estimation would be to measure the full 3D velocity vectors, since no assumptions on the flow and vessel geometry are required. This is possible with a 3D version of the TO method, but the method is still in its infancy and under development [21]. Until the method is realized on clinical ultrasound systems, accurate volume flow measurements with 1D and 2D systems are still the preferred methods for noninvasive volume flow estimation.

In this work, a vector velocity volume flow estimator and its sources of error are presented. The errors are investigated in a theoretical model, and the accuracy of the volume flow estimator under a realistic setup is measured by a commercial scanner on a flow phantom. Vector velocity volume flow estimates from *in vivo* scans of fistulas in hemodialysis patients are then used to

investigate the method and error correction under realistic clinical conditions for patients that are often difficult to scan. This paper is based on a conference publication [22]. It expands on the method for volume flow estimation, includes three additional sources of error, and presents flow phantom measurements.

2. Materials and methods

A volume flow estimator using vector velocities acquired with the TO approach is presented in this section along with an investigation of error sources. The theoretical analysis, measurements on a flow phantom, and procedures for a clinical study are also described.

2.1. Vector velocity estimation

Transverse oscillation is an angle-independent method for vector velocity estimation within the ultrasound scan plane [20]. By introducing a lateral oscillation in the pulse-echo field along with the conventional axial oscillation, the received signals become sensitive to both axial and lateral motion in the field. The transmitted field is weakly focused, and the laterally oscillating field is created in receive beamforming by changing the apodization function to contain two separated peaks. The axial velocity is estimated using a phase shift estimator as in conventional velocity imaging, while a special fourth order autocorrelation estimator is used for the transverse velocity component [23]. The method has been validated in a flow-rig [24], in the right common carotid artery [25], and used for elasticity imaging [26]. The technique is also available on commercial ultrasound systems (BK Medical, Herlev, Denmark).

2.2. Volume flow estimation

Vector velocities acquired with the TO approach are used in a volume flow estimator. Since velocities are only acquired in one scan plane along the vessel, three assumptions have to be made in order to obtain a volume flow estimate: It is assumed that flow is axisymmetric, the cross-sectional area of the vessel is circular, and that the velocity sampling is along a diameter of the vessel.

The volume flow Q of a fluid crossing a circular surface S at time t is:

$$Q(t) = \int_S \mathbf{v}(\mathbf{x}, t) \cdot \mathbf{e} dS, \quad (1)$$

where \mathbf{v} is the velocity vector at position \mathbf{x} with respect to an arbitrary origin, \mathbf{e} is a unit vector normal to the surface S , and \cdot is the dot product operator.

Consider a Vector Flow Image (VFI) at time t , where a line-by-line image has been acquired using focused beams. A longitudinal image of a section of the vessel is acquired, so that the image consists of velocity estimates along M parallel lines in the longitudinal direction. A 2D vector velocity estimate $\mathbf{v}(r, m, t)$ represents the velocity magnitude and direction of flow at a perpendicular distance r from the vessel's center axis, and the linear array scan gives parallel image lines denoted by m . Estimated vector velocities at r and along the ultrasound beam are used for volume flow calculation as shown in Fig. 1. The volume flow at line number m can be estimated as

$$Q(m, t) = \pi \int_{-R}^R \mathbf{v}(r, m, t) \cdot \mathbf{e} |r| dr, \quad (2)$$

which corresponds to a rotation of the vector velocity profile around the vessel axis. The radius of the vessel is R , and the projection of \mathbf{v} onto \mathbf{e} ensures that flow is normal to the cross-sectional area. Flow can be in any direction within the scan plane and the

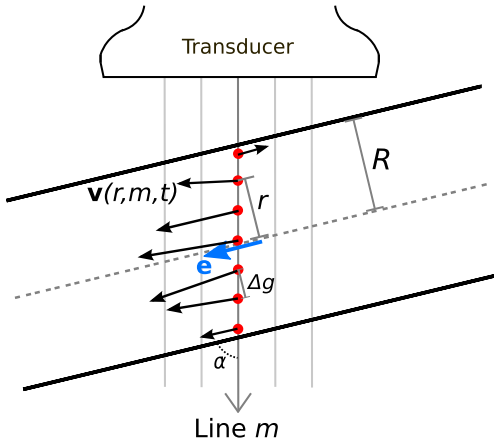


Fig. 1. Longitudinal view of a vessel and velocity estimation at positions along line m . The vector velocity sample $\mathbf{v}(r, m, t)$ is at a radial and perpendicular distance r from the center axis, the radius of the vessel is R , and the radial distance between velocity estimation points is Δg . The beam-to-flow angle is α , and \mathbf{e} is a unit vector normal to the cross-sectional vessel area.

directional information is provided by the TO method. Thereby, the estimator handles laminar flow along the vessel and also cases with varying flow angles along the ultrasound beam, see Fig. 1. The integral in (2) is converted into a summation of discrete values, when a finite number, N , of velocity estimates inside the vessel is used:

$$Q(m, t) = \pi \Delta g^2 \sum_{n=-N/2}^{N/2} \mathbf{v}(n, m, t) \cdot \mathbf{e} |n|. \quad (3)$$

The radial distance between velocity estimation points is Δg and substitutes dr so that $r = n\Delta g$. It can be considered a sum of volume flows through semi-annular rings, which each have an area of $\pi \Delta g^2 |n|$ and an associated velocity component $\mathbf{v}(n, m, t) \cdot \mathbf{e}$. The angle between \mathbf{e} and the beam direction is α and is used to calculate Δg ,

$$\Delta g = \Delta z \sin(\alpha), \quad (4)$$

where Δz is the axial distance between two velocity estimation points.

The mean volume flow during a scan sequence is found by averaging the estimates at all scan lines and over the number of frames N_f in a scan sequence,

$$Q = \frac{1}{MN_f} \sum_{t=1}^{N_f} \sum_{m=1}^M Q(m, t), \quad (5)$$

where M is the number of longitudinal image lines. For pulsatile flow, the averaging over N_f frames is for a whole number of cardiac cycles.

2.3. Sources of error

This paper investigates five sources of error, denoted A-E, affecting the accuracy of volume flow estimation using a commercial ultrasound system. The error sources are geometric errors and derived from a combination of system settings and practical considerations in reference to the suggested technique. An illustration of the error sources is shown in Fig. 2 and described in the following:

- A. A high spatial resolution is required for measuring the actual velocity profile, and it is dependent on the distance between velocity estimation points, Δg , which is larger than the system sampling interval. Δg is primarily determined by the emitted pulse length, which determines the correlation length for dependent velocity estimates. Therefore, the number of velocity samples inside the vessel and the size of semi-annular rings are related to Δg . Calculating volume flow through wide semi-annular rings can result in inaccurate estimation of the true volume flow.
- B. The radius of the vessel used for volume flow estimation, r_Q , is often estimated by measuring directly on the B-mode image or by using a blood-tissue discriminator. Some cases show that r_Q is estimated differently from what the true radius R is. This affects the accuracy of the estimated vessel area and, hence, the volume flow.
- C. The ultrasound beam is assumed to intersect the middle of the vessel, but it can be challenging for the examiner to align the scan plane with the vessel's center line. This results in sampling off-axis at a distance d_{off} from the center line. This error source was also investigated by [19] and has been included in this work for completeness.
- D. The cross-sectional blood vessel area is often elliptical rather than circular, due to plaque accumulation and that superficial vessels are easily compressed under the weight of a transducer. The assumption of a circular vessel area will in this case result in an underestimation of the volume flow proportional to the ratio of the elliptical diameters, d_2/d_1 [19].
- E. The cross-sectional area of an elliptical vessel is determined by the length of two perpendicular diameters along the major and minor axes of the ellipse. An error in locating the perpendicular diameters d_1 and d_2 , e.g., d_1 is measured at an angle θ from the minor axis, results in an incorrect estimate of the vessel area and volume flow.

2.4. Theoretical analysis

To investigate the effects of error sources in volume flow estimation, a theoretical investigation is made by using a numerical implementation of Womersley–Evans model for pulsatile flow [15,27]. Womersley–Evans model incorporates the pulsatile behavior of blood flow and creates more realistic physiological waveforms than a parabolic profile. The flow pattern is decomposed into sinusoidal components, which are added to attain velocity profiles in time and space. The generated velocity profiles are used in the volume flow estimator, and they are useful for investigating the volume flow error sources (A-E). The parameters varied in the analysis are the distance between velocity estimation points Δg , vessel radius for volume flow estimation r_Q , off-axis distance d_{off} , and angle θ of a non-perpendicular diameter d_1 . The obtained results are also used in Section 3.3.2 to correct for errors in measured vector velocity volume flow estimates.

In this study, velocity profiles were created for a number of time steps throughout a cardiac cycle to mimic pulsatile flow. Two characteristic, but very different waveforms from the human body, were used: a carotid and a femoral. Both waveforms have large accelerations, and the femoral waveform has also back-flow. Mean temporal velocity of the flow was 0.15 m/s, the heart rate was 62 beats/min, and Womersley's number was 1.05. With a normalized vessel radius of 1, Δg was fixed at 0.05. Volume flow was calculated from (3) for a number of time steps throughout a cardiac cycle by using the generated velocity magnitudes and Δg . The spatial average velocity was also calculated and multiplied by the cross-sectional area to find the volume flow for reference.

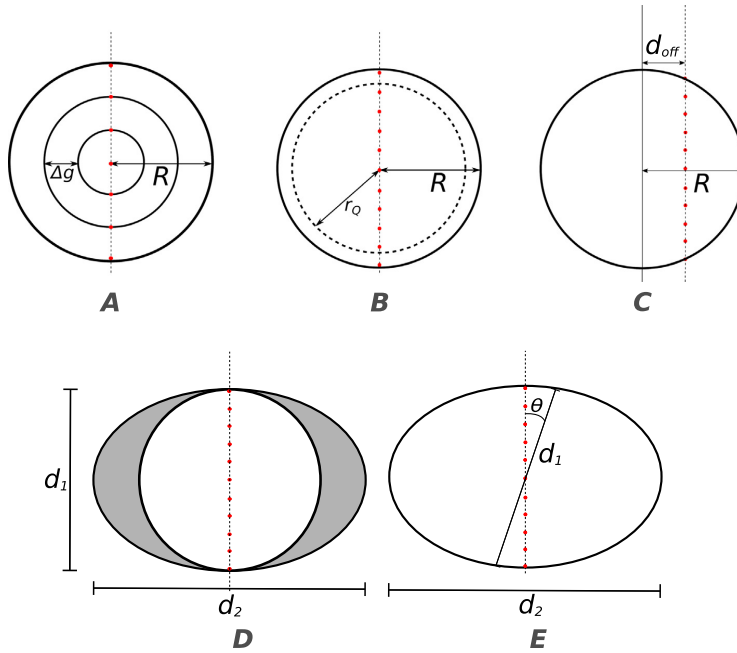


Fig. 2. Cross-sectional views of a vessel with the geometric factors affecting volume flow estimation. Distance between velocity estimation points Δg (A), radius of vessel, r_0 , used for volume flow estimation (B), beam off-axis (C), elliptic versus circular cross-section (D) and non-perpendicular diameters in an elliptical vessel (E).

Error sources result in wrong volume flow estimates, and the errors can be quantified based on the estimated and reference volume flow obtained from the theoretical model. Error is quantified with the deviation from average volume flow, \bar{Q}_{dev} .

$$\bar{Q}_{dev} = \frac{\bar{Q} - \bar{Q}_t}{\bar{Q}_t} \tag{6}$$

\bar{Q} is temporally averaged volume flow during a cycle, and \bar{Q}_t is the true temporally averaged volume flow.

2.5. Flow phantom measurements

Measurements of realistic flow profiles on a flow phantom were performed to validate the volume flow estimator and establish its accuracy, when using vector velocity estimates provided by a commercial scanner. Thereby, a setup with effects from echo canceling and vessel wall movement was also included. The measurements were conducted using an UltraView 800 ultrasound scanner (BK Medical, Herlev, Denmark) and a 9 MHz 128-element linear array transducer (8670, BK Medical). Flow was generated by a Compu-Flow 1000 pump (Shelley Medical Imaging Technologies, Toronto, Canada) connected to an 8-mm-diameter straight tube filled with a blood mimicking fluid for ultrasound (Shelley Medical Imaging Technologies). The flow tube was embedded in agar to mimic the characteristics of human tissue, and the distance from the tube center to the transducer was 27 mm. The pump was set to use a carotid waveform with an average volume flow of either 120, 240, 360 or 480 mL/min, the cardiac period was 840 ms, and the beam-to-flow angle was 90°. The pulse repetition frequency, f_{prf} , was adjusted for each scan to the lowest level without aliasing and was either 1.3, 2.1, 3.1, or 4.1 kHz. Wall filter and color gain was in each case adjusted to the level providing optimal filling of

the vessel without flow being visualized outside the vessel. The transducer was placed where the vessel had its widest diameter. Three uninterrupted 15-s. cine-loop video recordings were made with a frame rate of 15 Hz, which was limited by the memory capacity of the commercial ultrasound system.

2.6. Clinical study

The effects of error sources on volume flow were investigated for twenty patients with arteriovenous fistulas for hemodialysis. All patients had mature (> three months since creation), functional arteriovenous fistulas, and were not in risk of referral to intervention. Written informed consent was obtained. The local Ethics Committee waived approval, because ultrasound scanning of arteriovenous fistulas is considered a routine procedure.

Scans were performed by an experienced radiologist, and the same scanner and transducer as for the flow phantom measurements were used. The transducer was positioned on the fistula between puncture sites of the dialysis needles as illustrated in Fig. 3. Initially, each fistula was scanned with a cross-sectional view for orientation purposes and to measure two perpendicular diameters of the fistula. The fistula was then scanned longitudinally to record TO vector velocities in a plane along the fistula. Scans were performed with a light touch of the transducer on the skin to avoid deformation of the fistula. The angle of insonification was 90° in 19 of the fistulas and 70° for one fistula. The f_{prf} was adjusted for each fistula to the lowest level without aliasing, and seventeen of the fistulas were scanned with a f_{prf} of either 2.0, 3.0, or 4.1 kHz. The remaining three were scanned with a f_{prf} of 5.0, 7.0, and 11.9 kHz. The scans were performed just prior to dialysis, and the remaining settings and procedures were the same as for the flow phantom measurements. The scans were also

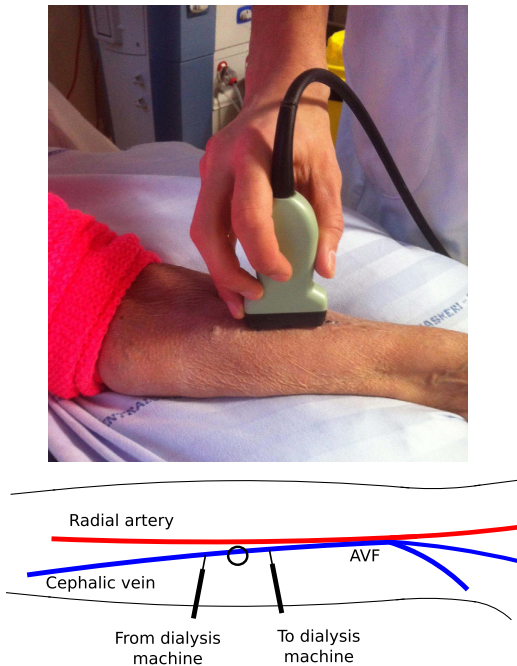


Fig. 3. Illustration of the *in vivo* measurement situation. The photo is from a scan of a patient's fistula just before dialysis session, and the illustration shows position of the transducer (black circle) on the fistula between the puncture sites of dialysis needles.

described by Hansen et al. [10], which used a simplified volume flow estimator and did not consider error sources.

The cross-sectional diameters d_1 and d_2 of the blood vessel were determined by measuring two diameters on a cross-sectional B-mode scan. The distance from the superficial to the deep tunica intima (d_1) and the mediolateral diameter (d_2) were measured manually using the built-in length gauge of the scanner (see also Fig. 7). From each recorded VFI frame, volume flow was calculated off-line using (3)–(5), and thereby the average volume flow during a scan sequence of 15 s. was calculated. Only a selected region corresponding to 15% of the middle part of the examined area was used for volume flow estimation (approximately $m = 60$ image lines, corresponding to 3 mm). This ensured a constant diameter of the investigated fistula and a nearly constant flow profile longitudinally. The distance Δg was 0.33 mm for a beam-to-flow angle of 90° . The cardiac pulse length was found by calculating the auto-correlation of the velocity magnitude at the vessel center for each scan sequence. Thereby, frames for a whole number of cardiac cycles were used in (5).

The width of the vessel in the scan plane was also estimated from VFI data in a longitudinal scan sequence. The scanner's blood-tissue discriminator sets the velocity outside of the flow region to zero. The vessel width d_{scanner} was found from the number of samples inside the flow region and Δg . Thereby, d_{scanner} and d_1 were used to investigate beam-vessel intersection.

Ultrasound Dilution Technique (UDT) is the reference and gold standard method in the clinic for measuring volume flow in arteriovenous fistulas [8]. UDT measurements were performed in this study for volume flow comparison. A Transonic HD03 Flow-QC Hemodialysis Monitor (Transonic Systems Inc., Ithaca, NY, USA)

was used for measuring UDT, where a known amount of indicator was injected in the blood stream to measure the change in blood protein concentration as a function of time.

UDT measurement Q_{UDT} and vector velocity volume flow measurement Q were compared by calculating the error Q_{err} .

$$Q_{\text{err}} = Q - Q_{UDT}. \quad (7)$$

Volume flow measurements were also analyzed using a two-way ANOVA with a null hypothesis of equal means between two methods. Patients were used as blocking and the significance level was 0.05.

3. Results

In this section, results from the theoretical analysis, flow phantom measurements, and clinical study are presented.

3.1. Theoretical analysis

The volume flow error is quantified for error sources A, B, C, and E. The error for source D was given in Section 2.3 according to the work in [19].

Fig. 4(a) shows the error in volume flow estimation as a function of the distance between velocity estimation points, Δg , for the carotid (red) and femoral (blue) waveform. The two curves are on top of each other, and the trend is parabolic with an increase in volume flow error for larger Δg . Increasing Δg , decreases the number of velocity estimates and, thereby, the spatial resolution of the estimated velocity profile. Additionally, the weight of each velocity estimate is larger, since the area of each semi-annular ring is increased.

An average fistula from the clinical study has dimensions $d_1 = 9.4$ mm and $d_2 = 10.2$ mm. With a four-cycle excitation pulse and center frequency of 9 MHz as in the scans, Δg was 0.33 mm, and this corresponds to 6% of an average fistula radius. This results in less than 2% average volume flow error according to Fig. 4(a).

The volume flow estimator relies on a proper measurement of the cross-sectional vessel area. Reducing the radius of the vessel used for volume flow estimation, $r_Q < R$, corresponds to excluding velocity estimates close to the vessel boundary, where the weight function $|n|$ has large values. The volume flow errors are shown as a function of r_Q in Fig. 4(b). No difference in volume flow error is obtained between the carotid and femoral waveforms. The figure shows that at least 85% of the vessel radius should be identified to achieve less than 5% average volume flow error. A vessel radius underestimated by 15% corresponds to 0.75 mm in the average fistula, which is not an unrealistic underestimation of the vessel lumen.

The influence of displacing the transducer relative to the vessel center, i.e., acquiring velocities along a line off the center axis, is shown in Fig. 4(c). The off-axis distance d_{off} from the vessel center is expressed as a percentage of vessel radius R , and the two graphs in Fig. 4(c) have the characteristic shape of a sigmoid curve. The curves for the carotid and femoral waveforms are on top of each other, except for off-axis distances less than 10%, where the difference is 1–2 percentage points. For the average fistula, an off-axis distance of 30% corresponds to 1.5 mm and results in 17% deviation from the average volume flow during a cardiac cycle.

The effects of not measuring d_1 and d_2 perpendicularly and along the major and minor axes of an ellipse are shown in Fig. 5. The angle θ is measured between d_1 and the minor axis and was varied from 0° to 45° . One of the diameters (d_2 on a B-mode image) was kept fixed in the calculation, while the length of d_1 was measured at each angle. The velocity profile was measured along the minor axis of the ellipse. Each of the curves in Fig. 5 corresponds

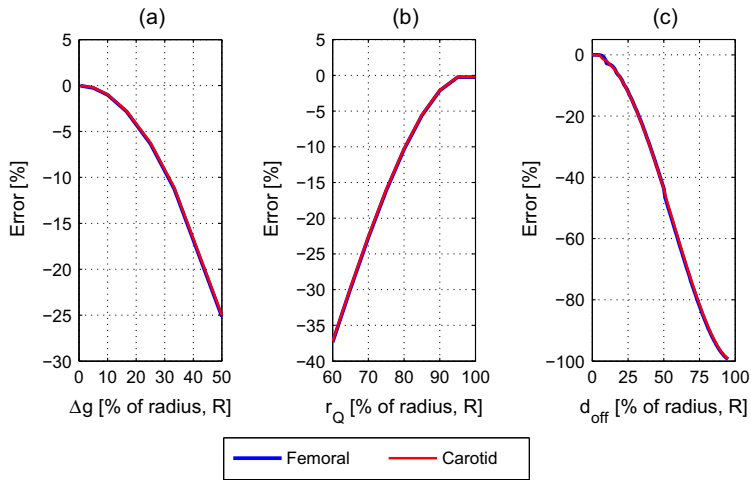


Fig. 4. Volume flow errors calculated as deviation of average volume flow for a femoral (blue) and carotid (red) waveform. In (a) for different distances between velocity estimation points, Δg ; in (b) as a function of vessel radius, r_Q ; and in (c) for a beam being off the vessel axis by the distance, d_{off} . All distances are expressed as a percentage of the radius, R . (For interpretation of the references to colour in this figure legend, the reader is referred to the web version of this article.)

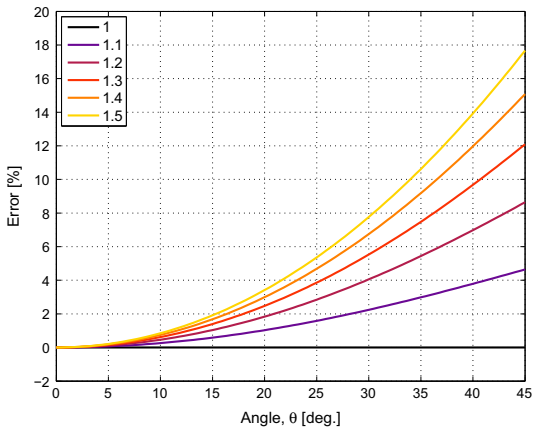


Fig. 5. Volume flow errors when using non-perpendicular diameters in elliptic vessels. The diameter d_1 is measured at angles θ from 0° to 45° from the minor axis. Each graph is for a specific elliptic geometry, d_2/d_1 .

to a specific elliptic geometry, d_2/d_1 , to include the effect of ellipticity. For increasing ellipticity and angle θ , the volume flow error increases. In general, volume flow is overestimated with more than 5% for an ellipticity larger than 1.2 and $\theta > 20^\circ$. For the average fistula, measuring the length of d_1 at 10° from the minor axis corresponds to an overestimation of volume flow by 0.6%.

3.2. Flow phantom measurements

Volume flow estimates for the flow phantom study were calculated from vector velocity data provided by the scanner. Instantaneous reference estimates are not provided by the pump, but the temporally averaged volume flow is. It is compared to measured volume flow using (6). Fig. 6 shows the volume flow error for four levels of true temporally averaged volume flow. The errors were

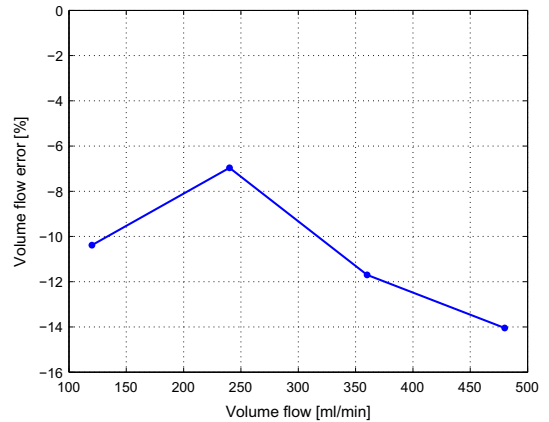


Fig. 6. The relative volume flow error for four volume flow measurements on the flow phantom. A carotid waveform was produced by the pump, and the temporally averaged volume flow was set to 120, 240, 360, and 480 ml/min.

calculated relative to the true volume flow and were between -7% and -14% . The flow phantom measurements thereby establish the accuracy of the volume flow estimator when using vector velocity estimates provided by the commercial scanner. Pulsatile flow with a carotid waveform was used both in the theoretical analysis and flow phantom measurements. Effects from echo canceling and vessel wall movement were included in the phantom measurement. It provides a more realistic measurement situation compared to the theoretical study, but is still a controlled setting compared to *in vivo*.

3.3. Clinical study

Velocity data from the clinical study, sources of error, and correction of volume flow estimates are investigated in this section.

A longitudinal scan of a fistula is shown to the left in Fig. 7, where a VFI is superimposed onto the B-mode image. Examples of velocity magnitudes measured at peak systole for two heart phases are shown to the right in the figure. Velocities are shown as a function of depth for a single scan line. The non-parabolic velocity profiles are used for volume flow estimation with the multi-point method in (3).

Fig. 8 shows velocities as a function of time for the center point on the VFI. Each of the figures are for a measurement on the same patient. Three cardiac cycles are identified on the top and middle figures, and the repeatable waveforms resemble a carotid waveform. However, clear cardiac cycles and waveforms are not always identified as shown in the bottom figure. Velocities vary around a mean value of 0.5 m/s and the maximum velocity is 0.8 m/s. The maximum velocity for all scans of the patients was 2.2 m/s, indicating that flow velocities can be several m/s.

3.3.1. Sources of error

Common errors made when estimating volume flow *in vivo* are presented: compression of the vessels, displacement of the transducer relative to the vessel center, and measuring non-perpendicular diameters. Investigations of errors related to the distance between velocity estimation points and blood-tissue discrimination (Cases A and B in Fig. 2) would require access to RF channel data acquisition. This was not possible with the used scanner and was therefore not investigated *in vivo*.

A B-mode image of a cross-section of an AVF and the diameters are shown in Fig. 9 (left). The image shows the superficially situated fistula and the curvature of the lower arm fistula. Measuring d_2/d_1 for all twenty patients gives an indication of how elliptic the cross-sectional fistulas are. A histogram of ellipticities, d_2/d_1 , among the patients is shown in Fig. 9 (right). The mean \pm one standard deviation (SD) of d_2/d_1 was 1.086 ± 0.105 , so that d_2 on average was 8.6% larger than d_1 . The figure shows that the smallest d_2/d_1 was 0.965, while the largest was 1.426. Additionally, no patients had perfectly circular vessels.

Beam-vessel intersection is investigated by using VFI data and B-mode images. The actual vessel diameter, d_{scanner} , is determined as the average width of the non-zero parts of the velocity profiles (see Fig. 7) and was compared to the diameter d_1 on a B-mode image for each patient. For half of the patients, d_{scanner} was larger than d_1 on the B-mode image of the cross-sectional vessel, indicating that the transducer was offset. For the rest of the patients, d_{scanner} was smaller than d_1 , i.e., the transducer was displaced,

and an off-axis distance relative to d_2 was calculated based on the elliptical dimensions of the fistula. By averaging the off-axis distances over all patients, the mean \pm one SD is 0.15 ± 0.08 cm. This corresponds to $28.5 \pm 11.3\%$ relative to the semi-major axis $d_2/2$.

The diameters in the fistula to the left in Fig. 9 are not perpendicular. The mean \pm one SD of the angle error θ is $1.7 \pm 1.1^\circ$ for all patients in the study. The maximum angle error for the non-perpendicular diameters was 3.5° , which results in less than 0.1% overestimation of volume flow according to the theoretical result in Fig. 5.

3.3.2. Correcting volume flow estimates

The effects of assuming circular vessels and the ultrasound beam being off-axis are demonstrated by calculating volume flow for each scanned patient. Since the measured diameters were almost perpendicular in all scans, the effects from this error source on volume flow were omitted. When the volume flow errors are identified, a correction of the estimates can be performed based on the theoretical analysis. This is explained in the following.

Initially, mean volume flow was estimated based on vector velocities by assuming a circular vessel area with $R = d_1/2$. Then, mean volume flow was estimated by assuming an elliptical vessel area by including d_2 . The volume flow error with respect to UDT is shown in the top part of Fig. 10 in the cases of assuming circular and elliptical vessel areas. The error is calculated using (7) and is plotted as a function of vessel geometry, d_2/d_1 , in Fig. 10. The larger the value of d_2/d_1 , the larger is the difference between assuming a circular and elliptic vessel. The figure shows that by using elliptical vessel geometries rather than circular, the volume flow error with respect to UDT was reduced for all patients, except two. Furthermore, one under estimation changed to an over estimation after applying the elliptical geometry.

The beam was off-axis ($d_{\text{scanner}} < d_1$) for ten of the patients, and the off-axis distances were calculated as explained in Section 3.3.1. The volume flow errors corresponding to off-axis distances were quantified theoretically in Fig. 4(c). This error can be compensated for by correcting the volume flow estimate. For example, for a 20% off-axis error, volume flow is underestimated with 8%, thus, a correction factor of $1/0.92 = 1.09$ is used. Velocities, distances and volume flow errors used in the theoretical model were normalized and provided relative correction factors to use in the clinical study. Correction factors from the carotid profile were used, and volume flow estimates were, thereby, off-axis corrected for patients with

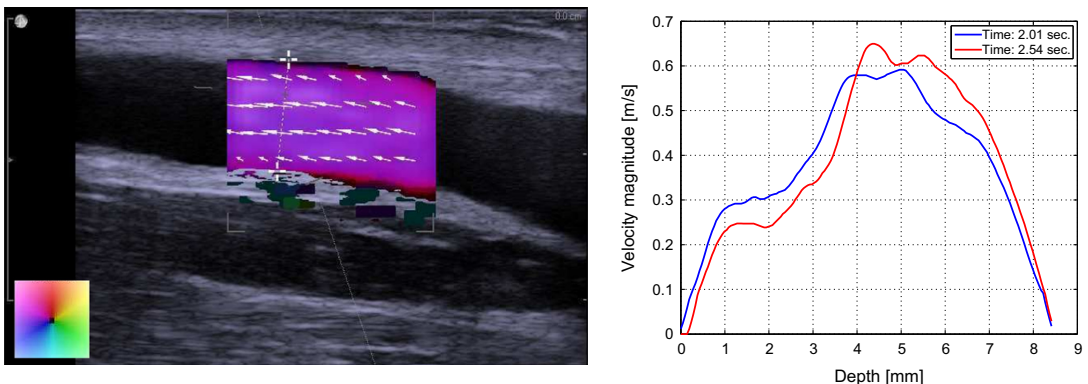


Fig. 7. Longitudinal VFI scan of a fistula (left), where the arrows indicate velocity direction and magnitude. Velocity profiles as a function of axial distance are shown to the right for two systolic heart phases.

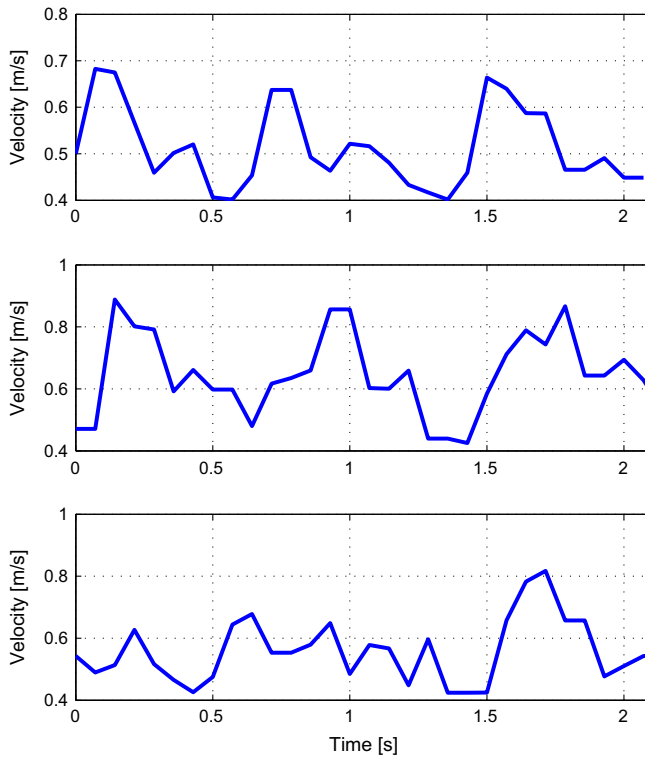


Fig. 8. Velocities as a function of time for the center point on the VFI in Fig. 7. Each of the three figures are for a measurement on the same patient.

an off-axis scan plane. The bottom part of Fig. 10 shows volume flow errors after off-axis correction, and the estimates are plotted as a function of the off-axis distances. Note, only patients with off-axis correction were included for the analysis in the bottom part of Fig. 10. The corresponding volume flow errors relative to UDT measurements are shown in Fig. 11.

The off-axis correction reduced volume flow errors with respect to UDT for all patients, except one. The error was not reduced for patients with off-axis distances less than 15%, while the error reduced when the distance was larger.

The absolute error of vector volume flow estimates relative to UDT measurements was calculated for each patient in the cases

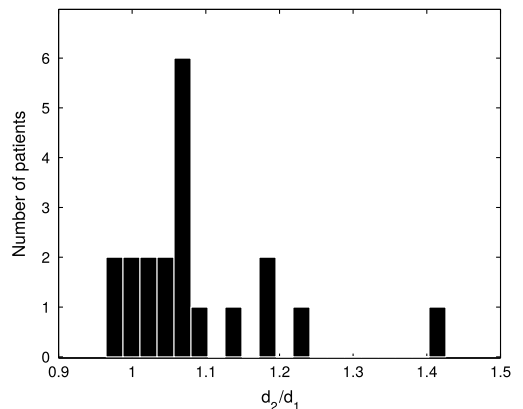
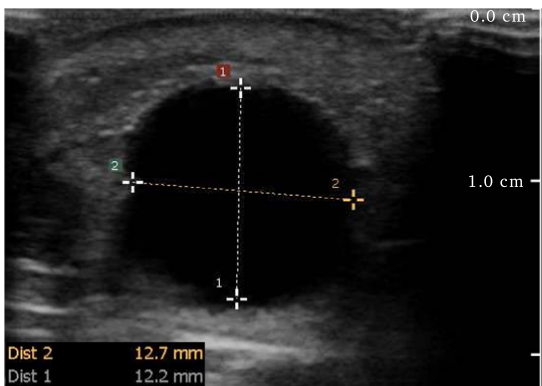


Fig. 9. The left figure shows a B-mode image of an arteriovenous fistula for measurement of the cross-sectional diameters d_1 and d_2 . The right figure shows a histogram of the ellipticities, d_2/d_1 , of the patients' fistulas.

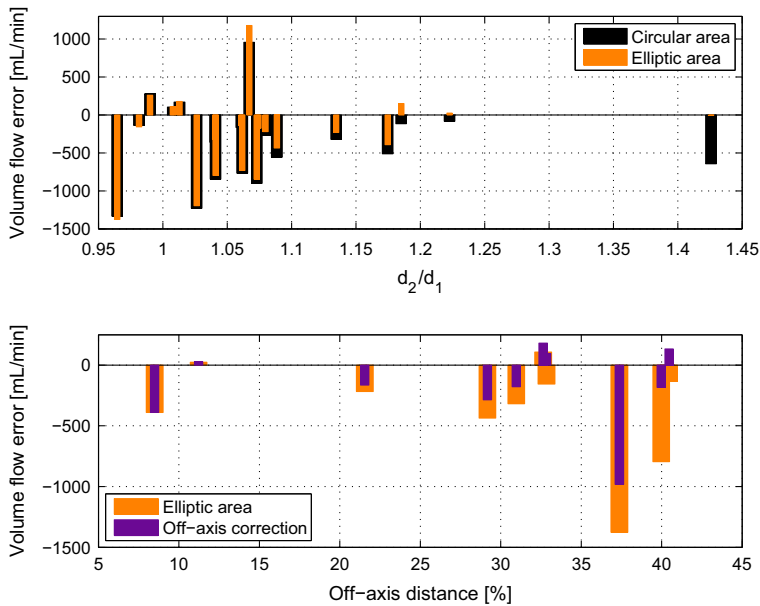


Fig. 10. Volume flow errors in mL/min with respect to UDT. Top figure: For each patient, volume flow error by assuming circular vessels (black) and assuming elliptical vessels (orange) are shown. Estimates are plotted as a function of vessel geometry d_2/d_1 . Bottom figure: volume flow error after off-axis correction (purple) for patients, where the beam was off-axis. Estimates are plotted as a function of off-axis distance. (For interpretation of the references to colour in this figure legend, the reader is referred to the web version of this article.)

of circular vessels, elliptical vessels, and off-axis corrections. The results of averaging the relative volume flow errors over all twenty patients are listed in Table 1. The decrease in error from using a circular area to using an elliptical area (including off-axis correction) was significant ($p = 0.008$). The decrease in absolute error from using a circular area to using an elliptical area (no off-axis correction) was also significant ($p = 0.04$).

4. Discussion

Sources of error in vector velocity volume flow estimation were investigated in a theoretical model and clinical study. Measurements on a flow phantom were made to establish the accuracy of volume flow estimates from a scanner used in the clinical study. The underestimation of volume flow by 7–14% in a realistic setup with vessel wall movement and echo canceling is in accordance with previous investigations of the TO method [24] and for volume flow using Doppler ultrasound and manual angle correction [5,17,19]. A bias in the estimation scheme can be accounted for as shown by Jensen [28], but is not yet implemented in the commercial scanners.

The theoretical analysis uses the classical Womersley–Evans model to quantify the sources of error. More complicated models could have been utilized to include the effects from tissue clutter [29,30]. However, Womersley–Evans model is well-established and considered adequate for investigating error sources related to volume flow estimation. Furthermore, velocity estimates obtained from flow phantom measurements were affected by tissue clutter, hence, the need for simulating this effect is reduced. Parameters related to the TO method for estimating vector velocities were not considered here, as they have already been investigated in the literature [24].

Carotid and femoral waveforms were used in the theoretical analysis to study flow representing physiologically realistic and common waveforms. No significant differences in volume flow error were obtained between the two waveforms, because temporally averaged estimates were used. Hence, the mean volume flow during a cardiac cycle is important, and not the temporal variations during a cycle. The carotid and femoral waveforms have different spatial velocity profiles, and it can explain the small differences for the off-axis analysis in Fig. 4(c). Measured velocities in the AVFs were shown in Fig. 8 (top and middle) and resemble a carotid waveform, however, AVFs also have different flow patterns as shown in Fig. 8 (bottom). The carotid waveform is, thus, a simplified but not unrealistic representation of flow in the studied AVFs. Volume flow was, thus, corrected based on temporally averaged estimates and using a correction factor derived from the theoretical analysis. Furthermore, the volume flow estimator assumes axisymmetric flow due to the acquisition of vector flow in a single scan plane. This is another limitation of the presented method, since flow in the AVF can be non-axisymmetric.

The theoretical analysis quantified the volume flow errors for several sources of error. Especially vessel radius estimation, vessel ellipticity, and off-axis sampling of the velocity estimates resulted in volume flow errors.

The true radius of a vessel *in vivo* is usually unknown, and the vessel radius can therefore only be estimated using ultrasound blood-tissue discrimination. The wall filter settings are crucial for detecting low velocities and to get an accurate estimate of $d_{scanner}$. While the basic settings of the wall filter were restricted by the scanner, it was, however, optimized by adjusting the wall filter frequency to provide optimal filling of the vessel without flow being visualized outside the vessel and cutting lower flow frequencies. Echo canceling, side lobes, and velocity estimator are also factors influencing flow estimation and thereby the estimate of $d_{scanner}$.

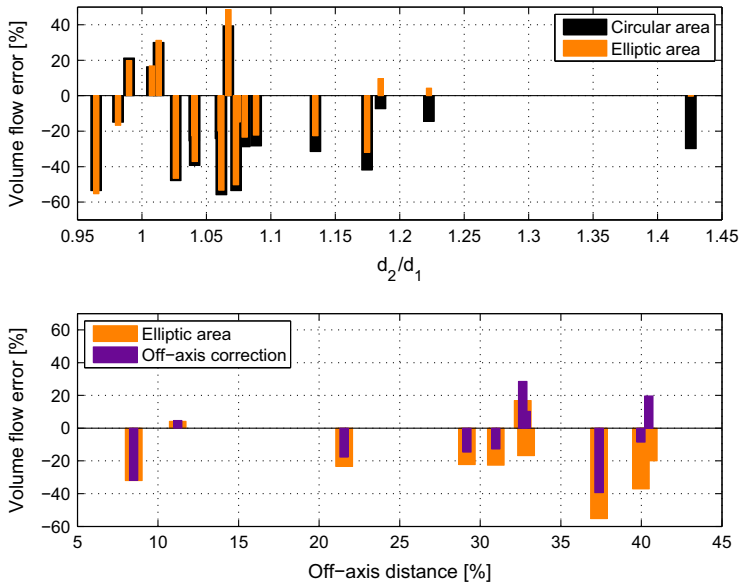


Fig. 11. Relative volume flow errors with respect to UDT. Top figure: For each patient, volume flow error by assuming circular vessels (black) and assuming elliptical vessels (orange) are shown. Estimates are plotted as a function of vessel geometry d_2/d_1 . Bottom figure: volume flow error after off-axis correction (purple) for patients, where the beam was off-axis. Estimates are plotted as a function of off-axis distance. (For interpretation of the references to colour in this figure legend, the reader is referred to the web version of this article.)

Table 1
Absolute volume flow error relative to Ultrasound Dilution Technique and averaged over all patients. Calculated for the three methods and shown as mean \pm 1 SD.

Methods	Error (%)
Circular area	31.2 \pm 14.1
Elliptic area	27.4 \pm 16.4
Elliptic area and off-axis correction	24.3 \pm 16.2

[24]. Another challenge in relation to this error source is the variation of the vessel diameter, which changes as a function of time in both arteries and veins as was investigated in [11]. This effect is partly taken into account as the discriminator will give different outputs depending on what is measured. Changes in the vessel diameter are a large field of research and several methods have applications in ultrasound flow and anatomical imaging. Tracking the wall movements as suggested by Rabben et al. [31] and Cinthio et al. [32] could provide insight into vessel diameter changes and be applied for volume flow estimation.

The clinical study showed that AVFs are elliptical vessels and that this should be taken into account when estimating the volume flow. The volume flow error with respect to UDT was reduced for all patients, except two, when using elliptical rather than circular geometry. This was shown in the top part of Fig. 10. A 90° rotation of the transducer was needed for measuring the elliptic cross-sectional diameters, however, transducer displacement could lead to the beam being off-axis. By using cross-sectional B-mode scans, it would be possible to obtain a guidance for beam-vessel intersection.

Moving the transducer from the vessel center results in considerable volume flow underestimation as shown in Fig. 4(c). The result is similar to results obtained in [19], which was applied for Doppler ultrasound and constant flow. The beam was off-axis for

half of the patients in this study, and the average off-axis distance was 28.5%. It corresponds to a 15% underestimation of volume flow according to the theoretical analysis. The results reveal that even though the scans were performed carefully by an experienced medical doctor, it was difficult to scan with the beam in the center of a vessel.

Duplex ultrasound flow measurements were 25–30% lower than UDT measurements in previous studies [9,33]. One should also be careful with comparing volume flow estimated with UDT and vector flow as there are difficulties with both methods. UDT is considered the gold standard for volume flow estimation in AVFs, but insufficient mixing of the diluting agent in the blood can lead to erroneous UDT flow measurements [8]. Vector flow scans and UDT measurements should be made in the very beginning of a dialysis session [33], but the measurements cannot be made at the exact same time. The time between vector flow scans and UDT measurements was, therefore, minimized as much as possible. Furthermore, the clinical results show that the TO method estimates the volume flow lower than UDT measurements in most cases. Underestimated volume flow estimates were also obtained for the flow phantom measurements.

Despite limitations of 2D vector velocity estimation in a single plane and the assumptions needed to estimate volume flow, the method is capable of noninvasive volume flow estimation *in vivo*. The presented method has quantified the accuracy of the estimator and is able to correct for the errors made in clinical scans. The reduction in relative volume flow error from using a circular area to using an elliptic area and off-axis corrected estimates showed this ability (Table 1). Influence of non-perpendicular diameters on volume flow estimation were minimal in this study. Volume flow was estimated in AVFs, but the technique and corrections can be applied for other vessels, where a linear array probe is suitable. The TO technique is implemented for linear array transducers on commercial BK scanners, and implementation of the technique

on phased array and convex array transducers increase the depth at which vessels can be investigated [28,34].

5. Conclusions

A vector velocity volume flow estimator and its sources of error were presented in this paper. Volume flow errors have been quantified using a theoretical model, flow phantom measurements, and the method has been investigated *in vivo* under realistic clinical conditions. It has been demonstrated that dimensions of elliptic vessels and beam-vessel intersection should be taken into account to avoid volume flow underestimation. The beam was on average $28.5 \pm 11.3\%$ off-axis in a clinical study of arteriovenous fistulas, and it could lead to 15% underestimated volume flow according to the theoretical analysis. This should be taken into account in the scan protocol for volume flow measurements, and could potentially be done by providing markers on the screen for guidance. Using an elliptical vessel area, rather than a circular, for volume flow estimation and correcting the beam for being off-axis reduced the error significantly ($p = 0.008$) from 31.2% to 24.3% relative to UDT measurements.

Acknowledgments

This work was supported by Grant 82-2012-4 from the Danish National Advanced Technology Foundation and by BK Ultrasound.

References

- [1] T. Wada, K. Kodaira, K. Fujishiro, T. Okamura, Correlation of common carotid flow volume measured by ultrasonic quantitative flowmeter with pathological findings, *Stroke* 22 (3) (1991) 319–323, <http://dx.doi.org/10.1161/01.STR.22.3.319>.
- [2] P. Wiese, B. Nonnast-Daniel, Colour Doppler ultrasound in dialysis access, *Nephrol. Dial. Transpl.* 19 (8) (2004) 1956–1963, <http://dx.doi.org/10.1093/ndt/gfh244>.
- [3] M. Allon, M.L. Robbin, Increasing arteriovenous fistulas in hemodialysis patients: problems and solutions, *Kidney Int.* 62 (4) (2002) 1109–1124, <http://dx.doi.org/10.1046/j.1523-1755.2002.00551.x>.
- [4] D. Shemesh, I. Goldin, D. Berelowitz, I. Zaghal, C. Zigelman, O. Olsha, Blood flow volume changes in the maturing arteriovenous access for hemodialysis, *Ultrasound Med. Biol.* 33 (5) (2007) 727–733, [doi:http://dx.doi.org/10.1016/j.ultrasmedbio.2006.11.019](http://dx.doi.org/10.1016/j.ultrasmedbio.2006.11.019).
- [5] K. Hoyt, F.A. Hester, R.L. Bell, M.E. Lockhart, M.L. Robbin, Accuracy of volumetric flow rate measurements: an *in vitro* study using modern ultrasound scanners, *J. Ultrasound Med.* 28 (11) (2009) 1511–1518.
- [6] H.J.T. Huijbregts, M.L. Bots, C.H.A. Wittens, Y.C. Schrama, F.L. Moll, P.J. Blankestijn, Hemodialysis arteriovenous fistula patency revisited: results of a prospective, multicenter initiative, *Clin. J. Am. Soc. Nephrol.* 3 (3) (2008) 714–719, <http://dx.doi.org/10.2215/CJN.02950707>.
- [7] W.L. Whittier, Surveillance of hemodialysis vascular access, *Seminars Intervent. Radiol.* 26 (2) (2009) 130–138, <http://dx.doi.org/10.1055/s-0029-1222457>.
- [8] N.M. Krivitski, Theory and validation of access flow measurement by dilution technique during hemodialysis, *Kidney Int.* 48 (1) (1995) 244–250.
- [9] C. Schwarz, C. Mitterbauer, M. Boczula, T. Maca, M. Funovics, G. Heinze, M. Lorenz, J. Kovarik, R. Oberbauer, Flow monitoring: performance characteristics of ultrasound dilution versus color Doppler ultrasound compared with fistulography, *Am. J. Kidney Dis.* 42 (3) (2003) 539–545, [http://dx.doi.org/10.1016/s0272-6386\(03\)00786-8](http://dx.doi.org/10.1016/s0272-6386(03)00786-8).
- [10] P.M. Hansen, J.B. Olesen, M.J. Pihl, T. Lange, S. Heerwagen, M.M. Pedersen, M. Rix, L. Lønn, J.A. Jensen, M.B. Nielsen, Volume flow in arteriovenous fistulas using vector velocity ultrasound, *Ultrasound Med. Biol.* 40 (11) (2014) 2707–2714.
- [11] R.W. Gill, Measurement of blood flow by ultrasound: accuracy and sources of error, *Ultrasound Med. Biol.* 11 (1985) 625–641.
- [12] C. Vergara, R. Ponzini, A. Veneziani, A. Redaelli, D. Neglia, O. Parodi, Womersley number-based estimation of flow rate with Doppler ultrasound: sensitivity analysis and first clinical application, *Comput. Meth. Prog. Bio.* 98 (2) (2010) 151–160, <http://dx.doi.org/10.1016/j.cmpb.2009.09.013>.
- [13] P.N. Burns, Measuring volume flow with Doppler ultrasound: an old nut, *Ultrasound Obstet. Gyn.* 2 (4) (1992) 238–241, <http://dx.doi.org/10.1046/j.1469-0705.1992.02040237-2.x>.
- [14] K.V. Canney, A. Swillens, L. Løvstakken, L. Antiga, P. Verdonck, P. Segers, The accuracy of ultrasound volume flow measurements in the complex flow setting of a forearm vascular access, *J. Vasc. Access* 14 (3) (2013) 281–290, <http://dx.doi.org/10.5301/jva.5000118>.
- [15] J.R. Womersley, Oscillatory motion of a viscous liquid in a thin-walled elastic tube. I: The linear approximation for long waves, *Phil. Mag.* 46 (1955) 199–221.
- [16] C.A.D. Leguy, E.M.H. Bosboom, A.P.G. Hoeks, F.N. van de Vosse, Model-based assessment of dynamic arterial blood volume flow from ultrasound measurements, *Med. Biol. Eng. Comput.* 47 (6) (2009) 641–648, <http://dx.doi.org/10.1007/s11517-009-0473-9>.
- [17] S. Ricci, M. Cinthio, A. Ahlgren, P. Tortoli, Accuracy and reproducibility of a novel dynamic volume flow measurement method, *Ultrasound Med. Biol.* 39 (10) (2013) 1903–1914.
- [18] A. Swillens, K.V. Canney, P. Segers, S. Ricci, P. Tortoli, The multigate Doppler approach for assessing hemodynamics in a forearm vascular access for hemodialysis purposes, in: *Proc. IEEE Ultrason. Symp.*, 2013, pp. 1494–1497, [doi:http://dx.doi.org/10.1109/ULSYM.2013.0379](http://dx.doi.org/10.1109/ULSYM.2013.0379).
- [19] P.A. Picot, P.M. Embree, Quantitative volume flow estimation using velocity profiles, *IEEE Trans. Ultrason. Ferroelec., Freq. Contr.* 41 (1994) 340–345.
- [20] J.A. Jensen, P. Munk, A new method for estimation of velocity vectors, *IEEE Trans. Ultrason. Ferroelec., Freq. Contr.* 45 (1998) 837–851.
- [21] M.J. Pihl, J.A. Jensen, A transverse oscillation approach for estimation of three-dimensional velocity vectors. Part I: Concept and simulation study, *IEEE Trans. Ultrason. Ferroelec., Freq. Contr.* 61 (2014) 1599–1607.
- [22] J. Jensen, J.B. Olesen, P.M. Hansen, M.B. Nielsen, J.A. Jensen, Accuracy and sources of error for an angle independent volume flow estimator, in: *Proc. IEEE Ultrason. Symp.*, 2014, pp. 1714–1717.
- [23] J.A. Jensen, A new estimator for vector velocity estimation, *IEEE Trans. Ultrason. Ferroelec., Freq. Contr.* 48 (4) (2001) 886–894.
- [24] J. Udesen, J.A. Jensen, Investigation of transverse oscillation method, *IEEE Trans. Ultrason. Ferroelec., Freq. Contr.* 53 (2006) 959–971.
- [25] K.L. Hansen, J. Udesen, C. Thomsen, J.A. Jensen, M.B. Nielsen, *In vivo* validation of a blood vector velocity estimator with MR angiography, *IEEE Trans. Ultrason. Ferroelec., Freq. Contr.* 56 (1) (2009) 91–100.
- [26] H. Liebgott, A. Basarab, P. Gueth, D. Friboulet, P. Delachartre, Transverse oscillations for tissue motion estimation, *Ultrasonics* 50 (6) (2010) 548–555.
- [27] D.H. Evans, Some aspects of the relationship between instantaneous volumetric blood flow and continuous wave Doppler ultrasound recordings III, *Ultrasound Med. Biol.* 8 (1982) 617–623.
- [28] J.A. Jensen, A.H. Brandt, M.B. Nielsen, Convex array vector velocity imaging using transverse oscillation and its optimization, *IEEE Trans. Ultrason. Ferroelec., Freq. Contr.* 62 (12) (2015) 2043–2053, <http://dx.doi.org/10.1109/TUFFC.2015.006970>.
- [29] A. Swillens, L. Løvstakken, J. Kips, H. Torp, P. Segers, Ultrasound simulation of complex flow velocity fields based on computational fluid dynamics, *IEEE Trans. Ultrason. Ferroelec., Freq. Contr.* 56 (3) (2009) 546–556, <http://dx.doi.org/10.1109/TUFFC.2009.1071>.
- [30] R.K. Warriner, K.W. Johnston, R.S.C. Cobbold, A viscoelastic model of arterial wall motion in pulsatile flow: implications for doppler ultrasound clutter assessment, *Physiol. Meas.* 29 (2) (2008) 157–179.
- [31] S. Rabben, S. Bjaerum, V. Sorhus, H. Torp, Ultrasound-based vessel wall tracking: An auto-correlation technique with RF center frequency estimation, *Ultrasound Med. Biol.* 28 (4) (2002) 507–517, [http://dx.doi.org/10.1016/S0301-5629\(02\)00487-8](http://dx.doi.org/10.1016/S0301-5629(02)00487-8).
- [32] M. Cinthio, A.R. Ahlgren, T. Janson, A. Eriksson, H.W. Persson, K. Lindstrom, Evaluation of an ultrasonic echo-tracking method for measurements of arterial wall movements in two dimensions, *IEEE Trans. Ultrason. Ferroelec., Freq. Contr.* 52 (2005) 1300–1311.
- [33] R.M. Huisman, M. van Dijk, S. de Bruin, J. Loonstra, W.J. Sluiter, C.J. Zeebregts, J.A.M. van den Dungen, Within-session and between-session variability of haemodialysis shunt flow measurements, *Nephrol. Dial. Transpl.* 20 (12) (2005) 2842–2847, <http://dx.doi.org/10.1093/ndt/gfi142>.
- [34] M.J. Pihl, J. Marcher, J.A. Jensen, Phased-array vector velocity estimation using transverse oscillations, *IEEE Trans. Ultrason. Ferroelec., Freq. Contr.* 59 (12) (2012) 2662–2675.

Accuracy and Sources of Error for an Angle Independent Volume Flow Estimator

Jonas Jensen, Jacob Bjerring Olesen, Peter Møller Hansen,
Michael Bachmann Nielsen, and Jørgen Arendt Jensen

Proceedings of IEEE International Ultrasonics Symposium, p. 1-4,

Accepted for poster presentation in Chicago, Illinois, United States, 2014.

Accuracy and Sources of Error for an Angle Independent Volume Flow Estimator

Jonas Jensen¹, Jacob Bjerring Olesen¹, Peter Møller Hansen^{1,2}, Michael Bachmann Nielsen² and Jørgen Arendt Jensen¹

¹Center for Fast Ultrasound Imaging, Dept. of Elec. Eng. Bldg. 349,
Technical University of Denmark, DK-2800 Lyngby, Denmark

²Department of Radiology, Copenhagen University Hospital, DK-2100 Copenhagen, Denmark.

Abstract—This paper investigates sources of error for a vector velocity volume flow estimator. Quantification of the estimator's accuracy is performed theoretically and investigated *in vivo*. Womersley's model for pulsatile flow is used to simulate velocity profiles and calculate volume flow errors in cases of elliptical vessels and not placing the transducer at the vessel center. Simulations show, i.e., that volume flow is underestimated with 5 %, when the transducer is placed 15 % from the vessel center. Twenty patients with arteriovenous fistulas for hemodialysis are scanned in a clinical study. A BK Medical UltraView 800 ultrasound scanner with a 9 MHz linear array transducer is used to obtain Vector Flow Imaging sequences of a superficial part of the fistulas. Cross-sectional diameters of each fistula are measured on B-mode images by rotating the scan plane 90 degrees. The major axis of the fistulas was on average 8.6 % larger than the minor axis, so elliptic dimensions should be taken into account in volume flow estimation. The ultrasound beam was on average 1.5 ± 0.8 mm off-axis, corresponding to 28.5 ± 11.3 % of the major semi-axis of a fistula, and this could result in 15 % underestimated volume flow according to the simulation. Volume flow estimates were corrected for the beam being off-axis, but was not able to significantly decrease the error relative to measurements with the reference method.

I. INTRODUCTION

Quantifying blood flow to organs is desirable for evaluating the pathological state of the vascular system, i.e., in the carotid artery or at arteriovenous fistulas in dialysis [1]. Among the simplest methods for estimating volume flow non-invasively is the single-point Doppler ultrasound method. The peak velocity is estimated at one location along the presumed centerline of a vessel, and by assuming steady flow and a perfect parabolic velocity profile, the volume flow is calculated based on a circular cross-sectional area of the vessel. A more accurate method is to estimate velocities at several points along the whole vessel diameter, since the actual velocity profile, rather than the assumed one, can be included in the estimator [2], [3]. The method resulted in biases of 5 % for constant flow in a phantom and when using conventional Doppler ultrasound for velocity estimation [3]. Doppler ultrasound estimates the velocity component along the ultrasound beam and a major limitation of the methods is, therefore, associated with determining the correct beam-to-flow angle, which introduces error in volume flow estimation. Furthermore, conventional Doppler ultrasound is challenging for estimation of flow in superficial vessels where flow is nearly transverse to the ultrasound beam.

Several methods have been proposed to remedy the angle dependency problem and extend the conventional ultrasound velocity estimate to vector estimates. Transverse Oscillation (TO) is a method capable of estimating the axial and lateral velocity components independent of each other [4]. By integrating the velocity field obtained from TO vector velocities over a circular cross-section of a vessel, volume flow estimation has been validated *in vivo* in the right common carotid artery and in arteriovenous fistulas [5], [6].

However, in the clinical application of the technique several challenges have been identified, and the sensitivity to deviations from the estimator assumptions should be quantified. The purpose of this paper is to identify the error sources for a vector velocity volume flow estimator and to study their effects on the accuracy of volume flow estimation. This is investigated theoretically and *in vivo*.

II. MATERIALS AND METHODS

A volume flow estimator using vector velocities acquired with the TO approach is presented in this section along with the investigated error sources. Methods for the theoretical and experimental procedures are also presented.

A. Volume Flow Estimation and Sources of Error

TO is an angle-independent method for vector velocity estimation within the ultrasound scan plane. By introducing a lateral oscillation in the pulse-echo field along with the conventional axial oscillation, the received signals become sensitive to both an axial and lateral motion in the field. The transmitted field is weakly focused, and the lateral oscillating field is created in the receive beamforming by changing the apodization function to contain two separated peaks. The axial velocity is estimated as in conventional Doppler ultrasound, while a special autocorrelation estimator is used for the transverse velocity component. The resulting 2D vector velocity estimate represents the velocity magnitude and direction of flow at a specific point, and the estimated velocity magnitudes at locations along a vessel diameter can be used for volume flow calculation. The volume flow Q of a fluid crossing a circular surface is estimated as

$$Q = \pi \cdot \Delta g^2 \sum_{n=-N/2}^{N/2} v_n \cdot |n|, \quad (1)$$

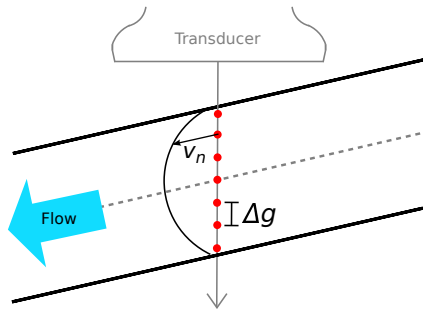


Fig. 1. Longitudinal view of a vessel and velocity estimation at points along the whole vessel diameter. The n th vector velocity sample is v_n and the distance between two samples is Δg .

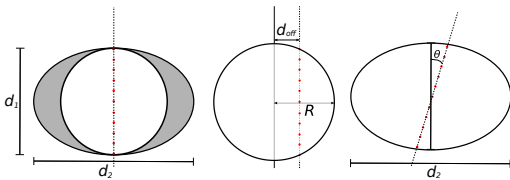


Fig. 2. Sources of error in volume flow estimation: elliptic cross-section (left), beam off-axis (middle) and beam steering in an elliptic vessel (right).

which is a rotation of each vector velocity sample v_n around the symmetry axis at the vessel center [3]. The finite number of velocity samples inside the vessel is N and the distance between two samples is Δg . It is assumed that flow is axisymmetric, the cross-sectional area of the vessel is circular, and that the velocity sampling is along a diameter of the vessel. A geometry of the methodology is shown in Fig. 1. When the beam is swept over a section of the vessel to give a VFI frame, the mean volume flow in the frame is found by averaging the estimates at all lateral positions.

This paper investigates three sources of error in volume flow estimation. An illustration of the errors is shown in Fig. 2. A problem with superficial vessels is that they are easily compressed under the weight of a transducer, which changes the cross-sectional blood vessel area from a circular to elliptical geometry. Another problem is that the ultrasound beam is assumed to intersect the middle of the vessel, but it can be challenging for the examiner to place the transducer at the vessel center. This results in sampling off-axis. Furthermore, the effect of steering the ultrasound beam in a direction that is not along one of the axes of an elliptic vessel should be studied. These three issues introduce error in volume flow estimation, and the error will be quantified in the following.

B. Simulations

To investigate the effect of beam-vessel intersection, a theoretical investigation was performed with Womersley's model for pulsatile flow [7]. Womersley's model incorporates the pulsatile behaviour of blood flow and creates more realistic physiological waveforms than a parabolic profile. The flow

pattern is decomposed into sinusoidal components and added to attain the velocity profile in time and space.

Velocity profiles were created for a number of time steps throughout a cardiac cycle to mimic flow in the carotid artery. The mean velocity of the flow was 0.15 m/s, the heart rate was 62 beats/min and the Womersley's number was 1.05. The volume flow was calculated from (1) for a number of time steps throughout a cardiac cycle by using the generated velocity samples and Δg . The spatial average velocity was also calculated and multiplied by the cross-sectional area to find the volume flow for reference.

C. Experimental Methods

The effects of vessel ellipticity and beam-vessel intersection on volume flow were investigated for twenty patients with arteriovenous fistulas for hemodialysis.

Scannings were performed with an UltraView 800 ultrasound scanner (BK Medical, Herlev, Denmark) and a 9 MHz linear array transducer (8670, BK Medical). Initially, each patient was scanned longitudinally and transversely directly on the fistula for orientation purposes and to measure two perpendicular diameters of the fistula. The transducer was then rotated 90° back to record blood flow longitudinally. The transducer was placed where the fistula had its widest diameter and data were recorded over a period of 15 s. The beam-to-flow angle was approximately 90° and the scans were performed just prior to dialysis. Details of the scanning procedure is described in [5].

From each recorded VFI frame, volume flow was calculated off-line as described in Section II-A, and thereby the average volume flow during a scan sequence of 15 s was calculated.

Ultrasound Dilution Technique (UDT) is the reference method for measuring volume flow in arteriovenous fistulas and was measured with a Transonic HD03 Flow-QC Hemodialysis Monitor in this study for volume flow comparison [8].

Cross-sectional diameters of a blood vessel were determined by measuring two perpendicular diameters on a B-mode image. The actual vessel diameter along the ultrasound beam was also estimated from VFI data in a scan sequence. The scanner has a build-in blood-tissue discrimination and sets the velocity to zero outside the flow region. Thus, the vessel width $d_{scanner}$ was found from the number of samples inside the flow region and Δg .

Volume flow measurements were analysed using a two-way ANOVA with a null hypothesis of equal means between two methods. Patients were used as blocking and the significance level was 0.05.

III. SIMULATION RESULTS

A. Elliptic Cross-section

Calculating volume flow through an elliptic and circular cross-section can be performed by multiplying each velocity estimate v_n with either the area of a circular semi-annulus A_{c_n}

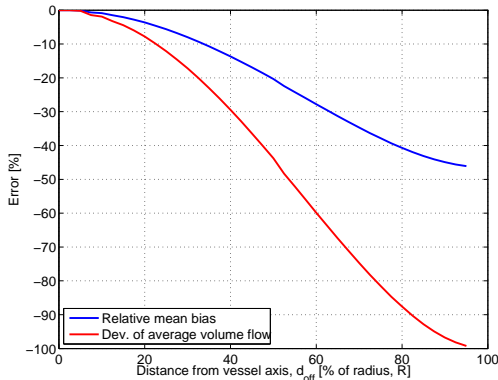


Fig. 3. Beam being off the vessel axis. The distance from the center of the vessel that the beam is off axis, d_{off} , is expressed as a percentage of radius, R . The blue graph is mean relative bias scaled with peak volume flow and the red graph is deviation of volume flow averaged over a cardiac cycle.

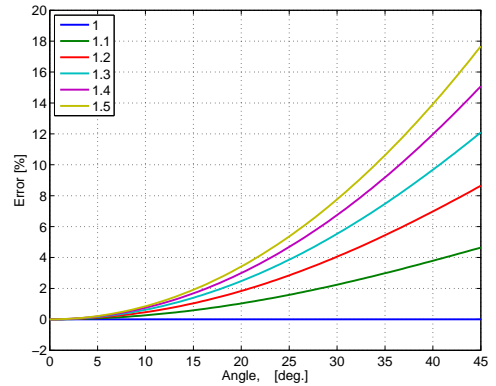


Fig. 4. Volume flow error when the ultrasound beam is steered from 0 to 45° in a vessel with elliptic cross-section. Each graph is for a specific elliptic geometry, d_2/d_1 .

or an elliptic semi-annulus A_{e_n} , respectively,

$$\frac{Q_{ellipse}}{Q_{circ}} = \frac{\sum_{n=-N/2}^{N/2} A_{e_n} v_n}{\sum_{n=-N/2}^{N/2} A_{c_n} v_n} = \frac{\sum_{n=-N/2}^{N/2} \frac{1}{2} \pi [d_{1n} d_{2n} - d_{1_{n-1}} d_{2_{n-1}}] v_n}{\sum_{n=-N/2}^{N/2} \frac{1}{2} \pi [d_{1n}^2 - d_{1_{n-1}}^2] v_n} \quad (2)$$

$$= \frac{\sum_{n=-N/2}^{N/2} [(n^2 \Delta h \Delta g) - (n-1)^2 \Delta h \Delta g] v_n}{\sum_{n=-N/2}^{N/2} [(n \Delta g)^2 - ((n-1) \Delta g)^2] v_n} \quad (3)$$

$$= \frac{\Delta h \cdot \sum_{n=-N/2}^{N/2} [2n-1] v_n}{\Delta g \cdot \sum_{n=-N/2}^{N/2} [2n-1] v_n} = \frac{d_2}{d_1}, \quad (4)$$

where d_1 is the vessel diameter along the ultrasound beam, d_2 is the diameter in the elevation plane and $\Delta h = d_2/N$. The derivation shows that if it is assumed that the vessel has a circular cross-section with diameter d_2 , the error in volume flow estimation is $(d_2/d_1) - 1$, if the true cross-section is elliptic.

B. Beam Off-axis

A full velocity distribution inside a circular vessel was obtained by rotating a simulated velocity half-profile symmetrically around the center axis. By sampling the full velocity distribution along a line off the vessel diameter, volume flow was calculated from the velocity samples by assuming a circular distribution of the samples and using (1). The volume flow was then compared to the true volume flow, and the estimation error is shown in Fig. 3. The off-axis distance d_{off} from the vessel center is expressed as a percentage of vessel radius R , and the blue graph represents the mean relative bias scaled with peak volume flow, while the red graph is the deviation of average flow in a cardiac cycle. Both graphs have the characteristic shape of a sigmoid curve.

C. Beam Steering in Elliptical Vessels

For volume flow estimation in an elliptical vessel, it is assumed that the ultrasound beam is steered in a direction along one of the diameters. The effect of steering in another direction is presented in this section. By keeping one of the diameters fixed (i.e., d_2 on a B-mode image) and measuring d_1 as the width of the actual velocity profile along the direction of the ultrasound beam, volume flow error was calculated for the beam steered from 0 to 45°. The result is shown in Fig. 4 for simulated velocity profiles, and each graph in the figure represent an elliptic geometry.

IV. EXPERIMENTAL RESULTS

A. Elliptic Cross-section

A B-mode image of a cross-section of an arteriovenous fistula and its diameters is shown in Fig. 5. Measuring d_2/d_1 for all 20 patients gives an indication of how elliptic the cross-sectional fistulas were. The mean \pm one std. of d_2/d_1 was 1.086 ± 0.105 , so that d_2 on average was 8.6 % larger than d_1 . To avoid underestimation of volume flow, the dimensions of an elliptic cross-section rather than circular should therefore be taken into account.

B. Beam Off-axis

To investigate beam-vessel intersection in a clinical study, a calculation of the actual vessel diameter, $d_{scanner}$, was performed. This diameter was compared to the diameter d_1 on the B-mode image for each patient. For half of the patients, $d_{scanner}$ was larger than d_1 on the B-mode image, indicating that the transducer was moved. For the rest of the patients, the beam was off-axis and an off-axis distance relative to d_2 was calculated based on the fistula dimensions. By averaging the off-axis distances over all patients, the mean \pm one std. is 0.15 ± 0.08 cm. This corresponds to 28.5 ± 11.3 % relative

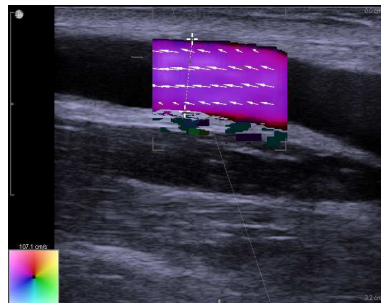
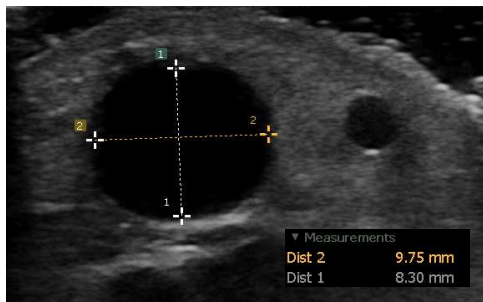


Fig. 5. Example of a B-mode image of an arteriovenous fistula for measurements of the cross-sectional diameters d_1 and d_2 (left) and a longitudinal VFI scan (right). The arrows indicate velocity direction and magnitude.

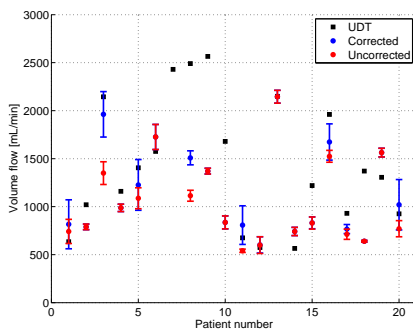


Fig. 6. Volume flow estimates corrected for the beam being off-axis (blue), uncorrected estimates (red), and UDT measurements (black). Each bar represents the mean \pm 1 std.

to d_2 . The results indicate that even though the scans were performed carefully by an experienced medical doctor, it was difficult to scan with the beam in the center of a vessel.

For patients where the beam was off-axis ($d_{\text{scanner}} < d_1$), the volume flow estimates were corrected. The off-axis distance for each patient and correction factors based on the simulated results in Fig. 3 (red graph) were used to calculate corrected volume flow estimates. Fig. 6 shows the results for each patient.

The uncorrected volume flow estimates deviate with a mean \pm one std. of $26.3 \pm 16\%$ compared to the UDT measurements. The deviation of volume flow after correction of the beam being off-axis is $23 \pm 15\%$. Therefore, the correction is able to decrease the error relative to UDT, however, not significantly ($p = 0.92$).

V. DISCUSSION AND CONCLUSION

The effects of vessel ellipticity and not placing the ultrasound transducer at the vessel center have been presented for vector velocity volume flow estimation. The errors have been quantified theoretically and studied *in vivo*. It has been shown that the dimensions of elliptic vessels and beam-vessel

intersection should be taken into account to avoid volume flow underestimation. When the beam is, i.e., 15 % from the vessel center, volume flow is underestimated with 5 %. The beam was on average $28.5 \pm 11.3\%$ off-axis for the clinical study and could lead to 15 % underestimated volume flow according to the simulation. A correction for the beam being off-axis was not able to significantly decrease the error, but difficulties with UDT comparison should be taken into account [5].

A 90° rotation of the transducer is needed for measuring elliptic cross-sectional diameters, however, the transducer rotation can lead to the beam being off-axis. It is therefore recommended to use cross-sectional B-mode scans as guidance for beam-vessel intersection.

ACKNOWLEDGEMENT

This work was supported by grant 82-2012-4 from the Danish National Advanced Technology Foundation and by BK Medical.

REFERENCES

- [1] P. Wiese and B. Nonnast-Daniel, "Colour doppler ultrasound in dialysis access," *Nephrology Dialysis Transplantation*, vol. 19, no. 8, pp. 1956–1963, 2004.
- [2] P. A. Picot and P. M. Embree, "Quantitative volume flow estimation using velocity profiles," *IEEE Trans. Ultrason., Ferroelec., Freq. Contr.*, vol. 41, pp. 340–345, 1994.
- [3] S. Ricci, M. Cinthio, Å. Ahlgren, and P. Tortoli, "Accuracy and reproducibility of a novel dynamic volume flow measurement method," *Ultrasound Med. Biol.*, vol. 39, no. 10, pp. 1903–1914, 2013.
- [4] J. A. Jensen and P. Munk, "A New Method for Estimation of Velocity Vectors," *IEEE Trans. Ultrason., Ferroelec., Freq. Contr.*, vol. 45, pp. 837–851, 1998.
- [5] P. M. Hansen, J. B. Olesen, M. J. Pihl, T. Lange, S. Heerwagen, M. M. Pedersen, M. Rix, L. Lønn, J. A. Jensen, and M. B. Nielsen, "Volume flow in arteriovenous fistulas using vector velocity ultrasound," *Ultrasound Med. Biol.*, p. Accepted for publication, 2014.
- [6] K. L. Hansen, J. Udesen, C. Thomsen, J. A. Jensen, and M. B. Nielsen, "In vivo validation of a blood vector velocity estimator with MR angiography," *IEEE Trans. Ultrason., Ferroelec., Freq. Contr.*, vol. 56, no. 1, pp. 91–100, 2009.
- [7] J. R. Womersley, "Oscillatory motion of a viscous liquid in a thin-walled elastic tube. I: The linear approximation for long waves," *Phil. Mag.*, vol. 46, pp. 199–221, 1955.
- [8] N. M. Krivitski, "Theory and validation of access flow measurement by dilution technique during hemodialysis," *Kidney International*, vol. 48, no. 1, pp. 244–250, jul 1995.